Very short baseline neutrino oscillations study with the STEREO detector at ILL; calibration of the STEREO detector

Loïc-René Labit

UNIVERSITÉ SAVOIE MONT BLANC

THÈSE

Pour obtenir le grade de

DOCTEUR DE L'UNIVERSITÉ SAVOIE MONT BLANC

Spécialité : **Physique Subatomique et Astroparticules**

Arrêté ministériel : 25 Mai 2016

Présentée par

Loïc-René LABIT

Thèse dirigée par **Dominique DUCHESNEAU** et
co-encadrée par **Pablo DEL AMO SANCHEZ**

préparée au sein du **Laboratoire d'Annecy de Physique des Particules**
dans **l'École Doctorale Physique (Grenoble)**

Étude des oscillations de neutrinos à très courtes distances dans le détecteur STEREO à l'ILL, et calibration de celui-ci

Thèse soutenue publiquement le **16 Novembre 2021**,
devant le jury composé de :

M. Pablo DEL AMO SANCHEZ
Maître de conférence, USMB-LAPP, Co-encadrant
M. Dominique DUCHESNEAU
Directeur de recherche, LAPP-CNRS, Directeur de thèse
M. Carlo GIUNTI
Directeur de recherche, INFN-Turin (Italie), Examinateur
M. Stéphane JEZEQUEL
Directeur de recherche, LAPP-CNRS, Président
Mme Cécile JOLLET
Maître de conférence, CENBG-Univ. Bordeaux, Rapporteur
M. David LHUILLIER
Directeur de recherche, CEA-Saclay, Examinateur
M. Laurent SIMARD
Maître de conférence, IJCLab-Univ. Paris-Sud, Rapporteur
Mme Alessandra TONAZZO
Professeure, APC-Univ. Paris, Examinatrice

UNIVERSITÉ
SAVOIE
MONT BLANC

Very short baseline neutrino oscillations study with the STEREO detector at ILL; calibration of the STEREO detector

Loïc-René LABIT

February 14, 2022

ABSTRACT

During the last decades, several parameters describing the neutrino oscillation phenomenon have been characterized thanks to reactor neutrino experiments, in particular with the precise measurement of the mixing angle θ_{13}. However, following a reactor antineutrino flux re-estimation in 2011, a ∼6% deficit, known as the Reactor Antineutrino Anomaly, between measured and predicted reactor antineutrino fluxes, has been observed. The Reactor Antineutrino Anomaly (RAA) could be explained by the addition of a fourth neutrino mass eigenstate resulting in a yet unobserved oscillation. Since a fourth active neutrino would be in disagreement with the Z boson decay width measurement performed at LEP, this additional neutrino can not couple through weak interactions and is therefore called a "sterile" neutrino. The oscillation parameters that best explain the RAA are a mixing angle value of $\sin^2 2\theta_{new} = 0.17$ and a mass splitting value $\Delta m^2_{new} = 2.3$ eV^2.

The STEREO experiment was designed to test this oscillation hypothesis independently of predicted antineutrino spectra and fluxes, using the antineutrinos emitted by the compact core of the research reactor at the Laue-Langevin Institute in Grenoble, France. The target, located at about 10 m from the core, is segmented into six cells, allowing for a measurement of the antineutrino energy spectrum at various baselines [9-11m], sensitive to the oscillation toward a sterile neutrino that would distort each cell's spectrum differently. The detection of the antineutrinos is based on the Inverse Beta Decay (IBD) process in a gadolinium-doped liquid scintillator. The precise understanding of the detector response is paramount to the measurement and the analysis of the neutrino spectra.

In the first part of this thesis, we will present a study of the non-linearity of the detector response. The non-linearity of the detector response is investigated with radioactive calibration sources emitting gamma particles at various energies. In particular, an AmBe source, which is also a neutron emitter, allows to probe the response at high energy. We will describe a procedure that permits a reduction of the neutron background of this source. A sub-percent agreement between data and simulation of the detector non-linearity has been reached.

In a second part, an analytical modelisation of the detector response is presented. The detector response is characterised by a limited number of parameters. The small number of parameters brings more flexibility to study the effect of a change or miscalibration of the detector response on the extraction of the oscillation parameters. The inclusion of systematic uncertainties on the detector response is facilitated in this framework. In particular, cosmogenic Boron events are used as a control sample to estimate systematic uncertainties on the detector energy scale.

Finally, a prediction independent analysis of the neutrino data is performed to extract the oscillation parameters using the analytical model of the detector response. A statistical analysis of the signal significance is made to produce the excluded area of the oscillation parameter space using a 2-dimensional Feldman-Cousins confidence interval approach. In the context of neutrino oscillation searches, the normal χ^2 law conditions are not met, hence the χ^2 distributions are computed by generating numerous pseudo-experiments. The no-oscillation hypothesis is not rejected, however the best-fit point of the RAA is excluded at ∼99% confidence level.

RÉSUMÉ

Au cours des dernières décennies, plusieurs paramètres décrivant les oscillations de neutrinos ont été mesurés grâce aux expériences de neutrino auprès des réacteurs, le dernier étant la détermination très précise de l'angle de mélange θ_{13}. Cependant, à la suite de la réévaluation des flux d'antineutrino des réacteurs en 2011, un déficit de $\sim$6% entre flux observé et flux prédit, nommé Anomalie des Antineutrinos de Réacteur (RAA), a été constaté. L'anomalie des antineutrinos de réacteur pourrait être expliquée par l'addition d'un quatrième état de masse du neutrino permettant une oscillation encore inobservée. Puisqu'un quatrième état actif du neutrino serait en désaccord avec la largeur de désintégration du boson Z mesuré au LEP, ce neutrino additionnel ne peut pas interagir par interaction faible, il est donc qualifié de "stérile". Le meilleur ajustement des paramètres d'oscillation expliquant la RAA est un angle de mélange $\sin^2 2\theta_{new} = 0.17$ et un écart de masse $\Delta m^2_{new} = 2.3$ eV^2.

L'expérience STEREO a été conçue pour tester cette hypothèse d'oscillation indépendamment des prédictions de flux ou de spectre, en utilisant les antineutrinos émis par le coeur compact du réacteur de recherche de l'Institut Laue-Langevin à Grenoble. La cible, située à environ 10 m du cœur du réacteur est segmentée en 6 cellules, permettant une mesure des spectres en énergies des antineutrinos à plusieurs distances [9-11m], une oscillation vers un neutrino stérile modifierait différemment le spectre mesuré dans chaque cellule. La détection des antineutrinos dans STEREO se base sur le processus de désintégration bêta inverse dans un liquide scintillant dopé au gadolinium. La compréhension fine de la réponse du détecteur est cruciale pour la mesure des spectres en énergie des neutrinos et leur analyse.

Dans la première partie de cette thèse, nous présentons une étude de la non-linéarité de la réponse du détecteur. La non-linéarité de la réponse est examinée avec des sources radioactives émettrices de particules gamma à différentes énergies. En particulier, la source AmBe, qui est également émettrice de neutrons, permet d'évaluer la réponse à haute énergie. Nous décrivons une procédure permettant de réduire le bruit de fond neutron de cette source. Un accord entre données et simulation de la non-linéarité du détecteur meilleur que le pourcent a été atteint.

Dans une seconde partie, une modélisation analytique de la réponse du détecteur est présentée. La réponse du détecteur est caractérisée par un petit nombre de paramètres, ce qui amène une plus grande souplesse pour étudier les effets d'un changement de réponse ou d'un étalonnage erroné de la réponse du détecteur, dans le cadre de l'extraction des paramètres d'oscillation. Dans ce cadre, l'inclusion des incertitudes systématiques sur la réponse du détecteur est facilitée. En particulier, les événements du bore cosmogénique sont utilisés comme échantillon de contrôle pour estimer les

incertitudes systématiques sur l'échelle en énergie du détecteur.

Finalement, une analyse des données neutrino indépendante des prédictions est réalisée pour extraire les données d'oscillation en utilisant le modèle analytique de la réponse du détecteur. Une analyse statistique du signal est faite pour produire les contours d'exclusion de l'espace des paramètres d'oscillation, en utilisant l'approche bidimensionnelle des intervalles de confiance de Feldman-Cousins. Dans le contexte de la recherche d'une oscillation de neutrino, les conditions pour appliquer la loi normale de χ^2 ne sont pas vérifiées, par conséquent, les distributions de χ^2 sont calculées en générant de nombreuses pseudo-expériences. L'hypothèse de non-oscillation n'est pas rejetée, mais le meilleur ajustement de la RAA est exclu à $\sim$99% de niveau de confiance.

REMERCIEMENTS

Cette thèse ne saurait prétendre être complète sans quelques mots de remerciements aux personnes qui l'ont rendu possible.

Tout d'abord, je tiens à remercier les membres du jury qui m'ont fait l'honneur d'accepter de lire ma thèse et de juger mon travail; et en particulier mes deux rapporteurs Mme Cécile Jollet et M. Laurent Simard auxquels j'ai eu l'indécence de remettre une partie de mon travail à la dernière minute et qui ont eu l'élégance de ne jamais le mentionner.

Toute cette aventure n'aurait pas eu lieu sans Cécile qui m'a initié au travail de recherche (et aux neutrinos). Sa pédagogie, sa rigueur et son dévouement, ont certainement contribué à mon désir de continuer dans la recherche (et dans les neutrinos), et pour cela merci.

Bien entendu, ce travail n'aurait pas été possible sans Pablo qui a dirigé mon travail. Je n'imagine pas un meilleur directeur de thèse que Pablo, qui m'a accompagné avec beaucoup de pédagogie, de patience et de bienveillance tout au long de cette thèse et n'aura pas hésité à sacrifier ses nuits pour que ce manuscrit puisse voir le jour. Je suis très fier du travail que l'on a réalisé ensemble, cela n'a pas été facile mais on aura réussi à le faire chanter ce RooSTER !!

Ces années de thèse n'auraient pas eu la même saveur sans mon collègue et ami, Henri (à moins que ce ne soit Harry?!) Pessard dont les "caprices" tardifs toujours accompagnés d'un chocolat chaud étaient un réconfort quasi-journalier.

Je salue au passage mes autres collègues et amis du groupe neutrino: Laura qui tient plus de la grande sœur que de la collègue de bureau et reine incontestée des puzzles qui égayaient l'un de mes nombreux bureaux. Pablito mon partenaire sur les bancs de cinéma à qui je souhaite le meilleur pour sa rédaction (c'est un plat qui se mange sans sauce ;)) et sa soutenance à venir. Isabelle que je veux remercier pour m'avoir permis de trouver un enseignement à dispenser à l'IUT. Oliver, bien que notre overlap au LAPP fut court, c'était un plaisir de faire ta connaissance. Dominique, leader incontesté du groupe Neutrino avec qui les discussions sont toujours passionnées et passionnantes.

Je n'oublie pas tous les bons moments partagés avec les jeunes et les moins jeunes du LAPP, en particulier les soirées passées en compagnie de notre couple LAPP-LAPTH préféré Carole et Jordan, je suis convaincu que la dolce vita a Padova va bien vous réussir.

J'ai une pensé particulière pour Simone qui a suivi la rédaction de ce manuscrit avec beaucoup d'attention, et dont le soutien psychologique apporté à travers nos moments d'échange fut une véritable aide. $\epsilon\upsilon\chi\alpha\rho\iota\sigma\tau\omega$!

Je souhaite également inscrire quelques mots de remerciement pour mon papa et sa compagne qui n'ont pas hésité à faire le déplacement pour venir m'écouter parler pendant des heures du neutrino et le tout en anglais, par dessus le marché.

On m'en voudrait si je ne mentionnais pas mon fidèle compagnon à quatre pattes, Moustique, qui après avoir assisté à une bonne vingtaine de répétitions est certainement le plus grand expert mondial en physique du neutrino de son espèce.

Pour finir, merci à tous ceux qui de près ou de loin ont permis la réalisation de cette thèse et ont fait de mes années dans la Venise des Alpes, un moment de bonheur.

CONTENTS

CHAPTER 1

NEUTRINO PHYSICS: THEORETICAL AND EXPERIMENTAL CONTEXT

CONTENTS

1.1 History of the neutrino

1.1.1 Postulate and discoveries

Continuous β spectrum and Nitrogen anomaly

Following his work on the Radium nucleus decay Chadwick discovered in 1914, that, unlike α and γ radiation which are emitted with discrete energy values, the β radiation has a continuous energy spectrum [Cha14]. This was confirmed later in 1927 by the work of Ellis and Wooster [EW27]. This observation seemed to violate the energy conservation law in a two-body decay. Two interpretations of these results were possible:

- In the β decay process, the conservation of energy holds only on a statistical standpoint.
- The conservation of energy holds strictly for each event but an additional escaping radiation is emitted together with the β radiation.

At that time, the idea that nuclei were constituted of protons and electrons was commonly admitted. However, following the advance of the quantum mechanics theory, according to which particles are either fermions with a half-integer spin or bosons with an integer spin and since both protons and electrons were found to be fermions, it was deduced that the parity of the nuclei's electric charge should determine the spin-state of the nucleus. This conclusion was not confirmed experimentally as observed with Nitrogen, for example, that has a charge number of 7 and a spin 1 [Kro28].

In his famous letter [Pau78] (Figure 1.1), Pauli attempted to solve both the continuous β spectrum and the anomalous spin of N, by introducing a new electrically neutral particle, that would be a constituent of the nucleus and emitted simultaneously to the electron in a β decay. Following, the discovery of the neutron by Chadwick in the following years, the mysterious neutral particle emitted simultaneously to the electron in a β decay was baptised *neutrino*[1] by Fermi in his theory of the β decay [Fer34].

[1] Literally: small neutron

Discovery of the $\overline{\nu_e}$

A few decades after being postulated, the neutrino was officially discovered by Cowan and Reines in 1956 [CRH+56]. The experiment designed by Cowan and Reines was based on the Inverse Beta Decay process (IBD) (detailed in the following chapter), in which an antineutrino interacts with a proton to give a positron and a neutron. Cowan and Reines' detector consisted of two 200 litres tanks, filled with water and doped with Cadmium, interspersed in three 1400 litres tanks filled with liquid scintillator seen by 100 phototubes. The detection signal is based on the coincidence between two annihilation γ and the neutron capture on Cadmium a few microseconds later (see Figure 1.2). The detector was located near a nuclear reactor of the Savannah River Site.

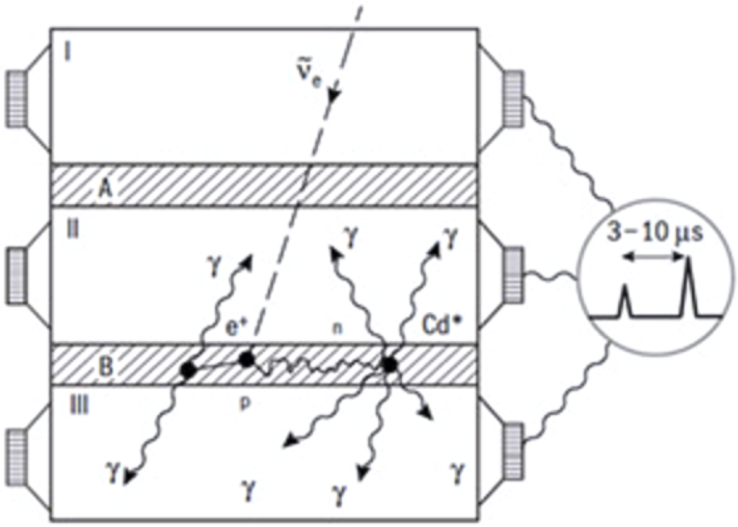

Figure 1.2: Schematic view of the functionment principle of Cowan and Reines' experiment at the Savannah River nuclear power plant. It consisted of three 1400 litres tanks of liquid scintillator (I,II,III) and two 200 litres of Cadmium doped water tanks (A,B). The detection principle was based on the time coincidence between the positron and the capture of the neutron produced in the Inverse Beta Decay process. This principle is still used nowadays.

The principles used by Cowan and Reines to detect the neutrino are still used nowadays, by many reactor antineutrino experiments and among them, the STEREO experiment. Reines (Cowan having passed away in 1974) was awarded the Nobel prize in physics in 1995[2] for his discovery of the neutrino. Their work also confirmed the very small value of the neutrino interaction cross-section: $\sigma_{IBD} \sim 6\times10^{-44}$ cm^2.

Discovery of ν_μ and ν_τ

In 1962, a new type of neutrino was discovered by Steinberger, Lederman and Schwartz [DGG+62]. In their experiment, Steinberger et al. observed that neutrinos produced by pion decay produce muons but do not produce electrons when interacting, and hence are different particles from the neutrinos of the β decay.

[2]This year is also the birth year of the author of this thesis, the two events are probably not related though.

Abschrift/15.12.30 PM

Offener Brief an die Gruppe der Radioaktiven bei der Gauvereins-Tagung zu Tübingen.

Abschrift

Physikalisches Institut
der Eidg. Technischen Hochschule
Zürich

Zürich, 4. Dez. 1930
Gloriastrasse

Liebe Radioaktive Damen und Herren,

Wie der Ueberbringer dieser Zeilen, den ich huldvollst anzuhören bitte, Ihnen des näheren auseinandersetzen wird, bin ich angesichts der "falschen" Statistik der N- und Li-6 Kerne, sowie des kontinuierlichen beta-Spektrums auf einen verzweifelten Ausweg verfallen um den "Wechselsatz" (1) der Statistik und den Energiesatz zu retten. Nämlich die Möglichkeit, es könnten elektrisch neutrale Teilchen, die ich Neutronen nennen will, in den Kernen existieren, welche den Spin 1/2 haben und das Ausschliessungsprinzip befolgen und sich von Lichtquanten ausserdem noch dadurch unterscheiden, dass sie nicht mit Lichtgeschwindigkeit laufen. Die Masse der Neutronen müsste von derselben Grössenordnung wie die Elektronenmasse sein und jedenfalls nicht grösser als 0,01 Protonenmasse.- Das kontinuierliche beta- Spektrum wäre dann verständlich unter der Annahme, dass beim beta-Zerfall mit dem Elektron jeweils noch ein Neutron emittiert wird, derart, dass die Summe der Energien von Neutron und Elektron konstant ist.

Nun handelt es sich weiter darum, welche Kräfte auf die Neutronen wirken. Das wahrscheinlichste Modell für das Neutron scheint mir aus wellenmechanischen Gründen (näheres weiss der Ueberbringer dieser Zeilen) dieses zu sein, dass das ruhende Neutron ein magnetischer Dipol von einem gewissen Moment μ ist. Die Experimente verlangen wohl, dass die ionisierende Wirkung eines solchen Neutrons nicht grösser sein kann, als die eines gamma-Strahls und darf dann μ wohl nicht grösser sein als $e \cdot (10^{-13}$ cm).

Ich traue mich vorläufig aber nicht, etwas über diese Idee zu publizieren und wende mich erst vertrauensvoll an Euch, liebe Radioaktive, mit der Frage, wie es um den experimentellen Nachweis eines solchen Neutrons stände, wenn dieses ein ebensolches oder etwa 10mal grösseres Durchdringungsvermögen besitzen würde, wie ein gamma-Strahl.

Ich gebe zu, dass mein Ausweg vielleicht von vornherein wenig wahrscheinlich erscheinen wird, weil man die Neutronen, wenn sie existieren, wohl schon längst gesehen hätte. Aber nur wer wagt, gewinnt und der Ernst der Situation beim kontinuierliche beta-Spektrum wird durch einen Ausspruch meines verehrten Vorgängers im Amte, Herrn Debye, beleuchtet, der mir kürzlich in Brüssel gesagt hat: "O, daran soll man am besten gar nicht denken, sowie an die neuen Steuern." Darum soll man jeden Weg zur Rettung ernstlich diskutieren.- Also, liebe Radioaktive, prüfet, und richtet.- Leider kann ich nicht persönlich in Tübingen erscheinen, da ich infolge eines in der Nacht vom 6. zum 7 Dez. in Zürich stattfindenden Balles hier unabkömmlich bin.- Mit vielen Grüssen an Euch, sowie an Herrn Back, Euer untertänigster Diener

gez. W. Pauli

Figure 1.1: Public letter to the group of the Radioactives at the district society meeting in Tubingen: Physikalisches Institut Zurich, 4. Dec. 1930. Technischen Hochschule Gloriastr. Zurich
Dear Radioactive Ladies and Gentlemen, As the bearer of these lines, to whom I graciously ask you to listen, will explain to you in more detail, how because of the "wrong" statistics of the N and ^{6}Li nuclei and the continuous β-spectrum, I have hit upon a desperate remedy to save the "exchange theorem" of statistics and the law of conservation of energy. Namely, the possibility that there could exist in the nuclei electrically neutral particles, that I wish to call neutrons, which have spin $\frac{1}{2}$ and obey the exclusion principle and which further differ from light quanta in that they do not travel with the velocity of light. The mass of the neutrons should be of the same order of magnitude as the electron mass and in any event not larger than 0.01 proton masses. - The continuous, β-spectrum would then become understandable by the assumption that in, β-decay, a neutron is emitted in addition to the electron such that the sum of the energies of the neutron and electron is constant.
Now the question that has to be dealt with is which forces act on the neutrons? The most likely model for the neutron seems to me, because of wave mechanical reasons (the details are known by the bearer of these lines), that the neutron at rest is a magnetic dipole of a certain moment μ. The experiments seem to require that the effect of the ionization of such a neutron cannot be larger than that of a γ-ray and then μ should not be larger than $e\times10^{-13}$ cm.
For the moment, however, I do not dare to publish anything of this idea and I put to you, dear Radioactives, the question of what the situation would be if one such neutron were detected experimentally if it would have a penetration power similar to, or about 10 times larger than, a γ-ray.
I admit that on a first look my way out might seem to be unlikely, since one would certainly have seen the neutrons by now if they existed. But nothing ventured nothing gained, and the seriousness of the matter with the continuous β-spectrum is illustrated by a quotation of my honored predecessor in office, Mr. Debye, who recently told me in Brussels: "Oh, it is best not to think about it, like the new taxes." Therefore one should earnestly discuss each way of salvation. - So, dear Radioactives, examine and judge it. - Unfortunately I cannot appear in Tübingen personally, since I am indispensable here in Zurich because of a ball on the night of 6^{th} to 7^{th} December. - With my best regards to you, and also to Mr. Back, your humble servant, W. Pauli
Translation from [Win91].

The discovery of the τ lepton in the mid 70's at SLAC suggested the existence of a third type of neutrino associated to the τ lepton. The tau neutrino was successfully observed in 2000 by the DONUT experiment from charmed mesons decay [K+01].

Neutrino helicity: the Goldhaber experiment

In 1958, Goldhaber et al. designed and operated an elegant experiment to determine the chirality of the neutrino [GGS58]. The experiment stands on an ingenious point: when an excited nucleus deexcites by γ emission, the energy of the γ does not equal exactly the difference in nuclear levels of the nucleus because of the nucleus recoil. However, if the emitting nucleus moves in the same direction as the γ emission, the Doppler shift can balance the missing energy allowing resonant absorption. This phenomenon was used with the ^{152m}Eu nucleus which decays by electron capture with a lifetime of ~9 hours. The ^{152m}Eu decays to the excited state of ^{152}Sm which return to its ground state by γ emission:

$$\begin{array}{ccccccccccccc} ^{152m}Eu & + & e^- & \rightarrow & ^{152}Sm^* & + & \nu_e & \rightarrow & ^{152}Sm & + & \gamma & + & \nu_e \\ (0) & + & (\pm\frac{1}{2}) & \rightarrow & (\pm 1) & + & (\mp\frac{1}{2}) & \rightarrow & (0) & + & (\pm 1) & + & (\mp\frac{1}{2}) \end{array}$$

where the number in parenthesis are the spin projections of the particles. If the γ is emitted in opposite direction to the neutrino, the nucleus recoils from the neutrino emission in the same direction as the γ emission and resonant scattering happens. Since the γ has opposite spin to the neutrino, the γ has the same helicity as the neutrino.

The results reported by Goldhaber were compatible with 100% of left handed helicity neutrinos. Neutrinos being relativistic, the helicity eigenstate is identical to the chirality eigenstate. Since only left-chiral neutrinos are produced by the weak interactions, right-chiral neutrinos need not exist. The mass term of fermions arises from the coupling of the left and right chirality states, hence the neutrino was believed to be massless at that time.

Limit on the number of active neutrino

A limit on the number of neutrinos coupling to the weak interaction (named "active neutrinos" hereafter) is given by the invisible decay width of the Z boson measured by the experiment of the Large Electron Positron collider (LEP) at CERN in the 90's. The invisible decay width of the Z boson is given by:

$$\Gamma_{inv} = \Gamma_Z - \Gamma_{q\bar{q}} - 3 \times \Gamma_{l\bar{l}} = N_\nu \times \Gamma_{\nu\bar{\nu}} \tag{1.1}$$

It is interpreted as the decay of the Z boson in the neutrino-antineutrino channel. The combination of ALEPH, DELPHI, OPAL and L3 experiments results (see Figure 1.3) leads to a number of active neutrinos compatible with 3 [S+06]:

$$N_\nu = 2.984 \pm 0.008 \tag{1.2}$$

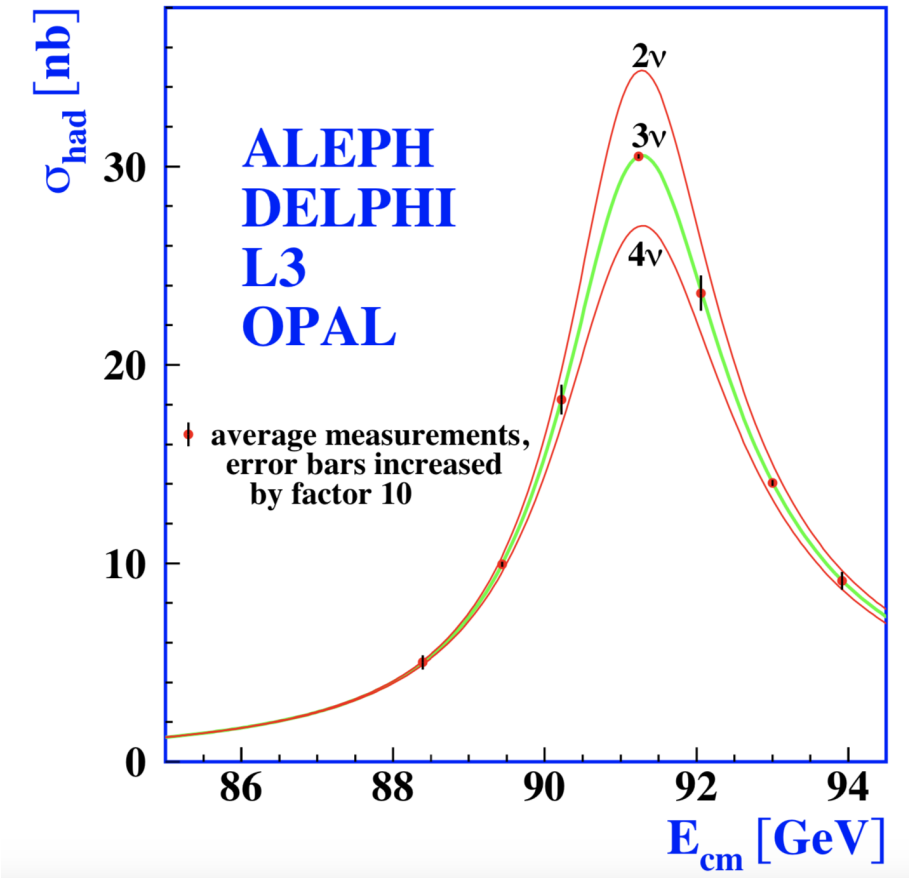

Figure 1.3: Cross section for hadron production around the Z boson resonance. The prediction for 2, 3 and 4 active neutrinos with Standard Model couplings and negligeable mass is given by the solid line curves.

1.1.2 Neutrino oscillations

The solar anomaly

In 1968, Davis designed an experiment to detect solar neutrino by inverse beta decay on Chlorine [DHH68]:

$$\nu_e + {}^{37}Cl \rightarrow e^- + {}^{37}Ar \tag{1.3}$$

where the subsequent ${}^{37}Ar$ is radioactive and its decay can be detected. The experiment was located 1500 m underground at the Homestake Mine and consisted in $\sim 4\times10^5$ litres of perchloroethylene (C_2Cl_4).

The observation of the neutrino produced in the sun's thermonuclear reactions is a good test of the solar standard model. The relevant thermonuclear reactions taking place in the sun are given in Table 1.1 [CG09], their energy spectrum is given in Figure 1.4 [Mir09]. The energy threshold of the reaction (1.3) is 814 keV, hence the experiment was blind to the *pp* channel of solar nuclear reactions.

Name	Reaction	Predicted Rate (on Cl) [SNU]
pp	$p + p \rightarrow d + e^+ + \nu_e$	
^7Be	$^7Be + e^- \rightarrow ^7 Li + \nu_e$	1.15
^8B	$^8B \rightarrow ^8 Be^* + e^+ + \nu_e$	5.67
pep	$P + e^- + p \rightarrow d + \nu_e$	0.68
hep	$^4He + e^+ + \nu_e$	
Total		$7.6^{+1.3}_{-1.1}$

Table 1.1: Sun's thermonuclear reactions relevant for neutrino physics; the interaction rate on Cl is given in *Solar Neutrino Unit* (1 SNU = 10^{-36} ν capture/atom/s).

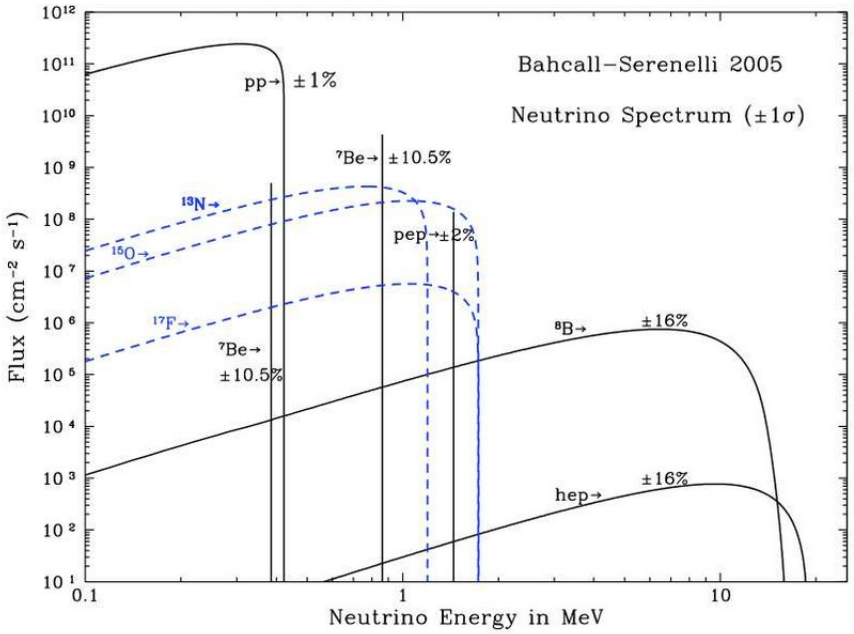

Figure 1.4: Solar neutrino energy spectra predicted by the solar standard model [BSB05]

The Homestake experiment reported a detected neutrino rate:
$R_{det} = 2.56 \pm 0.23$ [SNU], which is about one third of the expectations.

The discrepancy between the prediction and the measurement was long attributed to problems either in the solar standard model or in the experiment, before being confirmed by other transmutation experiments such as GALLEX [H+96] and SAGE [A+96]. The GALLEX and SAGE experiments used Gallium instead of Chlorine which allows to decrease the energy threshold of the reaction to ∼233 keV and hence be sensitive to the *pp* channel. These experiments detected a rate about 60 % of the predicted rate, which was once again confirmed by GALLEX' follow-up experiment GNO [Bel01].

A different approach from element transmutation experiments is water Cerenkov experiments, in which the neutrino is detected by the Cerenkov light it emits when interacting in a water target. The Kamioka Nucleon Decay Experiment (Kamiokande) [F+96] and its successor, the 50 kTon detector Super-Kamiokande [F+99] were based on this principle. The energy threshold for these experiments is about 5 MeV, thus they are mainly sensitive to the ^8B and *pep* channels. Both of them reported a deficit of about 50% compared to the predicted rate, but confirmed that the detected neutrinos were coming from the direction of the sun.

All experiments were consistent with the fact that they observed less neutrinos than predicted by the solar standard model, however, the solar standard model could not be proved wrong either.

An alternative explanation had been put forward: back in 1957, Pontecorvo suggested that neutrinos could oscillate between neutrino and antineutrino: $\nu \leftrightarrow \overline{\nu}$ [Pon57], in the manner of neutral kaons: $K^0 \leftrightarrow \overline{K^0}$. At that time only one flavour of neutrino was known. Some years later, in 1962, Maki, Nakagawa and Sakata revisited the idea of Pontecorvo and suggested an oscillation between two flavours of neutrino [MNS62].

The observed deficit could be explained by an oscillation from the electron neutrino produced in the sun toward the other neutrino flavours, which could not be observed by the detection technique used in these experiments because the neutrino energy was too low to produce the associated lepton through a Charged Current[3].

A proof of the neutrino oscillation was brought by the Sudbury Neutrino Observatory (SNO) in 2002 [A+02a]. The experiment consisted in a 1 kTon Cerenkov detector, but unlike the Kamioka detectors, heavy water (D_2O) was used instead of regular water. The heavy water allows for three distinct reactions to happen:

- The charged current reaction (CC) is an inverse beta decay of the proton in the deuterium, this channel is only sensitive to the electron neutrino: $\nu_e + d \rightarrow p + p + e^-$.
- The neutral current reaction (NC) is the spallation of the neutron in the deuterium nucleus; this channel is sensitive to all flavours of neutrino: $\nu_{e,\mu,\tau} + d \rightarrow n + p + \nu_{e,\mu,\tau}$.
- The elastic scattering (ES) of an electron, this channel is sensitive to all flavours of neutrino as well: $\nu_{e,\mu,\tau} + e^- \rightarrow \nu_{e,\mu,\tau} + e^-$.

In the first results presented by the SNO collaboration, only the charged current and the elastic scattering channel were used. They reported (in units of $10^6\, cm^{-2}\, s^{-1}$):

$$\phi_{CC} = 1.75 \pm 0.07\,(stat.)\, {}^{+0.12}_{-0.11}\,(syst.) \pm 0.05\,(theo.)$$

$$\phi_{ES} = 2.39 \pm 0.34\,(stat.)\, {}^{+0.15}_{-0.14}\,(syst.)$$

These results can be unfolded to give the electron neutrino flux and the muon plus tau neutrino fluxes:

$$\phi_e = 1.76^{+0.05}_{-0.03}\,(stat.) \pm 0.009\,(syst.)$$

$$\phi_{\mu\tau} = 3.41 \pm 0.45\,(stat.)\, {}^{+0.48}_{-0.45}\,(syst.)$$

The conclusion is that the muon and tau neutrino component from the solar neutrino is non-zero unlike what is expected, and the comparison with the expected flux of solar neutrinos from the solar standard model shows that the total neutrino flux is in agreement with the expectation (see Figure 1.5), indicating that electron neutrinos change flavour during their propagation toward the Earth.

[3] The current refers to the gauge boson that mediates the interaction: $W^\pm$ for the charged current and Z^0 for the neutral current.

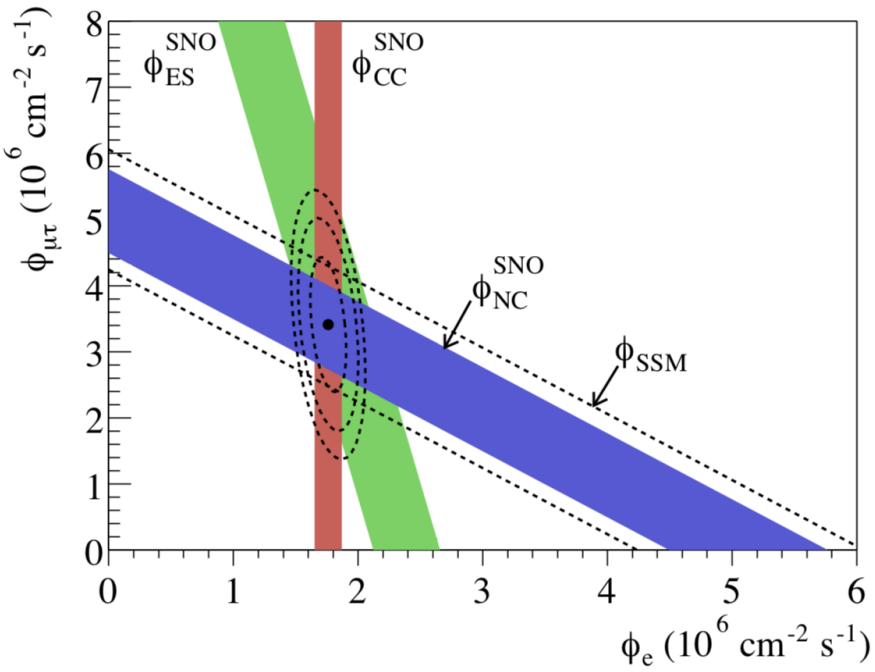

Figure 1.5: ν_μ and ν_τ flux versus ν_e flux from the ^8B solar reaction, the dashed line shows the flux predicted from the solar standard model ϕ_{SSM}. The bands shows the $\pm 1\sigma$ uncertainty. The intersection shows the best fit of ϕ_e and $\phi_{\mu\tau}$ and the elliptic dashed line, the confidence level at 68, 95 and 99%.

The atmospheric anomaly

Since the 80's another source of neutrinos has been studied: the neutrinos produced by the interaction of the cosmic rays with the upper atmosphere of the Earth. When a cosmic ray interacts with the Earth atmosphere it produces a hadron shower mainly composed of pions. The pions decay giving muons and muon neutrinos. Muons decay as well, giving muon neutrinos and electron neutrinos:

$$\begin{aligned} \pi^\pm \rightarrow \quad & \mu^\pm \quad + \nu_\mu(\overline{\nu_\mu}) \\ & \mu^\pm \quad \rightarrow e^\pm + \nu_e(\overline{\nu_e}) + \overline{\nu_\mu}(\nu_\mu) \end{aligned}$$

For neutrinos with energy of the order of the GeV, twice more ν_μ than ν_e are expected. However, experiments such as IMB [BS+95],MACRO [A+98] Soudan [A+97], Kamiokande [F+94] and Super-Kamiokande [F+98] reported about equal proportion of ν_μ and ν_e.

The Super-Kamiokande experiment studied the atmospheric neutrino flux as a function of the incoming direction. They reported that the proportion of ν_μ was higher for neutrinos coming from the top of the detector (with a baseline L$\sim 10^1$ km) than for the neutrinos coming from the bottom of the detector (with a baseline L$\sim 10^4$ km: these neutrinos are produced in the upper atmosphere and go through the Earth before interacting in the detector). The number of ν_μ and ν_e as a function of the zenithal angle θ are presented in Figure 1.6. The neutrinos are split according to their energy: sub-GeV are events with E<1.33 GeV and multi-GeV are events with E>1.33 GeV. The MC prediction in the case of non-oscillation is also presented as well as the best fit of the $\nu_\mu \rightarrow \nu_\tau$ oscillation.

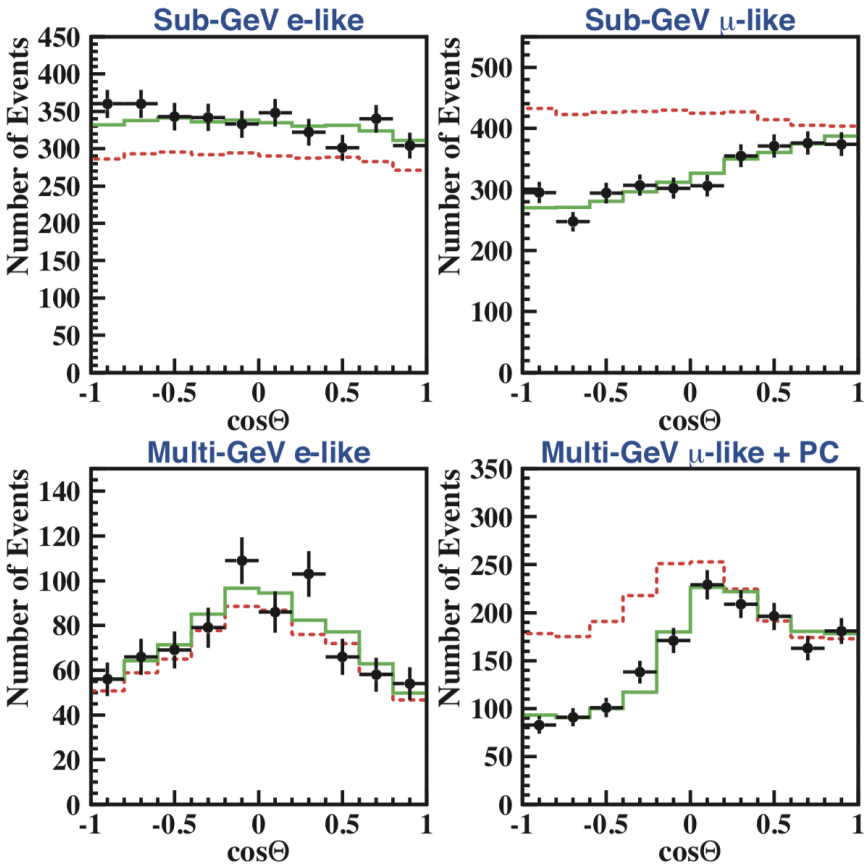

Figure 1.6: Number of electron (left) and muon (right) neutrino events as a function of the zenithal angle Θ, for E<1.33 GeV (sub-GeV, top) and E>1.33 GeV events (multi-GeV, bottom). The red dashed line is the MC prediction in the case of non-oscillation and the green dashed line the best fit with a $\nu_\mu \rightarrow \nu_\tau$ oscillation [F+98]

Thanks to the sensitivity to the $\frac{L}{E}$ variable, the measurements of the Super-Kamiokande experiment brought the first experimental proof of the oscillatory nature of the neutrino.

This oscillatory nature of the neutrino was later confirmed by the KamLAND experiment [A+05]. This experiment, located in the Kamioka mine, consisted in a liquid scintillator detector and measured antineutrinos coming from various nuclear reactors. Their result is presented in Figure 1.7. They also tested two other hypothesis in addition to neutrino oscillations: the neutrino decay and the neutrino decoherence.

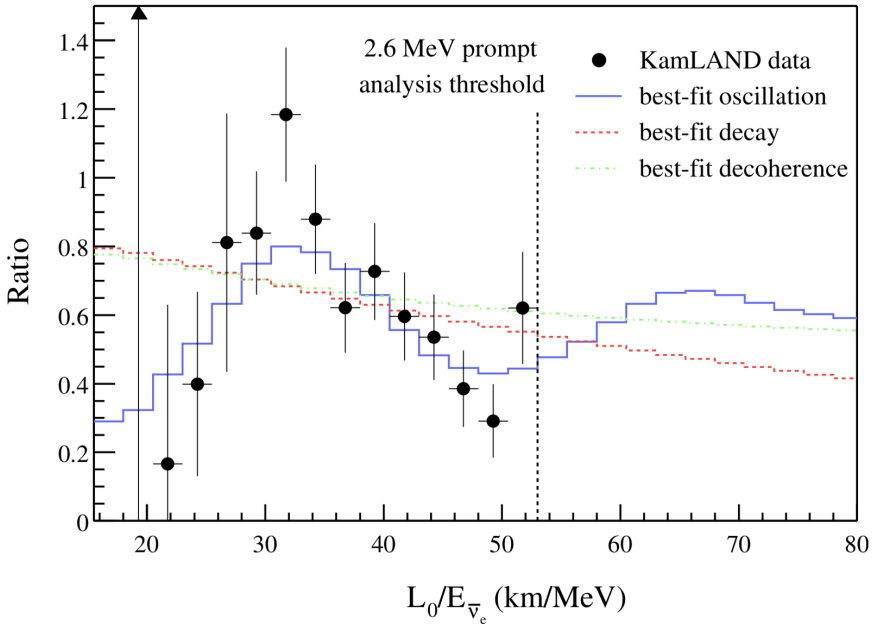

Figure 1.7: Ratio between observed $\overline{\nu_e}$ and the prediction of the no oscillation hypothesis as a function of $\frac{L}{E}$, The solid blue line shows the best fit of the oscillation hypothesis, the red dashed line shows the neutrino decay hypothesis and the green dashed line shows the decoherence hypothesis [A+05].

In 2015, Takaaki Kajita from the Super-Kamiokande collaboration and Arthur B. McDonald from the Sudbury Neutrino Observatory collaboration were awarded the Nobel prize in physics "*for the discovery of neutrino oscillations, which shows that neutrinos have mass*" [Nob].

Although, as we will see in the next sections, neutrinos in the Standard Model of particle physics are massless, in order to oscillate they require a mass, highlighting the need for physics beyond the Standard Model.

1.2 Neutrino in the Standard Model of Particle Physics

1.2.1 Free fermion in the Standard Model

The Standard Model (SM) is the Quantum Field Theory that describes the elementary particles of matter and their interactions through the electromagnetic, strong and weak forces.

Dirac equation

In 1928, Dirac formulated his famous eponym equation and succeeded in formulating a theory that is consistent with both quantum mechanics and special relativity:

$$(i\gamma^\mu \partial_\mu - m)\Psi = 0 \tag{1.4}$$

where $\partial_\mu = (\frac{\partial}{\partial t}, \vec{\nabla})$ and γ^μ are a set of 4×4 matrices called the Dirac γ matrices. These matrices satisfy the anticommutation relation:

$$\{\gamma^\mu, \gamma^\nu\} = \gamma^\mu\gamma^\nu + \gamma^\nu\gamma^\mu = 2g^{\mu\nu} \tag{1.5}$$

where $g_{\mu\nu}$ is the metric (+,-,-,-), and the condition:

$$\gamma^0\gamma^{\mu\dagger}\gamma^0 = \gamma^\mu \tag{1.6}$$

where $\gamma^{\mu\dagger}$ is the conjugate transpose of γ^μ. The Dirac representation of the γ matrices is given by:

$$\gamma^0_D = \begin{bmatrix} \mathbb{I} & 0 \\ 0 & -\mathbb{I} \end{bmatrix} \tag{1.7}$$

$$\gamma^{i=1,2,3}_D = \begin{bmatrix} 0 & \sigma_i \\ -\sigma_i & 0 \end{bmatrix} \tag{1.8}$$

where σ_i are the 2×2 Pauli spin matrices. However, this representation is not unique and physical predictions do not depend on the choice of representation. In addition to the γ^μ matrices, it is handy to define the γ^5 matrix (sometimes called the chirality matrix) :

$$\gamma^5 = i\gamma^0\gamma^1\gamma^2\gamma^3 \tag{1.9}$$

It is always possible to project a spinor Ψ on its chiral components Ψ_R and Ψ_L which are the eigenvectors of the γ^5 matrix. From γ^5, we can build the orthogonal chirality projection operators:

$$\begin{aligned} P_R &= \frac{1+\gamma^5}{2} \\ P_L &= \frac{1-\gamma^5}{2} \end{aligned}$$

The chirality projectors satisfy the following properties:

$$\begin{aligned} P_R + P_L &= \mathbb{I} \\ P_R P_R &= P_R \\ P_L P_L &= P_L \\ P_R P_L &= P_L P_R = 0 \end{aligned}$$

The solutions of the Dirac equation describe non-interacting, massive $\frac{1}{2}$-spin particles, or in other words, free Dirac fermions. Indeed, the Dirac equation admits four independent solutions for a given energy-momentum: two solutions with positive energy, corresponding to the spin-up and spin-down states of a particle, and two negative energy solutions, corresponding to spin-up and spin-down antiparticles.

Weyl representation

Another representation of the γ matrices is the Weyl representation:

$$\gamma^0_W = \begin{bmatrix} 0 & -\mathbb{I} \\ -\mathbb{I} & 0 \end{bmatrix} \tag{1.10}$$

$$\gamma^{i=1,2,3}_W = \begin{bmatrix} 0 & \sigma_i \\ -\sigma_i & 0 \end{bmatrix} \tag{1.11}$$

or in a more compact manner:

$$\gamma^\mu_W = \begin{bmatrix} 0 & \overline{\sigma}^\mu \\ -\sigma^\mu & 0 \end{bmatrix} \tag{1.12}$$

with the 2×2 matrices: $\sigma^\mu = (1, \vec{\sigma})$ and $\overline{\sigma}^\mu = (-1, \vec{\sigma})$.

It can be shown that in this representation the Dirac equation can be written as a system of two coupled equations, writing the four-component Dirac spinor $\Psi = \begin{pmatrix} \phi \\ \chi \end{pmatrix}$, ϕ and χ are called Weyl spinors:

$$\begin{cases} i\sigma^\mu \partial_\mu \phi = -m\chi \\ i\overline{\sigma}^\mu \partial_\mu \chi = m\phi \end{cases} \tag{1.13}$$

It becomes obvious that in the case of $m = 0$, both equations decouple. In addition, in this representation, the chirality matrix γ^5 is diagonal:

$$\gamma^5_C = \begin{bmatrix} \mathbb{I} & 0 \\ 0 & -\mathbb{I} \end{bmatrix} \tag{1.14}$$

Hence, the Weyl spinors correspond to pure chiral states, this is why the Weyl representation is also called the chiral representation.

The Weyl spinor describes a massless fermion: in this case the fermion has a pure chiral state. The neutrino was long thought to be a Weyl fermion, because it was believed to be massless, and only left-handed neutrinos had been observed. The observation of neutrino oscillations requires neutrinos to be massive fermions and consequently can not be Weyl fermions. No elementary particles in the Standard Model are Weyl fermions.

Majorana representation

In 1937, Majorana searched for purely real spinor solutions of Dirac's equation, by imposing the reality condition: $\Psi = \Psi^*$. Spinors satisfying the reality condition are called Majorana spinors. These solutions can be found if the Dirac operator is hermitian $(i\gamma^\mu \partial_\mu - m)$. This arises naturally in the Majorana representation of the γ matrices, in this representation all of the γ matrices are purely imaginary:

$$\gamma^0_M = \begin{bmatrix} 0 & \sigma^2 \\ \sigma^2 & 0 \end{bmatrix} \tag{1.15}$$

$$\gamma^1_M = i\begin{bmatrix} \sigma^3 & 0 \\ 0 & \sigma^3 \end{bmatrix} \tag{1.16}$$

$$\gamma^2_M = \begin{bmatrix} 0 & -\sigma^2 \\ \sigma^2 & 0 \end{bmatrix} \tag{1.17}$$

$$\gamma^3_M = -i\begin{bmatrix} \sigma^1 & 0 \\ 0 & \sigma^1 \end{bmatrix} \tag{1.18}$$

In addition, we define the charge conjugation operation[4], physically the charge conjugation corresponds to transforming a particle in its anti-particle:

$$\Psi \mapsto \Psi^c : \Psi^c = C\overline{\Psi}^t \tag{1.19}$$

where $\overline{\Psi}^t = (\Psi^\dagger \gamma^0)^t$ is the adjoint spinor and C is the charge conjugation matrix.

The charge conjugation matrix is representation dependent, but a basis independent definition is given by:

$$C\gamma^\mu C^{-1} = -(\gamma^\mu)^t \tag{1.20}$$

[4] up to a constant phase η, that has no physical importance

In the Majorana representation, the charge conjugation matrix is given by :

$$C = \begin{bmatrix} 0 & -i\sigma^2 \\ -i\sigma^2 & 0 \end{bmatrix} \tag{1.21}$$

It follows that, if the spinors check the reality condition: $\Psi = \Psi^*$, then $\Psi^c = C\overline{\Psi}^t = -C\gamma^0\Psi^* = \Psi^* \Rightarrow \Psi^c = \Psi$. In other words, a Majorana fermion (described by a Majorana spinor) is its own antiparticle. The nature of the neutrino, that is to say, whether the neutrino is a Dirac or a Majorana fermion, is not yet determined.

1.2.2 Interactions in the Standard Model

In the previous section, we gave the equation describing a free fermion in the SM. However, the Standard Model describes three of the four fundamental interactions: the electromagnetic interaction, the strong and weak interaction.

Electromagnetic interaction

The electromagnetic interaction is described by the quantum electrodynamics theory (QED) and arises naturally when you consider a local gauge invariance.

If we suppose the physics invariant under a local phase transformation given by:

$$\Psi(x) \mapsto \Psi'(x) = e^{iq\chi(x)}\Psi(x) \tag{1.22}$$

The Dirac equation becomes:

$$\begin{aligned} i\gamma^\mu\partial_\mu(e^{iq\chi(x)}\Psi) &= me^{iq\chi(x)}\Psi \\ i\gamma^\mu(\partial_\mu + iq\partial_\mu\chi)\Psi &= m\Psi \end{aligned}$$

which differs from the Dirac equation, hence the Dirac equation for a free fermion is not invariant under this local phase transformation. To retrieve the invariance, the Dirac equation must be modified to include a new field, A_μ:

$$i\gamma^\mu(\partial_\mu + iqA_\mu)\Psi - m\Psi = 0 \tag{1.23}$$

which is invariant under the local phase transformation, provided that

$$A_\mu \mapsto A'_\mu = A_\mu - \partial_\mu\chi \tag{1.24}$$

We note here that gauge invariance is obtained by replacing the partial derivative in Dirac's quation with a covariant derivative:

$$\partial_\mu \mapsto D_\mu = \partial_\mu + iqA_\mu \tag{1.25}$$

The new term in the Dirac equation, $q\gamma^\mu A_\mu\Psi$, is an interaction term. In fact, A_μ corresponds to the photon field which is the carrier of the electromagnetic interaction, and the coupling constant q is the electric charge. The neutrino however is electrically neutral, hence $q = 0$ and it does not interact through the electromagnetic interaction.

Strong interaction

Similarly, the strong interaction arises when we suppose a more complicated local phase transformation. This transformation arises from $SU(3)$ symmetry, whereas QED comes from $U(1)$ symmetry (a thorough review of group theory is beyond the scope of this thesis):

$$\Psi(x) \mapsto \Psi'(x) = e^{(ig_s\alpha(x)\cdot\hat{T})}\Psi(x) \tag{1.26}$$

where $\hat{T}$ are the generators of $SU(3)$ and are related to the Gell-Mann matrices. To be invariant under this local phase transformation, we have to add eight new fields G^a_μ to the Dirac equation:

$$i\gamma^\mu(\partial_\mu + ig_s G^a_\mu T^a)\Psi - m\Psi = 0 \tag{1.27}$$

With the new fields transforming as:

$$G^k_\mu \to G^{k'}_\mu = G^k_\mu - \partial_\mu\alpha_k - g_s\zeta_{ijk}\alpha_i G^j_\mu \tag{1.28}$$

The last term of the equation comes from the fact that the Gell-Mann matrices do not commute, and ζ_{ijk} is defined by: $[M_i, M_j] = 2i\zeta_{ijk}M_k$ with M the Gell-Mann matrices. Physically, the eight fields describe the eight possible gluon particles, and the gluon self-interaction is described by the last term of the equation. The charge associated to the strong interaction is called colour charge and can take three values (r, b and g), hence the name describing this interaction: Quantum Chromodynamics. Only colour charged particles couple to gluons; leptons, and in particular neutrinos, are colourless fermions and so they do not interact through the strong force.

Weak interaction

As we have seen until now, neutrinos are not electrically charged, and they are not colour charged either, so they do not interact through electromagnetic or strong interactions. They do, however, take part in weak interaction processes such as the neutron's decay or inverse beta decay.

Weak interactions also stem from invariance under a local phase transformation, such as eq. 1.26, except for the gauge group being $SU(2)$ instead of $SU(3)$ or $U(1)$ (strong and electromagnetic interactions, respectively).

Taking the Lagrangian density of an interaction $\mathscr{L}$, the conserved current of the interaction is given by:

$$j^\mu = \frac{\delta\mathscr{L}}{\delta(\partial_\mu\Psi)}\delta\Psi \tag{1.29}$$

The requirement of the interaction to be Lorentz invariant limits the possible form of the current to five possible bilinear combinations: scalar and pseudoscalar, vector and axial-vector and tensor. The allowed forms of the current are given in Table 1.2:

Type	Expression	Number of components	Mediator spin
Scalar	$\overline{\Psi}\Phi$	1	0
Pseudoscalar	$\overline{\Psi}\gamma^5\Phi$	1	0
Vector	$\overline{\Psi}\gamma^\mu\Phi$	4	1
Axial-vector	$\overline{\Psi}\gamma^\mu\gamma^5\Phi$	4	1
Tensor	$\overline{\Psi}(\gamma^\mu\gamma^\nu - \gamma^\nu\gamma^\mu)\Phi$	6	2

Table 1.2: Allowed Lorentz invariant forms of the conserved current

In particular, the conserved current for QED and QCD takes the form of a vector current.

The number of independent components of the current corresponds to the number of polarisation states of the mediator boson; for example, a vector current has 4 components $\mu = 0, 1, 2, 3$, but one of the components is fixed by the gauge-fixing condition, hence the 3 remaining independent components correspond to (2J+1) polarisation states, which yield a spin J=1 boson.

As demonstrated by Wu's experiment [WAH+57] in 1957, parity is not conserved in the weak interactions. The different allowed forms of currents have different behaviour under parity reversal: scalar and axial-vector do not change sign under parity reversal, pseudoscalar and vector do change sign, whereas the scalar product of two vectors or axial-vectors is unchanged under parity reversal and the scalar product of vector and axial-vector does change sign under parity.

An amplitude consisting of the product of vector and axial-vector currents does not suffice to give experimentally observable parity violation since the rates of processes, such as the one observed in Wu's experiment, are given by the *square* of the amplitude. Hence, the parity violation term in the current must be compared to a parity conserving term in order to have observable consequences:

$$j^{\mu} = \overline{\Psi}(g_V \gamma^{\mu} + g_A \gamma^{\mu} \gamma^5)\Phi \tag{1.30}$$

with g_V the vector coupling constant and g_A the axial vector coupling constant. In the limit where $|g_V| = |g_A| = g$, the current can be rewritten, highlighting the chiral nature of a parity violating interaction:

$$j^{\mu} = \overline{\Psi} 2g\gamma^{\mu} \left(\frac{1 \pm \gamma^5}{2} \right) \Phi \tag{1.31}$$

that is to say, $j^{\mu} = \overline{\Psi} 2g\gamma^{\mu} P_L \Phi$ for the $-$ sign and $j^{\mu} = \overline{\Psi} 2g\gamma^{\mu} P_R \Phi$ for the $+$ sign. Eq: 1.31 is in agreement with the experimental fact (see section 1.1.1 Neutrino helicity: the Goldhaber experiment) that only, left-handed neutrino were observed.

The weak interaction can be better understood in the framework of the electroweak interaction. In the electroweak interaction, the Lagrangian is invariant under a local gauge of the $SU(2)_L \otimes U(1)_Y$ (with L denoting the weak isospin and Y the hypercharge). This invariance requires the addition of four new fields: three W bosons of the weak isospin T and one B boson from the hypercharge Y.

Physically however, the three W bosons and the B bosons are not observed; what is observed are the $W^{\pm}$, Z^0 bosons that arise as linear combinations of the W and B bosons from the spontaneous symmetry breaking induced by the Higgs mechanism.

In this context, left-handed leptons[5] (or right handed anti-leptons) form weak isospin doublets, whereas right-handed leptons (left-handed anti-leptons) are weak isospin singlets:

$$\begin{pmatrix} \nu_{\ell_L} \\ \ell_L \end{pmatrix}, \ \ell_R, \text{ with } \ell = e, \mu, \tau. \tag{1.32}$$

1.3 Neutrinos beyond the Standard Model

Neutrinos were long thought to be massless, however, their experimentally observed oscillatory nature requires that they are massive, however small the mass may be.

[5] This is also true for quarks

In this chapter section we will explain the origin of the mass of the charged leptons through the Higgs mechanism and present some of the most well-known models for the mass of the neutrinos.

1.3.1 Origin of the neutrino's mass

Origin of the mass: the Higgs mechanism

In the Dirac Lagrangian:[6]

$$\mathscr{L} = \overline{\Psi}(i\partial\!\!\!/ - m)\Psi \tag{1.33}$$

the mass term is given by $-m\overline{\Psi}\Psi$. We can write the mass term in the chiral basis:

$$-m\overline{\Psi}\Psi = -m[\overline{\Psi_L}\Psi_R + \overline{\Psi_R}\Psi_L] \tag{1.34}$$

since left-handed leptons are isospin doublets and right-handed leptons are isospin singlets, they do not have the same transformation under the electroweak group symmetry: $SU(2)_T \otimes U(1)_Y$:

$$\begin{aligned} \Psi_L &\mapsto \Psi'_L = e^{i(\alpha T + \beta Y)}\Psi_L \\ \Psi_R &\mapsto \Psi'_R = e^{i\beta Y}\Psi_R \end{aligned}$$

This implies that the Dirac mass term is not invariant under transformation of the $SU(2)_T \otimes U(1)_Y$ group of symmetry, hence this mass term is forbidden.

Actually, the mass of fermions and massive gauge bosons are provided by the Higgs[7] mechanism [EB64, Hig64, GHK64, Kib67].

The Higgs mechanism takes place in the electroweak theory given by the local gauge invariance under $SU(2)_L \otimes U(1)_Y$. The minimal Higgs model is composed of a charged and a neutral scalar field arranged in a weak isospin doublet:

$$\phi = \begin{pmatrix} \phi^+ \\ \phi^0 \end{pmatrix} = \frac{1}{\sqrt{2}} \begin{pmatrix} \phi_1 + i\phi_2 \\ \phi_3 + i\phi_4 \end{pmatrix} \tag{1.35}$$

The Lagrangian of the doublet is given by:

$$\mathscr{L} = (\partial_\mu \phi)^\dagger (\partial^\mu \phi) - V(\phi) \tag{1.36}$$

with $V(\phi)$ the Higgs potential given by: $V(\phi) = \mu^2 \phi^\dagger \phi + \lambda(\phi^\dagger \phi)^2$

To ensure that the photon remains massless, the vacuum expectation value (in other words the minimum of the field) of the charged scalar field must remain zero after the spontaneous symmetry breaking, hence the vacuum expectation value is given by: $\frac{1}{\sqrt{2}} \begin{pmatrix} 0 \\ v \end{pmatrix}$.

Then we can expand the field around the vacuum expectation value:

$$\phi(x) = \frac{1}{\sqrt{2}} \begin{pmatrix} \phi_1(x) + i\phi_2(x) \\ v + \eta(x) + i\phi_4(x) \end{pmatrix} \tag{1.37}$$

---

[6] in [GK07] it is advocated that the Lagrangian should be written $\mathscr{L} = \overline{\Psi}(i \overleftrightarrow{\partial\!\!\!/} - m)\Psi$ with $\overleftrightarrow{\partial_\mu} = \frac{\partial_\mu - \overleftarrow{\partial_\mu}}{2}$ and $\Psi\overleftarrow{\partial_\mu} = \partial_\mu \Psi$ because the Lagrangian is explicitly real, as a it should be.

[7] "Higgs mechanism should be renamed the "ABEGHHK'tH mechanism""- Peter Higgs (for all the people who contributed to its discovery: Philip Warren Anderson, Robert Brout, François Englert, Gerry Guralnik, Dick Hagen, Peter Higgs, Tom Kibble and Gerard 't Hooft

This expression can be simplified, which will simplify the expression of the Lagrangian as well, by taking the appropriate choice of gauge[8].
Taking the Unitary gauge :

$$\phi(x) = \frac{1}{\sqrt{2}}\begin{pmatrix} 0 \\ v + h(x) \end{pmatrix} \tag{1.38}$$

The $SU(2)_L \otimes U(1)_Y$ gauge invariance is obtained by replacing the partial derivative by the covariant derivative:

$$\partial_\mu \mapsto D_\mu = \partial_\mu + i g_w T \cdot W_\mu(x) + i g' \frac{Y}{2} B_\mu \tag{1.39}$$

where T are the generators of the $SU(2)$ group, related to the Pauli spin-matrices. Provided that the three gauge fields $W_\mu^{1,2,3}$ and the B_μ gauge field transform accordingly, under $SU(2)_L \otimes U(1)_Y$ local gauge transformations.

If we substitute the covariant derivative in the Lagrangian, and we diagonalise the resulting equations to find the mass eigenstates A^μ and Z^μ, we get:

$$\frac{1}{8} v^2 (A_\mu Z_\mu) \begin{bmatrix} 0 & 0 \\ 0 & g_W^2 + g'^2 \end{bmatrix} \begin{pmatrix} A^\mu \\ Z^\mu \end{pmatrix} \tag{1.40}$$

We effectively recover a massless photon A_μ and a massive Z boson: $m_Z = \frac{1}{2} v \sqrt{g_W^2 + g'}$.

The Higgs mechanism thus generates the mass of the $W^\pm$ and Z gauge boson in the electroweak theory by spontaneously breaking the $SU(2)_L \otimes U(1)_Y$ symmetry.

Interestingly enough, the Higgs mechanism can also generate the mass of the fermions. We denote L_L the $SU(2)$ doublet of left-handed fermions and ℓ_R the corresponding right-handed singlet and an arbitrary unitary transformation U.

We have:

$$L_L \mapsto L'_L = U L_L \tag{1.41}$$
$$\phi \mapsto \phi' = U\phi \tag{1.42}$$

and the transformation of the adjoint is given by:

$$\overline{L_L} \mapsto \overline{L'_L} = \overline{L_L} U^\dagger \tag{1.43}$$

It follows:

$$\overline{L_L}\phi \mapsto (\overline{L_L}\phi)' = \overline{L_L} U^\dagger U \phi = \overline{L_L}\phi \tag{1.44}$$

Let's consider that U is a $SU(2)_L$ transformation, consequently $\overline{L_L}\phi$ are invariant under such transformation, when combined with a right-handed singlet ℓ_R: $\overline{L_L}\phi\ell_R$ the term is invariant[9] under $U(1)_Y$. Obviously the Hermitian conjugate $(\overline{L_L}\phi\ell_R)^\dagger = \overline{\ell_R}\phi^\dagger L_L$ is also invariant.

So we can introduce in the Lagrangian an invariant term of the form $-g_f(\overline{L_L}\phi\ell_R + \overline{\ell_R}\phi^\dagger L_L)$, called a "Yukawa interaction".

As an example, we will take the Lagrangian for the $SU(2)_L$ doublet of the electron and electron neutrino:

$$\mathscr{L}_e = -g_e \left[\left(\overline{\nu_e}\ \overline{e}\right)_L \begin{pmatrix} \phi^+ \\ \phi^0 \end{pmatrix} e_R + \overline{e_R} \left(\phi^{+*}\ \phi^{0*}\right) \begin{pmatrix} \nu_e \\ e \end{pmatrix}_L \right] \tag{1.45}$$

[8] If we were to compute the Lagrangian now, we would obtain terms corresponding to unphysical massless Goldstone bosons, this term can be simplified without impact on the physical meaning providing the correct choice of gauge

[9] because the hypercharge of the three terms compensate each other

which gives, after spontaneous break of the symmetry, and taking the unitary gauge as previously:

$$\mathscr{L}_e = -\frac{g_e}{\sqrt{2}} v(\overline{e}_L e_R + \overline{e}_R e_L) - \frac{g_e}{\sqrt{2}} h(\overline{e}_L e_R + \overline{e}_R e_L) \tag{1.46}$$

The last term represents an interaction with an excitation of the Higgs field. The first term is the mass term of the electron, which depends on the Yukawa coupling g_e and the vacuum expectation value of the Higgs field:

$$m_e = \frac{v g_e}{\sqrt{e}} \tag{1.47}$$

It must be noted that, since the non-zero vacuum expectation value arises in the lower part of the $SU(2)_L$ doublet (for the neutral scalar field component of the Higgs doublet), the mechanism described above can only generate the mass of the charged leptons, not the neutrinos.

The Dirac neutrino mass term

The simplest way to extend the Standard model to generate a mass for the neutrinos is to allow the existence of a right-handed neutrino. This is called "minimally extended Standard Model".

To generate the neutrino mass, we introduce a Yukawa interaction between the $SU(2)$ isospin doublet, the right-handed neutrino and the charge conjugate of the Higgs field: $\overline{L}_L \phi^c \nu_R + \overline{\nu_R} \phi^{c\dagger} L_L$. The charge conjugate of the Higgs field is given by:

$$\phi^c = \begin{pmatrix} -\phi^{0*} \\ \phi^- \end{pmatrix} \tag{1.48}$$

It follows (for the electron neutrino, for example):

$$\mathscr{L}_\nu = -g_\nu \left[\begin{pmatrix} \overline{\nu_e} & \overline{e} \end{pmatrix}_L \begin{pmatrix} -\phi^{0*} \\ \phi^- \end{pmatrix} \nu_{e_R} + \overline{\nu_{e_R}} \begin{pmatrix} -\phi^{0*} & \phi^- \end{pmatrix} \begin{pmatrix} \nu_e \\ e \end{pmatrix}_L \right] \tag{1.49}$$

which, after symmetry breaking and unitary gauge choice, yields:

$$\mathscr{L}_e = -\frac{g_\nu}{\sqrt{2}} v(\overline{\nu_{e_L}} \nu_R + \overline{\nu_{e_R}} \nu_{e_L}) - \frac{g_\nu}{\sqrt{2}} h(\overline{\nu_{e_L}} \nu_{e_R} + \overline{\nu_{e_R}} \nu_{e_L}) \tag{1.50}$$

The first term corresponds to the mass term of the neutrino, which depends on the Yukawa coupling constant and the vacuum expectation value of the Higgs. It is generally referred to as Dirac neutrino mass term, by opposition to the Majorana neutrino mass term that we will describe in the next section. If the neutrino mass arises from this mechanism only, we would expect that the mass of the neutrinos to be of the same order of magnitude as for the charged leptons. However, we know experimentally that their mass is very much smaller than the charged leptons'.

It must be noted that these right-handed neutrinos do not participate in the charged current weak interaction, because of the V-A structure of the interaction. Moreover, they are electrically neutral and colourless, hence they do not interact through any fundamental interaction described by the Standard Model. This is why they are called ***sterile*** neutrinos; they do, however, interact through the gravitational interaction.

The Majorana neutrino mass term

Another possible mass term is the so-called Majorana mass term. In a Dirac mass term, we couple both chiral components of a single field: $m(\overline{\Psi_L}\Psi_R + \overline{\Psi_R}\Psi_L)$; in a Majorana mass term, however, we couple a chiral component to its charge conjugate:

$$m(\overline{\Psi_L}(\Psi_L)^c + \overline{(\Psi_L)^c}\Psi_L) \tag{1.51}$$

It can be shown that $(\Psi_L)^c$ has right-handed chirality and the term $m\overline{\Psi_L}(\Psi_L)^c$ does not vanish.

We can construct a Majorana mass term from the left-handed chiral component as above, or from the right-handed chiral component. We will consider both possibilities in the next section.

The Seesaw mechanism

The most general allowed Lagrangian to generate the neutrino mass is composed of a Dirac mass term and two Majorana mass terms:

$$\begin{aligned}\mathscr{L}_{Seesaw} = m_D(\overline{\nu_L}\nu_R + \overline{\nu_R}\nu_L) + \frac{1}{2}m_L(\overline{\nu_L}(\nu_L)^c + \overline{(\nu_L)^c}\nu_L) \\ + \frac{1}{2}m_R(\overline{(\nu_R)^c}\nu_R + \overline{\nu_R}(\nu_R)^c)\end{aligned} \tag{1.52}$$

or equivalently:

$$\mathscr{L}_{Seesaw} = m_D\overline{\nu_L}\nu_R + \frac{1}{2}m_L\overline{\nu_L}(\nu_L)^c + \frac{1}{2}m_R\overline{(\nu_R)^c}\nu_R + \text{h.c.}^{10} \tag{1.53}$$

The first term of the Lagrangian is the Dirac mass term, while the other two terms are Majorana mass terms. We note that the Majorana mass term couples a particle to its antiparticle. While this is (only) possible for neutrinos because they are electrically neutral, this breaks the lepton number conservation law. However, this is not outrageous since the lepton number conservation is an accidental conservation and does not stand on any intrinsic gauge symmetry of the model.

The latter equation can be rewritten in matrix form:

$$\mathscr{L}_{Seesaw} = \frac{1}{2}\begin{pmatrix}\overline{\nu_L} & \overline{(\nu_R)^c}\end{pmatrix}\begin{bmatrix}m_L & m_D \\ m_D & m_R\end{bmatrix}\begin{pmatrix}(\nu_L)^c \\ \nu_R\end{pmatrix} \tag{1.54}$$

The Majorana mass term constructed from the left chiral component is forbidden because it is not invariant under $SU(2)_L$ transformations, hence we have $m_L = 0$. The Majorana mass term constructed from the right-handed chiral component, on the contrary, is invariant under $SU(2)_L$ transformations and can be kept in the Lagrangian. As we can see, the mass matrix is not diagonal, which means that the neutrino flavour fields are not mass eigenstates but rather a linear combination of the mass eigenstates. We will see in the next section that this fact is at the root of the oscillation mechanism.

In order to recover the mass eigenvalues, we diagonalise the mass matrix and we find the two eigenvalues mass eigenvalues:

$$m_\pm = \frac{m_R}{2}\left[1 \pm \sqrt{1 + 4\frac{m_D^2}{m_R^2}}\right] \tag{1.55}$$

[10] h.c. stands for hermitian conjugate

Thus, the Seesaw mechanism provides a way to have very small active neutrino masses. In the limit of a very large Majorana mass $m_R >> m_D$, we end up with one large mass eigenvalue, $m_+ = m_N \approx m_R$, and one very small mass eigenvalue, $m_- = m_\nu \approx \frac{m_D^2}{m_R}$, if the Dirac mass m_D is of similar size to the mass of the other fermions, and the Majorana mass is large enough for the lighter mass eigenvalue to be $m_\nu << 1\ eV$.

We can also determine the physical neutrino corresponding to the previous mass eigenvalues:

$$\nu = \cos\theta(\nu_L + (\nu_L)^c) - \sin\theta(\nu_R + (\nu_R)^c) \tag{1.56}$$

$$N = \cos\theta(\nu_R + (\nu_R)^c) + \sin\theta(\nu_L + (\nu_L)^c) \tag{1.57}$$

where $\tan\theta \approx \frac{m_D}{m_R}$.

It can be shown that the large mass neutrino state N is almost entirely right-handed, and consequently sterile. The Seesaw mechanism is an elegant hypothesis to explain the very small neutrino masses.

1.3.2 Neutrino oscillation mechanism

Neutrino oscillations are a well-established experimental fact. In this section we will give an overview of the oscillations theoretical framework.

Neutrino mixing

In the previous section, we saw that the mass of the neutrino arises from a mass term in the Lagrangian that can be either Dirac, Majorana or a sum of Dirac and Majorana mass terms and the Seesaw mechanism was derived in the context of a single neutrino. The mass term can be generalized to the three neutrino flavours. There is no reason to assume that the interaction (or flavour) states are eigenstates of the mass matrix (mathematically this translates as a non-diagonal mass matrix). However, we can go from the flavour eigenstates to the mass eigenstates by a change of basis, hence the flavours eigenstates are related to the mass eigenstates by a unitary matrix U_{PMNS}[11]:

$$\begin{pmatrix} \nu_e \\ \nu_\mu \\ \nu_\tau \end{pmatrix} = \underbrace{\begin{bmatrix} U_{e1} & U_{e2} & U_{e3} \\ U_{\mu 1} & U_{\mu 2} & U_{\mu 3} \\ U_{\tau 1} & U_{\tau 2} & U_{\tau 3} \end{bmatrix}}_{U_{PMNS}} \begin{pmatrix} \nu_1 \\ \nu_2 \\ \nu_3 \end{pmatrix} \tag{1.58}$$

Neutrino oscillation in vacuum

In the theory of neutrino oscillation [BBGK95], the neutrino oscillation is described using ordinary quantum mechanics. Neutrinos (antineutrinos) are produced in their flavour eigenstate $\nu_\alpha(\overline{\nu_\alpha})$ with $\alpha = e, \mu, \tau$ through charged current weak interaction simultaneously to the corresponding charged anti-lepton (lepton) $\ell_\alpha^+(\ell_\alpha^-)$.

As seen in the previous section, because of the mass term, flavour eigenstates do not correspond to mass eigenstates but rather to a linear combination of mass eigenstates, which we can write, using Dirac's famous *Bra-Ket* notation:

$$|\nu_\alpha\rangle = \sum_k U_{\alpha k}^* |\nu_k\rangle \tag{1.59}$$

[11] For Pontecorvo, Maki, Nakagawa, Sakata from the work of Jiro Maki, Masami Nakagawa and Shoichi Sakata who theorised the neutrino oscillation after Bruno Pontecorvo suggested an oscillation between neutrino and antineutrino could exist

with U the PMNS matrix and k the mass eigenstates. The unitarity of the PMNS matrix imposes that the flavour eigenstates are orthogonal to each other as long as the mass eigenstates are orthogonal to each other:

$$\langle \nu_\alpha | \nu_\beta \rangle = \delta_{\alpha\beta} \tag{1.60}$$
$$\langle \nu_k | \nu_j \rangle = \delta_{kj} \tag{1.61}$$

The number of mass eigenstates is not limited; however if there are more than three mass eigenstates, the corresponding flavour eigenstates must be sterile. Oscillation toward these hypothetic sterile flavour states could be observed by disappearance experiments (such as STEREO).

Mass eigenstates are eigenstates of the Hamiltonian $\mathscr{H}$, hence we have:

$$\mathscr{H} |\nu_k\rangle = E_k |\nu_k\rangle \tag{1.62}$$

with the energy eigenvalue given by Einstein's energy-momentum relation:

$$E_k = \sqrt{\vec{p_k}^2 + m_k^2} \tag{1.63}$$

Since the masses of the neutrinos are known to be very small, a good approximation (often called ultrarelativistic limit) of the energy is given by[12]:

$$E_k = \sqrt{p_k^2 + m_k^2} \approx p_k + \frac{m_k^2}{2p_k} \approx E + \frac{m_k^2}{2E} \tag{1.64}$$

and the propagation in time is dictated by the Schrödinger equation:

$$i\frac{\partial}{\partial t} |\nu_k(t)\rangle = \mathscr{H} |\nu_k(t)\rangle = E_k |\nu_k(t)\rangle \tag{1.65}$$

The plane wave solution to this equation is given by:

$$|\nu_k(t)\rangle = e^{-iE_k \cdot t} |\nu_k\rangle \tag{1.66}$$

From there we can determine the propagation of the flavour eigenstates:

$$|\nu_\alpha(t)\rangle = \sum_k U_{\alpha k}^* |\nu_t(t)\rangle = \sum_k U_{\alpha k}^* e^{iE_k \cdot t} |\nu_k\rangle \tag{1.67}$$

From equation 1.59, it is straightforward to show:

$$|\nu_k\rangle = \sum_\alpha U_{\alpha k} |\nu_\alpha\rangle \tag{1.68}$$

It comes that the flavour state can be written as a function of the other flavour eigenstates:

$$|\nu_\alpha(t)\rangle = \sum_{\beta=e,\mu,\tau} \left[\sum_k U_{\alpha k}^* e^{-iE_k \cdot t} U_{\beta k} \right] |\nu_\beta\rangle \tag{1.69}$$

Finally, we project on the β flavour eigenstate to get the transition probability from the flavour α to the flavour β:

$$\mathscr{P}_{\nu_\alpha \to \nu_\beta}(t) = |\langle \nu_\beta | \nu_\alpha(t) \rangle|^2 = \sum_k \sum_j U_{\alpha k}^* U_{\beta k} U_{\alpha j} U_{\beta j}^* e^{-i(E_k - E_j)\cdot t} \tag{1.70}$$

[12] Taylor expansion of $f(x) = \sqrt{a+x} = \sqrt{a} + \frac{x}{\sqrt{a}} + \mathscr{O}(x^2)$ and then $p_k \approx E_k$

where $E_k - E_j \approx \frac{m_k^2 - m_j^2}{2E} = \frac{\Delta m_{kj}^2}{2E}$

Moreover, experimentally it is easier to measure the distance traveled by the neutrino between the source and the detector rather than the time between the production and the detection[13]. Since the neutrino travels at nearly the speed of light, we can substitute t by the baseline L in natural units ($c = 1$). Hence,

$$\mathscr{P}_{\nu_\alpha \to \nu_\beta}(L,E) = \sum_k \sum_j U_{\alpha k}^* U_{\beta k} U_{\alpha j} U_{\beta j}^* e^{-i\frac{\Delta m_{kj}^2}{2E} \cdot L} \tag{1.71}$$

Making use of the unitarity relation and splitting the complex quantity into real and imaginary parts, we get:

$$\mathscr{P}_{\nu_\alpha \to \nu_\beta}(L,E) = \delta_{\alpha\beta} - 4\sum_{k>j} Re[U_{\alpha k}^* U_{\beta k} U_{\alpha j} U_{\beta j}^*] \sin^2\left(\frac{\Delta m_{kj}^2 L}{4E}\right) + 2\sum_{k>j} Im[U_{\alpha k}^* U_{\beta k} U_{\alpha j} U_{\beta j}^*] \sin\left(\frac{\Delta m_{kj}^2 L}{2E}\right) \tag{1.72}$$

The transition probability for antineutrinos can be computed replacing U_{PMNS} by U_{PMNS}^*:

$$\mathscr{P}_{\overline{\nu_\alpha} \to \overline{\nu_\beta}}(L,E) = \delta_{\alpha\beta} - 4\sum_{k>j} Re[U_{\alpha k}^* U_{\beta k} U_{\alpha j} U_{\beta j}^*] \sin^2\left(\frac{\Delta m_{kj}^2 L}{4E}\right) - 2\sum_{k>j} Im[U_{\alpha k}^* U_{\beta k} U_{\alpha j} U_{\beta j}^*] \sin\left(\frac{\Delta m_{kj}^2 L}{2E}\right) \tag{1.73}$$

The difference between the transition probability for neutrino and antineutrino is the sign of the imaginary part. If the CP symmetry is not violated, $\mathscr{P}_{\nu_\alpha \to \nu_\beta} = \mathscr{P}_{\overline{\nu_\alpha} \to \overline{\nu_\beta}}$ which requires that the imaginary part is zero, meaning that the imaginary part would be responsible for CP violation. CP violation is related to the matter-antimatter asymmetry of the universe.

The transition probability does not depend on the absolute mass of the neutrino, only on the difference of the squared mass, so oscillation experiments can not measure the absolute masses of the neutrinos.

Two flavours oscillation

A specific case arises when one of the mass spliting Δm_{kj}^2 can be neglected compared to the other. This was the case in the atmospheric anomaly for example, where the ν_e could be neglected, because two of the mass states are almost degenerate compared to the third one: $|\Delta m_{32}^2| \approx 33 \times |\Delta m_{12}^2|$. This is also the case for the search of sterile neutrino in the STEREO experiment, where the sterile neutrino mass is much bigger than the active neutrino masses: $m_s >> m_1, m_2, m_3 \Rightarrow \Delta m_{s1}^2 \approx \Delta m_{s2}^2 \approx \Delta m_{s3}^2 \approx m_s^2$.

In this case, we can express the flavour states as:

$$\begin{pmatrix} \nu_\alpha \\ \nu_\beta \end{pmatrix} = \begin{bmatrix} \cos\theta & \sin\theta \\ -\sin\theta & \cos\theta \end{bmatrix} \begin{pmatrix} \nu_1 \\ \nu_2 \end{pmatrix} \tag{1.74}$$

[13] This assumption is well illustrated by the regrettably famous supraluminic neutrino problem [A+12]

From which we find[14]:

$$\mathscr{P}_{\nu_\alpha \to \nu_\beta}(L,E) = \sin^2(2\theta)\sin^2\left(1.267 \times \frac{\Delta m^2[\mathrm{eV}^2]\cdot L[\mathrm{m}]}{E[\mathrm{MeV}]}\right) \tag{1.75}$$

where the 1.267 prefactor is a dimensional constant, and because of unitarity, we have:

$$\mathscr{P}_{\nu_\alpha \to \nu_\alpha}(L,E) = 1 - \mathscr{P}_{\nu_\alpha \to \nu_\beta}(L,E) \tag{1.76}$$

Neutrino oscillation in matter: the MSW effect

When neutrinos propagate through matter, the potential created by the electron of the medium will modify the oscillation probability, this effect is called the MSW effect [Wol78, Smi03] named after Mikheyev, Smirnov and Wolfenstein.

The electron neutrinos are sensitive to the charged current potential created by the electron of the matter and the neutral current potential created by all the matter, whereas the other neutrino flavours are only sensitive to the neutral current potential.

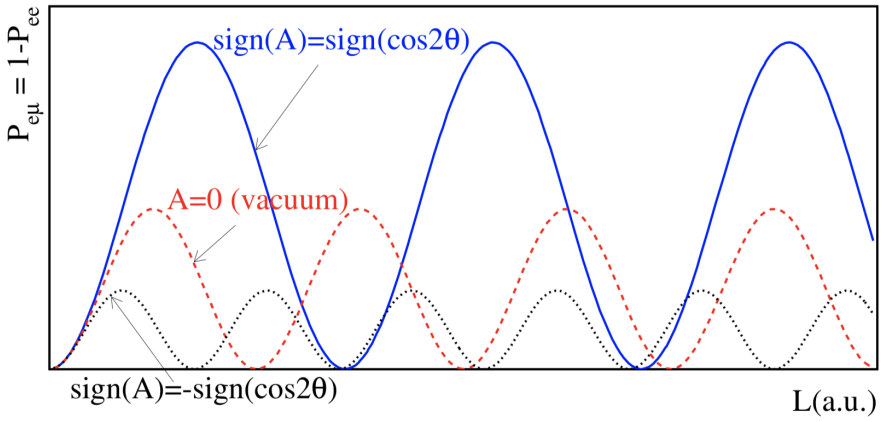

Figure 1.8: Oscillation probability of $\nu_e \to \nu_\mu$ as a function of the baseline L. Three cases are presented: vacuum oscillation (red), enhanced oscillation (blue) and reduced oscillation (black).

The neutrino oscillation in matter can be enhanced or reduced depending on how the ratio A of the electronic potential over the squared mass difference Δm^2 compares to the mixing angle (see Annexe A The MSW effect). Since this enhancement of the oscillation in matter by the MSW effect depends on the sign of Δm^2, it is possible to take advantage of the MSW effect to determine the sign of Δm^2.

Neutrino oscillation parameters measurement

The PMNS matrix is often presented as the product of 4 matrices, three rotation matrices (that correspond to the oscillations for a given $\frac{L}{E}$ range: atmospheric, solar or reactor neutrino) and a diagonal Majorana phase matrix that is present only if neutrinos are Majorana Since the Majorana phase matrix is diagonal the oscillation phenomenon

[14]The complete derivation follows the previous general 3-flavour derivation and can be found in the litterature

is independent of the nature of the neutrino:

$$U_{PMNS} = \underbrace{\begin{bmatrix} 1 & 0 & 0 \\ 0 & c_{23} & s_{23} \\ 0 & -s_{23} & c_{23} \end{bmatrix}}_{atmospheric} \underbrace{\begin{bmatrix} c_{13} & 0 & s_{13}e^{-i\delta} \\ 0 & 1 & 0 \\ s_{13}e^{i\delta} & 0 & c_{13} \end{bmatrix}}_{reactor} \underbrace{\begin{bmatrix} c_{12} & s_{12} & 0 \\ -s_{12} & c_{12} & 0 \\ 0 & 0 & 1 \end{bmatrix}}_{solar} \underbrace{\begin{bmatrix} i & 0 & 0 \\ 0 & e^{i\alpha} & 0 \\ 0 & 0 & e^{i\beta} \end{bmatrix}}_{Majorana} \tag{1.77}$$

with $c_{ij} = \cos\theta_{ij}$ and $s_{ij} = \sin\theta_{ij}$ ($\theta_{ij} = \theta_{12}, \theta_{23}, \theta_{13}$ are the mixing angles), δ is the Dirac CP phase, which accounts for possible CP violation in the neutrino oscillation process, and α and β are the Majorana phases. As explained in the previous section, the vacuum oscillation dependency on the mass differences is within a *squared* sine, which means that vacuum oscillation experiments are not sensitive to the sign of the mass differences. Hence more than one mass ordering is possible.

The sign of one of the mass splitting, Δm^2_{12}, has been determined thanks to solar neutrinos [MS16]. Indeed, solar neutrinos travel through the sun before reaching the Earth and in doing so they are sensitive to the matter effect, which modifies the oscillation probability in a way that depends on the sign of the mass splitting. The sign of one of the mass splitting Δm^2_{12} determined, we end up with two possible mass orderings as shown in Figure 1.9.

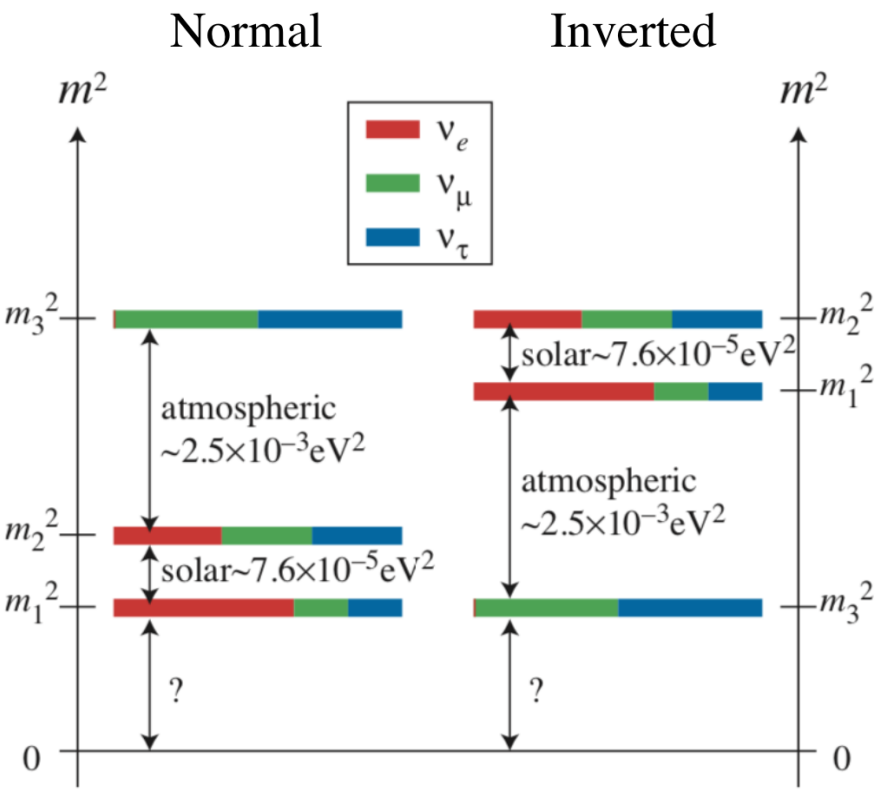

Figure 1.9: The two possible mass hierarchies: Normal ordering (left) and the Inverted ordering (right). The colours are a visual representation of the proportion $|U_{\alpha i}|^2$ of each flavour state $\alpha = e, \mu, \tau$ in the mass state $i = 1, 2, 3$.

To determine all these parameters, an ambitious experimental program has been carried out since several decades. As of 2020, the mixing angles and mass splittings are known with few percent uncertainties: c.f. Table 1.3 giving the parameters values obtained in a global fit of several experiments [dSFG+21], and the 2D acceptance

contours in Figure 1.10. In this fit, the normal mass ordering is favoured at 2.5σ significance.

	Normal ordering		Inverted ordering	
Parameter	Best fit $\pm 1\sigma$	3σ range	Best fit $\pm 1\sigma$	3σ range
Δm^2_{21} $[10^{-5}\text{eV}^2]$	$7.50^{+0.22}_{-0.20}$	6.94-8.14	$7.50^{+0.22}_{-0.20}$	6.94-8.14
$\lvert\Delta m^2_{31}\rvert$ $[10^{-3}\text{eV}^2]$	$2.55^{+0.02}_{-0.03}$	2.47-2.63	$2.45^{+0.02}_{-0.03}$	2.37-2.53
$\sin^2 2\theta_{12}/10^{-1}$	3.18 ± 0.16	2.71-3.69	3.18 ± 0.16	2.71-3.69
$\sin^2 2\theta_{23}/10^{-1}$	5.74 ± 0.14	4.34-6.10	$5.78^{+0.10}_{-0.17}$	4.33-6.08
$\sin^2 2\theta_{13}/10^{-2}$	$2.200^{+0.069}_{-0.062}$	2.000-2.405	$2.225^{0.064}_{-0.070}$	2.018-2.424
δ_{CP}/π	$1.108^{+0.13}_{-0.12}$	0.71-1.99	$1.58^{+0.15}_{-0.16}$	1.11-1.96

Table 1.3: Global fit of the neutrino parameters as of 2020, the value are obtained from [dSFG+21]

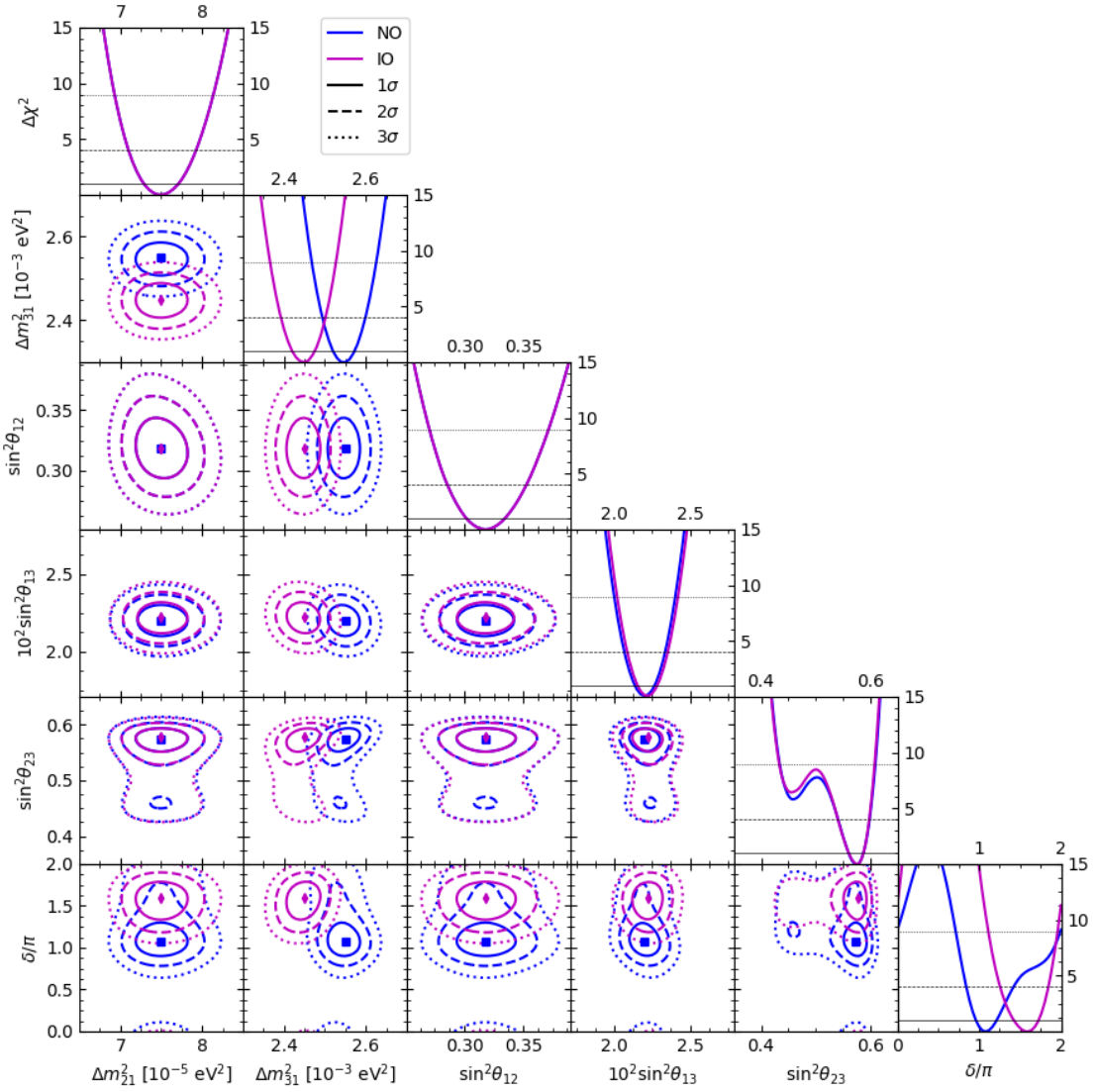

Figure 1.10: Global fit of the neutrino parameters as of 2020 from [dSFG+21]. The 2D acceptance contour at 1σ (solid line), 2σ (dashed line) and 3σ (dotted line) C.L. of one parameter vs the others, as well as the projection of the 2D $\Delta\chi^2$ distributions are presented for the normal ordering of the mass hierarchy (blue) and inverted ordering (magenta).

1.4 Open questions in neutrino physics

Although most oscillation parameters have now been measured with few percent precision, some questions remain unanswered:

- The absolute mass of neutrinos is not yet measured, and oscillation experiments are not sensitive to it, so other types of experiments must be designed to perform this measurement
- Neither of the two possible mass hierarchies is ruled out
- The nature of the neutrino: is the neutrino a Dirac or a Majorana fermion? This question, too, requires specific experiments and can not be answered by oscillation experiments.

- The δ_{CP} phase seems to be non-zero, however its value is not yet precisely measured. Is the CP-violation in the leptonic sector enough to explain the universe matter-antimatter asymmetry?
- Are there sterile neutrinos?

1.4.1 Absolute mass of the neutrino

As of today, the absolute mass of the neutrino is still unknown, only bounds on its mass have been established. A lower bound on the heaviest neutrino mass can be computed from the oscillation experiments: the heaviest neutrino can not have a mass m^2 smaller than the larger Δm^2, hence

$$m \geq \sqrt{\Delta m^2_{32}} \sim 0.04 \text{ eV} \tag{1.78}$$

Astrophysical constraint on the neutrino mass

From the 1987A supernova, which occurred on February 23^{rd} 1987 in the Magellanic Cloud, a constraint on the mass of the electron neutrino could be established.

The Kamiokande, IMB and Baksan [AAVK87] experiments observed the neutrino blast that followed the supernova, three hours earlier than the optical signal. The neutrinos were detected during a time interval $\Delta t \sim 10$ s. Massive neutrinos travel at a speed $v \approx 1 - \frac{m_\nu^2}{2E_\nu^2}$. The distance between the Earth and the Magellanic Cloud is $L \sim 50$ kpc. The detected neutrinos had a mean energy $< E_\nu > \sim 25$ MeV and an energy dispersion $\Delta E_\nu \sim 10$ MeV.

From that, we can derive an upper limit on the mass of the neutrino:

$$\Delta t \sim L\Delta(v^{-1}) \sim L\frac{m_{\nu^2}}{2E_\nu^2}\frac{\Delta E_\nu}{< E_\nu >} \tag{1.79}$$

The combined results of the three experiences [LL02] amount to:

$$m_{\nu_e} < 5.7\ eV \text{ (95\% C.L.)} \tag{1.80}$$

Direct measurement

The mass of the electron neutrino can be deduced from the study of the energy spectrum of a β decay. The maximum energy that the electron can take corresponds to:

$$E^e_{max} = Q - m_{\nu_e} \tag{1.81}$$

where Q is the Q-value of the decay. The tail of the electron spectrum in the case of a massless neutrino and a neutrino with a mass $m_{\nu_e} = 1$ eV are presented in Figure 1.11. To perform this measurement, the spectrometer needs an outstanding energy resolution.

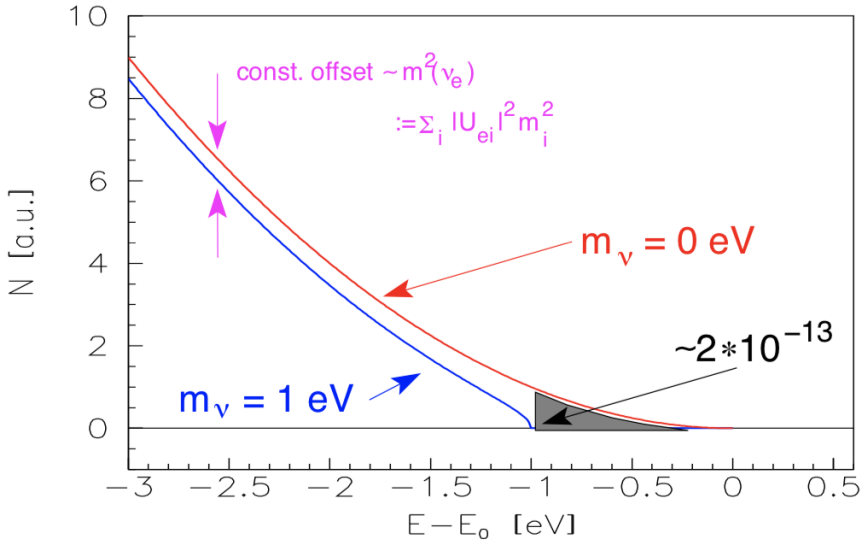

Figure 1.11: Tail of the β energy distribution in the case of a massless ν_e (red) and a the case of $m_{\nu_e} = 1$ eV

In 2019 the KATRIN experiment reported an improved upper limit on the neutrino mass [A+19a]:

$$m_{\overline{\nu_e}} < 1.1 \text{ eV (at 90\% C.L.)} \tag{1.82}$$

improving by almost a factor 2 the last limit provided by the MAINZ [WDB+99] and TROITSK [A+11] experiments.

1.4.2 Mass ordering problem

As explained above, the neutrino mass ordering is not yet established. Since the sign of only one mass splitting has been determined, two different orderings are possible: the Normal ordering and the Inverted ordering (see Figure 1.9). Although the current data favours the normal ordering, the inverted ordering is not ruled out.

Normal or Inverted mass hierarchy

Future large scale experiments such as DUNE [A+20a], Hyper-Kamiokande [Wal19] and JUNO [Lu21] will be able to determine the mass hierarchy.

Both DUNE and Hyper-Kamiokande will rely on the matter effects to determine the mass hierarchy; JUNO will take a different approach, since the matter effects are negligible for JUNO.

The Jiangmen Underground Neutrino Observatory (JUNO) experiment is currently under construction. It consists in a 20 kTon liquid scintillator detector located at a distance $L \sim 53$ km from various commercial nuclear reactor in China. The detector baseline is chosen as to be sensitive to both Δm^2_{21} and Δm^2_{31}. In this case, the survival

probability of the antineutrinos is given by:

$$\mathscr{P}(\overline{\nu_e} \to \overline{\nu_e}) = 1 - \cos^4\theta_{13}\sin^2 2\theta_{12}\sin^2\left(\frac{\Delta m^2_{21} \times L}{4E_\nu}\right) - \sin^2 2\theta_{13}\left(\frac{\Delta m^2_{31} \times L}{4E_\nu}\right) - \sin^2\theta_{12}\sin^2 2\theta_{13}\sin^2\left(\frac{\Delta m^2_{21} \times L}{4E_\nu}\right)\cos\left(\frac{2|\Delta m^2_{31}| \times L}{4E_\nu}\right) \pm \frac{\sin^2\theta_{12}}{2}\sin^2 2\theta_{13}\sin\left(\frac{2\Delta m^2_{21} \times L}{4E_\nu}\right)\sin\left(\frac{2|\Delta m^2_{31}| \times L}{4E_\nu}\right)$$

The last term of the expression of the oscillation probability depends on the mass hierarchy, the normal ordering corresponding to the + solution and the inverted ordering to the −.

The energy spectrum of the antineutrinos for both normal and inverted ordering is given in Figure 1.12.

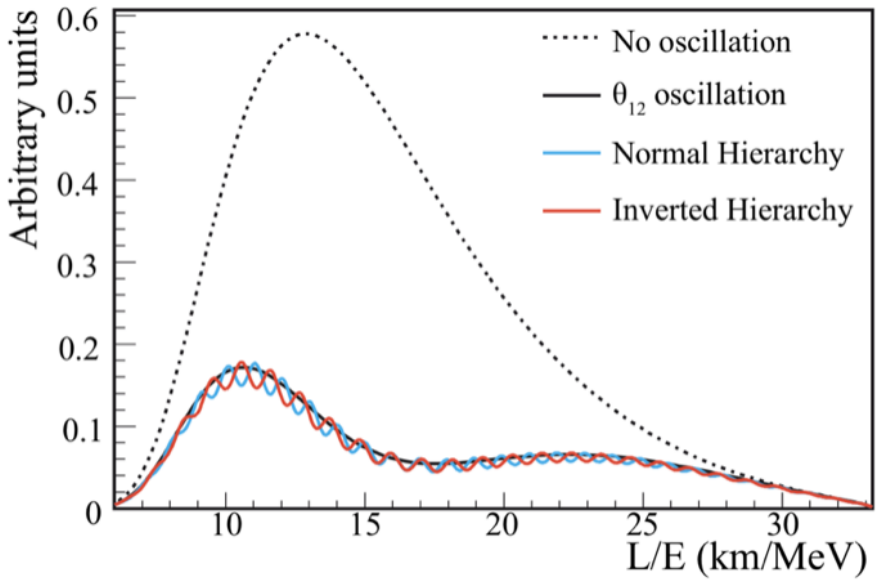

Figure 1.12: Effects of the mass hierarchy on the antineutrino energy spectrum for the JUNO experiment. Are presented: the reactor antineutrino spectrum without oscillation (dotted black), only the oscillation due to θ_{12} (solid black), and the complete oscillation for the normal (blue) and the inverted ordering (red).

1.4.3 Charge conjugation Parity violation

δ_{CP} phase

As of today, CP conservation is excluded at $\sim 2.5\sigma$ in global fits, however, tension between the long baseline accelerator experiments T2K and NOνA [NBP+19] exists.

The next generation of experiments will be able to give a definite answer; in particular, the DUNE experiment is designed to make the measurement of the CP phase.

The DUNE experiment will consist in a near detector located at Fermilab and a far detector consisting in a modular Liquid Argon Time Projection Chamber (LArTPC) detector with a fiducial mass of 40 kTons located 1.5 km underground at the Sanford Underground Research Facility (SURF). A beam of ν_μ or $\overline{\nu_\mu}$ will be fired from Fermilab and detected in the DUNE far detector with a baseline $L \sim 1300$ km.

The difference between $\mathscr{P}(\nu_\mu \to \nu_e)$ and $\mathscr{P}(\overline{\nu_\mu} \to \overline{\nu_e})$ will allow a determination of δ_{CP}; the expected sensitivity to δ_{CP} is given in Figure 1.13 [A+20a].

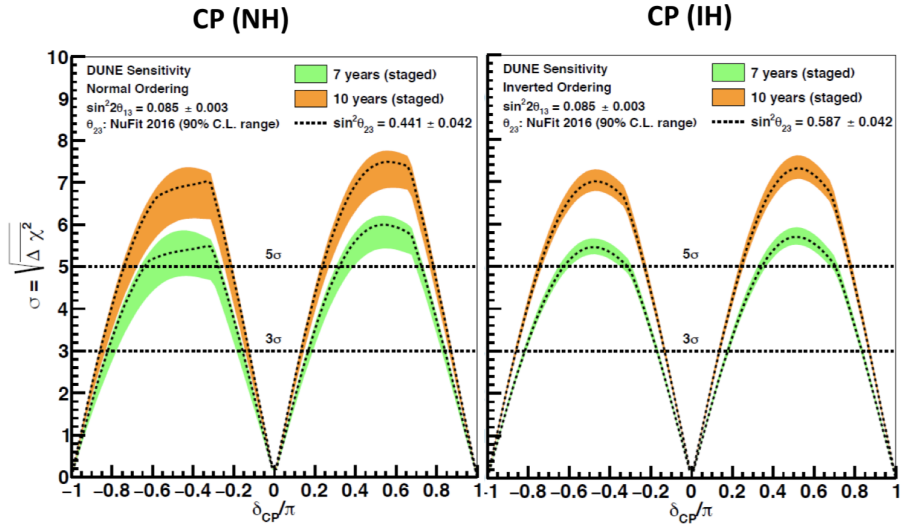

Figure 1.13: Expected sensitivity to δ_{CP} of the DUNE experiment after 7 years (green) and 10 years (orange) of data taking, for normal ordering (left) and inverted ordering (right).

1.4.4 Nature of the neutrino: Dirac or Majorana

The nature of the neutrino is not known at the moment. If the neutrino is a Majorana fermion, the neutrino and the antineutrino would be the same particle, which would allow processes that violate by 2 units lepton number conservation. Neutrinoless double β decay is an example of such process.

Neutrinoless double β decay

In 1939, Furry [Fur39] showed that a new process could happen if (and only if) the neutrino was a Majorana particle: the neutrinoless double β decay ($0\nu\beta\beta$), the Feynman diagram of this process is given in Figure 1.14.

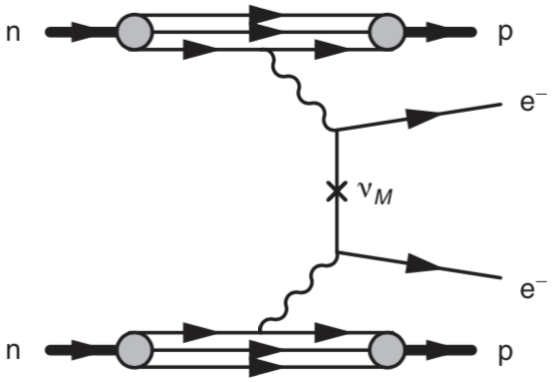

Figure 1.14: Feynman diagram of the neutrinoless double β decay process.

Some nuclei, for which the traditional $\beta^\pm$ decay is energetically forbidden, can

decay to a energetically more favorable nuclei by the double β decay process:

$$(Z,\ A) \rightarrow (Z+2,\ A) + 2e^- + 2\overline{\nu_e} \tag{1.83}$$

This process has been observed in the nuclei ^{82}Se, ^{100}Mo, or ^{116}Cd to name a few, despite the fact that it is a very rare process with a half-life $\tau_{\frac{1}{2}} \in [10^{19} - 10^{25}]$ years.

Experimentally, the sum of the energy of the two electrons produced by $0\nu\beta\beta$ $E_{0\nu\beta\beta}$ is a mono-energetic signal in the limit of a negligible nucleus recoil:

$$E_{0\nu\beta\beta} = Q_{0\nu\beta\beta} = [M(Z,A) - M(Z+2,A)] \tag{1.84}$$

whereas the sum of the energy of the two electrons produced by $2\nu\beta\beta$ would exhibit a broad energy spectrum.

The predicted rate of $0\nu\beta\beta$: $R_{0\nu\beta\beta}$ is proportional to (the square of) the nuclear matrix element of the reaction $\mathscr{M}_{nucl}$ and the effective mass $m_{\beta\beta}$:

$$R_{0\nu\beta\beta} \propto |m_{\beta\beta}|^2 \times |\mathscr{M}_{nucl}|^2 \tag{1.85}$$

where the effective mass depends on the PMNS matrix and the eigenvalue of the mass eigenstates:

$$m_{\beta\beta} = \sum_{i=1}^{3} U_{ei}^2 m_i \tag{1.86}$$

This implies that the $0\nu\beta\beta$ rate depends on the mass hierarchy, and in particular the inverted hierarchy would induce larger rates.

The actual best limit on the $0\nu\beta\beta$ rate is provided by the KamLAND-Zen experiment for ^{136}Xe [GGH+16], it is shown in Figure 1.15 as a limit on the effective mass.

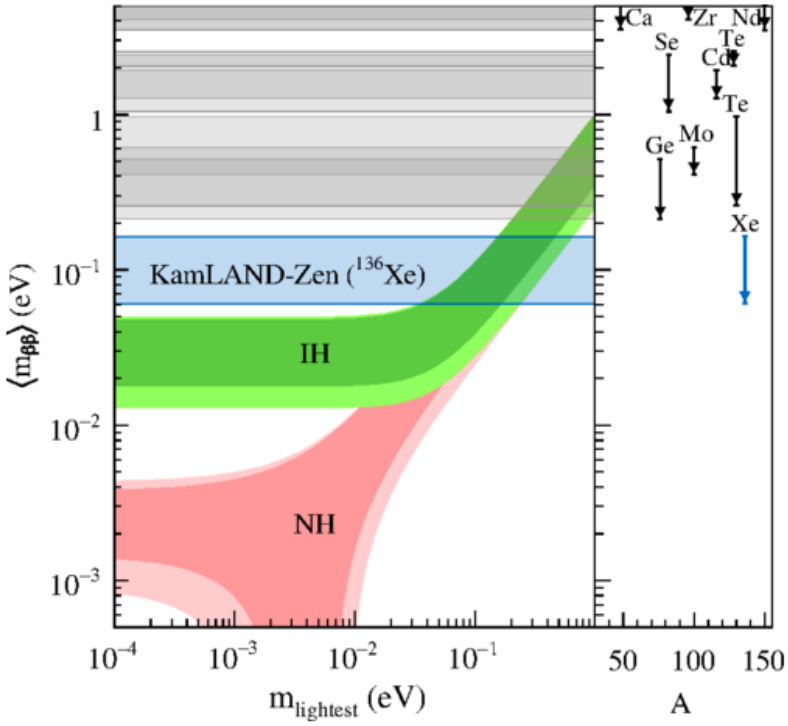

Figure 1.15: Effective mass versus the lightest neutrino mass, the limit obtained by the KamLAND-Zen experiment is represented by the light blue band, the green band is the allowed parameter space for the inverted ordering and the red band is the allowed parameter space for the normal hierarchy

1.4.5 Sterile neutrinos

Despite the great success of the three flavour neutrino oscillation theory that solved the solar and atmospheric neutrino anomalies, other anomalies are being investigated nowadays. The calibration with a radioactive source of the GALLEX and SAGE experiments led to a deficit between the observed and predicted neutrino rates. This discrepancy is called "Gallium anomaly".

In addition, the Liquid Scintillator Neutrino Detector (LSND) looked at the appearance of $\overline{\nu_e}$ in a $\overline{\nu_\mu}$ beam and reported an excess of $\overline{\nu_e}$ that can not be explained by the three flavour neutrino oscillation.

Finally, the reactor antineutrino flux was reevaluated in 2011, which led to a deficit between measured and detected flux at short baselines This anomaly is called "Reactor Antineutrino Anomaly" (RAA).

All of these anomalies could be resulting from the existence of of a sterile neutrino state, which rekindled the experimental program investigating the existence of sterile neutrinos.

The Gallium anomaly

The solar neutrino experiments GALLEX [H$^+$98] and SAGE [A$^+$99] were calibrated using intense ^{51}Cr and ^{37}Ar radioactive sources positioned inside the detector. The ^{51}Cr source decays through electron capture to ^{51}V with a half-life of 27.7 days:

$$^{51}Cr + e^- \rightarrow ^{51}V + \nu_e \tag{1.87}$$

This decay produces three main neutrino lines with energy: 747 keV, 427 keV, 752 keV (the decay scheme is presented in Figure 1.16).

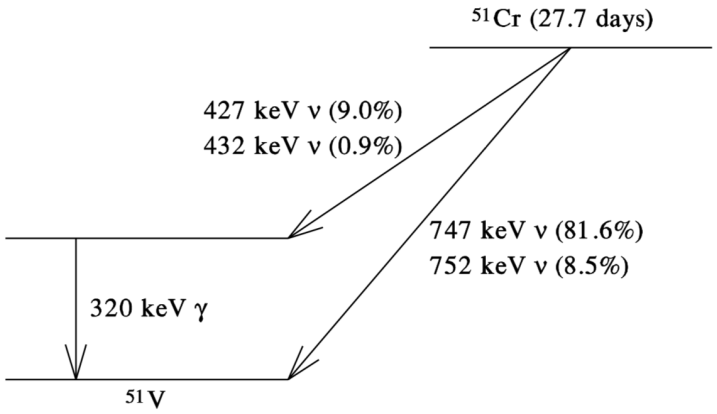

Figure 1.16: Decay scheme of the ^{51}Cr through electron capture

The neutrinos are then detected through Inverse Beta Decay on Gallium:

$$\nu_e + ^{71}Ga \rightarrow ^{71}Ge + e^- \tag{1.88}$$

The reported ratio between the predicted and measured rates is $\overline{R} = 0.84 \pm 0.05$ [GGL$^+$16] (see Figure 1.17)

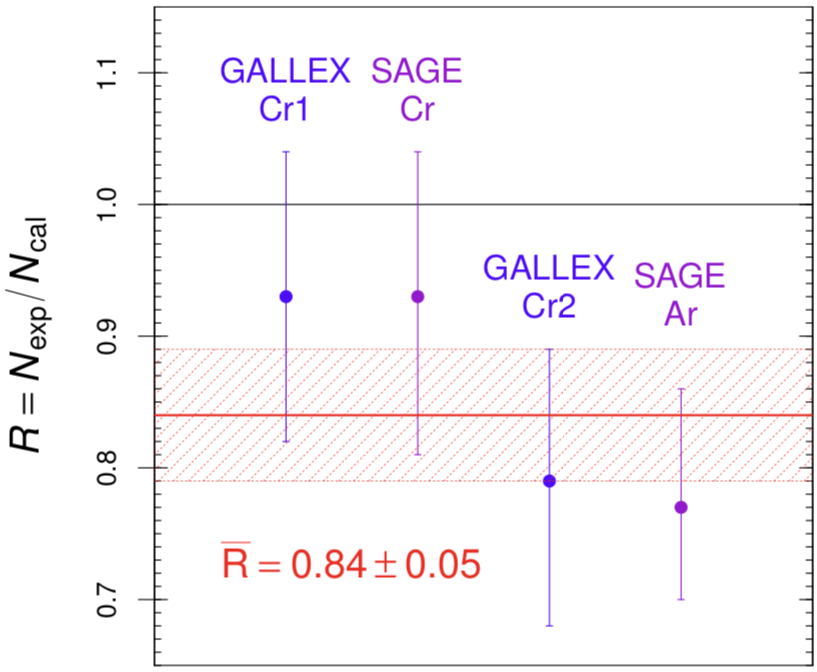

Figure 1.17: Ratio between observed and predicted number of events from the calibration sources in the GALLEX and SAGE experiments. The red shadowed band shows the uncertainty on the mean ratio (red line).

Recent results of the Baksan Experiment on Sterile Transitions (BEST) [B+21], which was designed to investigate the Gallium anomaly, confirm the anomaly observed by GALLEX and SAGE. The best fit of an oscillation toward a sterile neutrino explaining the anomaly, combining SAGE, GALLEX and BEST results, yields a mass splitting $\Delta m^2 = 1.25$ eV^2 and an oscillation amplitude $\sin^2 2\theta = 0.34$ (see Figure 1.18).

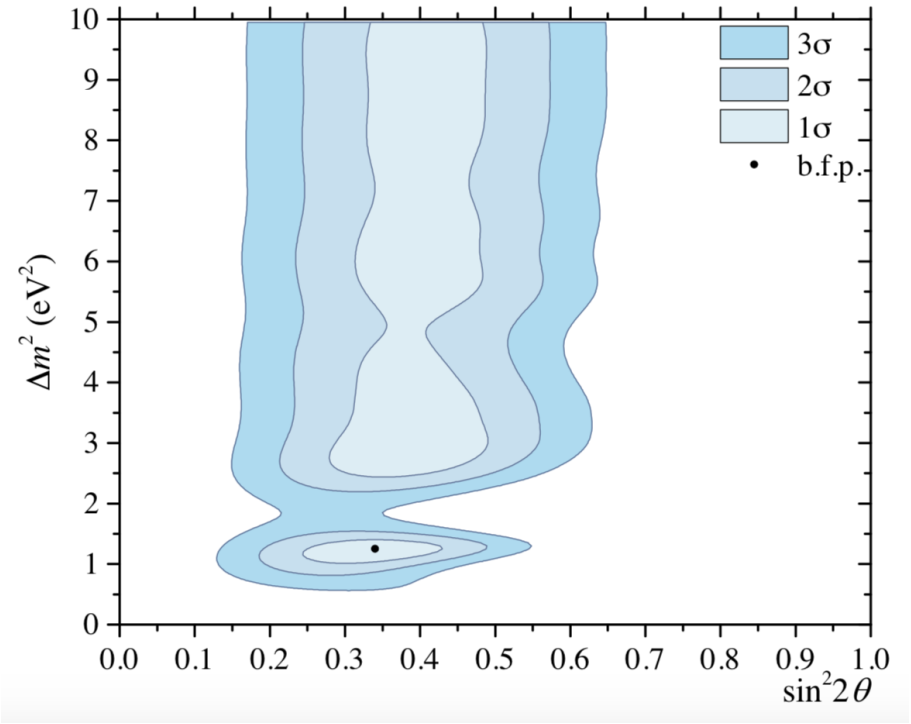

Figure 1.18: Acceptance contour for the oscillation parameters of the BEST, SAGE and GALLEX combined results, the best fit point is ($\Delta m^2 = 1.25$ eV^2, $\sin^2 2\theta = 0.34$).

The LSND anomaly

The LSND experiment, which was located at the Los Alamos Neutron Science Center, reported a 3.8σ significant excess of $\overline{\nu_e}$ in a $\overline{\nu_\mu}$ beam produced by μ^+ decay at rest [AA$^+$01]:

$$\mu^+ \to e^+ + \nu_e + \overline{\nu_\mu} \tag{1.89}$$

The electron antineutrinos were detected at a baseline $L \sim 30$ m with energies ranging from ~ 20 to ~ 60 MeV.

LSND's results could be explained by a short baseline oscillation $\overline{\nu_\mu} \to \overline{\nu_e}$ generated by a mass splitting $\Delta m^2 \gtrsim 0.1$ eV^2. It has to be noted that a similar experiment, KARMEN [A$^+$02b], did not observe any excess at a baseline $L \sim 18$ m.

Later, the MiniBooNE experiment was set up at Fermilab to investigate the LSND anomaly. In their first result in 2007, the MiniBooNE experiment [AA$^+$07] did not observe any excess, but in 2010 they confirmed the LSND anomaly [AA$^+$10].

The Reactor Antineutrino Anomaly

The reactor antineutrino flux was reevaluated in 2011, during the development of the reactor neutrino experiment generation that measured θ_{13}. A first reevaluation was done by Mueller [M$^+$11], and was independently confirmed by Huber [Hub11]. This reevaluation reported a shift of $\sim +3\%$ in the total neutrino flux. The combined results of published experiments with a baseline $L < 100$ m had an observed to predicted rate of 0.976 ± 0.024 that shifted to 0.943 ± 0.023 with the new flux evaluation (see Figure 1.19), leading to a $\sim 6\%$ deficit at 98.6% C.L. called the Reactor Antineutrino Anomaly [MFL$^+$11] (RAA).

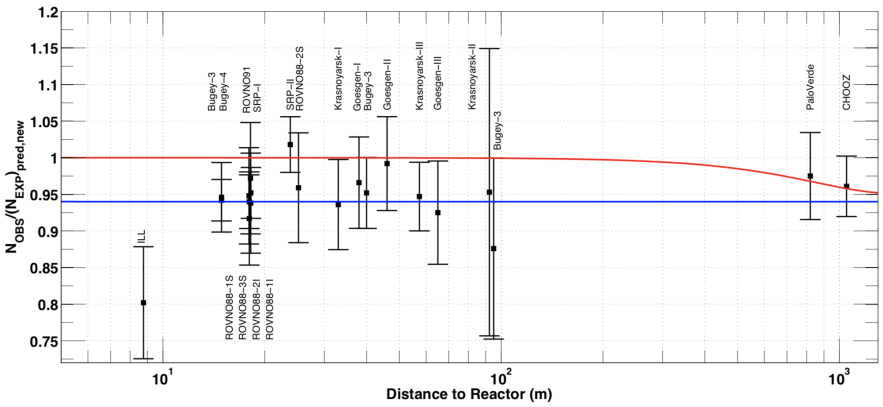

Figure 1.19: Ratio between experimental results and prediction, the mean ratio is 0.943 ± 0.023. The 3 neutrinos model is given by the red line, the 3+1 neutrinos model (3 active neutrinos and 1 sterile state) is given by the blue line.

Interpreting this deficit as an oscillation to a new sterile state, and combining the RAA anomaly with the GALLEX, SAGE and MiniBooNE results leads to an allowed region for the oscillation parameters $\sin^2 2\theta_{new}$ and Δm^2_{new} to the sterile state (see Figure 1.20). The combination favours $\sim 10\%$ amplitudes and oscillation frequencies down to $1-2$ eV^2.

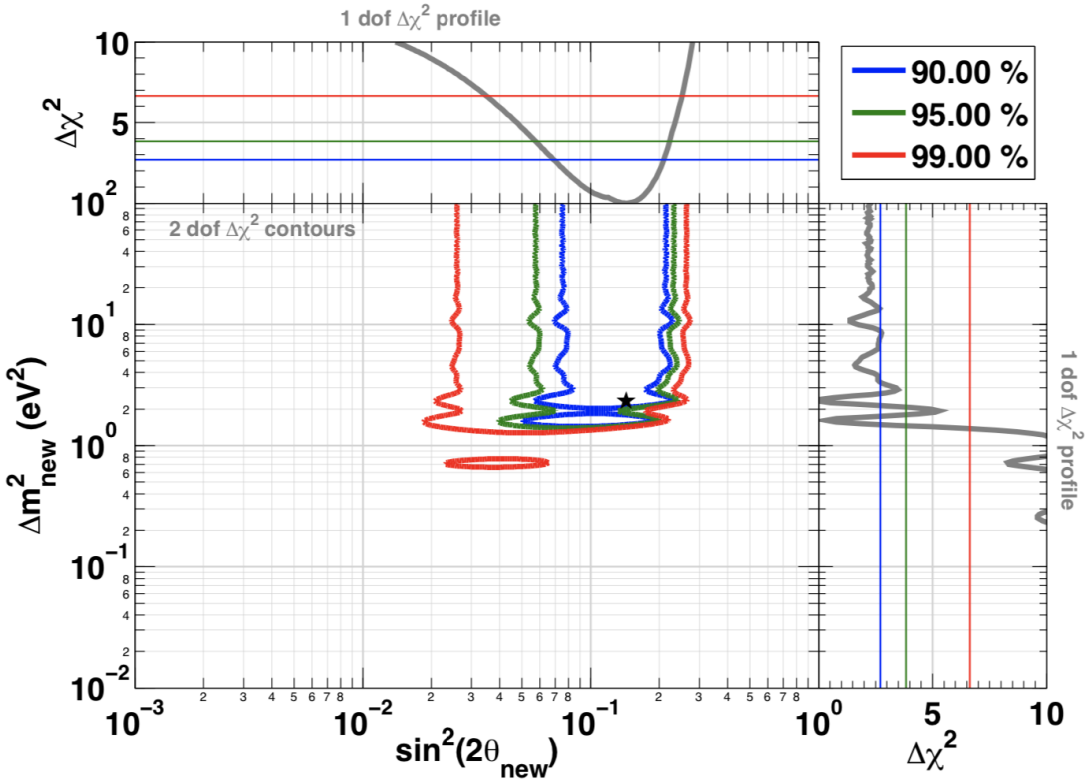

Figure 1.20: Acceptance contour of the oscillation parameter space obtained by combining the Reactor Antineutrino Anomaly, the GALLEX and SAGE calibration results, as well as MiniBooNE's constraints.

Antineutrino spectrum shape

In addition to the absolute neutrino rate discrepancy between data and the expectations, the measured shape of the reactor antineutrino energy spectrum disagrees with the predicted shape (with respect to the Huber-Mueller prediction [Hub11, M+11]).

This discrepancy takes the form of an excess of events at $\sim$ 5 MeV[15]. This excess was first observed by the RENO experiment [Seo15] and confirmed by the Daya Bay [A+16b] and Double Chooz experiments [dK+20a].

Although the precise shape of the bump differs from one experiment to another (see Figure 1.21), in the first approximation the excess is compatible with a $\sim$ 10% amplitude gaussian with a mean at ~5 MeV and a standard deviation ~0.5 MeV.

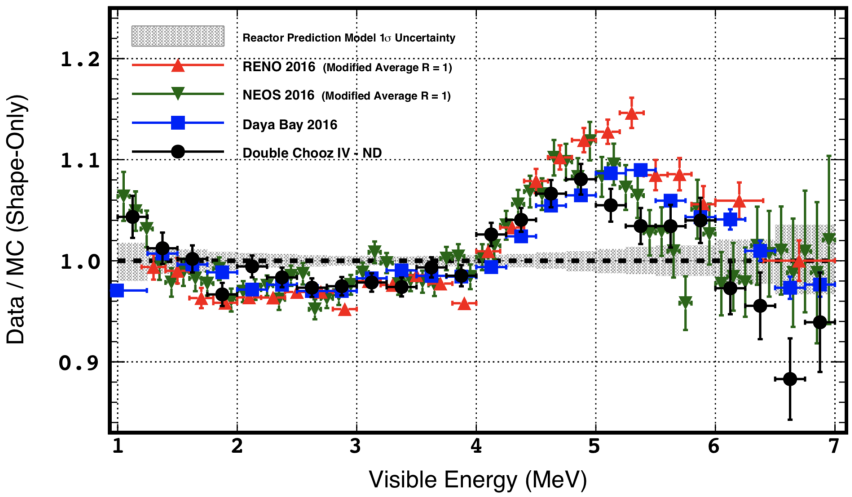

Figure 1.21: Ratio between the reactor antineutrino energy spectrum predicted by Huber-Mueller and the measurement of Double Chooz (black), Daya Bay (blue), NEOS (green) and RENO (red) [dK+20a]

The experiments reported that the excess was proportional to the reactor thermal power, excluding unaccounted reactor independent background as the cause for the excess. Moreover, the excess can not be explained by an oscillation toward a light sterile neutrino since it is observed at different baselines.

It is particularly interesting to compare spectra obtained from LEU and HEU reactors, since this would allow to disentangle the individual contributions of each fission isotope to the overall spectrum distortion.

1.5 Search for a light sterile neutrino

The $\sin^2 2\theta_{new}$ and Δm^2_{new} values favoured by the combination of the RAA and Gallium anomalies, around $\sim$ 10% and 2eV^2, respectively, imply observable oscillations on the scale of a few meters for neutrinos with energies of a few MeV. Thus, looking for oscillations of nuclear reactor neutrinos at short baselines becomes an efficient way of confirming or rejecting the sterile neutrino explanation to the Reactor and Gallium anomalies.

[15] often called "*5-MeV bump*" in the community

1.5.1 Experimental program

A large international experimental program has been developed in recent years to investigate the hypothesis of a light sterile neutrino in the context of the Reactor Antineutrino and Gallium anomalies.

In the 3+1 neutrinos framework (3 active neutrinos and 1 sterile state), the oscillation transition probability of $\nu_\alpha \to \nu_\beta$ is given by:

$$\mathscr{P}_{\nu_\alpha \to \nu_\beta} = \delta_{\alpha\beta} - 4|U_{\alpha 4}|^2(\delta_{\alpha\beta} - |U_{\beta 4}|^2)\sin^2\left(\frac{\Delta m^2_{41} L}{4E}\right) \tag{1.90}$$

which, in the case of disappearance experiments at nuclear reactors, simplifies to:

$$\mathscr{P}_{\overline{\nu_e} \to \overline{\nu_e}} = 1 - \sin^2(2\theta_{new})\sin^2\left(\frac{\Delta m^2_{new} L}{4E}\right) \tag{1.91}$$

The desirable features of all the experiments investigating the RAA are: short baseline, segmentation and good energy resolution. They can further be classified according to whether they use Highly Enriched Uranium reactor (HEU) or Lowly Enriched Uranium. Experiments such as DANSS and NEOS are located near commercial reactors with LEU cores whereas STEREO, PROSPECT, Neutrino-4 and SoLid are located near research reactors with HEU cores.

The Detector of reactor Anti-Neutrinos based on Solid Scintillator (DANSS) experiment

The DANSS experiment [A+18a] consists in a $\sim$ 1 m^3 plastic scintillator composed of 2500 scintillator bands covered by a thin layer of Gd for the neutron capture. The detector is located underneath the Kalinin Nuclear Power Plant (KNPP) reactor in Russia on a movable setup allowing three different baselines: 10.7 m, 11.7 m and 12.7 m.

The 3.1 GW$_{th}$ reactor of the (KNPP) allows DANSS to cumulate a high statistics which makes up for the large reactor core (3.2 m$\varnothing$ $\times$ 3.7 m h) which induces a large uncertainty on the baseline and the bad energy resolution $\sim$ 30% at 1 MeV.

In their published results, the DANSS experiment exclude the RAA best fit point at 5σ (see Figure 1.22).

The Neutrino Experiment for Oscillation at Short baseline (NEOS)

The NEOS experiment consists in a single volume of $\sim$800 kg of Gd-doped liquid scintillator, seen by 19 photomultipliers. The detector has an energy resolution of $\sim$ 5% at 1 MeV and is located at a baseline of $\sim$23.7 m from the 2.8 GW$_{th}$ reactor of the Hanbit Nuclear Power Complex in South Corea. Since the NEOS detector is a single volume detector located at a fixed distance from the reactor core, the oscillation hypothesis is probed by comparing the measured spectrum to a reference spectrum. In the case of NEOS, the reference spectrum is the spectrum measured by the Daya Bay experiment [A+16b].

NEOS' first results [K+17] are presented in Figure 1.22.

The Neutrino-4 experiment

The Neutrino-4 experiment is based on a Gd-doped liquid scintillator target of 1.8 m^3 segmented in 50 cells. The detector is positioned on a movable setup which allows for

different baselines, ranging from 6 to 12 m. It is located at the SM-3 reactor core of Russia's Research Institute of Atomic Reactors (NIIAR) in Dimitrovgrad, developing a thermal power of 100 MW_{th}. The detector exhibits an energy resolution of $\sim$ 16% at 1 MeV. However, since the detector is at surface level, it suffers from a high cosmic ray flux, and the signal to background ratio is only $\frac{S}{B} \sim 0.5$.

First results of Neutrino-4 are compatible with an oscillation signal with parameters $\Delta m^2_{new} = 7.22$ eV^2, $\sin^2_{new} 2\theta$ =0.35 at 3σ significance [S$^+$19]. Such an oscillation is excluded by the PROSPECT experiment [A$^+$18b]. We note that several critiques were raised by the community concerning the analysis of the Neutrino-4 experiment; in particular, the correctness of the statistical analysis is pointed out [DS20, A$^+$20e] , as well as an incomplete treatment of the detector's energy resolution effects [GLTZ21] .

The Precision Reactor Oscillation and SPECTrum (PROSPECT) experiment

The PROSPECT experiment consists in 4 Tons of liquid scintillator doped with Li. The 2.0 m×1.6 m×1.2 m volume is segmented in 11 × 14 rectangular cells seen by 2 photomultipliers one at each side of the cell.

The detector is located at $\sim$ 6.7 m of the High Flux Isotope Reactor (HFIR) in the Oak Ridge National Laboratory, which operates at 85 MW_{th}. The detector has a good energy resolution of 4.5% at 1 MeV.

The first results of the PROSPECT experiment [A$^+$18b] are presented in Figure 1.22.

The Short-baseline Oscillation with Lithium-6 Detector (SoLid) experiment

The Solid experiment [A$^+$21a] is located near the BR2 reactor in Belgium, and has acces to baselines between 6 and 9 m. The detector is based on a novel technology consisting in a higly segmented volume. It is composed of 5 modules made each of planes of 16×16 cubes of 5 cm made of polyvinyl toluene scintillator (PVT). Two of each cube's faces are coated with a layer of ^6Li complex in order to detect the neutron capture. The SoLid experiment has reported a signal to background ratio $\frac{S}{B} = 0.33$. As of today, the experiment has not yet published any results concerning neutrino oscillations.

The STEREO experiment

The STEREO experiment will be described thoroughly in the next chapter. Results from roughly half the whole dataset have been published by the STEREO collaboration (see Figure 1.22).

Current status of the Reactor Antineutrino Anomaly

A sizeable fraction of the RAA allowed oscillation parameter space is now excluded by the various short-baseline reactor oscillation experiments described above, as presented in Figure 1.22.

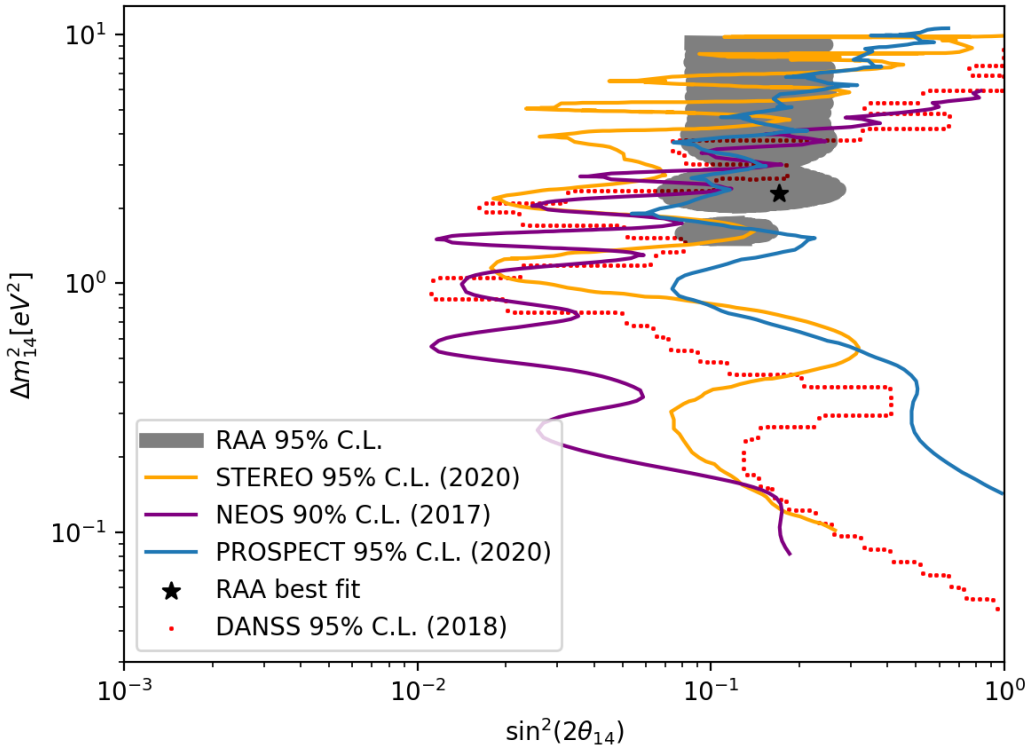

Figure 1.22: Exclusion contours of DANSS (dotted red), NEOS (violet), PROSPECT (blue) and STEREO (yellow) experiments. A sizeable fraction of the RAA allowed parameter space is excluded by the different experiments.

A very recent (2021) reevaluation of the reactor antineutrino spectra by Kopeïkin et al. at the National Research Centre Kurchatov Institute (KI) in Russia points out a possible normalisation problem in the β spectra measured at the Institut Laue-Langevin (ILL) in the 80's, which the Huber-Mueller prediction is based on. Specifically, new measurements of the ^{235}U and ^{239}Pu spectra have been carried out [KST21]. When the ILL ratio between the ^{235}U and ^{239}Pu β spectra is compared to the same ratio using the KI data, a normalisation difference of 5% is found (specifically, the ratios of the two datasets give 1.054 ± 0.002). The new prediction computed by Kopeïkin is compatible with the antineutrino flux normalisation measured by STEREO [A$^+$20b].

Recent results by the BEST collaboration seems to confirm the Gallium Anomaly [B$^+$21]. Since the sterile neutrino hypothesis is now strongly constrained by the short baseline reactor oscillation experiments, this contradiction points to a systematics problem on either side of the experimental program, or to a more complex description of the sterile neutrino oscillation than the 3+1 neutrino model.

1.6 Conclusion

In this chapter, we gave an overview of the theoretical and experimental context of the neutrino physics, and in particular we assessed the state of the art of the short-baseline reactor oscillation searches.

This thesis is devoted to the sterile neutrino problem and reports the search of an oscillation towards a sterile state using the STEREO detector. In the following chapter, we will give a detailed description of the STEREO apparatus and set-up.

Bibliography

[A+96] Dzh. N. Abdurashitov et al. The Russian-American gallium experiment (SAGE) Cr neutrino source measurement. *Phys. Rev. Lett.*, 77:4708–4711, 1996.

[A+97] W. W. M. Allison et al. Measurement of the atmospheric neutrino flavor composition in Soudan-2. *Phys. Lett. B*, 391:491–500, 1997.

[A+98] M Ambrosio et al. Measurement of the atmospheric neutrino induced upgoing muon flux using MACRO. *Phys. Lett. B*, 434:451–457, 1998.

[A+99] J. N. Abdurashitov et al. Measurement of the response of the Russian-American gallium experiment to neutrinos from a Cr-51 source. *Phys. Rev. C*, 59:2246–2263, 1999.

[A+02a] Q. R. Ahmad et al. Direct evidence for neutrino flavor transformation from neutral current interactions in the Sudbury Neutrino Observatory. *Phys. Rev. Lett.*, 89:011301, 2002.

[A+02b] B. Armbruster et al. Upper limits for neutrino oscillations muon-anti-neutrino —> electron-anti-neutrino from muon decay at rest. *Phys. Rev. D*, 65:112001, 2002.

[A+05] T. Araki et al. Measurement of neutrino oscillation with KamLAND: Evidence of spectral distortion. *Phys. Rev. Lett.*, 94:081801, 2005.

[A+11] V. N. Aseev et al. An upper limit on electron antineutrino mass from Troitsk experiment. *Phys. Rev. D*, 84:112003, 2011.

[A+12] T. Adam et al. Measurement of the neutrino velocity with the OPERA detector in the CNGS beam. *JHEP*, 10:093, 2012.

[A+16b] Feng Peng An et al. Measurement of the Reactor Antineutrino Flux and Spectrum at Daya Bay. *Phys. Rev. Lett.*, 116(6):061801, 2016. [Erratum: Phys.Rev.Lett. 118, 099902 (2017)].

[A+18a] I Alekseev et al. Search for sterile neutrinos at the DANSS experiment. *Phys. Lett. B*, 787:56–63, 2018.

[A+18b] J. Ashenfelter et al. First search for short-baseline neutrino oscillations at HFIR with PROSPECT. *Phys. Rev. Lett.*, 121(25):251802, 2018.

[A+19a] M. Aker et al. Improved Upper Limit on the Neutrino Mass from a Direct Kinematic Method by KATRIN. *Phys. Rev. Lett.*, 123(22):221802, 2019.

[A+20a] B. Abi et al. Long-baseline neutrino oscillation physics potential of the DUNE experiment. *Eur. Phys. J. C*, 80(10):978, 2020.

[A+20b] H. Almazán et al. Accurate Measurement of the Electron Antineutrino Yield of ^{235}U Fissions from the STEREO Experiment with 119 Days of Reactor-On Data. *Phys. Rev. Lett.*, 125(20):201801, 2020.

[A+20e] M. Andriamirado et al. Note on arXiv:2005.05301, 'Preparation of the Neutrino-4 experiment on search for sterile neutrino and the obtained results of measurements'. 6 2020.

[A+21a] Y. Abreu et al. SoLid: a short baseline reactor neutrino experiment. *JINST*, 16(02):P02025, 2021.

[AA+01] A. Aguilar-Arevalo et al. Evidence for neutrino oscillations from the observation of $\bar{\nu}_e$ appearance in a $\bar{\nu}_\mu$ beam. *Phys. Rev. D*, 64:112007, 2001.

[AA+07] A. A. Aguilar-Arevalo et al. A Search for Electron Neutrino Appearance at the $\Delta m^2 \sim 1eV^2$ Scale. *Phys. Rev. Lett.*, 98:231801, 2007.

[AA+10] A. A. Aguilar-Arevalo et al. Event Excess in the MiniBooNE Search for $\bar{\nu}_\mu \to \bar{\nu}_e$ Oscillations. *Phys. Rev. Lett.*, 105:181801, 2010.

[AAVK87] E. N. Alekseev, L. N. Alekseeva, V. I. Volchenko, and I. V. Krivosheina. Possible Detection of a Neutrino Signal on 23 February 1987 at the Baksan Underground Scintillation Telescope of the Institute of Nuclear Research. *JETP Lett.*, 45:589–592, 1987.

[B+21] V. V. Barinov et al. Results from the Baksan Experiment on Sterile Transitions (BEST). 9 2021.

[BBGK95] Samoil M. Bilenky, A. Bottino, C. Giunti, and C. W. Kim. Neutrino oscillations in the framework of three generation mixings with mass hierarchy. *Phys. Lett. B*, 356:273–281, 1995.

[Bel01] E. Bellotti. First results from GNO. *Nucl. Phys. B Proc. Suppl.*, 91:44–49, 2001.

[BS+95] R. Becker-Szendy et al. Neutrino measurements with the IMB detector. *Nucl. Phys. B Proc. Suppl.*, 38:331–336, 1995.

[BSB05] John N. Bahcall, Aldo M. Serenelli, and Sarbani Basu. New solar opacities, abundances, helioseismology, and neutrino fluxes. *Astrophys. J. Lett.*, 621:L85–L88, 2005.

[CG09] Robert N. Cahn and Gerson Goldhaber. *The Experimental Foundations of Particle Physics*. Cambridge University Press, 2 edition, 2009.

[Cha14] J. Chadwick. The intensity distribution in the magnetic spectrum of beta particles from radium (B + C). *Verh. Phys. Gesell.*, 16:383–391, 1914.

[CRH+56] C. L. Cowan, F. Reines, F. B. Harrison, H. W. Kruse, and A. D. McGuire. Detection of the free neutrino: A Confirmation. *Science*, 124:103–104, 1956.

[DGG+62] G. Danby, J. M. Gaillard, Konstantin A. Goulianos, L. M. Lederman, Nari B. Mistry, M. Schwartz, and J. Steinberger. Observation of High-Energy Neutrino Reactions and the Existence of Two Kinds of Neutrinos. *Phys. Rev. Lett.*, 9:36–44, 1962.

[DHH68] Raymond Davis, Jr., Don S. Harmer, and Kenneth C. Hoffman. Search for neutrinos from the sun. *Phys. Rev. Lett.*, 20:1205–1209, 1968.

[dK+20a] H. de Kerret et al. Double Chooz θ_{13} measurement via total neutron capture detection. *Nature Phys.*, 16(5):558–564, 2020.

[DS20] M. V. Danilov and N. A. Skrobova. Comment on “Analysis of the Results of the Neutrino-4 Experiment on the Search for the Sterile Neutrino and Comparison with Results of Other Experiments” (JETP Letters 112, 199 (2020)). *JETP Lett.*, 112(7):452–454, 2020.

[dSFG+21] P. F. de Salas, D. V. Forero, S. Gariazzo, P. Martínez-Miravé, O. Mena, C. A. Ternes, M. Tórtola, and J. W. F. Valle. 2020 global reassessment of the neutrino oscillation picture. *JHEP*, 02:071, 2021.

[EB64] F. Englert and R. Brout. Broken Symmetry and the Mass of Gauge Vector Mesons. *Phys. Rev. Lett.*, 13:321–323, 1964.

[EW27] Charles Drummond Ellis and W. A Wooster. The average energy of disintegration of radium E. *Proc. Roy. Soc. Lond. A*, 117(776):109–123, 1927.

[F+94] Y. Fukuda et al. Atmospheric muon-neutrino / electron-neutrino ratio in the multiGeV energy range. *Phys. Lett. B*, 335:237–245, 1994.

[F+96] Y. Fukuda et al. Solar neutrino data covering solar cycle 22. *Phys. Rev. Lett.*, 77:1683–1686, 1996.

[F+98] Y. Fukuda et al. Evidence for oscillation of atmospheric neutrinos. *Phys. Rev. Lett.*, 81:1562–1567, 1998.

[F+99] Y. Fukuda et al. Measurement of the solar neutrino energy spectrum using neutrino electron scattering. *Phys. Rev. Lett.*, 82:2430–2434, 1999.

[Fer34] E. Fermi. An attempt of a theory of beta radiation. 1. *Z. Phys.*, 88:161–177, 1934.

[Fur39] W. H. Furry. On transition probabilities in double beta-disintegration. *Phys. Rev.*, 56:1184–1193, 1939.

[GGH+16] A. Gando, Y. Gando, T. Hachiya, A. Hayashi, S. Hayashida, H. Ikeda, K. Inoue, K. Ishidoshiro, Y. Karino, M. Koga, S. Matsuda, T. Mitsui, K. Nakamura, S. Obara, T. Oura, H. Ozaki, I. Shimizu, Y. Shirahata, J. Shirai, A. Suzuki, T. Takai, K. Tamae, Y. Teraoka, K. Ueshima, H. Watanabe, A. Kozlov, Y. Takemoto, S. Yoshida, K. Fushimi, T. I. Banks, B. E. Berger, B. K. Fujikawa, T. O’Donnell, L. A. Winslow, Y. Efremenko, H. J. Karwowski, D. M. Markoff, W. Tornow, J. A. Detwiler, S. Enomoto, and M. P. Decowski. Search for majorana neutrinos near the inverted mass hierarchy region with kamland-zen. *Phys. Rev. Lett.*, 117:082503, Aug 2016.

[GGL+16] S. Gariazzo, C. Giunti, M. Laveder, Y. F. Li, and E. M. Zavanin. Light sterile neutrinos. *J. Phys. G*, 43:033001, 2016.

[GGS58] M. Goldhaber, L. Grodzins, and A. W. Sunyar. Helicity of Neutrinos. *Phys. Rev.*, 109:1015–1017, 1958.

[GHK64] G. S. Guralnik, C. R. Hagen, and T. W. B. Kibble. Global Conservation Laws and Massless Particles. *Phys. Rev. Lett.*, 13:585–587, 1964.

[GK07] Carlo Giunti and Chung W. Kim. *Fundamentals of Neutrino Physics and Astrophysics*. 2007.

[GLTZ21] C. Giunti, Y. F. Li, C. A. Ternes, and Y. Y. Zhang. Neutrino-4 anomaly: oscillations or fluctuations? *Phys. Lett. B*, 816:136214, 2021.

[H+96] W. Hampel et al. GALLEX solar neutrino observations: Results for GALLEX III. *Phys. Lett. B*, 388:384–396, 1996.

[H+98] W. Hampel et al. Final results of the Cr-51 neutrino source experiments in GALLEX. *Phys. Lett. B*, 420:114–126, 1998.

[Hig64] Peter W. Higgs. Broken Symmetries and the Masses of Gauge Bosons. *Phys. Rev. Lett.*, 13:508–509, 1964.

[Hub11] Patrick Huber. On the determination of anti-neutrino spectra from nuclear reactors. *Phys. Rev. C*, 84:024617, 2011. [Erratum: Phys.Rev.C 85, 029901 (2012)].

[K+01] K. Kodama et al. Observation of tau neutrino interactions. *Phys. Lett. B*, 504:218–224, 2001.

[K+17] Y. J. Ko et al. Sterile Neutrino Search at the NEOS Experiment. *Phys. Rev. Lett.*, 118(12):121802, 2017.

[Kib67] T. W. B. Kibble. Symmetry breaking in nonAbelian gauge theories. *Phys. Rev.*, 155:1554–1561, 1967.

[Kro28] R. de L. Kronig. Der drehimpuls des stickstoffkerns. *Naturwissenschaften*, 16(19):335–335, May 1928.

[KST21] V. Kopeikin, M. Skorokhvatov, and O. Titov. Reevaluating reactor antineutrino spectra with new measurements of the ratio between ^{235}U and ^{239}Pu β spectra. 3 2021.

[LL02] Thomas J. Loredo and Don Q. Lamb. Bayesian analysis of neutrinos observed from supernova SN-1987A. *Phys. Rev. D*, 65:063002, 2002.

[Lu21] H. Lu. The physics potentials of JUNO. *Phys. Scripta*, 96(9):094013, 2021.

[M+11] Th. A. Mueller et al. Improved Predictions of Reactor Antineutrino Spectra. *Phys. Rev. C*, 83:054615, 2011.

[MFL+11] G. Mention, M. Fechner, Th. Lasserre, Th. A. Mueller, D. Lhuillier, M. Cribier, and A. Letourneau. The Reactor Antineutrino Anomaly. *Phys. Rev. D*, 83:073006, 2011.

[Mir09] L. Miramonti. Solar neutrino detection. 1123, 01 2009.

[MNS62] Ziro Maki, Masami Nakagawa, and Shoichi Sakata. Remarks on the unified model of elementary particles. *Prog. Theor. Phys.*, 28:870–880, 1962.

[MS16] Michele Maltoni and Alexei Yu. Smirnov. Solar neutrinos and neutrino physics. *Eur. Phys. J. A*, 52(4):87, 2016.

[NBP+19] Mohammad Nizam, Suman Bharti, Suprabh Prakash, Ushak Rahaman, and S. Uma Sankar. Tensions between the appearance data of T2K and NOνA. *Mod. Phys. Lett. A*, 35(06):06, 2019.

[Nob] https://www.nobelprize.org/prizes/physics/2015/press-release/.

[Pau78] W. Pauli. Dear radioactive ladies and gentlemen. *Phys. Today*, 31N9:27, 1978.

[Pon57] B. Pontecorvo. Inverse beta processes and nonconservation of lepton charge. *Zh. Eksp. Teor. Fiz.*, 34:247, 1957.

[S+06] S. Schael et al. Precision electroweak measurements on the Z resonance. *Phys. Rept.*, 427:257–454, 2006.

[S+19] A. P. Serebrov et al. First Observation of the Oscillation Effect in the Neutrino-4 Experiment on the Search for the Sterile Neutrino. *Pisma Zh. Eksp. Teor. Fiz.*, 109(4):209–218, 2019.

[Seo15] Seon-Hee Seo. New Results from RENO and The 5 MeV Excess. *AIP Conf. Proc.*, 1666(1):080002, 2015.

[Smi03] A. Yu. Smirnov. The MSW effect and solar neutrinos. In *10th International Workshop on Neutrino Telescopes*, pages 23–43, 5 2003.

[WAH+57] C. S. Wu, E. Ambler, R. W. Hayward, D. D. Hoppes, and R. P. Hudson. Experimental test of parity conservation in beta decay. *Phys. Rev.*, 105:1413–1415, Feb 1957.

[Wal19] John Walker. Physics potential of Hyper-Kamiokande for neutrino oscillation measurements. *PoS*, NuFact2019:040, 2019.

[WDB+99] Ch. Weinheimer, B. Degenddag, A. Bleile, J. Bonn, L. Bornschein, O. Kazachenko, A. Kovalik, and E. W. Otten. High precision measurement of the tritium β spectrum near its endpoint and upper limit on the neutrino mass. *Phys. Lett. B*, 460:219–226, 1999. [Erratum: Phys.Lett.B 464, 352–352 (1999)].

[Win91] K. Winter. *Neutrino Physics*. Cambridge Monographs on Particle Physics, Nuclear Physics and Cosmology. Cambridge University Press, 1991.

[Wol78] L. Wolfenstein. Neutrino Oscillations in Matter. *Phys. Rev. D*, 17:2369–2374, 1978.

CHAPTER 2

THE STEREO EXPERIMENT

CONTENTS

2.1 Introduction

As discussed in the previous chapter, the STEREO experiment, proposed in 2013, was designed to investigate the hypothesis of an oscillation toward a light sterile neutrino state ($\Delta m^2 \sim 1$ eV) as an explanation for the Reactor Antineutrino Anomaly (RAA) arising from the reactor antineutrinos flux re-estimation in 2011.

The experiment aims at either confirming or setting an upper limit on the existence of an oscillation toward a light sterile neutrino. The experiment is looking for the evolution of an oscillation pattern, for various short baselines, in the energy spectrum of the antineutrinos emitted by the Institute Laue-Langevin (ILL) nuclear reactor core located at Grenoble (FRANCE).

The following chapter will describe the concept of the STEREO experiment, the experimental conditions offered by the ILL, as well as the detector and its components.

2.2 Experimental concept

2.2.1 Oscillation signature

In order to unambiguously observe an oscillation phenomenon induced by a light sterile neutrino state independently from a prediction of the flux or energy spectrum shape, we want to measure the relative distortion of the antineutrino energy spectrum induced by the oscillation at different baselines (see figure 2.1). As a consequence, the detector must be located at a short distance (L$\sim$ few tens of m) from the neutrino source and must be able to resolve the energy and the distance travelled by the detected antineutrinos, hence sufficient energy and spatial resolution are needed.

The survival probability of an electronic antineutrino at a short baseline in the case of the existence of a light sterile neutrino state can be approximated by:

$$P(\overline{\nu_e} \rightarrow \overline{\nu_e}) = 1 - \sin^2(2\theta_{new}) \sin^2(1.27 \frac{\Delta m^2_{new} \times L}{E}) \tag{2.1}$$

Thus, the survival probability of an electronic antineutrino depends on both the energy of the particle and the distance travelled between its emission and its detection vertices. This results in a baseline dependent oscillation pattern in the antineutrino energy spectrum. The distance between two oscillation extrema is about 2 m for the RAA Δm^2_{new} value.

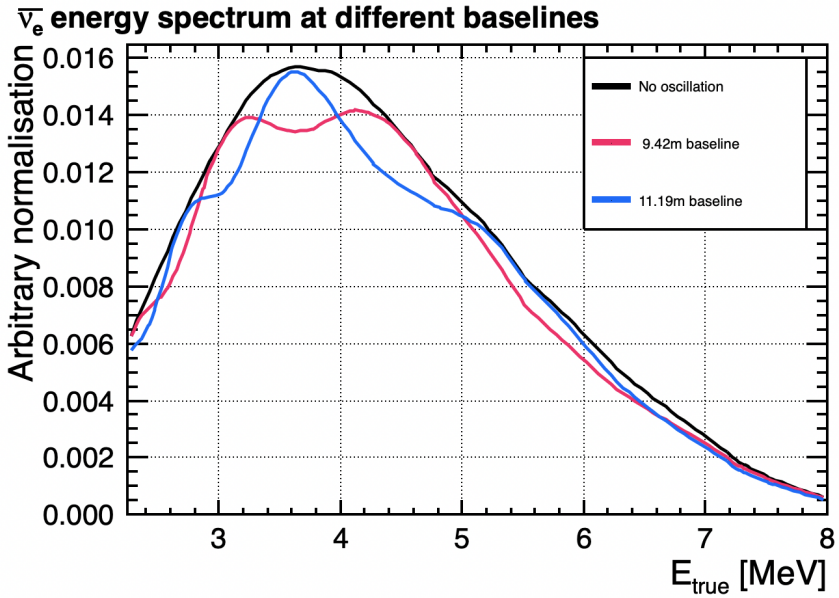

Figure 2.1: Energy spectrum prediction for antineutrino in the non-oscillation hypothesis and 2 different baselines: 9.42 m (red) and 11.19 m (blue) corresponding respectively to STEREO closest and farthest cells for an oscillation at the RAA best fit value ($\sin^2(2\theta_{new})$=0.14, Δm^2_{new}=2.40 eV^2)

2.2.2 Detection principle

Unlike the charged leptons, which can be detected by the ionisation of the matter they traverse, neutrinos do not interact electromagnetically and can only be detected by the means of an electroweak interaction mediated by a $W^{\pm}$ or Z^0 gauge bosons. The charged current interaction of an electronic antineutrino $\overline{\nu_e}$ on a proton, known as Inverse Beta Decay process (IBD) and described by the following Feynman diagram, yields a positron and a neutron:

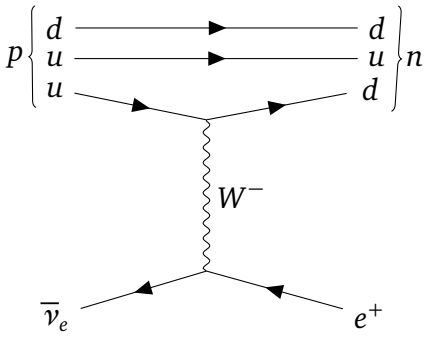

Figure 2.2: Feynman diagram of the Inverse Beta Decay process.

The identification of an IBD interaction is based on the detection of space-time correlated signals, an immediate signal called prompt signal and a delayed signal. This strategy was developed by Cowan and Reines in the 1950's and allowed them to discover the electronic antineutrino. Indeed, the space-time correlation permits to discriminate the neutrino signal from the ambient background due to natural radioactivity even if the signal's rate is several order of magnitude smaller than the ambient background. As an example, the trigger rate of STEREO is ∼1 kHz from which only ∼5×10^{-3}Hz are neutrinos events.

The prompt signal is given by the deposition of the positron energy. In the case of STEREO, the positron deposits its kinetic energy in the liquid scintillator mainly through ionization and possibly by bremsstrahlung for the most energetic ones. The positron will then annihilate with an electron giving rise to two 511 keV back-to-back γ. Those γ will deposit their energy in the liquid scintillator through Compton scattering and photoelectric effects. These processes are considered to be instantaneous compared to the liquid scintillator response time.

The delayed signal is given by the neutron capture on a nucleus. After its creation, the neutron will thermalise quickly by elastic scattering on the hydrogen nuclei present in the liquid scintillator. After thermalisation, the neutron will diffuse until it is captured by a nucleus, a few tens of microseconds later. In the absence of neutron-absorbing elements, the neutron is generally captured on hydrogen, the de-excitation of the hydrogen nuclei releases a 2.2 MeV γ.

In the case of STEREO, the liquid scintillator is doped with gadolinium (Gd), which is a highly neutron-absorbing element, therefore most of the neutron captures take place on Gd.

Reactor antineutrino energy spectrum

In nuclear reactors, a self-sustained controlled chain reaction takes place. The capture of a thermal neutron on a heavy fissile actinide element such as ^{235}U or ^{239}Pu produces highly unstable nuclei that quickly fission in two daughter nuclei and two or three fast neutrons. This reaction liberates about 200 MeV of energy. The neutron capture cross-section is much higher for thermal neutrons ($\sim$600 barns for ^{235}U) than for fast neutrons ($\sim$1 barn for ^{235}U) [JBB+12], therefore, to sustain the chain reaction, one of the neutrons is moderated.

The daughter nuclei are neutron-rich with an $\frac{N}{Z}$-ratio > 1.55, hence each daughter nuclei undergoes an average of three β^- decays before reaching stability. Consequently, there are about 6 β^- decays per fission, an $\overline{\nu}_e$ is emitted in each, this leads to a total of 2×10^{20} $\overline{\nu}_e$ per second per GW of thermal power. More than 99% of all reactor antineutrinos with an energy above the IBD threshold are due to only four fissile isotopes: ^{235}U, ^{239}Pu, ^{238}U, ^{241}Pu.

That being said, a calculation of the resulting neutrino flux from first principles is made difficult by the superposition of the thousands of β-decay branches of the fission fragments of those four isotopes. In practice, reactor neutrino fluxes for the ^{235}U, ^{239}Pu, ^{241}Pu isotopes are obtained through inversion of measured β-spectra obtained in the 1980s at Institut Laue-Langevin (ILL) [vHS82, SCGV85, HSG+89]. The total β-spectra for ^{238}U was obtained later in 2013 by a German group in Garching since this isotope is only fissioned by fast neutrons [HGH+14].

In 2011, a re-evaluation of the $\overline{\nu}_e$ spectrum was performed [MLF+11, Hub11] the result for ^{235}U, ^{239}Pu and ^{241}Pu are presented in Figure 2.3.

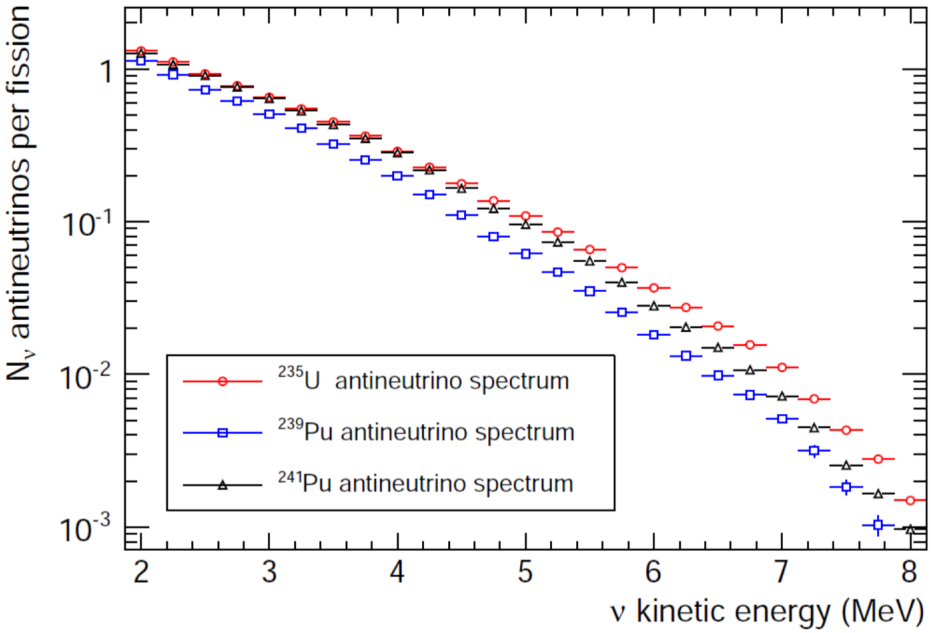

Figure 2.3: Re-evaluated reactor $\overline{\nu}_e$ spectra for ^{235}U, ^{239}Pu and ^{241}Pu [MLF+11]

The energy spectrum of antineutrino interacting in the detector (Figure 2.5) is given by the product of the reactor energy spectrum (Figure 2.4a) and the IBD cross-section (Figure 2.4b) weighted by the proton density in the detector.

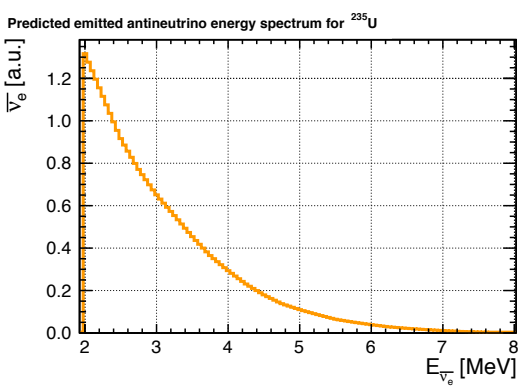

(a) Electronic antineutrino energy distribution coming from ^{235}U fission reaction [Hub11].

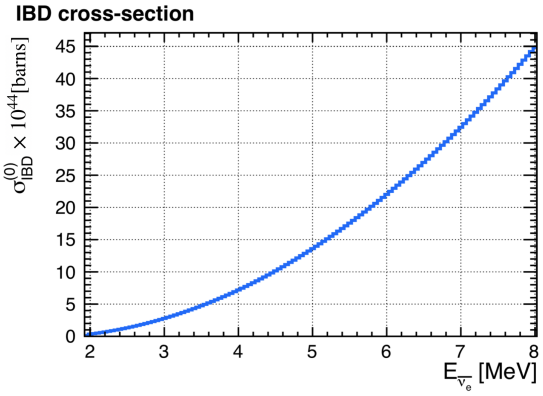

(b) IBD cross-section computed from equation (2.7) leaving out the 10^{-44} factor.

Figure 2.4: Emitted antineutrino energy spectrum and IBD cross-section.

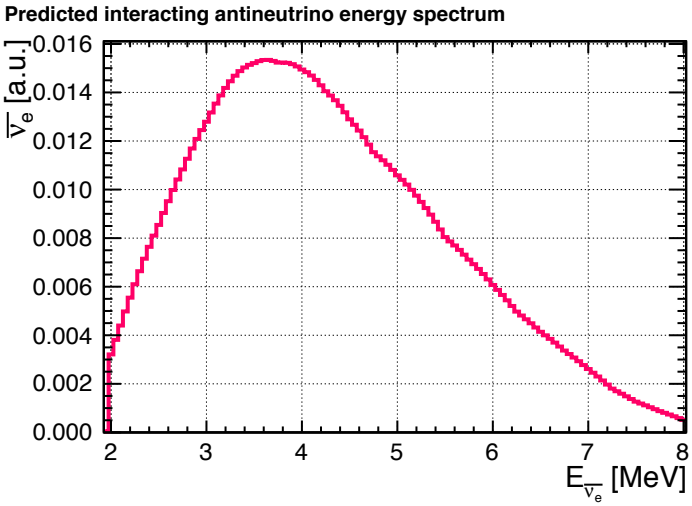

Figure 2.5: Interacting antineutrino energy spectrum coming from the product of the emitted spectrum (2.4a) and the IBD cross-section (2.4b).

Energy threshold

In order for the IBD to happen the antineutrino energy has to be higher than a threshold value. From kinematical considerations, the energy in the centre of mass frame must be greater or equal to the mass of the products of the reaction (taking $c = 1$):

$$\sqrt{s} \geq m_n + m_e \tag{2.2}$$

Where $\sqrt{s}$ is the energy in the centre of mass frame:

$$s = (E_{\overline{\nu}_e} + E_p)^2 - (\vec{p}_{\overline{\nu}_e} + \vec{p}_p)^2 \tag{2.3}$$

The threshold energy for heavier nuclei is much higher than for hydrogen which can be considered as a free proton. Moreover, in the case of an interaction on a nucleus other

than hydrogen, the neutron would remain bound to the nuclei and doing so would not be detected. Considering the reaction on a free proton at rest and neglecting the antineutrino mass:

$$s = (m_p)^2 + 2E_{\bar{\nu}_e} m_p \tag{2.4}$$

It finally yields:

$$E_{\bar{\nu}_e} \geq \frac{(m_e + m_n)^2 - (m_p)^2}{2m_p} \approx 1.806 \text{ MeV} \tag{2.5}$$

Hence the incoming antineutrino must have an energy greater than 1.806 MeV to be detectable by inverse beta decay.

Inverse Beta Decay cross-section

The IBD cross-section can be written in first approximation, valid at the reactor neutrino energies, as [VB99]:

$$\sigma^{(0)}_{IBD} = \frac{2\pi^2}{m_e^5 \tau_n f} E^{(0)}_{e^+} p^{(0)}_{e^+} \tag{2.6}$$

where τ_n is the neutron lifetime, f is the phase-space factor of the neutron decay including Coulomb, weak magnetism and radiative corrections effects. The computation of the numerical value of the pre-factor leads to:

$$\sigma^{(0)}_{IBD} \approx 9.62 \times E^{(0)}_{e^+} p^{(0)}_{e^+} \times 10^{-44} \text{cm}^2 \text{MeV}^{-2} \tag{2.7}$$

In the energy range of the reactor neutrino, where the previous approximations are valid, the IBD cross-section rises with the neutrino energy (see Figure 2.4b).

Relation between neutrino and positron energy

Since, the antineutrino is not directly observed, only the positively charged positron subsequent to the IBD process can be detected. The relation between the antineutrino and the positron energy can be derived from energy-momentum conservation:

$$E_{\bar{\nu}_e} = \frac{m_p E_{e^+} + (m_n^2 - m_p^2 - m_e^2)/2}{m_p - E_{e^+} + \cos(\theta)\sqrt{E_{e^+}^2 - m_e^2}} \tag{2.8}$$

where θ is the angle between the positron and antineutrino directions. For the reactor antineutrino energy, we can approximate this expression at zeroth order in $\frac{E_{e^+}}{m_p}$ [VB99] , which gives:

$$\begin{aligned} E_{\bar{\nu}_e} &\approx \frac{E_{e^+} + (m_n^2 - m_p^2 - m_e^2)/(2m_p)}{1 - (E_{e^+}/m_p)} \\ &\approx [E_{e^+} + \Delta] \times (1 + O(\tfrac{E_{e^+}}{m_p})) \end{aligned} \tag{2.9}$$

where $\Delta = (m_n^2 - m_p^2 - m_e^2)/(2m_p) \approx m_n - m_p = 1.29$ MeV. Neglecting the kinetic energy of the neutron (0.02 MeV on average), the visible energy is the sum of the kinetic energy of the positron and the energy coming from the γ resulting of the positron annihilation:

$$E_{vis} = E_{e^+} + m_e \tag{2.10}$$

It finally yields:

$$\begin{aligned} E_{\bar{\nu}_e} &= E_{vis} - m_e + \Delta \\ &= E_{vis} + 0.78 \text{ MeV} \end{aligned} \tag{2.11}$$

Gd isotope	Abundance [%]	$\sum_i E_{\gamma i}$ [keV]	σ [barns]
^{152} Gd	0.20	6247	735
^{154} Gd	2.18	6438	85
^{155} Gd	14.80	8536	60900
^{156} Gd	20.47	6360	1.5
^{157} Gd	15.65	7937	254000
^{158} Gd	24.84	5942	2.20
^{160} Gd	21.86	5635	0.77

Table 2.1: Table of the thermal neutron capture cross-section, isotopic abundance and total energy of the γ-cascade for various Gd isotopes [ABB+03]

However in practice, this conversion is not directly used. Indeed, some γ deposit only a fraction of their energy in the liquid scintillator, as they can interact in an inactive part of the detector, escape after a Compton scattering or escape altogether. Moreover, other effects must be taken into account such as the detector energy resolution or the non-linearity of the detector response. That is why in practice, the IBD signal is simulated taking into account all known detector effects, and the simulated reconstruction is compared to data.

Delayed signal

Gd has the highest thermal neutron capture cross-section $\sigma \approx 4.8\times10^4$ barns [CHO+11]. The addition of Gd reduces the neutron capture time, and spatial separation from the prompt signal, which reduces the probability of reconstructing an accidental coincidence with a background event. Moreover, the γ cascade coming from the Gd de-excitation, following the neutron capture, amounts to a total energy of about 8 MeV, which is well above natural radioactivity and can be easily detected. The thermal neutron capture cross-section for the various isotopes of the Gd, their natural abundance and the total energy of the cascading γ are presented in Table 2.1.

As mentioned above, since it is advantageous that the neutron capture takes place on Gd rather than on H, the proportion of Gd in the liquid was chosen to favour the Gd capture. To do so, the macroscopic neutron capture cross-section was computed taking into account the proportion of each isotope. The proportion of Gd was set to 0.2 wt.% [BGL+19]. If we take into account the atomic density of each isotope, we can compute the macroscopic cross-section see Figure 2.6.

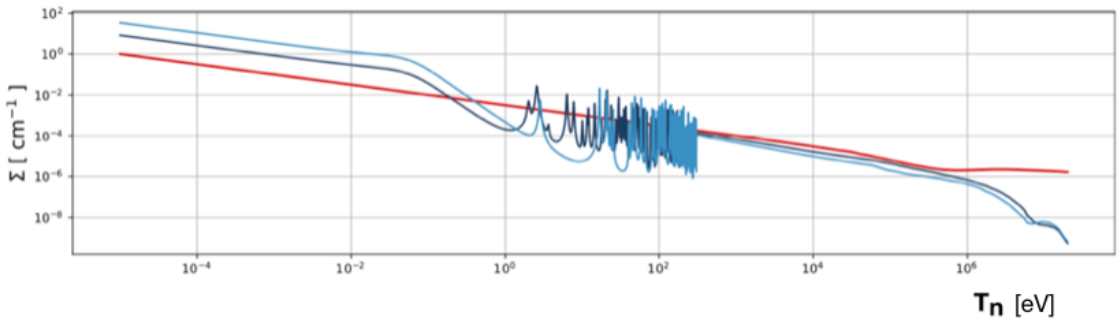

Figure 2.6: Macroscopic cross-section of the neutron capture on H(red), ^{155}Gd (dark blue) and ^{157}Gd (light blue) as a function of the neutron kinetic energy coming from the ENDF/B-VII.1. data base.

The probability that the capture takes place on Gd is $\sim$ 10 times greater than for the capture on H. The capture time τ_i for thermal neutron on the three main capturing isotopes can be computed from the macroscopic cross-section: Σ_i:

$$\tau_i = \frac{< L_i >}{< v >} = \frac{1}{< v > \Sigma_i} = \frac{1}{\Sigma_i} \times \sqrt{\frac{m_n}{2E_n}} \tag{2.12}$$

where $< L_i >$ is the neutron mean free path associated with the ith isotope. The value of the capture time and the macroscopic cross-sections for the three isotopes are given in Table 2.2.

Isotope	Σ_i [cm^{-1}]	τ_i [μs]
^{155}Gd	0.2	23
^{157}Gd	1	5
^{1}H	0.02	239

Table 2.2: Capture time and macroscopic cross-section for the three isotopes responsible for most of the thermal neutron capture in the STEREO liquid scintillator.

The time gap between the prompt and delayed signal is the sum of the thermalisation time and the capture time. In STEREO, because of the concentration of the three isotopes, the mean capture time is 16.07 $\pm$ 0.02 μs, whereas the mean thermalisation time is $\sim$8 μs.

Consequently, the identification of an IBD event in the STEREO detector consists in the detection of a prompt signal ($\sim$2-8 MeV) and a delayed signal ($\sim$5-10 MeV) in a time window of $\sim$50 μs.

2.2.3 Experimental site

The Institut Laue-Langevin (ILL), located in Grenoble (France), is an international science research centre founded in 1967 in honour of german Nobel prize laureate Max Von Laue and french physicist Paul Langevin. It accommodates annually more than 1500 researchers in various fields such as chemistry, biology, physics of materials. It provides one of the most intense thermal neutron beam in the world, the intense continuous neutron flux in the moderator reaches: 1.5×10^{15} cm^2·s^{-1}.

ILL Research reactor

The neutrino source used by the STEREO experiment is the ILL's Réacteur à Haut Flux (RHF). The RHF aims at producing a high neutron flux therefore its characteristics differs from commercial reactors which are designed to produce electricity on a large scale.

The nuclear fuel element (see Figure 2.7) takes the form of a hollow aluminium cylindrical vessel with an internal radius of 14.0 cm and an external radius of 19.5 cm for a height of 80.0 cm. It consists of an assembly of 280 long and thin curved plates (80 cm$\times$1.27 mm) (see Figure 2.7). These dimensions have to be put in regards with commercial reactor's ones which can exceed 4 m diameter. The 42 m^3 of heavy water (D_2O) coolant circulates between the plates at a flow rate of 2.2 m^3·h^{-1}, it also plays the role of moderator. The 8.6 kg of uranium enriched in ^{235}U at 93% serving as nuclear fuel are located in the fins. The central space is occupied by a nickel control rod.

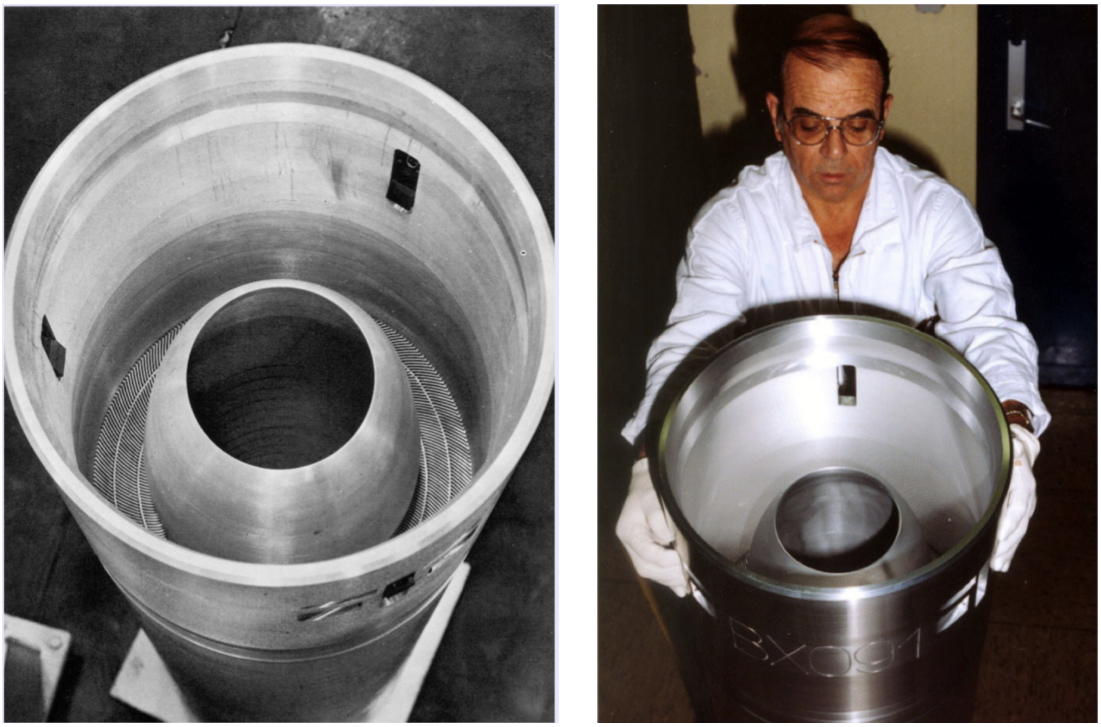

Figure 2.7: The fuel element assembly, the central space is occupied by the control rod, the nuclear fuel is in the fins in between which circulates the heavy water coolant. [JAC06]

The aluminium vessel containing the fuel element is immersed in a 6 m diameter × 8 m pool of demineralised light water, providing shielding against radiations (see Figure 2.8). Irradiation channels in aluminium convey the neutrons to the experiments directly from inside the reactor vessel where the neutron flux is high.

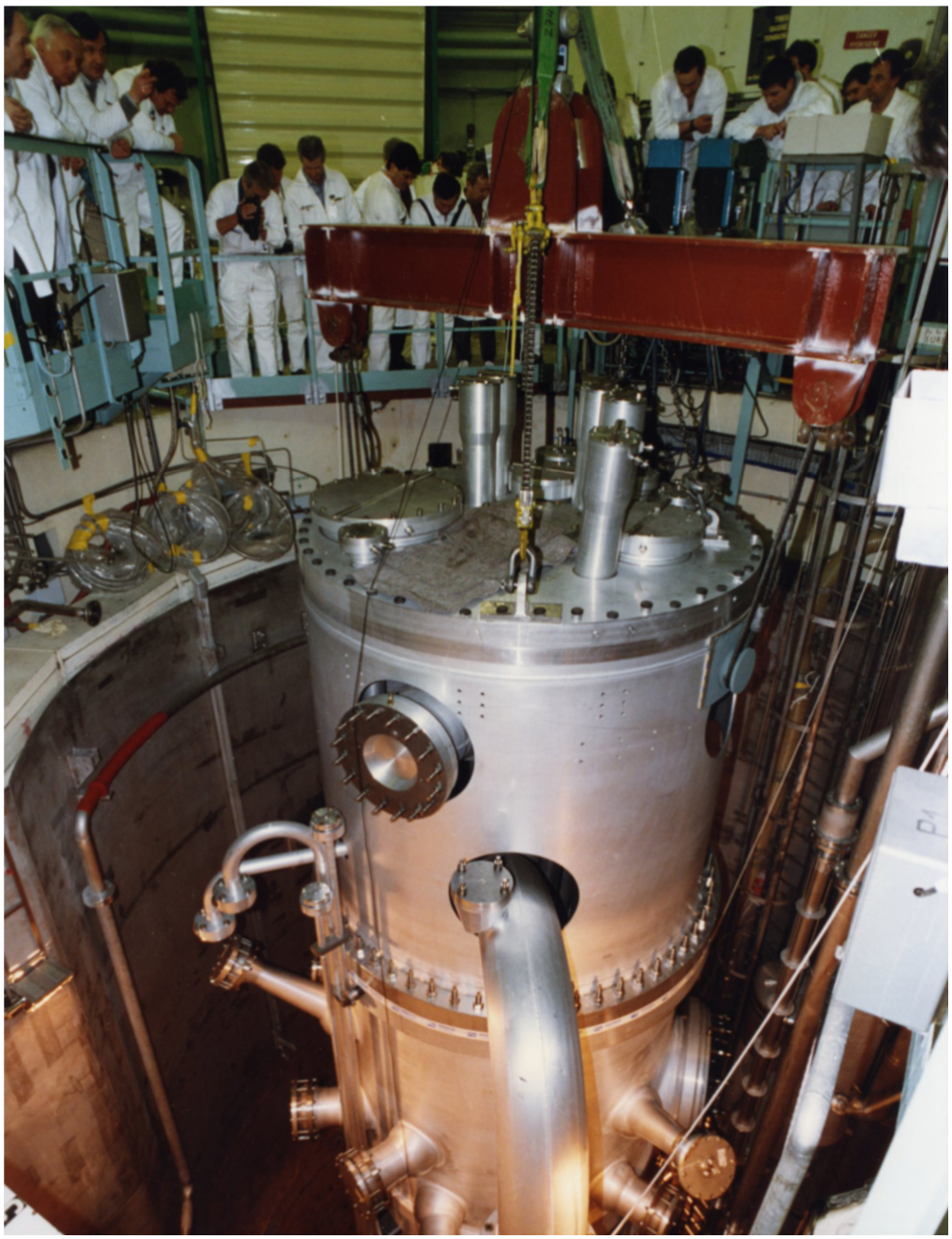

Figure 2.8: Installation of the reactor vessel in the light water pool [JAC06]

The RHF is generally in operation for 3 to 4 cycles per year interspersed with short ($\sim$ 1 to 3 months) shutdowns, a cycle corresponding to 45 days at the nominal power of 58.3MW$_{th}$. STEREO's data acquisition, however, took place in a period of increased reactor maintenance, reducing the number of cycles to 2 to 3 per year. The reactor was operated below nominal power, at a range lying between 50 and 56 MW but constant for a respective cycle, in order to lengthen the duration of these cycles. The total thermal power of the RHF is computed by the ILL, it is the sum of the thermal power produced by the reactor core P_{th} and the mechanical power of the coolant flow P_{pumps} which dissipates inside the moderator tank:

$$P_{th}^{tot} = P_{th} + P_{pumps} \tag{2.13}$$

$P_{pumps} = 0.7 \pm 0.1$ MW [RAP17]. The total thermal power is estimated from the

enthalpy change of the instrumented coolant circuits and is given by:

$$P_{th}^{tot} = \sum_{c} q_v \times \left[\rho(T_d)C_p(T_d)T_d - \rho(T_u)C_p(T_u)T_u\right] \tag{2.14}$$

where q_v is the volumic flow rate, ρ is the volumic mass of the fluid, C_p is the calorific capacity, T is the temperature, and indices u and d denote quantities measured upstream and downstream of the moderator tank, respectively. The sum runs over four instrumented circuits c. The primary heavy water circuit carries 96% of the total power. The flow rate of the primary heavy water circuit is measured by the Venturi effect induced by a calibrated diaphragm. The propagation of all uncertainties leads to a total of 1.44% relative uncertainty, with the main contribution (0.9%) coming from the calibration of the diaphragm performed in the 1970s with a 1:1 scale mock primary circuit [Fil17].

The RHF characteristics present both benefits and drawbacks for the STEREO experiment: The compactness of the reactor core allows a very good spatial resolution on the baseline, with an uncertainty of about $\sim$ 15 cm. The STEREO detector located at $\sim$ 10 m, has access to baselines ranging from 9.2 m to 11.4 m. This configuration is ideal to measure a short baseline oscillation corresponding to a mass splitting of $\Delta m^2 \sim 1$ eV^2, which suits the sterile neutrino explanation of the RAA.

On the other hand, the presence of a large amount of aluminium in the structure of the reactor core necessitates a correction in the computation of the antineutrino spectra. Indeed, radioactive decay of ^{28}Al created by radiative capture on ^{27}Al contributes to the antineutrino spectra. Besides, the 93%-enriched in ^{235}U fuel guarantees that $\sim$ 99% of fission comes from this isotope allowing a nearly pure measurement of the antineutrino spectra of this isotope. Such a measurement might be helpful to understand the event of excess around 5 MeV, commonly referred to as "the 5-MeV bump" reported by several reactor antineutrino experiments [A$^+$17, dK$^+$20b].

A very important point for neutrino experiments running on the surface is that the operating periods are interspersed by short reactor shutdowns. These are critical since they allow the experiment to take reactor-off data necessary to evaluate the cosmic background.

The reactor antineutrino flux is given by:

$$\phi_{\overline{\nu}_e} = \frac{P_{th}}{< E_{th}^f >} \times N_{\nu,\mathrm{IBD}}^f \tag{2.15}$$

with $< E_{th}^f >$ the mean thermal energy released per fission and N_ν^f the number of emitted neutrino per fission. Taking $N_{\nu,\mathrm{IBD}}^f(^{235}U) \approx 1.9$[1] and $< E_{th}^f > \approx$ 200MeV for antineutrinos emitted above the IBD threshold, and a mean thermal power $P_{th} \approx$ 50MW, it yields:

$$\phi_{\overline{\nu}_e}^{\mathrm{ILL}} \approx 3 \times 10^{18}\ \overline{\nu}_e \cdot \mathrm{s}^{-1} \tag{2.16}$$

From the emitted antineutrino flux we can estimate the rate of detected antineutrinos:

$$R_{\overline{\nu}_e}^{det} = \phi_{\overline{\nu}_e}^{\mathrm{ILL}} \times \tau_{int}^{TGLS} \times \epsilon_d \tag{2.17}$$

where $\tau_{int}^{TGLS} \approx 2.7{\times}10^{-21}$ is the fraction of antineutrinos interacting in the detector (it is evaluated through MC simulation and includes the solid angle, the IBD cross-section and the proton density inside the detector) and $\epsilon_d \approx 0.60$ is the detection efficiency

[1] This number is obtained by integrating the antineutrino spectrum (Figure 2.3) for ^{235}U from the IBD threshold energy.

for antineutrinos passing all selection cuts. Hence the rate of antineutrinos detected in STEREO is:

$$R_{\overline{\nu}_e}^{det} \approx 400\ \overline{\nu}_e \cdot \text{day}^{-1} \tag{2.18}$$

Experimental hall

As stated previously, to be sensitive to an oscillation hypothesis that is likely to explain the RAA, the detection must be done at short baseline. Consequently, the STEREO detector was positioned at $\sim$ 10 m of the reactor, accessing a range of baselines between 9.4 m and 11.2 m. The STEREO detector was located in the PN3 casemate on the experimental floor, referred to as "niveau C" (Figure 2.9).

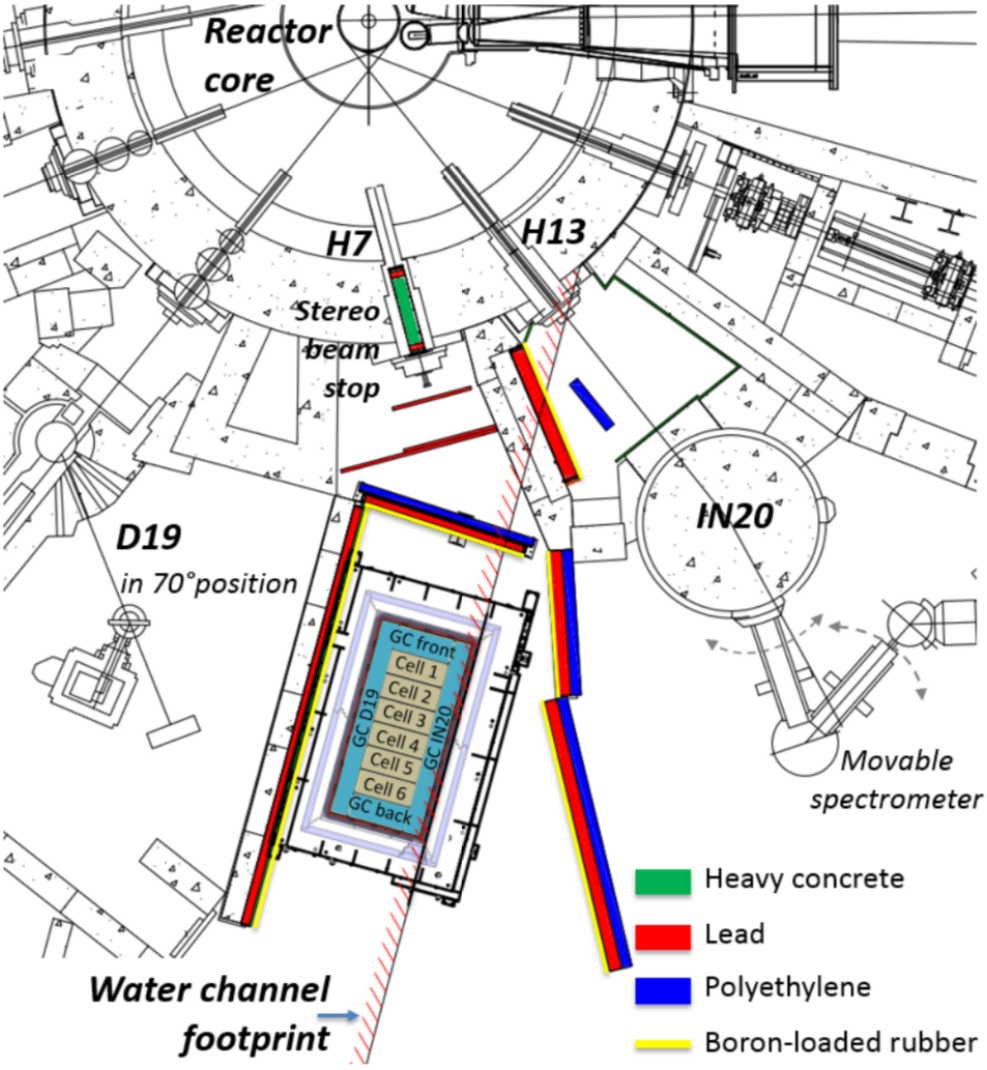

Figure 2.9: Part of the plan of the experimental floor near the RHF, including the position of the STEREO detector and its 2 closest neighbouring experiments, D19 and IN20. The detector is located in front of the H7 beam tube used by a former experiment and is now sealed off with a heavy concrete and lead cap. The wall between the PN3 casemate and its neighbours were reinforced with lead (red), polyethylene (blue) and boron-loaded rubber (yellow). The STEREO detector was turned off-axis of the reactor in order to be aligned with the water channel located on the top floor. The water channel provides additional shielding against cosmic for a total of $\sim$ 15 m.w.e

The PN3 casemate is located under a water channel, consisting of a U-shaped struc-

ture with 1.9 m thick concrete walls on the sides and a 2.5 m thick floor, filled with up to 6 m of water (Figure 2.10), the water level is not constant but is closely monitored. This water channel serves as intermediate storage for the RHF spent fuel. Part of the D_2O primary cooling circuit passes under the PN3 casemate, the activated heavy water can be a source of background for STEREO.

The STEREO detector is positioned to optimise the area covered by the water channel footprint, in doing so the detector is slightly off-axis of the reactor. The water channel together with the reactor building itself provides a free additional shielding against the cosmic background for $\sim$ 15 m.w.e.

The PN3 casemate allocated to STEREO is situated on top of several load-bearing walls, allowing a high floor load of 10 t/m^2. This feature makes the installation of heavy lead and concrete shielding around STEREO possible.

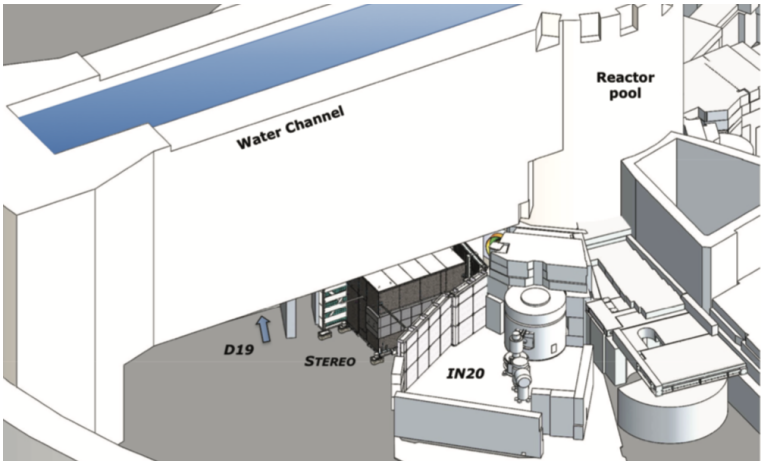

Figure 2.10: 3D modelisation of the STEREO detector under the water channel

The STEREO detector is surrounded by two neutron scattering experiments, IN20 and D19. On the left-hand side of the STEREO detector in Figure 2.9 is the thermal neutron single crystal diffractometer D19[2].

The wall between the D19 and STEREO zones consist of 30 cm of concrete coated with a B_4C mat, on the STEREO side of the wall a 10 cm thick layer of lead is present. This separating wall goes up to 2.4 m shielding the detector, the muon veto located above the detector is not shielded by the concrete wall, however, a separation curtain consisting of B_4C mats and hydrogenous fire protection foam occupies the space above the concrete wall up to the water channel above.

The D19 instrument induces a background of thermal neutron and γ produced in neutron capture reactions.

On the right-hand side of the STEREO detector in Figure 2.9 is the thermal neutron 3-axis spectrometer IN20. The IN20 instrument[3] is used for inelastic scattering experiments in various magnetic environments, in particular, samples can be put in a strong magnetic field up to 15 T. The intense magnetic fields generated by the IN20 instrument, could lead to a magnetic field of the order of some hundredth of μT at the STEREO position, degrading the efficiency of the Photo-multiplier tubes, highlighting the need for a specific magnetic shielding.

[2]This instrument used a monochromatic thermal neutron beam for the determination of crystal structure with unit cells of the order of 10^2 to 10^6 Å

[3]It has various applications such as the study of spin waves and their coupling to lattice modes, crystal field excitations, thin-film magnetism,...

The separation wall between the IN20 and STEREO areas is composed of 15 cm of Borated Polyethylene (BPE) and 15 cm of lead enclosed in a non-magnetic stainless steel support frame. Similarly to the other side, the wall is 2.4 m tall and does not cover the muon veto. The wall is surmounted with 1 m of B_4C.

2.2.4 Backgrounds

Any event that could mimic a prompt or a delayed signal is a potential source of background in STEREO. An intense neutron and γ ambiance on site is induced by the operation of the RHF. The reactor core produces fast neutrons and high energy γ can come directly from the core, or the activation of the surrounding materials. Finally, cosmic muons can produce fast neutrons and radioactive isotopes by spallation or capture.

The background can be categorized as correlated or accidental, depending on the associated physical process. For the accidental background, prompt and delayed signals have an independent origin. γ rays produced by natural radioactivity or by neutron captures constitute the main contribution to the accidental background.

For the correlated background, prompt and delayed signals share the same origin. The correlated background is dominated by cosmic rays-induced events. Indeed, cosmic rays can produce fast neutrons by spallation on the material surrounding the detector. When fast neutrons reach the liquid scintillator, they will induce proton recoils, which can mimic a prompt signal. The delayed signal is provided by the subsequent capture of the neutron on Gd, giving an overall signal falsely resembling an IBD signature.

Cosmic background

Cosmic rays constitute the main source of correlated background. Inside cosmic rays, the muonic component is $\sim$ 10 times greater than hadronic or electronic components [P+16]. The integrated flux of vertical muon with energy above 1 GeV at sea level is about 70 $Hz{\cdot}m^{-2}{\cdot}sr^{-1}$ [P+16].

The muon flux as a function of the incident angle was measured at the PN3 casemate (see Figure 2.11). A detector composed of 2 boards of plastic scintillator positioned on top of one another with a distance of 20 cm, was used to perform this measurement in the PN3 casemate as well as outside the reactor building. The outside measurement follows the typical $\cos^2(\theta)$ law. However, at the PN3 casemate, the muon flux is greater on the IN20 site, this is explained by the position of the water channel, which covers the D19 side of the PN3 casemate (see Figure 2.9).

Additionally, the measurement outside the reactor building and at the PN3 casemate shows an attenuation factor $\gtrsim$3, this is due to the reactor building and the water channel, the value of 15 m.w.e. of shielding provided by the reactor building and the water channel was deduced from this attenuation factor.

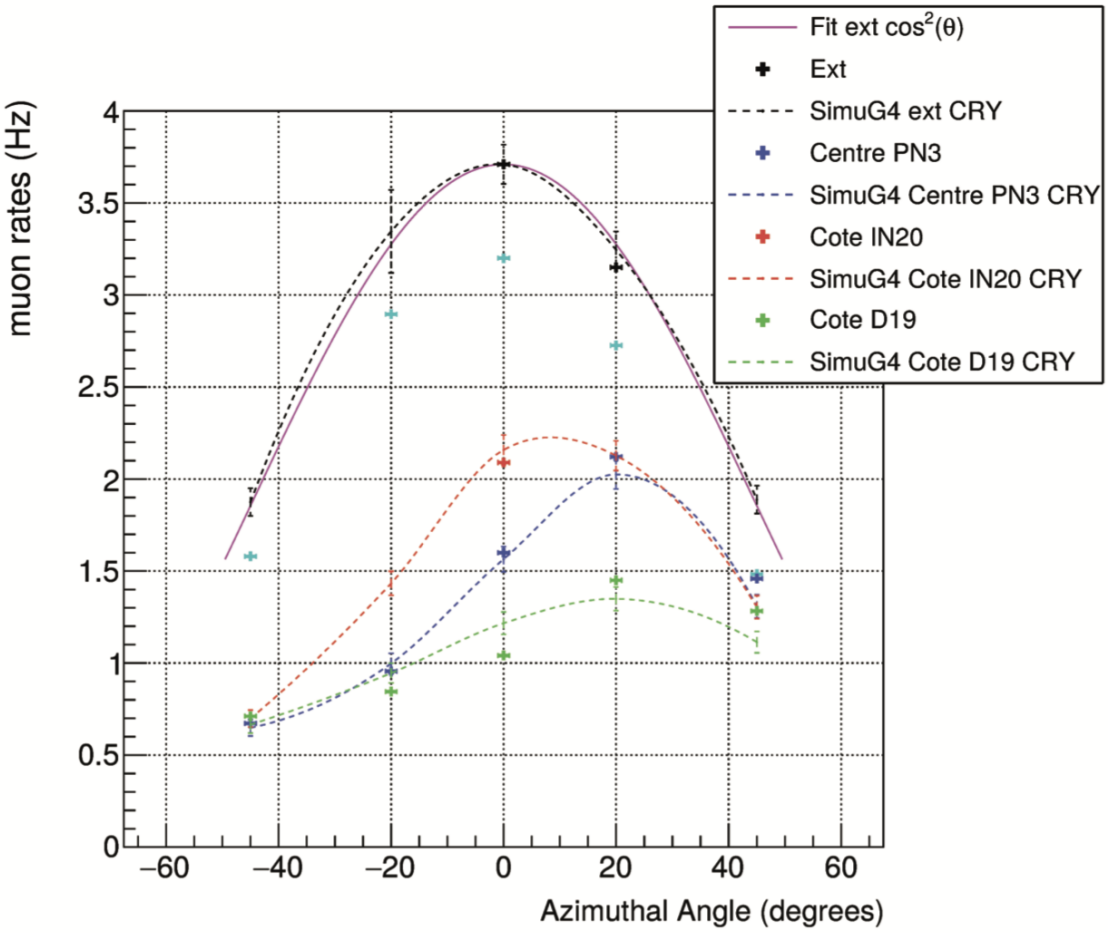

Figure 2.11: Muon flux measured at different locations: outside the reactor building (Black), at the centre of the PN3 casemate (blue), on the IN20 (orange) and D19 side (green). Dotted lines correspond to simulation using the Cosmic-ray Shower Library and a complete description of the reactor building using GEANT4.

Most muons reach the earth as Minimum Ionizing Particles (MIP) and deposit $\sim$ 2 MeV·cm^{-1}. It is then very easy to tag a muon in the detector as long as it travels more than a few cm in the detector, its deposited energy exceeding the maximum energy of neutrinos $\sim$ 8 MeV. However, muons give rise to a correlated background by spallation of heavy nuclei in the surrounding materials. Indeed, fast neutrons produced by the spallation interaction of the muon on heavy nuclei of the surrounding materials such as the lead of the detector shielding and next to the separation walls. This fast neutron with an energy of a few MeV can enter the detector and produce correlated signals mimicking an IBD process, the fast neutron can induce one or several proton recoils mimicking a prompt signal before being captured on Gd giving a delayed signal. In this case, the proton recoil can be identified by the time profile of light emission, which will be different for a proton than for an e^+ or e^-. This technique is called pulse-shape discrimination (PSD).

In addition, it is also possible that two neutrons are captured in the time window of an IBD, in this scenario the discrimination is challenging, although the larger distribution of energy among neighboring cells in n-Gd events compared to e^+ could be used against this background as it was shown in the thesis of L. Manzanillas [Man16]. Another correlated signal can arise from spallation resulting in cosmogenic radioactive isotopes such as ^{8}He, ^{9}Li or ^{11}Li. These isotopes undergo β decay followed by neutron emission, giving a signature very close to an IBD process.

Reactor induced correlated background

Expected reactor induced background takes the form of fast neutron coming from the reactor, giving a correlated pair in a similar way as fast neutron coming from cosmic muon spallation.

Since the energy spectrum of fast neutrons emitted by the reactor become negligible above $\sim$ 10 MeV and that proton recoils arising from neutron scattering in the detector are heavily quenched, reactor induced background is expected at low energy $\leq$ 4 MeV, moreover, since the neutron needs to undergo several scattering to reach the internal detector the energy of these neutrons is likely to be well below this limit.

To evaluate this potential source of background the rate of proton recoils identified by PSD in IBD candidates is compared between reactor-off and reactor-on data. A detailed description of this study can be found in the PhD thesis of L. Bernard [Ber19].

The study shows that although the presence of this background can not be ruled out, the rate is negligible for reconstructed energies above $\sim$2.5 MeV; for energies below $\sim$2.5 MeV, the IBD spectrum is corrected from the few percent bias due to the reactor-induced background and a conservative uncertainty of 100% of the bias is assigned.

Gamma and thermal neutron background

The H7 and H13 beam tubes, located in front of the PN3 and IN20 casemates respectively, are the main source of neutron background coming from the reactor core.

The H7 beam tube has been sealed off with a cap composed of concrete, lead and boron, to reduce the flux of thermal and fast neutrons coming from the reactor core. The neutron flux at the end of the H7 beam tube is estimated to be $\sim 1\times 10^{-4}$ n$\cdot$s$^{-1}\cdot$cm^{-2} [Peq15].

Additionally, the neutron beams used by the neighbouring instrument, although they do not directly enter the PN3 casemate, are collimated in which process neutrons undergo many scatterings. Consequently, the neutron flux reaching the PN3 casemate is mainly composed of thermal neutrons. Measurements of the thermal neutron flux inside the PN3 casemate were performed using an ^{3}He tube detector, the flux was measured to be as high as 100 n$\cdot$s$^{-1}\cdot$cm^{-2}. This neutron flux contributes to the γ background by capture on heavy nuclei such as Fe, Al, Cu, which following decay leads to the production of high energy γ. The neutron background is continuously monitored by BF_3 and ^{3}He proportional counters, one of them is installed inside the STEREO shielding to ensure sensitivity to fast neutrons.

γ particles constitute a source of accidental background. The most annoying γ are produced by the deexcitation of the nuclei obtained by β decay following the neutron capture on heavy atoms of the materials surrounding the detector.

High energy γ come from the neutron capture on steel (7.6 MeV) and aluminium (7.7 MeV). In addition, irradiation of the heavy water in the primary cooling circuit passing underneath the STEREO detector leads to the creation of ^{16}N:

$$^{16}\mathrm{O} + n \rightarrow ^{16}\mathrm{N} + p \tag{2.19}$$

The β decay of ^{16}N lead to an excited state of ^{16}O. The deexcitation of ^{16}O gives rise to a variety of γ with energies up to 8.9 MeV, but the main branch leads to a γ of energy 6.1 MeV. A summary table of the most pertinent nuclei giving rise to γ with energies between 2 and 8 MeV is given in Table 2.3.

At low energy, the main contribution to the γ background comes from natural radioactivity and the 1294 keV γ ray coming from the activation by neutron capture on

Isotope	$\sigma_{\text{th. capt.}}$ [b]	E_γ [keV] (br. ratio)
^{1}H	0.33	2223 (100%)
^{56}Fe	2.59	7631 (29%) 7646 (25%)
^{27}Al	0.23	7724 (27%)
^{56}Cu	4.47	7916 (33%)
^{16}O	$\sim$ 0.10 (fast neutron)	6128 (67%) 7115 (5%)

Table 2.3: Summary table of radiative neutron capture pertinent for γ background evaluation [Pri].

^{40}Ar present in the air. Fast variation of the argon contribution (factor $\sim$ 5) was observed during reactor-on periods, this variation can be explained by the short lifetime of the activated argon ($\sim$ 110 min), and convection movement of the air inside the experimental hall [Kan17]. A campaign of measurement took place at the ILL using a germanium detector to characterise the γ background with high resolution. Detailed studies about measured spectra in various shielding configurations can be found in the PhD thesis of F. Kandzia [Kan17].

The γ flux at the PN3 casemate before the installation of the shielding was measured to be $\sim$ 14.7 kHz·cm^{-2} for energies above 2 MeV [Peq15]. The measured background was compared to the maximum acceptable background to achieve a signal to background ratio of $\sim$ 1.5. In order to reach such a signal to background ratio, the shielding was designed to provide an attenuation factor of the order of $\sim 10^{-5}$ - 10^{-6} on the γ rate [Zso16].

2.2.5 Shielding

As stated in the previous section the important rate of γ at the STEREO location needs to be met with an adapted shielding in order to reach a reasonable background-to-signal ratio.

Passive shielding

The STEREO detector is located at the end of the H7 beam tube (see Figure 2.9). In order to design an adapted seal for this beam tube several MCNPX simulations were performed. The final design resulting from these simulations consist of, as seen from the detector, 8 cm of lead, 1 m of heavy concrete, 8 cm of lead and 2 cm of Boral.

The border of the H13 casemate toward STEREO was reinforced with borated polyethylene to protect from neutron scattering on the beam elements. A pre-existing lead wall inside the H13 casemate toward STEREO was enlarged passing from 10 to 20 cm of lead and the wall was coated with boron-loaded rubber. Additional shielding walls were installed to protect STEREO from the reactor and neighbouring instruments.

The wall in front of STEREO between the detector and the reactor is composed of 10 cm of polyethylene and 10 cm of lead. For the D19 side wall, 10 cm of the 40 cm concrete wall were removed and replaced by 10 cm of lead. On the IN20 side, the 15 cm lead wall was enlarged with 15 cm of borated polyethylene.

Both front and side walls are 2.4 m high, effectively shielding the detector but not the muon veto placed on top of the detector at a height of $\sim$3 m. The mechanical frames of every wall were covered by boron-loaded rubber to prevent neutron capture on steel.

The internal neutrino detector is enclosed in a passive shielding of ∼65 tons composed of 5% borated polyethylene and an outer layer made of lead. This shielding is designed to protect the neutrino detector from the external γ background and cosmic muon induced background. The role of the borated polyethylene is to moderate and capture neutrons while the lead is used to mitigate the γ background.

The 6.1 tons of polyethylene shielding are distributed around the detector with various thicknesses. To protect the neutrino detector from fast neutrons induced by cosmic muon spallation in the top lead layer and the transfer channel, a 297 mm thick layer of polyethylene is placed on top of the detector. The layer thickness is 200 mm underneath the detector. The polyethylene layer on the detector sides is only 147 mm. This reduced thickness is acceptable since the outer volume of the Gamma-catcher serves as an additional shielding layer.

The lead layer of the shielding for a total weight of 58.9 tons is 10 cm thick on the sides. The thickness underneath the detector is 20 cm. This greater thickness underneath the detector aims at absorbing high energy γ coming from the decay of ^{16}N produce by activation of O in the heavy water coolant circuit passing underneath the STEREO area. The top layer is 15 cm as there were indications of neutron captures in the heavy concrete surrounding the water channel on top of the detector.

The lead and polyethylene shielding is supported by a strong steel girder frame structure (see Figure 2.12). Two small apertures were made to pass the cables, the inner calibration tubes and the rail for the underneath calibration system. A third larger one is a trapezoidal aperture, closed by a sliding door presenting the same shielding as the wall. This aperture allows access to the outer calibration system.

A 25.6 cm deep muon veto water tank is located above the shielding on top of the detector. The whole construct is enclosed in soft iron plates (10 mm thick) coated with B_4C.

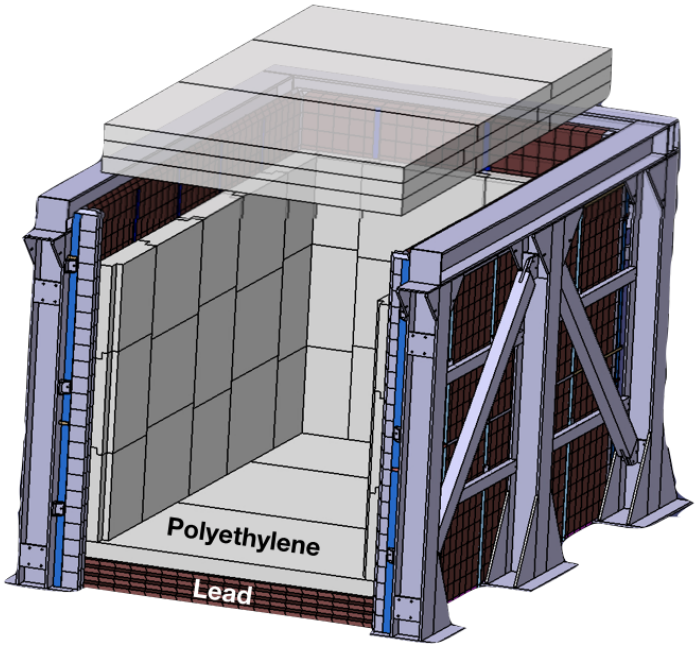

Figure 2.12: Lead and polyethylene layer of shielding inside the girder structure.

Muon veto

A muon veto was placed on top of the detector's shielding to address cosmic muon induced background (see Figure 2.13a). It is a Cherenkov detector consisting of a demineralised water tank of 396 cm × 240 cm for a depth of 25.6 cm covering the whole detector and its shielding. A wavelength shifter is added to the water it permits to shift the Cherenkov photons wavelength from the UV range to $\sim$ 420 nm corresponding to the PMT maximum quantum efficiency, which reaches $\sim$ 25%.

The wavelength shifter is the 4-Methylumbelliferone (4MU), various concentrations of 4MU were tested from 2 to 10 ppm, showing a linear increase of the optical photon detection for the lowest concentrations and saturation for the highest concentrations. The final design has a concentration of 6 ppm. This concentration was tested for more than a year in a prototype with no indications of ageing effects on the response.

The sides of the water tank are lined with sheets of highly diffusive $Tyvek$ 1059B to maximise the total collected light on all PMTs. The light is collected by 20 8-inches $Hamamatsu$ photomultiplier tubes (R5912). The photocathode of the PMTs is immersed in the water.

The PMTs are calibrated using a LED system, which is also used in the STEREO detector. The trigger is set on the charge collected by a group of 4 PMTs, this strategy reduces the γ contamination, compared to a single PMT trigger. The collected charge for a vertical muon passing through the water tank reaches 530 p.e.

The average muon rate in the muon veto reaches 600 Hz at 1020 hPa of atmospheric pressure, a time variation of a few percent is observed. This variation is correlated to the water level in the reactor and transfer pools.

In order to compute the efficiency of the muon veto, we identify the muon passing through the muon veto by selecting vertical muons in the STEREO detector. Vertical muons deposit their energy only in one cell. Cosmic muons deposit $\sim$ 2 MeV·cm^{-1} in the liquid scintillator, a path of a few centimetres in the detector is enough to give energy deposits well above the neutrino maximum energy, giving a clear identification of vertical muons.

The veto efficiency remained constant at 99.5 ± 0.1% during the whole data acquisition. Moreover, the efficiency has been shown to be identical during reactor-on and off period with an uncertainty of 0.1 %, leading to a negligible systematic uncertainty on the neutrino rate.

(a) (b)

Figure 2.13:
(a) Assembly of the muon veto and its 20 8-inches PMTs.
(b) Zoom on a veto PMT: we can distinguish in white the 2 cylindrical layers of mu-metal shielding the PMT from stray magnetic fields.

Magnetic shielding

The design of the magnetic shielding was based on simulations, the details of this study can be found in [Kan17].

Without magnetic shielding, the maximum stray field arising from the operation of the IN20 magnet at 13.5 T was measured to be 0.41 mT at the detector PMT bay and 0.42 mT in the veto PMT bay. The final design of the magnetic shielding consists of layers of soft iron and mu-metal. A first layer of 10 mm of soft iron surrounds the detector shielding and veto (see Figure 2.14). A layer of 1.5 mm thick mu-metal surrounds the internal detector. In addition, a cylinder consisting of 2 layers of mu-metal (1 mm thick each) was placed around each veto PMTs' photocathode (see Figure 2.13b), a single layer cylinder was used for the internal detector PMTs.

For the muon veto, the PMTs signal amplitude varied up to 20 % for the PMTs along the IN20 side, when the IN20 instrument was operated at high magnetic fields. However, this variation did not induce efficiency variation in the muon veto. For the internal detector PMTs, a variation of the PMT signal is more critical as it would induce a bias in the energy measurement. Fortunately, no visible effects of the stray magnetic fields could be reported on the internal detector PMTs.

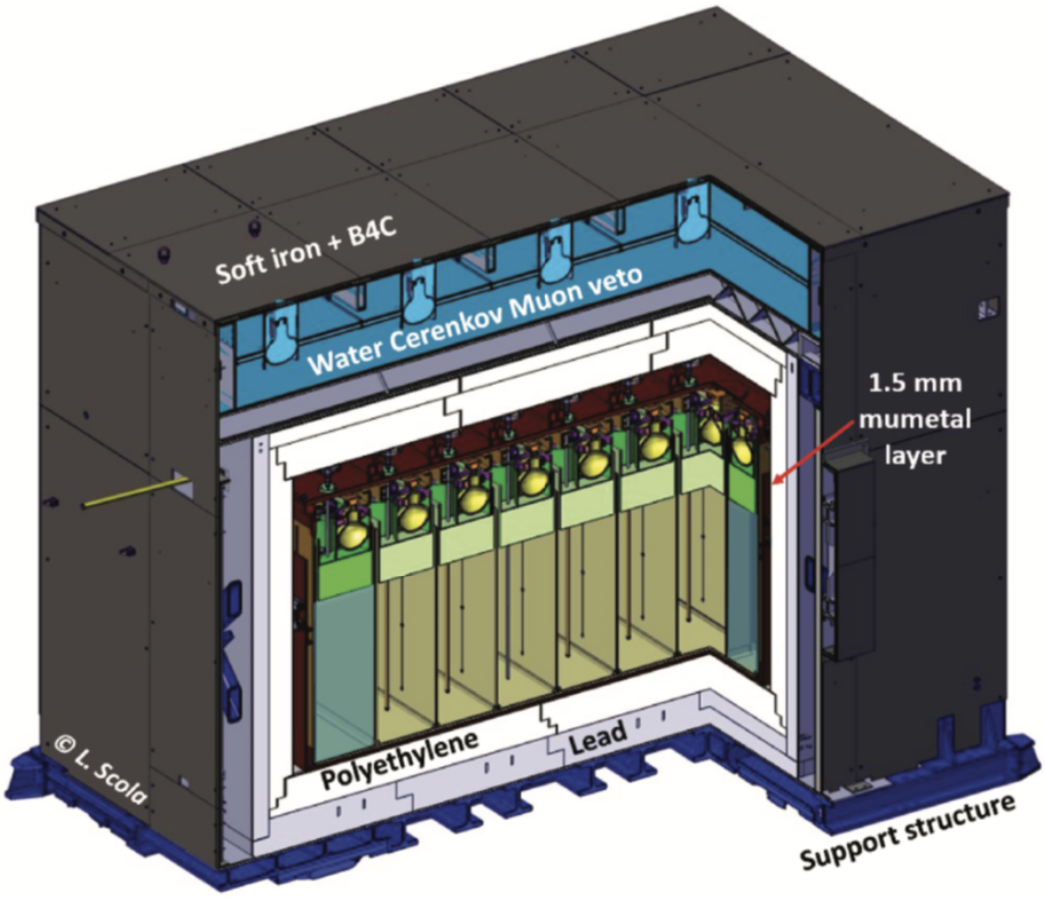

Figure 2.14: Sectional view of the STEREO detector inside the shielding layer of lead,polyethylene and mu-metal surmounted by the muon veto, the whole construct is encapsulated in a layer of soft iron and B_4C.

2.3 The STEREO detector

The STEREO detector is based on the well-established liquid scintillator technology, its peculiarity lies in its segmented design.

2.3.1 Detector design

Inner detector

The most central part of the detector is named the Target (TG).

It is made of an acrylic tank with 12 mm thick walls, with inner dimensions L×l×h = 2.233 m×0.889 m×1.230 m. It is divided lengthwise into six similar and optically isolated cells separated by 2×4 mm thick acrylic walls surrounding a reflective film, the inner dimensions of one cell being 368 mm×889 mm×918 mm. This tank is encased in a larger double-walled stainless steel vessel with inner dimensions L×l×h = 3.096 m×1.536 m×1.505 m delimiting an outer volume around the target. This outer volume is called the Gamma-Catcher (GC).

The purpose of the GC is to detect escaping γ from events inside the TG. A secondary purpose is to be a veto against external background. The GC is split into four cells: two cells adopting the same geometry as the TG cells and placed on the sides of

the first and sixth TG cells named respectively GC front and GC back; the other two cells are 30 cm wide and cover the full length of the vessel, they are called GC IN20 and GC D19 (see Figure 2.15).

To prevent the degradation of the optical properties of the liquid scintillator by water or oxygen absorption, the inner detector vessel is filled with gaseous nitrogen with a slight overpressure of 10 to 30 mbar. Additionally, the relevant experimental parameters such as temperature, pressure, liquid levels, high-voltage and so on, are monitored over time.

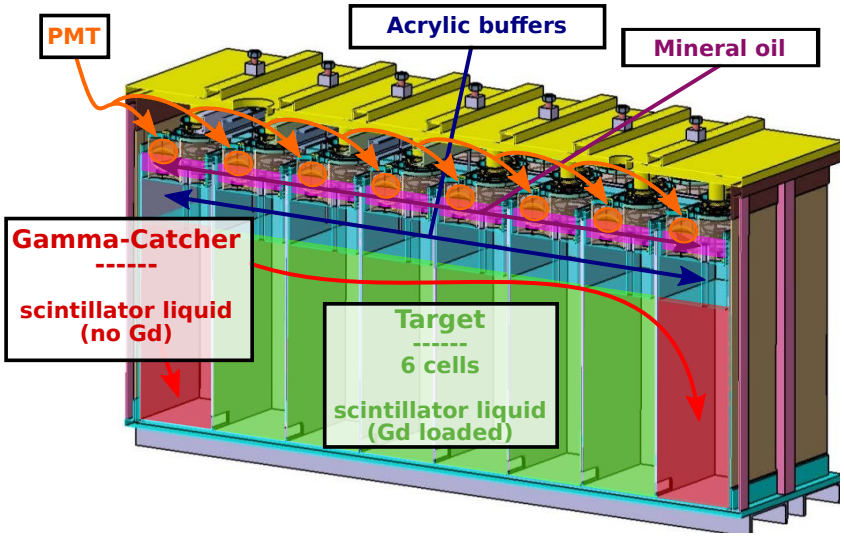

Figure 2.15: Sectional view of the inner detector

The Side walls and the bottom of every cell are rendered highly reflective thanks to a specular reflective film $VM2000^{TM}$ Enhanced Specular Reflector (ESR). This reflective layer has three purposes: keeping the cells optically separated, maximising the amount of light collected by the PMTs and reducing the position dependence in the light collection.

The ESR film shows a very high reflectivity above 98 % for wavelength in the visible range and all angles of incidence [MBH+05] as long as the film is in the air. However, once the film is immersed in the liquid its optical properties change and the reflectivity drops for angles above 60°, for the wavelength of interest. Taking this effect into account, the walls were designed to keep the ESR film in the air: the film is inserted between two acrylic plates and an air gap between the parts is guaranteed by a 100 μm thin nylon net (see Figure 2.16). Thanks to this design the walls are perfect mirrors for angles above 42° (total reflection on the acrylic-air interface) and very good mirrors for smaller angles (98 % reflectivity on $VM2000^{TM}$) (see Figure 2.17).

Despite the effort to make the cells as optically separated as possible, an optical cross-talk between the cells exist. It is due to the border of the cells where the sealing of the air gap allows the light to pass from one cell to another. The detector was designed to limit the optical cross-talk between the cells and between the TG and the GC at a few percent level.

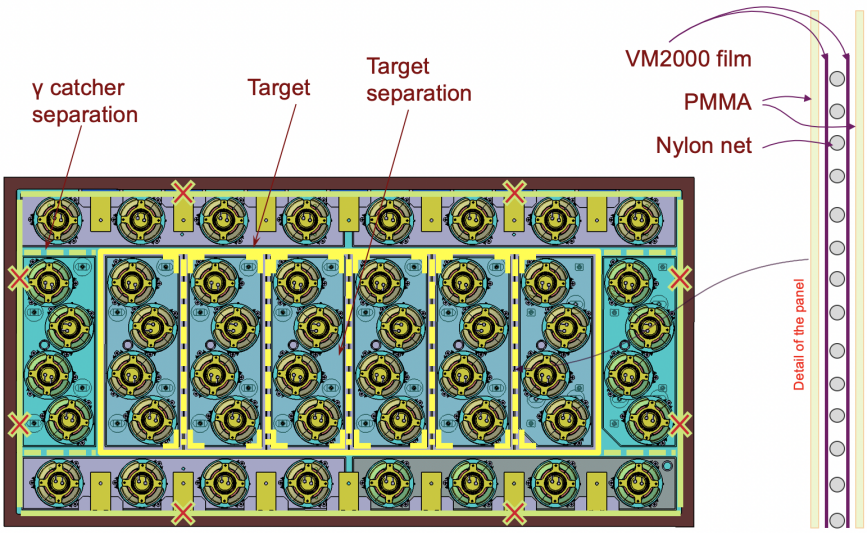

Figure 2.16: Top view of the internal detector and design of the separation walls

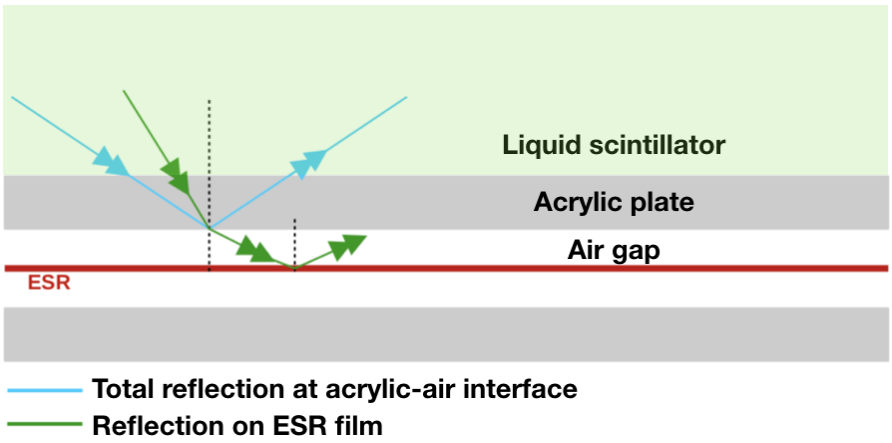

Figure 2.17: Principle of the separation walls

Photomultiplier tubes

The collection of the scintillation light is performed by 48 photomultiplier tubes (PMTs) placed on top of the cells. The PMTs are 8-inches *Hamamatsu* R5912-100. The photocathode is made of Bialkali (Sb-Rb-Cs, Sb-K-Cs), with the highest quantum efficiency reaching $\sim$ 35 % around 400 nm (see Figure 2.18), which corresponds to the wavelength of the scintillation light.

The PMT bases have been tuned to minimize non-linearity, the latter being below 1 % when there are less than 1500 photoelectrons (p.e.) per PMT. This corresponds to the signal of a 10 MeV neutrino interacting in the TG. The high-voltage has been set as to have uniform PMTs' gain, showing a residual dispersion below 1.5 %.

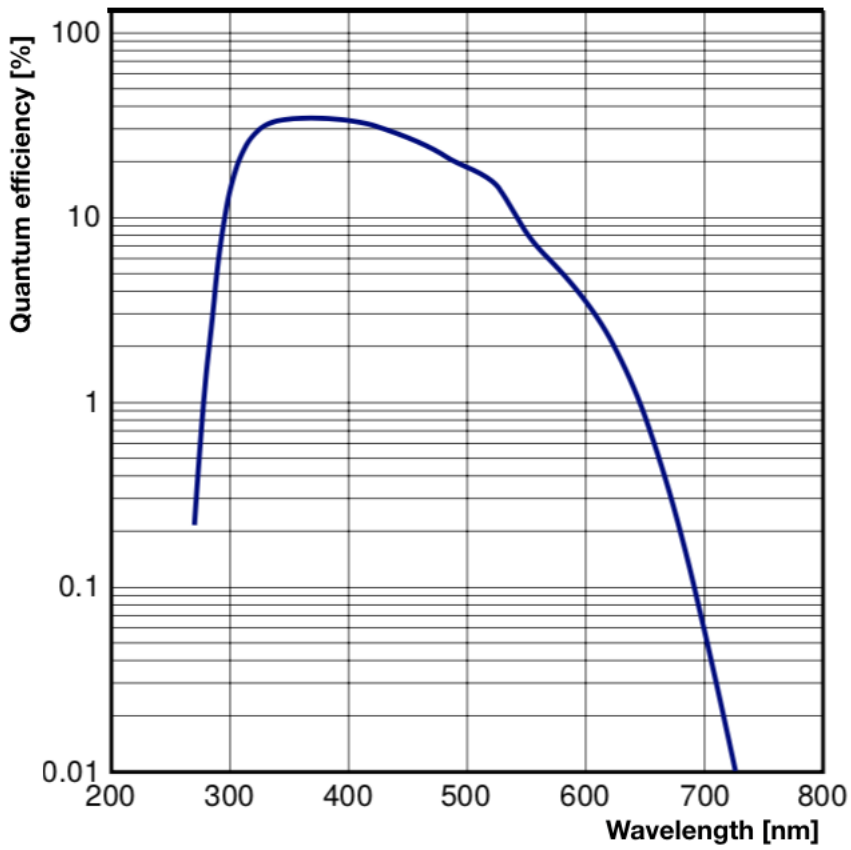

Figure 2.18: Quantum efficiency of the R5912-100 PMTs as a function of the light wavelength.

To distribute more homogeneously the light amongst the PMTs of the same cell, the PMTs are placed on a 20 cm thick acrylic buffer, immersed in a bath of mineral oil that ensures the optical coupling. The liquid scintillator, the acrylic buffer and the mineral oil have all the same refractive index. Each TG cell, as well as GC front and back, has 4 PMT's laid out in quincunx (see Figure 2.16). In the long GC, the 8 PMTs are aligned.

Each PMT is inside a cylinder layer of mu-metal (see Figure 2.19) that shields it from stray magnetic fields coming from the IN20 magnet.

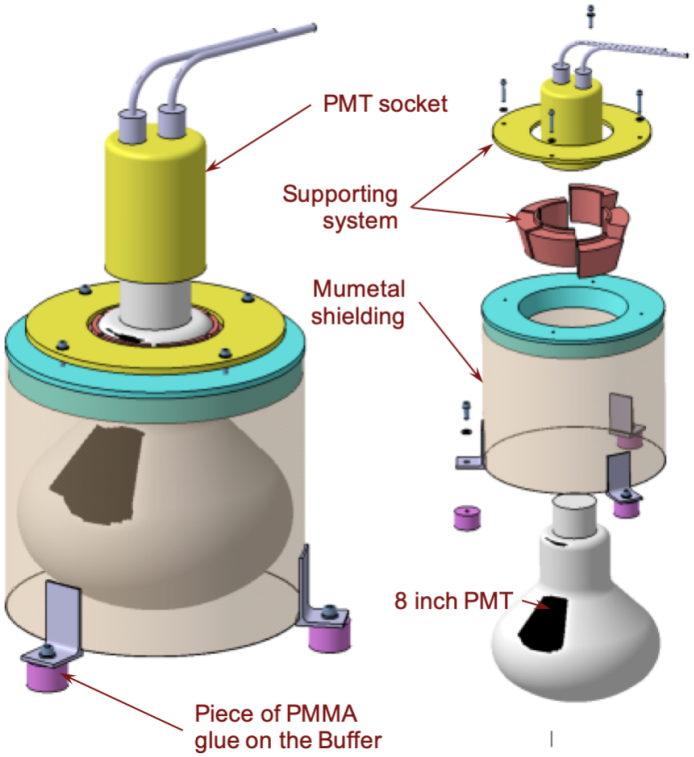

Figure 2.19: PMT assembly in its mu-metal magnetic shielding

2.3.2 Liquid scintillator

Liquid scintillator composition

The liquid scintillator composition of STEREO was designed taking into account the need for high transparency to the scintillation light, high light yield, compatibility with the detector materials, and good pulse shape discrimination capabilities (PSD). Additionally, since the detector is operated at a close distance from a nuclear reactor, safety has to be taken into considerations so a high flashpoint is required.

The use of Linear Alkyl Benzene (LAB) was decided as it checks several conditions mentioned above: it is highly transparent to wavelength above 400 nm, it is mostly inert chemically and has a high flashpoint of $\sim$ 140 °C. LAB represents 73.0 wt.% of the LS. Nevertheless, LS based on LAB shows poor pulse shape discrimination capabilities and lower light yield. In order to improve these two characteristics ortho-phenyl-xylyl-ethane (PXE) (19.5 wt.%) and di-isopropyl-naphthalene (DIN) (4.9 wt.%) were added to the LS, improving the light yield and PSD performance, at the cost of slightly worse transparency.

The TG is filled with gadolinium (Gd) loaded liquid scintillator at a level of 0.2 wt. %. The metalo-organic complex: Gd-β-diketonate ($Gd(thd)_3$) is first completely dissolved in tetrahydrofuran (THF). The resulting proportion of Gd complex in the TG LS is 0.9 wt.% the same 0.9 wt.% proportion is used for the THF. The presence of THF in the TG LS lowers the flashpoint to $\sim$ 74 °C. The last components of the LS are the wavelength shifters: the combination of di-phenyloxazole (PPO) and bis-methyl-styryl-benzene (bis-MSB) was used with respective concentrations of 0.8 wt.% (7 $g{\cdot}l^{-1}$) and 0.002 wt.% (20 $mg{\cdot}l^{-1}$). The composition of the GC LS is the same as the TG LS apart from the absence of Gd and THF. The adjunction of the Gd complex lowers the light yield in the TG LS. Indeed, the Gd complex has absorption bands

Component	Concentration	CAS Number
LAB (linear alkyl benzene)	73.0 wt.%	67774-74-7
PXE (ortho-phenyl-xylyl-ethane)	19.5 wt.%	6196-95-8
DIN (di-isopropyl-naphtalene)	4.9 wt.%	38640-62-9
$Gd(thd)_3$ (Gd-tris-(2,2,6,6-tetramethyl -heptane-3,5-dionate)	0.9 wt.%	14768-15-1
THF (tetrahydrofuran)	0.9 wt.%	1099-99-9
PPO (2,5-diphenyloxazole)	0.8 wt.% (7 $g \cdot l^{-1}$)	92-71-7
bis-MSB (4-bis-(2-methylstyryl)benzene)	0.002 wt.% (20 $mg \cdot l^{-1}$)	13280-61-0

Table 2.4: Composition of the STEREO's Target liquid scintillator

in the same wavelength region as the primary wavelength shifter. The Gd complex being non-fluorescent, photons absorbed by the Gd complex are lost to scintillation. A table summarising the liquid composition is given in Table 2.4 (more details are given in [BGL+19]).

Liquid scintillator properties

To prevent the degradation of the detector resolution by vertical inhomogeneity due to light absorption by the LS itself, the attenuation of the liquid must be above 4 m for wavelength in the 430 nm region. The attenuation length was measured to be 6.9 m for the TG LS and 9.7 m for the GC LS at 430 nm. The light intensity and the attenuation length as a function of the wavelength are presented in Figure 2.20.

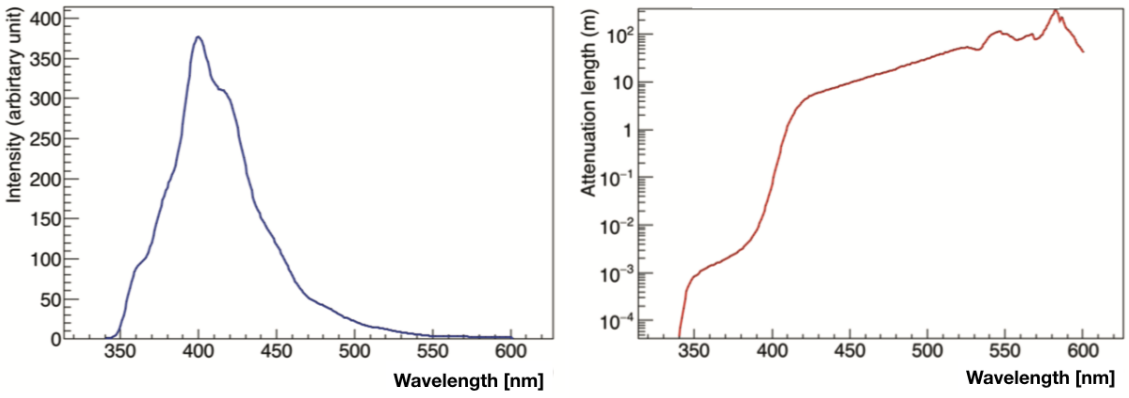

(a) (b)

Figure 2.20: Intensity of the light emitted by the liquid scintillator as a function of the wavelength (2.20a) and attenuation length of the liquid scintillator as a function of the wavelength (2.20b).

The properties of the liquid are summarised in Table 2.5

In order to measure the neutrino flux, the number of protons n_p in the Target must be known:

$$n_p = \frac{f_H \times m_{LS}}{m_H} \tag{2.20}$$

where f_H is the relative hydrogen fraction, m_{LS} the mass of the LS and m_H the hydrogen mass. The hydrogen fraction was precisely measured at the Technische Universität München using CHN analysis, the resulting hydrogen fraction is 11.45±0.11 wt.%.

Properties	TG LS	GC LS
Attenuation length (430 nm)	6.9 m	9.7 m
Light yield [photon·MeV^{-1}]	6500	8400
Density (20°C)	0.887	0.884
H fraction	11.45 wt.%	
Refractive index (25°C)	1.50	1.50
Flashpoint	74 °C	>100 °C

Table 2.5: Properties of the liquid scintillator used in STEREO.

The hydrogen mass is known with high accuracy: m_H=1.673533×10^{-27} g. A total of 1602±2 kg of LS fill the Target. This leads to a proton number of n_p=1.096±0.011×10^{29}in the TG LS.

Particles interaction in a liquid scintillator

When a charged particle passes through the scintillator, it loses energy through electromagnetic interactions with the electrons and nuclei of the medium. For positrons coming from an IBD process whose energy ranges between ∼1 and ∼8 MeV (positrons with energy below ∼1 MeV are not used in practice), interactions happen predominantly on electrons, which induces the excitation and ionization of the molecules. The energy loss can be computed from the Bethe-Bloch formula:

$$\frac{dE}{dx} = -4\pi N_A r_e^2 m_e c^2 \frac{Z}{A}\frac{1}{\beta^2}\times \left[ln\left(\frac{\gamma m_e c^2 \beta\sqrt{\gamma-1}}{I\sqrt{2}}\right)+\frac{1}{2}(1-\beta^2)-\frac{2\gamma-1}{2\gamma^2}ln2+\frac{1}{16}\left(\frac{\gamma-1}{\gamma}\right)^2\right] \quad (2.21)$$

where N_A is the Avogadro number, r_e is the radius of the electron, Z is the charge number, A is the weight number and I is the mean excitation energy characterising the absorber material. For particles with higher energy, the $Bremsstrahlung$ effect, consisting in the emission of photons by the decelerating particle in the Coulomb field of the nuclei is also a source of energy loss. Additionally, if the particle moves faster than the speed of light in the medium, Cerenkov light emission takes place but the energy loss coming from Cerenkov radiation is small compared to the energy loss coming from ionisation and $Bremsstrahlung$.

Similarly, the interaction of photons with matter will depend on the particle energy. Photons can undergo photoelectric effect and matter-antimatter pair production in which cases they are completely absorbed, or they can undergo Compton scattering. The energy needed to perform the photoelectric effect is ad minima the ionisation energy of the electron, however, the photoelectric effect cross-section decreases with energy. In the nonrelativistic regime the photoelectric effect cross-section is well approximated by the Born formula:

$$\sigma_{p.e.} = \sqrt{\frac{32}{\epsilon^7}}\alpha^4 Z^5 \sigma_{Th}^e \quad (2.22)$$

where $\epsilon = E_\gamma/m_e c^2$ and σ_{Th}^e is the Thomson cross-section for elastic scattering of photons on electrons. In the case of STEREO, the photoelectric effect is dominant up to 50 keV, where Compton scattering takes over as the dominant process. We note

here that the energies of STEREO's calibration γ are in this regime (see Table 2.7). The Compton scattering cross-section is given by the Klein-Nishina formula:

$$\sigma_{KN} = 2\pi r_0^2 \left[\frac{1+k}{k^2} \left(\frac{2+2k}{1+2k} - \frac{ln(1+2k)}{k} \right) + \frac{ln(1+2k)}{2k} - \frac{1+3k}{(1+2k)^2} \right] \tag{2.23}$$

with $k = \frac{h\nu}{m_e c^2}$. Additionally, the maximal transferable energy via Compton scattering, known as "Compton edge", is given by:

$$E_{c.e.} = E \left(1 - \frac{1}{1 + \frac{2E}{m_e c^2}} \right) \tag{2.24}$$

Lastly, at high energy (above 20 MeV) the dominant process is the pair production. In this process, an electron-positron pair is produced in the Coulomb field of the nucleus (see Figure 2.21).

The prompt signal of an IBD event is produced by the interaction of a positron in the liquid scintillator. The energy loss of the positron energy is well approximated by the energy loss of an electron given in equation 2.21. It is followed by the emission of two 511 keV annihilation γ, from its annihilation with an electron of the LS. The delayed signal, however, originates from the cascade of γ coming from the neutron capture on Gd. These γ have energy ranging between 0.511 to ~7 MeV, hence they interact dominantly via the Compton effect, producing a large number of lower energy electrons.

The conversion length for a 1 MeV γ in the LS is about 16 cm, protons travel a few tens of μm. Thermal (fast) neutrons thermalise in the LS after a few mm (cm), but they can diffuse after thermalisation, making the distance between emission and capture of the order of ~10 cm. Electrons (and positrons) of a few MeV lose all their energy in a few mm.

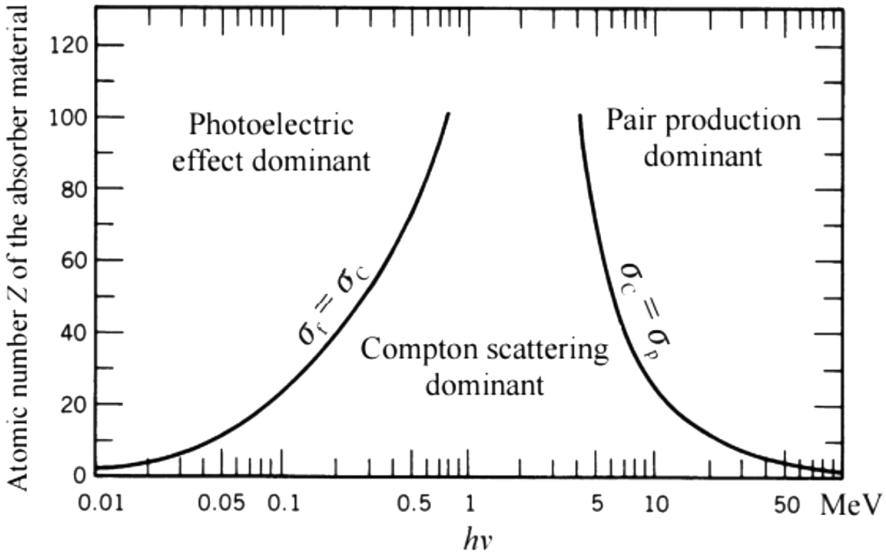

Figure 2.21: The different process of photon interaction with matter depends on the charge number of the material. At low energy, the dominant effect is the photoelectric effect. At medium energy, the Compton scattering becomes the dominant effect and at high energy, the matter-antimatter pair production is the dominant effect.

Scintillation mechanism

The energy deposited via ionisation and excitation of the molecules in a scintillator results in luminescence emission. Luminescence is a property of conjugated and aromatic organic molecules that originates from the electronic structure of these molecules.

The electronic structure of the carbon atoms in the molecule is largely responsible for the structure of the molecule. In its ground state the electronic structure of the C atom is $1s^2$, $2s^2$, $2p^2$ (see Figure 2.22).

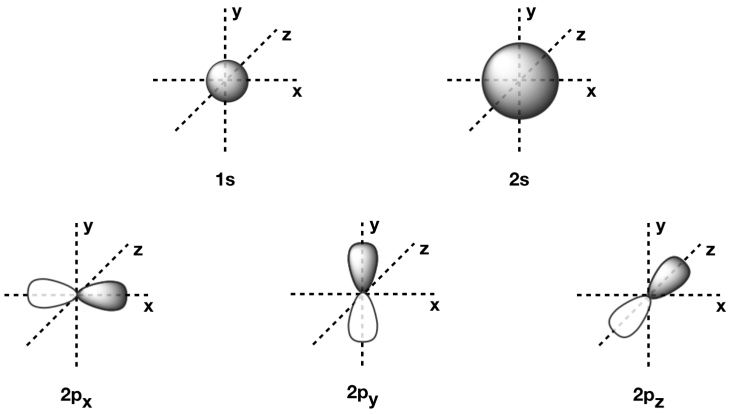

Figure 2.22: Electronic orbitals of a carbon atom in its ground state.

Upon formation of a cyclic aromatic hydrocarbon molecule such as benzene, the s orbital and two among the tree p orbital combine to form three hybrid orbitals named sp^2, the remaining p orbital (say p_y) stays unchanged. This is called trigonal or sp^2 hybridisation. The three sp^2 hybrid orbitals share the same plane (say xz plane), they are spaced out from each other with equal angles of 120°. Bonds arising from axial overlap of orbitals (meaning they are symmetrical by rotation around the bonding axis) are called σ-bonds. Bonds arising from lateral overlap of orbitals are called π-bonds.

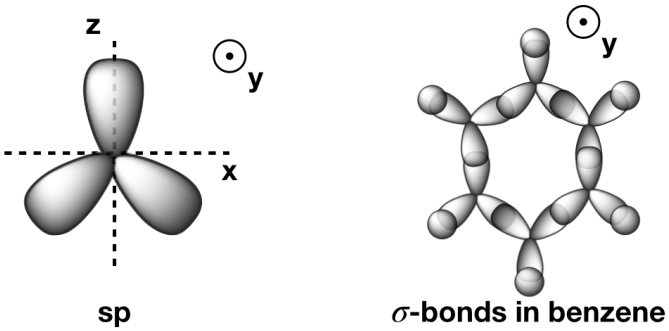

Figure 2.23: sp^2 hybrid orbitals and σ-bonds in a benzene molecule

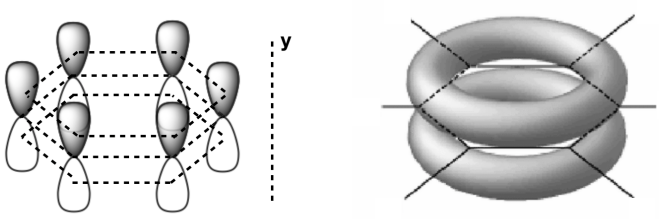

Figure 2.24: p-orbitals in benzene leads to delocalised π-bonds.

In benzene, two of the three sp hybrid orbitals of 2 carbon atoms overlap forming the localized C-C σ-bond, the remaining sp hybrid orbital interact with the s orbital of a hydrogen atom forming the C-H σ-bond (see Figure 2.23). All the σ-bonds are coplanar. Moreover, the unhybridised p_y orbitals interaction is maximal when their nodal planes are coplanar, resulting in a planar benzene molecule. The interaction of the six p_y orbitals in the benzene form a delocalised π-bond (see Figure 2.24).

Delocalised π-bonds happen similarly in other aromatic and conjugated molecules. The luminescence of these molecules is due to the excited states of these π-orbitals. The typical electronic energy level of an organic molecule that displays π-bonds is given in Figure 2.25.

The π-orbital can occupy a sequence of singlet states S_0,S_1,S_2,... up to the π-orbital ionisation energy I_π (see Figure 2.25). In addition to the electronic levels, there are vibrational sublevels with much smaller spacing: S_{00},S_{01},...,S_{10},S_{11},... Similarly, the π-orbital can occupy a sequence of triplet states T_1,T_2,... The transition from the S_1 excited states to the ground state (or its vibrational sublevel) is accompanied by the emission of a photon. The photon emission can be triggered by populating any of the excited singlet states, however, no radiative transition between states higher than S_1 and the ground state, or any other lower state is generally observed. This is due to the very quick radiationless internal conversion between neighbour states, with a characteristic time of $\sim 10^{-11}$ s with is much shorter than the radiative lifetime $\sim 10^{-8}$ - $\sim 10^{-9}$s.

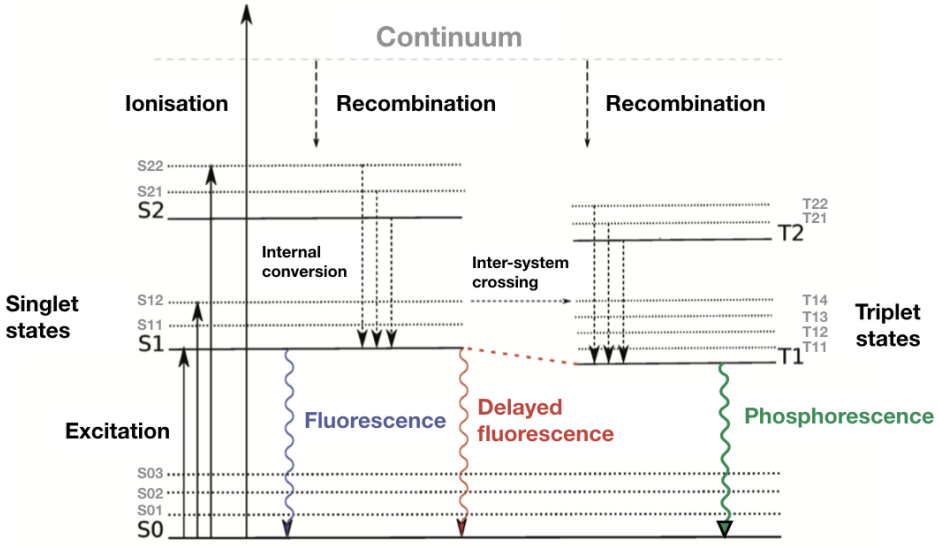

Figure 2.25: Typical energy level scheme of the π-bond in an aromatic hydrocarbon. S states are singlets whereas T states are triplets. Scintillation light (fluorescence) is emitted when the orbital transition from the S_1 state to the ground state S_0, delayed fluorescence happens when 2 molecules in a T_1 state interact to give a molecule in an S_0 state and a molecule in an S_1 state. Direct transition from the T_1 state to the ground state (phosphorescence) is highly suppressed because it is a spin-forbidden process [Bir64] [Hor74].

If a higher singlet states $S_{i>1}$ is populated, it will return to the S_1 state by radiationless internal conversion and then the transition from the S_1 state to the ground state is accompanied by the emission of a photon, this phenomenon is known as fluorescence. Similarly, if a higher triplet state is populated, it will return to the T_1 state by radiationless conversion. However, the transition from the T_1 state to the ground state, known as phosphorescence is spin-forbidden and the decay time for this process is of the order of $\sim 10\ \mu s$ to several seconds. In practice, this phenomenon is superseded by the delayed fluorescence process, in which two molecules in a T_1 state interact to give a molecule in S_1 state and a molecule in a S_0 state:

$$T_1 + T_1 \rightarrow S_1 + S_0 \tag{2.25}$$

The typical decay time of the delayed fluorescence process is ~100 ns.

Considering the excitation of the scintillator by charged particles, the following processes can occur:

- excitation into π-orbital excited singlet states;
- π-orbital ionisation;
- excitation and ionisation of other orbitals (σ, 1s)

The last process does not lead to light emission.

The main fast scintillation emission is due to the first process that populates the singlet states. The second process leads to the population of the triplet states and

singlet states by ion recombination. From simple statistical consideration, it is obvious that the ion recombination is more likely to lead to triplet state population than to singlet. The indirect transition from the triplet state to the ground state (delayed fluorescence) is responsible for the slow component of the scintillation emission. The typical decay time for the fast component is in the range of ∼2-30 ns whereas the slow component is generally ∼ 100 ns.

In first approximation, the amount of scintillation light emitted by the LS is proportional to the energy loss of the particle, the energy loss for electrons being given by equation 2.21. However, for particles with high ionisation and excitation density, the amount of light emitted by the LS is reduced. Additionally, the energy loss (and so the ionisation and excitation density), increases with diminishing particle energy. This effect is called ionisation quenching and is with the Cerenkov effect the source of the LS non-linearity, a topic that will be discussed further in chapter 3 STEREO's energy non-linearity in Phase II.

The ionisation quenching affects primarily the intensity of the fast scintillation component but has little effect on the intensity of the slow component. Besides, the decay times of the components is unchanged by $\frac{dE}{dx}$. Hence the time profile of the light emission intensity (pulse shape) depends on the $\frac{dE}{dx}$. For given particle energy, the energy loss $\frac{dE}{dx}$ depends on the nature of the particle. This property is the basis of the pulse shape discrimination technique (PSD), and it allows to differentiate amongst different types of particles (mainly hadrons: proton, α and electrons: $e^{\pm}$,γ).

2.3.3 Pulse Shape Discrimination

As explained above, the intensity of scintillation light induced by an event as a function of time can be split into at least two components: a fast component resulting from the fluorescence and a slow component resulting from the delayed fluorescence; other components (as phosphorescence) are generally negligible.

The total intensity as a function of the time is described by:

$$I(t) = I_1 e^{-\frac{t}{\tau_2}} + I_2 e^{-\frac{t}{\tau_2}} \tag{2.26}$$

The amplitude of the component (I_1, I_2) are functions of the energy loss ($\frac{dE}{dx}$) of the particle, hence at given particle energy, the amplitude of the component is linked to the nature of the particle, as an example a neutron's relative amplitude of the slow component will be higher than a γ's (see Figure 2.26).

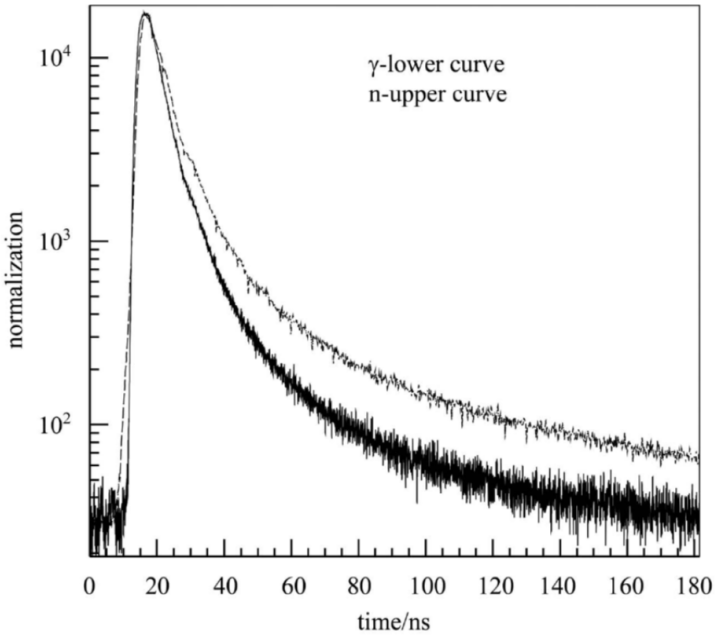

Figure 2.26: Time profile of light emission of a LAB-based (LAB + 3g·l^{-1} PPO + 15g·l^{-1} bis-MSB) in response to γ (lower curve) and neutron (upper curve) irradiation [LXC+11].

The interest of the Pulse Shape Discrimination lies in the ability to discriminate electronic recoils (associated with an IBD event) from proton recoils (produced during the thermalisation of fast neutrons associated with background events).

PSD definition in STEREO

In STEREO the observable used to encompass the information of the pulse shape is the ratio between the tail of the distribution of collected charge (Q_{tail}) and the full distribution of collected charge (Q_{tot}) in the cell with the most charge:

$$Q_{tail}/Q_{tot} = \frac{Q_{tail}^{cell}}{Q_{tot}^{cell}} = \frac{\sum_{i=0}^{N_{PMT}} Q_{tail}^{i}}{\sum_{i=0}^{N_{PMT}} Q_{tot}^{i}} \tag{2.27}$$

Where N_{PMT} is equal to four in all cells except in the long GC where there are 8 PMTs.

The beginning of the pulse t_{CFD} is determined with a constant fraction discrimination algorithm (CFD), t_{CFD} sets the beginning of the charge integration for Q_{tot}. The total charge integration is performed on N_{tot} samples of 4 ns. The tail charge integration corresponds to the N_{tail} last samples of N_{tot}. In other words, the tail charge integration is performed on N_{tail} samples and starts at t_{CFD} + N_{tot} - N_{tail}. These definitions are illustrated in Figure 2.27.

In normal operation conditions, in order to limit the acquisition dead time, the shape of the pulse is not saved to memory, only the Q_{tail} and Q_{tot} observables are.

Phase	N_{tot}	N_{tail}	$N_{samples}$	FOM
I	47	36	60	0.6
II	50	34	63	0.7

Table 2.6: Integration parameters value for phase I and II (a description of the different phases of data acquisition are presented in section 2.5), the FOM is given at 2.2 MeV

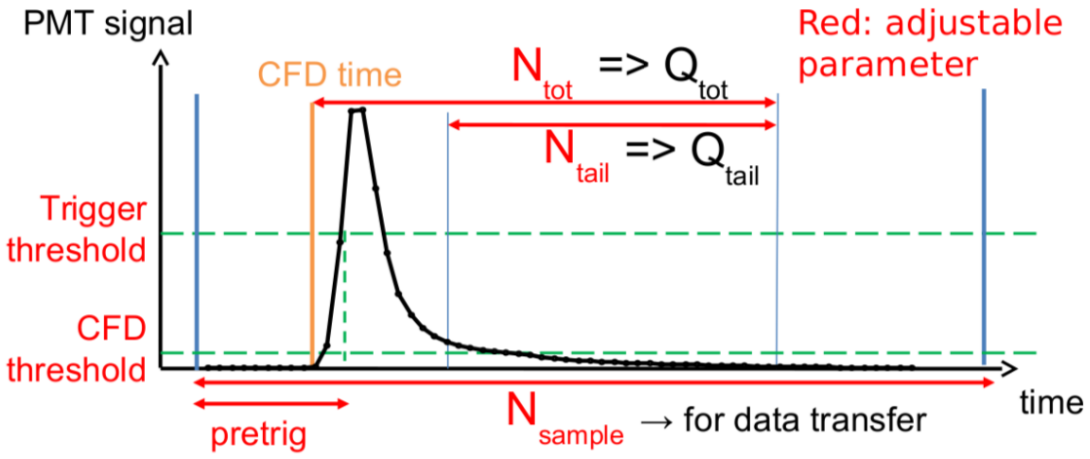

Figure 2.27: Treatment of the PMTs signal by the acquisition system. The t_{CFD} determination fixes the origin of the integration windows for the determination of the Q_{tot} and Q_{tail}.

Figure Of Merit

The parameters N_{tot} and N_{tail} were studied using an AmBe source.

The Figure of Merit describes the separation of the PSD variable (in STEREO Q_{tail}/Q_{tot}) distributions for different particles (see Figure 2.28). In STEREO, we want to discriminate electronic recoil from proton recoil, hence the FOM is given by:

$$FOM = \frac{1}{2\sqrt{2\ln 2}} \cdot \frac{|\mu_\gamma - \mu_p|}{\sigma_\gamma + \sigma_p} \tag{2.28}$$

For phase I, the chosen values of the integration parameters (see Table 2.6) lead to a Figure Of Merit (FOM) of the PSD of 0.6. For phase II, the values were re-optimised and a FOM of 0.7 was reached.

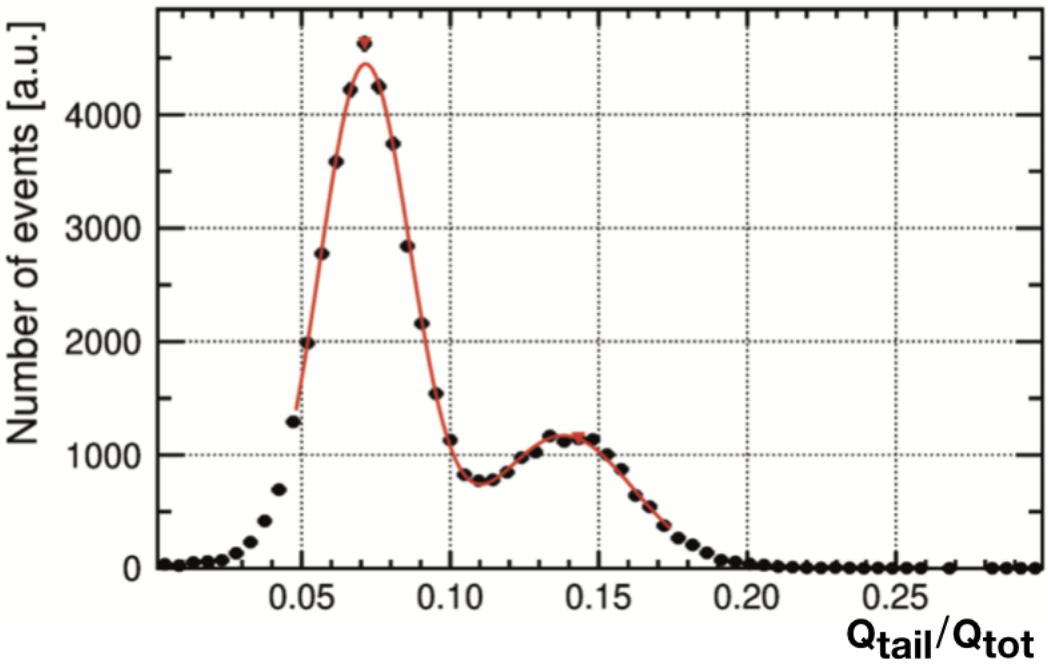

Figure 2.28: Distribution of Q_{tail}/Q_{tot} at 2.2 MeV for the AmBe source in Cell6. The distribution on the left corresponds to the electronic recoil, the distribution on the right to the proton. The FoM is 0.71

PSD stability

It has been shown that the PSD is dependent on the z-position of the event in the cell, with variations of the mean of the distribution of ∼10 % inside a cell. Additionally, the mean of the PSD distribution is highly correlated to the temperature inside the detector as can be seen in Figure 2.29. The mean of the PSD distribution can be plotted as a function of the temperature and can be adjusted with a first-degree polynomial. The PSD can then be corrected from the temperature effect. This temperature correlation seems to affect electronic recoil and proton recoil in the same manner. A detailed description of this correction is given in the thesis of L. Bernard [Ber19].

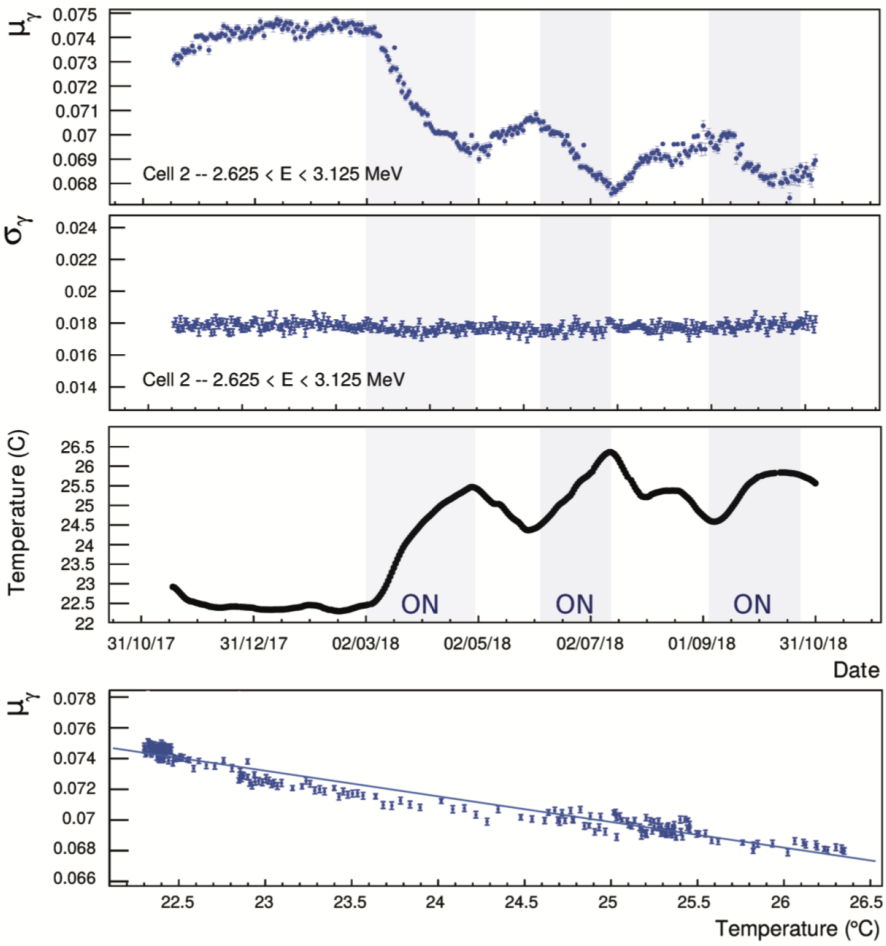

Figure 2.29: Time evolution of the Q_{tail}/Q_{tot} observable. The first top plot shows the time evolution of the mean of the PSD distribution of electronic recoils which is highly correlated to the temperature in the STEREO detector (3^{rd} plot). The second top plot shows the time evolution of the standard deviation of the PSD distribution of electronic recoils, that shows no sign of time evolution. The bottom plot shows the mean of the PSD distribution as a function of the temperature in the detector, the data are fitted with a linear polynomial. The slope of the polynomial gives the correction that needs to be applied on the PSD variable.

2.3.4 Calibration systems

STEREO is equipped with several calibration systems whose purpose is to characterise all relevant aspects of the detector response: energy scale, PMT gain, scintillation response, optical model, non-uniformities, PSD,... For this purpose, the STEREO detector uses a LED monitoring system and a radioactive source calibration system.

LED monitoring system

The main purpose of the LED system is the precise and periodic calibration of the PMTs gain via the single photo-electron method.

The LED system consists of five remote LED boxes located outside the shielding. The LED boxes are controlled by a LED board, in each box a total of 6 LEDs and LED drivers and a temperature sensor are present. Five out of six LEDs are blue ones and the remaining one is a UV LED. The UV light allows to excite directly the wavelength shifter.

The light emitted by the LEDs is carried from the LED boxes via optical fibres to diffusive Teflon balls placed in the detector liquid at 6 different locations in the GC and 3 different z-position in each of the 6 target cells. The muon veto is also calibrated by the LED system, the light of the LED boxes is injected at 12 different locations in the muon veto (see Figure 2.30).

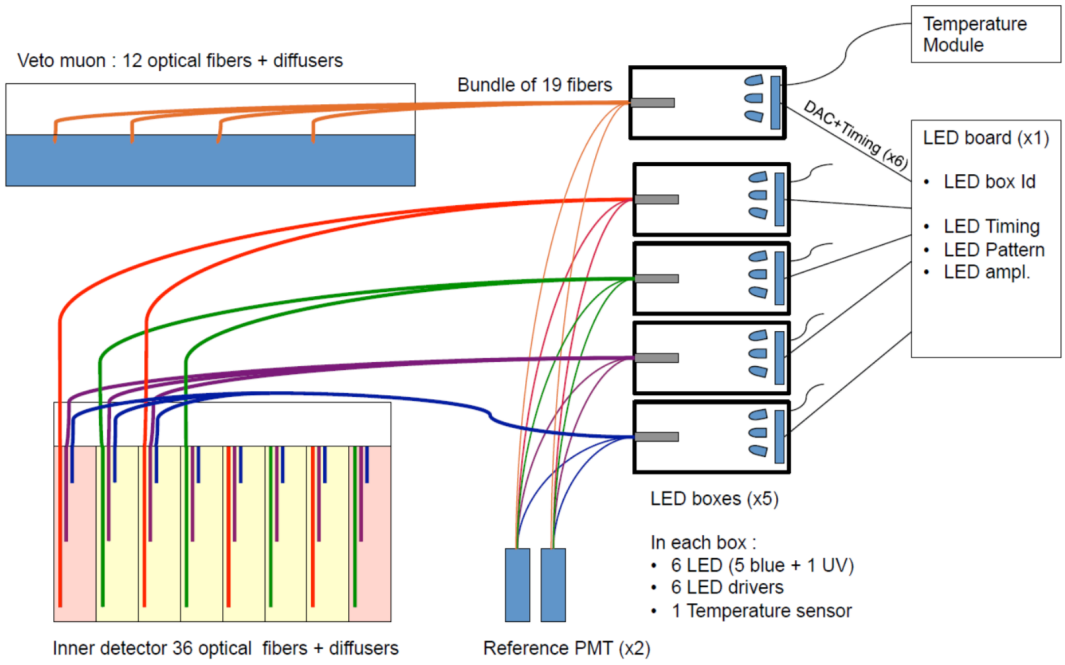

Figure 2.30: LED calibration system, One LED board controls five remote LED boxes composed of 6 LEDs injecting light at 3 different z-position in the target cell and 6 different locations in the GC, as well as 12 different locations in the muon veto.

The calibration of the PMTs gain occurs every two hours, via their single photo-electron response [BBG+94]. To do so, low-intensity light pulses are injected by the 465 nm LEDs. The distribution of the collected charge (see Figure 2.31) is then fitted with a model of the convolution of the PMT response and background processes. The model of the response function includes the photo-conversion and electron collection at the first dynode, the background processes include the pedestal and small amplitude artefacts inherent to the PMT operation (such as photoelectric effect happening on the first dynode, and other phenomena). The result of the fit is shown in Figure 2.31. The first peak corresponding to the pedestal (sometimes referred to as baseline) of the PMT, the second peak correspond to a single photo-electron, the third gaussian to 2 photo-electron, and so on. The accuracy on the single photo-electron peak position Q_{PE} is of the order of 0.5 %.

The amount of charge Q_{ADC} returned by the PMT depends on the amplification factor *A*. The gain calibration allows to determine the number of photo-electrons N_{PE} for a given amount of ADC charge. The proportionality factor between ADC charge and number of photo-electrons (in other words the gain of the PMT) G_{PMT} is given by the difference of the pedestal and the mean of the single photo-electron, in STEREO the pedestal position Q_{Bg} is compatible with 0:

$$G_{PMT} = Q_{PE} - Q_{Bg} = Q_{PE} \tag{2.29}$$

During the LED calibration the amplification factor is 20 times the amplification

Source	^{68}Ge	^{137}Cs	^{54}Mn	^{65}Zn	^{24}Na	AmBe
γ-ray energy [MeV]	0.511	0.662	0.835	1.11	1.37	2.22($H(n,\gamma)$)
	0.511	–	–	–	2.75	4.43
Initial activity [kBq]	90	37	90	3.3	5.9	250×10^3(^{241}Am)

Table 2.7: List of γ and neutron sources available to calibrate the STEREO detector.

factor for normal operating conditions, hence in normal operating conditions the number of photo-electrons is given by:

$$N_{PE} = \frac{20 \cdot (Q_{ADC}^{\text{norm. oper.}} - Q_{Bg})A}{(Q_{PE} - Q_{Bg}) \times A} = \frac{20 \cdot Q_{ADC}}{G_{PMT}} \tag{2.30}$$

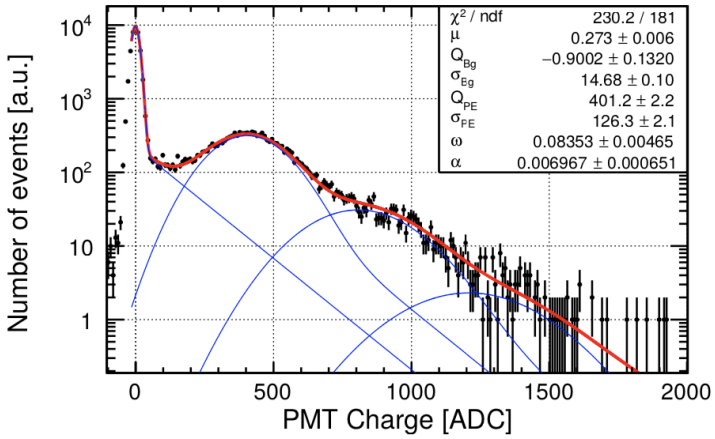

Figure 2.31: Distribution of collected charge for a PMT submitted to low-intensity light. The distribution is fitted with a model including the response function and the background processes, the first peak corresponding to the pedestal, the second peak to the response to a single photon, the third to two photons, and so on.

In addition to the PMT gain calibration, the LED system is used to monitor the light attenuation in the liquid scintillator and the linearity of the PMTs and electronic response.

Radioactive sources calibration systems

A first mean of calibration is the use of radioactive sources. The list of available sources is presented in Table 2.7. The radioactive sources can be deployed in or around the STEREO detector by three different means with a positioning uncertainty smaller than 1 cm.

Sources can be inserted at any z-position inside the TG cells through vertical calibration tubes at the exception of cell 3 where the tube is used solely to fill the detector with the LS. The calibration tubes are in the centre of the cells in the widthwise direction but not in the lengthwise direction. They are 6 cm away from the closest adjacent cell and 31 cm away from the other cell.

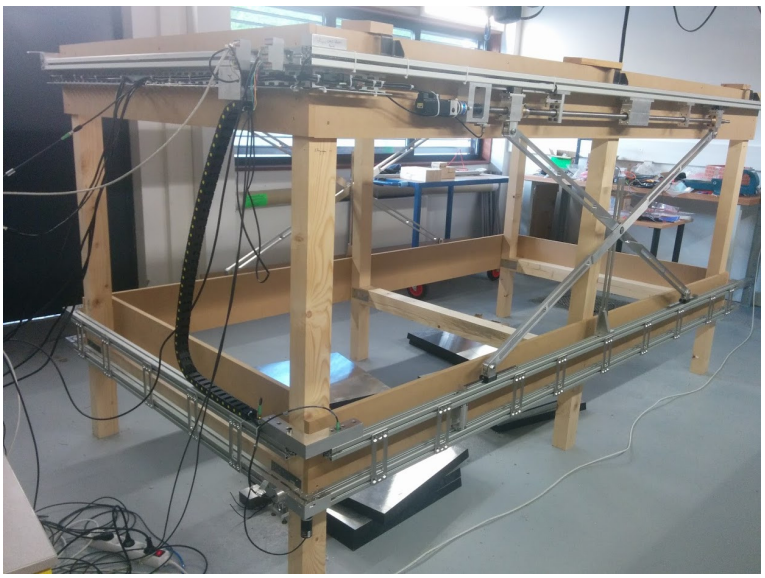

Figure 2.32: Pantograph calibration system on its test bench.

Secondly, a semi-automatised source positioning system called *pantograph* (see Figure 2.32), is used to deploy the sources outside the detector steel vessel at any position and around the detector at a height ranging between 15 cm and 90 cm above the cell floor. It is composed of two rails on top of each other, separated by a 10 cm gap, that surround the detector vessel and guide a wheeled, small (3.5 cm × 3.5 cm × 10 cm) aluminium source-holder (see Figure 2.33).

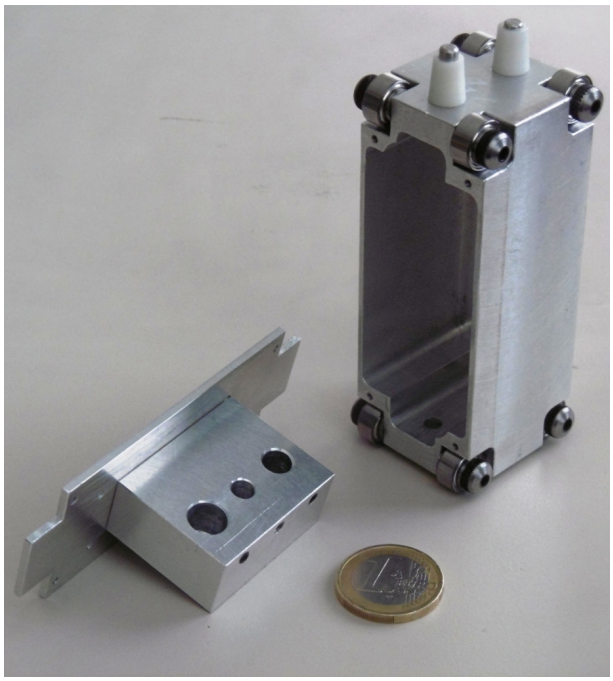

Figure 2.33: Aluminium source-holder

The source-holder is pulled around the guiding rails by a stepper motor[4] thanks to a vectran cable. The position of the source-holder is determined by a rotary external encoder[5], thus avoiding localisation errors if the traction cable were to slide over the

[4] A Phytron ZSS33 stepper motor driven by a Phytron MCC1 controller
[5] Industrial Sensor & Solutions (ISS), IS240 model

motor wheel. The rails are moved up and down thanks to one motor on each long side of the vessel working in a master-slave configuration[6]. All movements (around the vessel, and up/down) are bounded by inductive sensors that detect the presence of the movable parts and stop the motion. The sensors also serve the purpose of re-calibrating the position of the source-holder at each iteration.

Figure 2.34: Underneath semi-automatised calibration system. The model installed in the STEREO experiment was 5 m long

Additionally, a second semi-automatised system[7] (see Figure 2.34) allows to position a source underneath the detector vessel at any position in the lengthwise position along the central axis of the detector with a sub-mm precision. The ensemble of the calibration systems are illustrated in Figure 2.35.

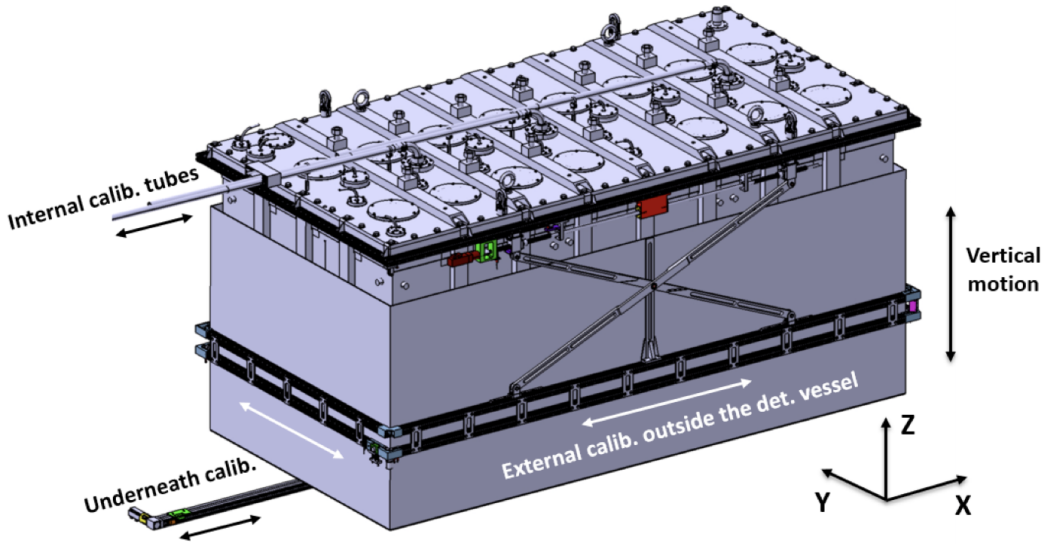

Figure 2.35: Calibration systems used to deploy radioactive sources in and around the STEREO detector vessel.

The use of radioactive γ sources allows to characterise the energy scale response for most of the energy range of interest. The use of the AmBe source which is a neutron emitter allows to characterise the detector response to fast neutrons (PSD) as well as thermalised neutrons (neutron capture by the Gd, which is the delayed signal of an IBD event).

[6]Two brushless Delta ECMA motors driven by two Delta ASDA 2 servo controllers
[7]HepcoMotion PDU2 belt driven linear actuator

2.3.5 Electronics and data acquisition

The STEREO experiment has a dedicated electronic system, described in [B+16].

Design of the electronic system

The electronic system consists in ten 8-channel front-end electronic boards (FE8), a trigger and readout board (TRB) a LED board that drives the LED boxes used in the PMT calibration (refer to section 2.3.4 LED monitoring system). The electronic boards are seated in a single crate using the MicroTCA standard.

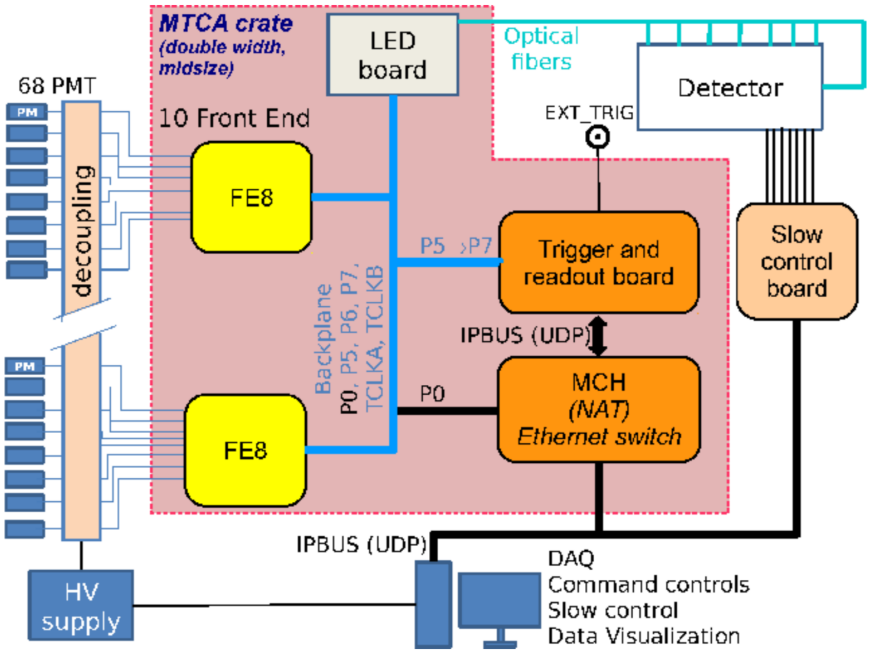

Figure 2.36: Overview of the STEREO DAQ electronic system. The MicroTCA crate is equipped with ten 8-channels front-end boards (FE8), one LED board, and one trigger and readout board (TRB) [B+16].

The FE8 boards have two possible amplifying regimes: ×1 for normal operation and ×20 for the single photo-electron calibration. The signal coming from the PMTs is sampled at a rate of 250 MHz (4 ns samples) by a 14-bit Analog to Digital Converter (ADC), and the samples are stored in a circular buffer.

The noise due to the electronics, including the PMT bases and the FE8 board, is low enough to ensure sensitivity to small PMT signals (10 p.e. in ×1 amplifying and 1 p.e. in ×20 amplifying regime). A Field Programmable Gate Array presenting a first-order high pass Infinite Impulse Response filter (IRR) processes the digitised signals to guarantee a null baseline and allows a faster baseline recovery after high energy events (cosmic muons).

A first-level trigger (T1) is implemented by the FE8 boards. An adjustable amplitude (1 sample) or charge (sum of several samples) threshold is applied on individual channels of the TG, GC and muon veto. The trigger can be applied on the sum of 4 or 8 channels to prevent triggering on noise. For the TG and GC clusters of the PMT channels in the same cell are made. In the muon veto, adjacent PMTs channels are clustered.

Electronic non-linearity

The linearity of the PMT+ electronic set has been tested using the LED calibration system.

Combining the light emitted by several LEDs and comparing it to the reference signal corresponding to a single LED allows testing the linearity for the whole energy range of interest. The result of this linearity test is presented in Figure 2.37 and shows that the non-linearity is less than ±1% for all energies and all channels.

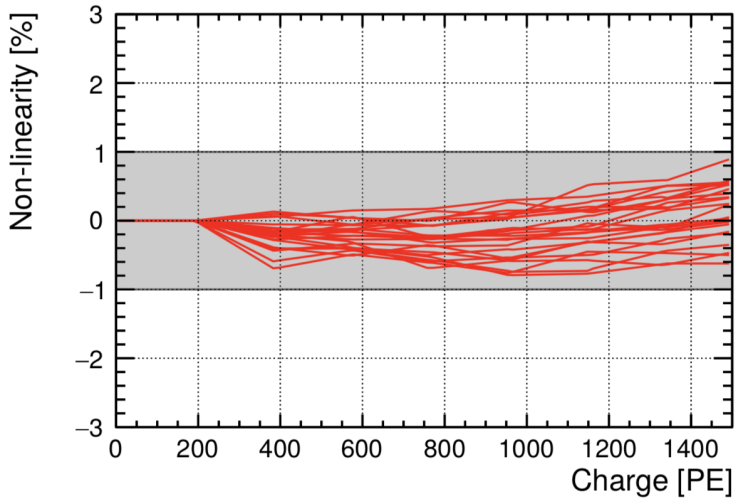

Figure 2.37: Result of the non-linearity test for the PMT+electronics set for a single PMT. The test is performed by combining the light of several LEDs. The non-linearities are contained in ±1 % for every channel.

Data acquisition

For neutrino runs the T1 is set on the charge summed over 10 samples, of a cluster of 4 channels, the T1 threshold was set to 1600 ADC corresponding to about 300 keV deposited in one cell. The trigger in the muon veto is set to 650 ADC corresponding to 32 p.e. in order to record muon events interacting solely in the muon veto. The muon veto signal is used offline to reject delayed background events.

If T1 criteria are met the acquisition starts. The beginning of the pulse on each individual channel is determined by a Constant Fraction Discriminator algorithm (CFD) and the total and tail charge (refer to section 2.3.3 PSD definition in STEREO) are computed. Under normal operating conditions, only the CFD time, the total and tail charge for all channels are provided to the TRB, this limits the dead time due to the data transfer. It is possible to transfer full samples for debugging or PSD study purposes. The allowed instantaneous trigger rate is 3.6 MHz.

A second level trigger (T2) can be set on processed data to reject uninteresting events (too low or too high energy). Events that pass T2 are sent to the computer disk memory. The time of the event is registered with a precision of 4 ns, to do this the combination of the computer clock and the 250 MHz TRB clock is used: the computer clock gives the time of the event with a precision of 1 s and the TRB clock gives the relative time between 2 consecutive events with a 4 ns precision.

Data are processed and transferred following the First In First Out strategy (FIFO). If the TRB FIFO queue is full, T1 events are rejected. The time during which the acquisition is stopped is measured, allowing for an offline correction of the dead-time. The acquisition rate varies from 1 to 2 kHz for neutrino runs in normal operating

conditions, the relative dead-time associated with this acquisition rate is less than 0.02 % and is negligible. During calibration with high activity sources, the dead-time can reach a non-negligible value.

A specific data acquisition software developed within the NOMAD framework of the ILL [MCE+12] was created for STEREO. This software manages the acquisition and allows to set all the acquisition parameters (T1, T2, number of samples, amplifying regime, and so on).

Detector monitoring

The monitoring data coming from a variety of sensors located inside and outside the detector and measuring temperature, pressure, liquid levels and magnetic fields as well as the PMTs voltages and currents, MicroTCA crate and acquisition rate are saved in the database every minute. All these data are available with a web software made inhouse by the STEREO collaboration.

2.4 Detector response

2.4.1 Light collection

As stated previously the different cells of the detector were designed to be mostly optically independent from each other. However, despite the efforts made, an optical cross-talk exists between the cells. Keeping track of the optical cross-talk is necessary to understand the detector response, especially the cross-talk between TG and GC since the GC LS has a different light yield than the TG LS (refer to 2.3.2 Liquid scintillator composition).

Optical cross-talk between cells

The light leaks coefficient from cell i to cell j (L_{ij}) describes the relative amount of light collected in cell j for an energy deposit in cell i:

$$L_{ij} = \frac{Q_j}{Q_i} \tag{2.31}$$

This definition is not exactly the same as the physical light cross-talk as Q_i and Q_j depend on the collection efficiency of their respective cell. Two complementary and independent methods have been developed to determine L_{ij}, the first one is based on the full energy deposit events of the ^{54}Mn source.[8]

This method presents the advantage of being sensitive to the dependence on the z-position of the cross-talk by varying the z-position of the ^{54}Mn source inside the calibration tube. Averaging the light cross-talk for the different z-position results in the mean light cross-talk.

The second method uses high energy events (10 to 40 MeV) coming from cosmic muons during neutrino runs. These events are more homogeneously distributed inside the cell volume and as no specific calibration is required since these events happen during normal neutrino runs, they allow to monitor the light cross-talk on an hourly basis.

[8] As a reminder this source emits a γ with energy 0.835 MeV.

Time evolution of the light cross-talk

During the first stage of the experiment (Phase I), unforeseen leakage of liquid scintillator inside the air gap of the reflective walls assembly resulted in a fast increase of the light cross-talk between the cells (see Figure 2.38a).

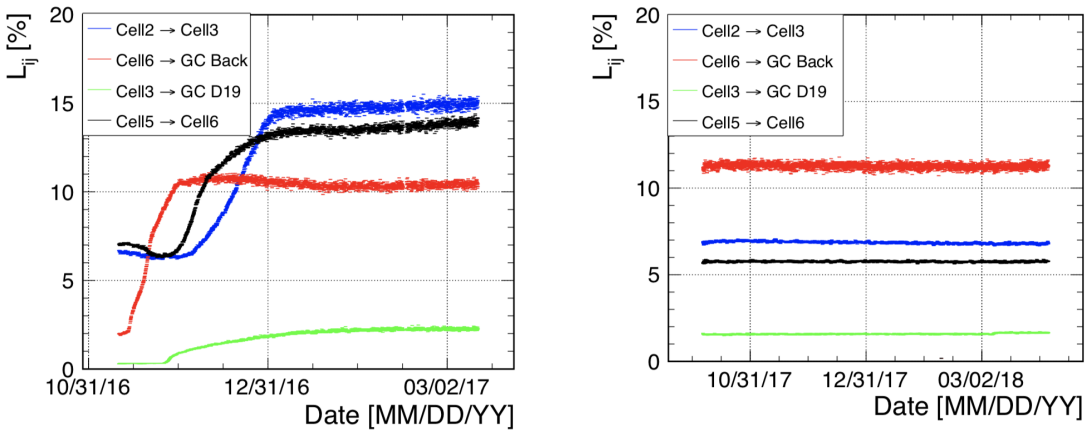

(a) (b)

Figure 2.38: Time evolution of selected light leaks coefficient for Phase I (2.38a) and Phase II (2.38b) obtained with the cosmic muon method. The repair work performed on the TG cells' separation walls between Phase I and II resulted in more stable and reduced cross-talk (except for Cell 6→GC Back).

During the long reactor shutdown, the detector was open and the reflective walls separating the TG cells were repaired. The subsequent light cross-talk were in general lower and more stable during the second phase of operation (Phase II) (see Figure 2.38b).

2.4.2 Energy reconstruction

Cell by cell calibration

The charge collected in a cell i in p.e., Q_i, is proportional to the deposited energy in the cell i E_i^{dep}. The coefficient of proportionality, called calibration coefficient C_i is given by:

$$C_i = \frac{Q_i}{E_i^{dep}} \tag{2.32}$$

The deposited energy E_i^{dep} is a few percent less than the nominal energy of the γ due to energy deposition in dead material such as the source holder, calibration tube, acrylic walls, and so on. In practice, the value of E_i^{dep} is obtained through MC simulation.

To compute the calibration coefficient the ^{54}Mn source is deployed in the calibration tube of the cell at 5 different z-position, for the GC the external calibration system is used. The Full Energy Deposit events (FED) in the cell are selected, because of the light cross-talk between the cells even if the γ deposits all its energy inside a single cell, some light will be seen by the other cells. So to select the FED events a cut on the charge seen by the other cell (first neighbours) must be applied, obviously, this cut depends on the value of the light leaks coefficient:

$$Q_j \leq Q_i \times c \times L_{ij} \tag{2.33}$$

where the parameter c set the tightness of the cut (a typical value of c is ∼2).

Very good agreement of the measured charge between MC and data is obtained for the FED selection (see Figure 2.39).

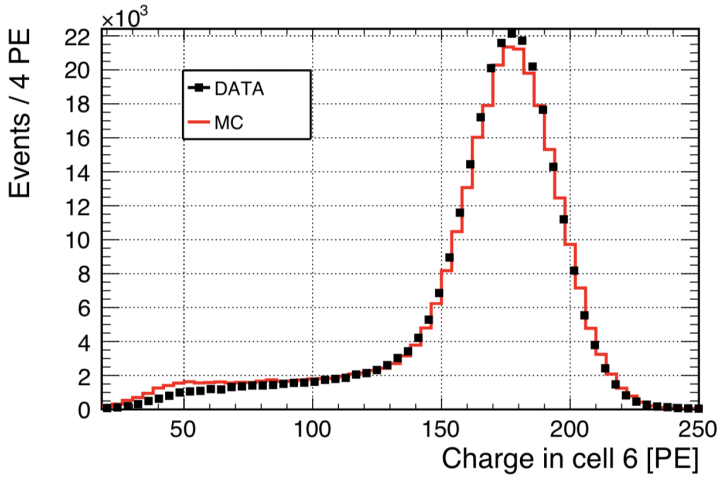

Figure 2.39: Data (black) and Monte Carlo simulation (red) of the charge spectra for the ^{54}Mn source deployed in cell 6 at mid-height (z=45cm).

Dependence of the Q_i with the z-position is observed, the variation of the Q_i value inside a cell is around 4 %. However this variation is well described by the MC simulation, the agreement between MC and data is at the sub-percent level for all z-position except for the very top position z=80 cm, where the agreement is at the percent level (see Figure 2.40).

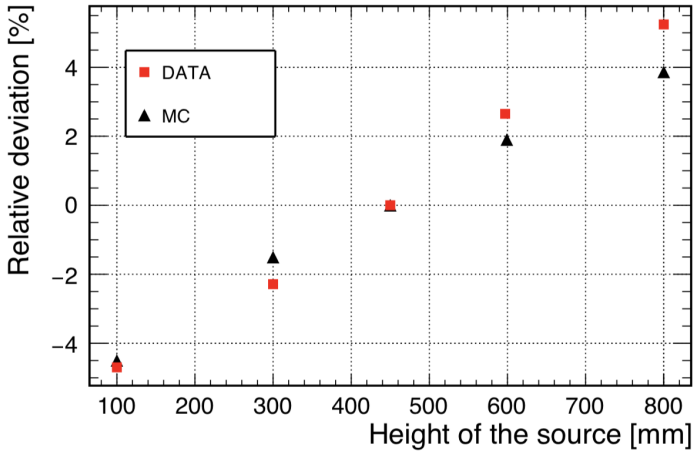

Figure 2.40: Variation of the charge peak value at different z-position relative to the charge peak value at z=45 cm in TG cell 6.

For the long GC cells, a reduced vertical non-uniformity is observed with a variation of the Q_i of ±2 %, however, the variation along the long axis is more significant with a 6 to 8 % variation between the centre and the edges.

Energy reconstruction of energy deposit across several cells

A high accuracy description of the light cross-talk between cells and moreover their variation with time would be difficult and unpractical to implement in the MC simula-

tion, since it would require as many simulation as there are variations of the cross-talk. That is why a procedure to reconstruct the energy corrected at first order for all light collection effects has been implemented.

For a single cell energy deposition the charge response of the 4 PMTs of the cell reads:

$$Q_i = E_i C_i \tag{2.34}$$

With C_i, the calibration coefficient defined in the previous section. The light cross-talk implies that the neighbouring cells give a charge response :

$$Q_j = L_{ij} Q_i \tag{2.35}$$

This yields to

$$Q_j = E_i C_i L_{ij} \tag{2.36}$$

The detector is divided into 10 optical volumes (GC Front, TG Cell 1 to 6, GC back, GC D19 and GC IN20). Energy deposit distributed among the 10 optical volumes leads to a charge in cell j given by:

$$Q_j = \sum_{i=0}^{9} E_i C_i L_{ij} \tag{2.37}$$

By definition of the light leaks coefficient L_{ii}=1. Posing the matrix notation M_{ij}=$C_i L_{ij}$ we get:

$$\begin{pmatrix} Q_0 \\ Q_1 \\ \vdots \\ Q_9 \end{pmatrix} = M \begin{pmatrix} E_0 \\ E_1 \\ \vdots \\ E_9 \end{pmatrix} \tag{2.38}$$

Finally inverting the M matrix leads to the vector of deposited energy reconstructed from the detected charge:

$$\begin{pmatrix} E_0 \\ E_1 \\ \vdots \\ E_9 \end{pmatrix} = M^{-1} \begin{pmatrix} Q_0 \\ Q_1 \\ \vdots \\ Q_9 \end{pmatrix} \tag{2.39}$$

The calibration and light leaks coefficient are fixed in the simulation and an iterative procedure is performed for the data to make the reconstructed energy of the data match the reconstructed energy of the simulation.

First, the reference energy is constructed: the true deposited energy distribution given by the MC is convolved with the detector resolution and the most probable value of the convolution is taken as reference energy: E^{ref}.

The reconstructed energy for cell i E_i^{rec} obtained using the coefficient computed as presented in the previous section is compared to E_i^{ref} the difference is driven by the calibration coefficient C_i which is corrected. The vector of reconstructed energy is computed now including $E_{i\neq j}^{rec}$ the difference now is driven by the light leaks coefficient L_{ij} which is corrected.

These two steps are iteratively repeated until convergence is obtained. In practice, only a few iterations are necessary to obtain convergence and the correction to the initial coefficients is only a few percents (see Figure 2.41).

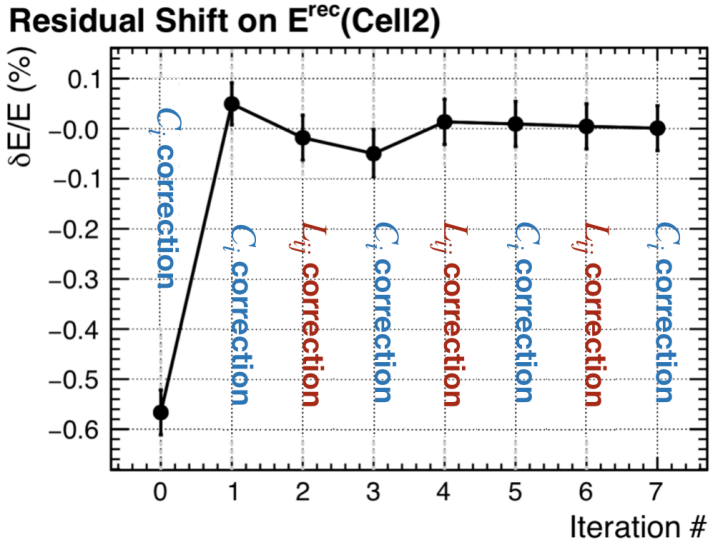

Figure 2.41: Iterative correction on the C_i and L_{ij} coefficients. The first two iterations are dedicated to the C_i correction. Starting from the third iteration, corrections on L_{ij} and C_i are applied alternately. The convergence of the reconstructed energy toward the reference energy is obtained after a few iterations.

This iterative procedure allows for an agreement of reconstructed energy between data and simulation at 0.2 %, this very good agreement can be seen in Figure 2.42.

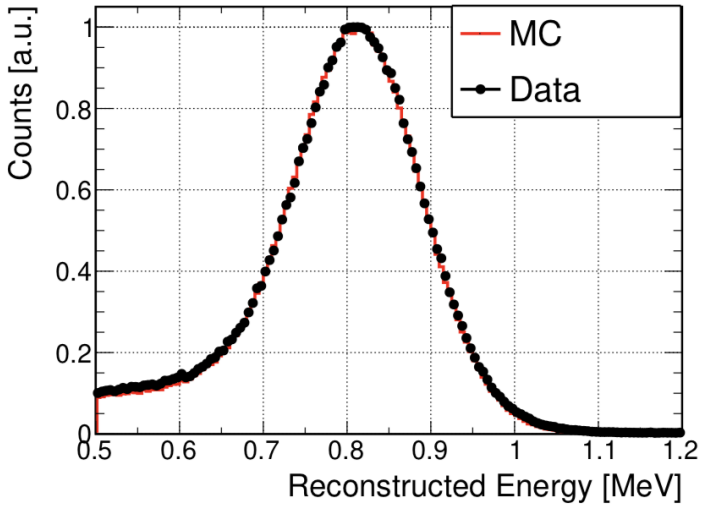

Figure 2.42: Comparison of the reconstructed energy for data (black) and simulation (red) after convergence of the iterative procedure for a ^{54}Mn source deployed in the centre of cell 6.

The detailed explanation of the energy reconstruction strategy is exhaustively documented in the PhD thesis of A. Blanchet [Bla19].

2.4.3 Monte Carlo simulation

A complete simulation of the detector was created using the Geant4 (v. 10) framework [A+03]. The simulation includes a complete description of the detector, the shielding, the various calibration systems and the muon veto. The main mechanical

parts, the liquid scintillators and the photomultipliers are implemented, special care was given to the treatment of the scintillator properties and the reflective walls.

Physical processes are simulated using the native Geant4 libraries (GLG4sim), from the primary particle interactions to the scintillation light collected by the PMTs, excepted the treatment of the Gd cascade which is performed with another code: FIFRELIN.

An approximate optical model was incorporated to take into account the loss of reflectivity in the walls in Phase I. The PMTs signal, as well as the electronic response, is simulated too. The output of the simulation code shares the same format as the real data hence can be analysed with the same codes as the real data.

Gd cascade simulation

As stated in the previous section, special treatment of the Gd deexcitation cascade is done using the FIFRELIN code developed and maintained by the CEA.

The Gd nuclear levels scheme is not experimentally well known up to the energies of the excited states relevant to the thermal neutron capture and so theoretical models are needed to describe the deexcitation. The FIFRELIN code samplea the nuclear levels from one of the most updated experimental database: Reference Input Parameter Library (RIPL-3) [C$^+$09].

The deexcitation is then simulated within a Monte Carlo Hauser-Feschbach framework based on Becvar's algorithm [Be8], finally, an extension to the γ, neutron emission is performed using Régnier's method [RLS15]. This approach describes more accurately the energy state and multiplicity of the deexcitation products.

In the STEREO simulation of neutron capture on Gd a high-statistic sample of the deexcitation products generated by FIFRELIN is used on an event-by-event basis to simulate the γ cascade. More details on the treatment of the Gd cascade using FIFRELIN can be found in [A$^+$20c].

The improvement in the agreement between data and simulation compared to the native Geant4 library (GLG4sim) and the FIFRELIN code can be seen in Figure 2.43. This improved agreement, allowed to reduce the systematic uncertainty assigned to the neutron capture efficiency.

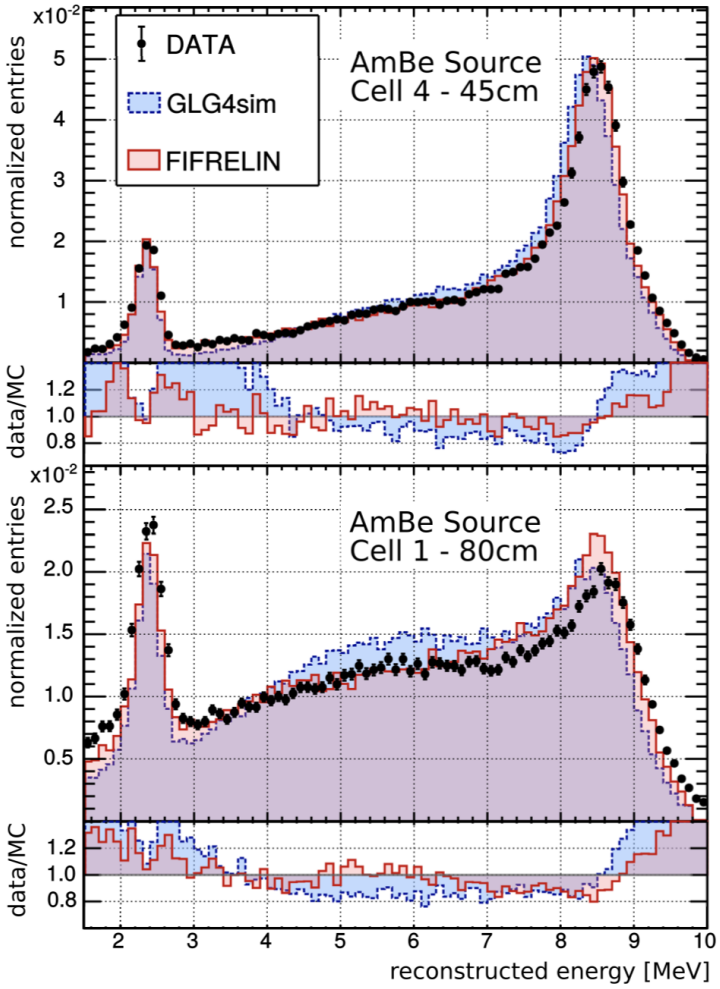

Figure 2.43: Reconstructed energy distribution of neutron captures coming from an AmBe source deployed in cell 4(1) at z=45(80) cm upper (lower) plot. Black points are real calibration data, FIFRELIN (GLG4sim) simulation is in red (blue).

2.4.4 Neutrino signal extraction

IBD candidate are selected by searching space-time correlated pairs of events, corresponding to the prompt and delayed signal.

Selection cuts

The first step to discriminate background from neutrino events is to apply a set of selection cuts on the IBD pairs candidate. The cuts have been chosen to maximise signal acceptance and background rejection hence minimising the uncertainty on the IBD rate. Besides cuts have been set so that their acceptance is stable under small cut variation. The acceptance of each cut a_{cut} is computed thanks to MC simulation.

$$a_{cut} = \frac{N_{\text{all cuts}}}{N_{\text{all cuts w/o studied cut}}} \tag{2.40}$$

The list of all selection cuts is given in Table 2.8.

The vertex cell is defined as the cell exhibiting the largest reconstructed prompt energy.

Table 2.8: Selection cuts for IBD candidates and the associated acceptance a_{cut}.

Type	#	Condition	a_{cut}%
Energy	1	1.625 MeV $<E_{prompt}^{detector}<$8.125 MeV	89.2
	2	4.5 MeV $< E_{delayed}^{detector}<$10.0 MeV	75.9
Coincidence	3	2 μs$<\Delta t_{prompt-delayed}<$70 μs	95.5
	4	$\Delta x_{prompt-delayed}<$600 mm	99.3
Topology	5	$E_{prompt}^{cell} <$ 1.0 MeV, neighbour cell	98.6
	6	$E_{prompt}^{cell} <$ 0.4 MeV, other cell	99.6
	7	$E_{delayed}^{Target}>$1.0 MeV	97.9
Rejection of muon-induced background	8	$\Delta t_{muon-prompt}^{veto} >100\mu s$	-
	9	$\Delta t_{muon-prompt}^{detector} >200\mu s$	-
	10	$\Delta t_{before\ prompt} >100\mu s$ and $\Delta t_{after\ delayed}>100\ \mu s$ for all events with $E_{event}^{detector}>$1.5 MeV	-
	11	$\frac{Q_{PMT\ max,\ prompt}}{Q_{cell,\ prompt}}<0.5$	99.3
Absolute $\overline{\nu_e}$ selection efficiency: 62% to 68.4%, depending on the cell			

Cut #1 selects prompt signals that have the reconstructed energy expected for a reactor antineutrino.

Cut #2 selects delayed signal from neutron captures on Gd, the total energy of the γ cascade is $\sim$8 MeV, the lower bound is set at 4.5 MeV to include as much as possible the events where part of the γ of the cascade escape detection, while at the same time avoiding the 2.2 MeV γ of the neutron capture on H.

Cut #3 exploits the time correlation between the prompt and delayed signal, the lifetime of the neutron (meaning the thermalisation time and capture time put together) is $\sim$16 μs in the STEREO TG LS. The lower bound set at 2 μs help to reject decays of stopping muons (the lifetime of the muon being 2.2 μs) which can mimic IBD events if the energy due to the muon track in the detector falls in the prompt energy window and the subsequent Michel-electron has energy falling in the delayed energy window. The upper bound is set to 70 μs corresponding to the point where the contribution of the accidental coincidences becomes dominant.

Cut #4 exploits the spatial correlation between the prompt and delayed signal since both prompt and delayed originate from the same IBD interaction vertex, which is not the case for accidental coincidences.

Cut #5 and #6 limit to only one 511 keV annihilation γ to be detected in a neighbouring cell, indeed since annihilation γ are emitted back to back there is a minute probability for both of them to be detected in the same neighbour cell.

Cut #7 requires that at least 1 MeV of energy must be deposited in the TG rejecting high energy events coming from the sides into the GC.

Cut #8 and #9 impose a dead time following the detection of a muon candidate in the muon-veto or the detector. A muon candidate in the detector is an event with total energy above 20 MeV.

Cut #10 helps to reject correlated background coming from multiple neutrons by imposing no events with more than 1.5 MeV to happen before or after an IBD candidate.

Finally cut #11 helps to reject muons stopping at the very top of the detector. Indeed such muons deposit only a small amount of energy in the detector and so are

not rejected by cut #9 but leaving only a small track in the detector they will produce light close to one of the PMTs, hence they produce an asymmetric light distribution.

The selection process of related signal and delayed triggers is often referred to as "pair search".

Neutrino signal extraction from PSD On-Off subtraction

The rate of IBD candidates is extracted from the PSD distributions in the reactor-on and reactor-off samples. The PSD reactor-on(off) distribution is split by cell l and energy bin i, denoted $\mathrm{ON}_{l,i}$ ($\mathrm{OFF}_{l,i}$). The reactor-off PSD distribution of correlated pairs (due to cosmic-induced correlated background) is modelled by $\mathrm{m}_{l,i}^{corr,OFF}$, whereas the reactor-on(off) accidental distribution is denoted as $\mathrm{ON}_{l,i}^{acc}$ ($\mathrm{OFF}_{l,i}^{acc}$) and is modelled by $\mathrm{m}_{l,i}^{acc,ON}$ ($\mathrm{m}_{l,i}^{acc,OFF}$).

The PSD distribution of accidental pairs is obtained by the time-shifted windows method. The PSD distribution of IBD events is modelled by a scaled gaussian distribution $\mathrm{G}^{\nu}(\mathrm{A}_{l,i},\mu_{l,i},\sigma_{l,i}^2)$, where $\mathrm{A}_{l,i}$, is the scaling factor measuring the IBD rate, $\mu_{l,i}$, is the mean of the distribution and $\sigma_{l,i}^2$ the standard deviation.

For each PSD bin p it yields:

$$OFF_{l,i,p}^{acc} \sim m_{l,i,p}^{acc,OFF} \tag{2.41}$$

$$OFF_{l,i,p} \sim m_{l,i,p}^{corr,OFF} + f^{acc,OFF} \times m_{l,i,p}^{acc,OFF} \tag{2.42}$$

$$ON_{l,i,p}^{acc} \sim m_{l,i,p}^{acc,ON} \tag{2.43}$$

$$ON_{l,i,p} \sim a_{l,i} \times m_{l,i,p}^{corr,OFF} + f^{acc,ON} \times m_{l,i,p}^{acc,ON} + G_p^{\nu}(A_{l,i},\mu_{l,i},\sigma_{l,i}^2) \tag{2.44}$$

where $a_{l,i}$ is a global scaling factor correcting for different mean atmospheric pressures between the ON and OFF samples, water channel level and possibly imperfections in the dead-time correction. $a_{l,i}$, $\mathrm{m}_{l,i,p}^{corr,OFF}$, $\mathrm{m}_{l,i,p}^{acc,ON}$, $\mathrm{m}_{l,i,p}^{acc,OFF}$, $\mathrm{A}_{l,i}$, $\mu_{l,i}$ and $\sigma_{l,i}^2$ are free parameters fitted simultaneously on the measured spectra. $\mathrm{f}^{acc,ON}$ and $\mathrm{f}^{acc,OFF}$ are correction factors accounting for the number of time-shifted windows used in the accidentals as well as the suppression time of accidentals in the coincidence window. Indeed, accidentals can be suppressed by correlated events in the coincidence window but not in the off-time windows.

This method does not assume any specific analytical shape of the models, except the gaussian modelling the IBD events. An illustration of the neutrino signal extraction for cell 2 and the energy bin [3.625,4.125] MeV is given in Figure 2.44.

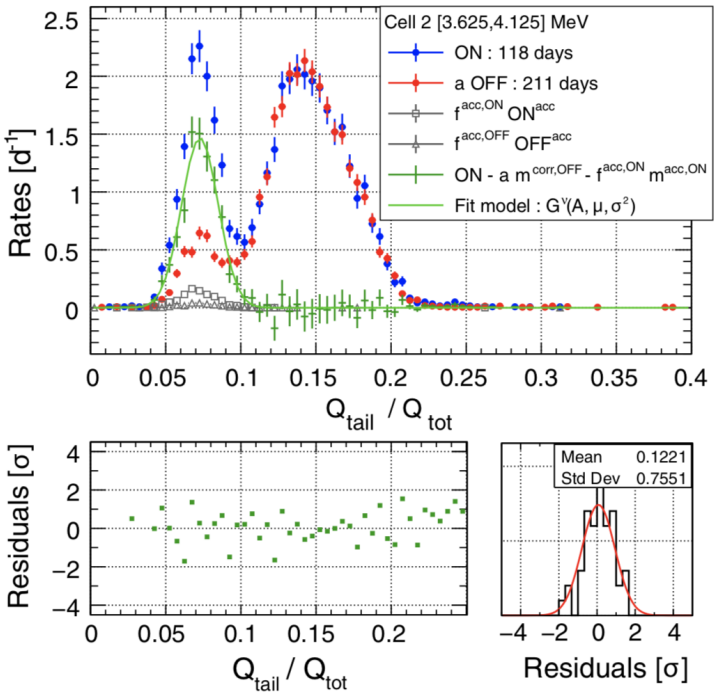

Figure 2.44: Top plot illustrates the IBD rate extraction for one energy bin of cell 2. It shows the PSD distribution of prompt candidates and accidentals measured during reactor-on and reactor-off periods. The correlated OFF distribution is scaled by a factor $a_{l,i}$ and the accidentals distributions are also scaled by their respective factor $f^{acc,ON/OFF}$. The green points show the extracted neutrino sample, it is fitted by a gaussian distribution to determine the IBD rate. The bottom plots show the residuals of the gaussian fit

2.5 Status of the experiment

The STEREO experiment was in operation from November 2016 to December 2020. The total data sample amounts to 366 days of 58 MW_{th} equivalent reactor-on days and 760 days of reactor-off data.

The data collection is split into 3 distinct samples labelled Phase I, Phase II and Phase III. Phase I accounts for 70 days of 58 MW_{th} equivalent reactor-on days and 28 reactor-off days. Phase II for 137 reactor-on and 377 reactor-off days and Phase III 174 reactor-on and 355 reactor-off days (see Figure 2.45).

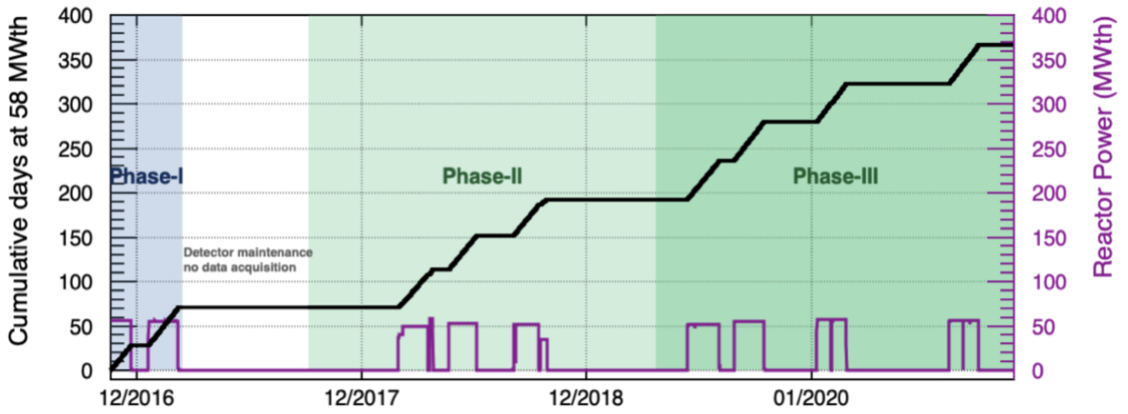

Figure 2.45: Cumulative days of data acquisition of the STEREO experiment, the total dataset amounts to 366 days of 58 MW_{th}-equivalent reactor-on days.

Phase I took place from November 2016 to March 2017. During Phase I several defects occurred, making the exploitation of acquired data more difficult, firstly the oil ensuring the optical coupling between the acrylic buffer and the PMTs in cell 4 and GC front spilt in the LS because of cracks in the acrylic. The loss of optical coupling, as well as the dilution of the LS, had significantly degraded the light collection in these cells. In addition, the air gap of the reflective walls was slowly filled with LS degrading the reflectivity of the walls and increasing the light cross-talk between cells making the energy reconstruction more challenging.

Following Phase I a long reactor maintenance shutdown and in particular the refurbishment of the H7 beam tube plug necessitated to remove the STEREO detector from the PN3 casemate, this time was used to open and repair the detector.

Phase II started in October 2017, the long reactor shutdown carried on until February 2018, this was an opportunity to acquire more than 100 days of reactor-off data and ensuring that the detector run in smooth and stable conditions.

Phase III started in April 2019 after the installation of additional shielding (water wall) in front of the STEREO detector. This additional shielding takes the form of high-density polyethylene tanks filled with water, it is originally a commercial modular rainwater storage system of the french company BZH2O branded *MURDEAU* (see Figure 2.46).

The water wall is composed of 4 modules and 2 half modules each module is 1.3 m high, 1.2 m wide and 41 cm thick with 8 mm walls containing 500 L of water for an empty weight of 45 kg. Modules are arranged in 2 columns for a total width of 2.43 m and 2 full rows plus a half row composed of 2 modules shopped in half in order to completely shield the STEREO detector, they are anchored to the floor with specific docks. The available space around STEREO is limited in height by the presence of the water channel at 3.55 m high, hence a complete third row (3.9 m) would have been too high. The goal of the water wall is to mitigate possible neutrons coming from the reactor.

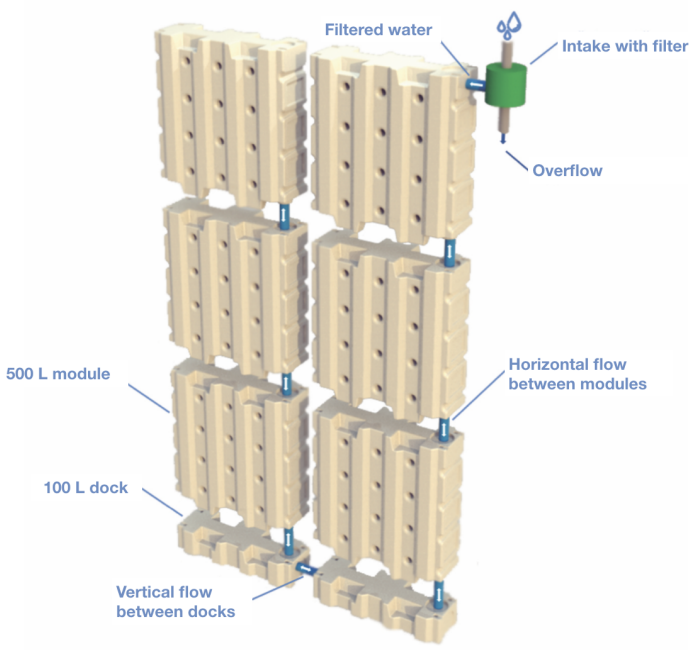

Figure 2.46: Design of the *MURDEAU* product, used in STEREO as an additional neutron shielding for Phase III of data acquisition.

About 95 % of the data taking time is devoted to reactor ON and OFF acquisition, the remaining 5 % corresponding to calibrations. The dead-time is negligible ($\leq$0.02 %).

Data taking stopped in November 2020, and the detector was dismounted between November 2020 and January 2021.

Scientific results

The STEREO experiment has already published results on both the reactor antineutrino rate and shape anomalies using roughly half of the total recorded data sample [A$^+$20d, A$^+$21b, A$^+$21b]. They provide the current most accurate measurement of the reactor antineutrino rate from a HEU reactor, a new reference measurement of the antineutrino reactor spectrum deconvolved from detector effects, and significant constraints on the allowed parameter space of the sterile neutrino hypothesis.

The reactor antineutrino spectrum shape and the unfolding procedure to deconvolve the measured spectrum from detector effects is presented in details in [A$^+$21b]. The reactor spectrum and its comparison to the Huber-Mueller model is given in Figure 2.47. The measurement confirms the existence of an excess of events around $\sim$5 MeV, the inclusion of the Phase III data will double the dataset statistics, hopefully allowing to determine if ^{235}U is the sole contributor to the excess.

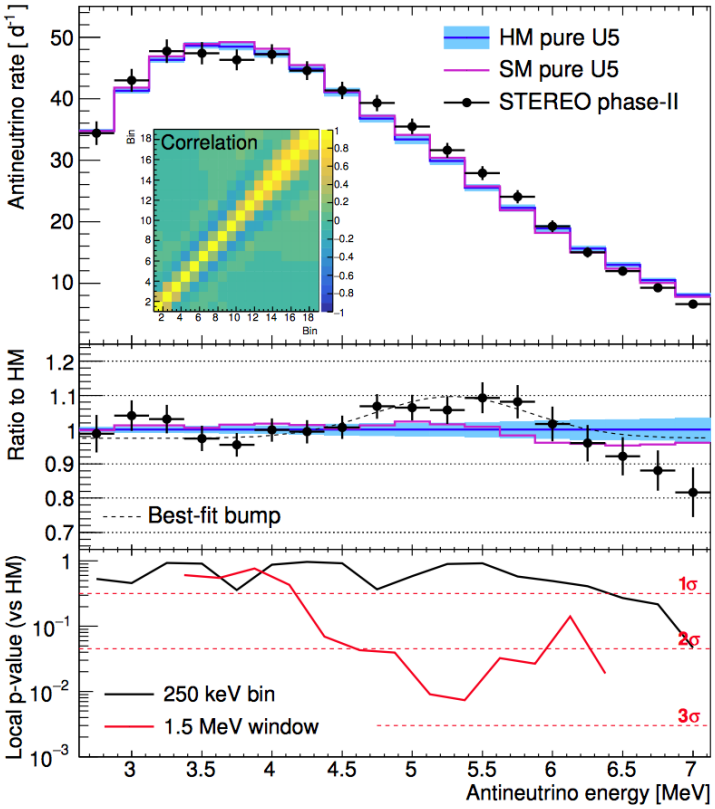

Figure 2.47: Unfolded ^{235}U antineutrino spectrum together with Huber-Mueller (HM) and Summation (SM) models normalised to the area of the spectrum (Top) the correlation matrix is also presented. The ratio between the unfolded spectrum and the HM model present an excess of events at ∼5 MeV that is best fitted with a gaussian of amplitude 12.1±3.4% and a mean 5.29±0.18 MeV (Middle). The local p-value that quantifies the disagreement between the unfolded spectrum and the HM model is given for each 250 keV bin and for a sliding window of 6 consecutive bins (1.5 MeV).

The measurement of the absolute rate is exhaustively described in [A$^+$20b], STEREO reports a rate deficit of 5.2±0.8(stat.) ±2.3(syst.) ±2.3(model)% compared to the Huber-Mueller model, consistent with the world average. This result is presented in Figure 2.48.

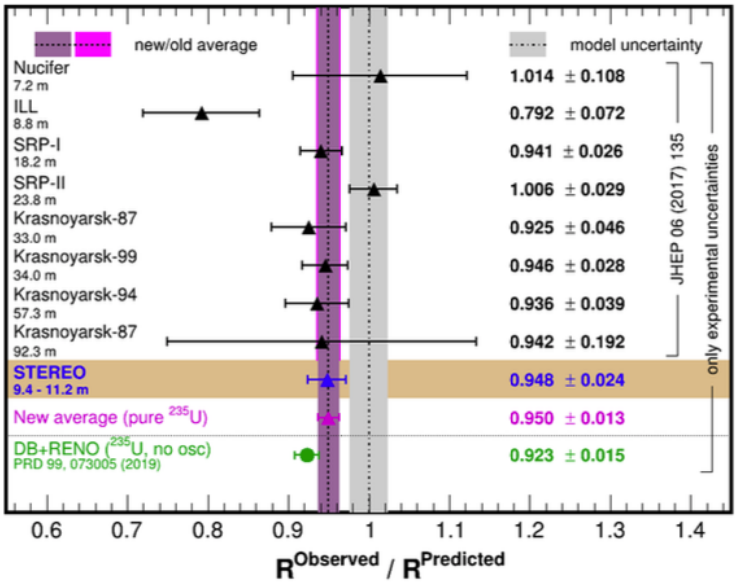

Figure 2.48: Ratio of measured antineutrino yields over the Huber-Mueller prediction for a collection of experiments at various baseline below 100 m. The experimental uncertainties are given by the error bars for each point, whereas the common model uncertainty of 2.4% is given by the gray band around unity.

The result of the sterile neutrino oscillation search obtained by STEREO on the Phase I and Phase II data are presented in thorough details in [A+20d]. Figure 2.49 presents the 95% confidence level (C.L.) exclusion contour obtained for Phase I and II data together with the expected sensitivity. Most of the RAA allowed parameter space is rejected at 95% C.L. and in particular the RAA best fit point is rejected at more than 99.9% C.L.

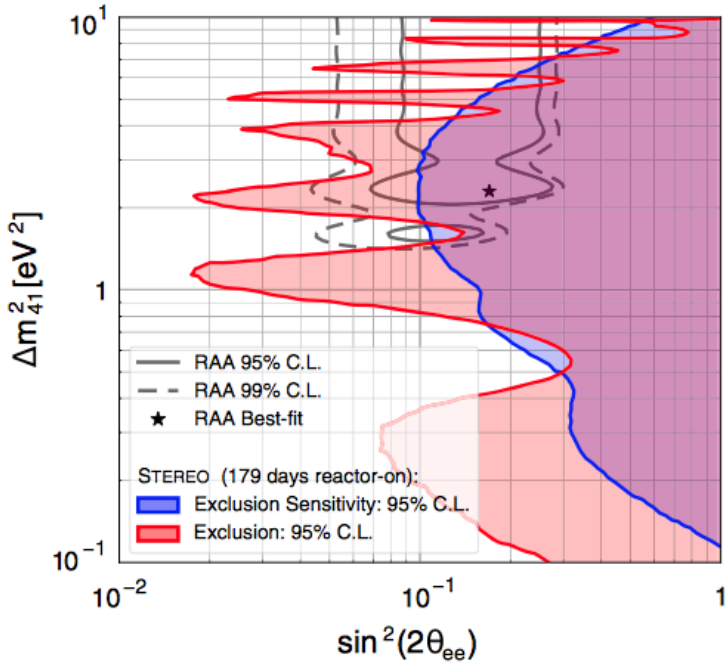

Figure 2.49: The area excluded at more than 95% C.L. of the oscillation parameter space is represented by the light red shaded area enclosed in the red exclusion contour obtained with Phase I + II data. The blue contour is the expected sensitivity. The allowed region of the RAA are represented by the grey contours for different confidence level. The best fit point of the RAA is given by the star.

It must be noted that the Phase III of data is currently being analysed; preliminary results were unveiled by the author of this Thesis on behalf of the STEREO collaboration at the 17th International conference on Topics in Astroparticle and Underground Physics (TAUP 2021) [LAB21].

The insight provided by the STEREO experiment tends to reject the sterile neutrino hypothesis to explain the observed deficit compared to the prediction. In addition, the spectral distortion observed at around 5 MeV points toward a mismodelisation of some effects in the prediction.

In the following, I describe my contributions to the analysis of the STEREO data, namely: the study of the non-linearity of the detector response in energy, and the search for a neutrino oscillation signal and its statistical interpretation.

Bibliography

[A+03] S. Agostinelli et al. GEANT4–a simulation toolkit. *Nucl. Instrum. Meth. A*, 506:250–303, 2003.

[A+17] Feng Peng An et al. Improved Measurement of the Reactor Antineutrino Flux and Spectrum at Daya Bay. *Chin. Phys. C*, 41(1):013002, 2017.

[A+20d] H. Almazán et al. Improved sterile neutrino constraints from the STEREO experiment with 179 days of reactor-on data. *Phys. Rev. D*, 102(5):052002, 2020.

[ABB+03] M. Apollonio, A. Baldini, C. Bemporad, E. Caffau, F. Cei, Y. Déclais, H. de Kerret, B. Dieterle, A. Etenko, L. Foresti, and et al. Search for neutrino oscillations on a long base-line at the chooz nuclear power station. *The European Physical Journal C*, 27(3):331–374, Apr 2003.

[A+20c] Helena Almazán Molina et al. Improved STEREO simulation with a new gamma ray spectrum of excited gadolinium isotopes using FIFRELIN. *Eur. Phys. J. A*, 55(10):183, 2019.

[B+16] O. Bourrion et al. Trigger and readout electronics for the STEREO experiment. *JINST*, 11(02):C02078, 2016.

[BBG+94] E. H. Bellamy, G. Bellettini, F. Gervelli, M. Incagli, D. Lucchesi, C. Pagliarone, F. Zetti, Yu. Budagov, I. Chirikov-Zorin, and S. Tokar. Absolute calibration and monitoring of a spectrometric channel using a photomultiplier. *Nucl. Instrum. Meth. A*, 339:468–476, 1994.

[Ber19] Laura Bernard. *Recherche d'un neutrino stérile avec l'expérience STEREO : détermination des spectres neutrinos et caractérisation du bruit de fond*. PhD thesis, LPSC, Grenoble, 2019.

[Be8] F. Bečvář. Simulation of cascades in complex nuclei with emphasis on assessment of uncertainties of cascade-related quantities. *Nuclear Instruments and Methods in Physics Research Section A: Accelerators, Spectrometers, Detectors and Associated Equipment*, 417(2):434–449, 1998.

[BGL+19] C. Buck, B. Gramlich, M. Lindner, C. Roca, and S. Schoppmann. Production and properties of the liquid scintillators used in the stereo reactor neutrino experiment. *Journal of Instrumentation*, 14(01):P01027–P01027, Jan 2019.

[Bir64] John B. Birks. *The Theory and practice of scintillation counting*. 1964.

[Bla19] Adrien Blanchet. *Recherche du neutrino stérile auprès du réacteur de l'ILL: expérience Stereo*. PhD thesis, IRFU, Saclay, 2019.

[C+09] R. Capote et al. RIPL – Reference Input Parameter Library for Calculation of Nuclear Reactions and Nuclear Data Evaluations. *Nucl. Data Sheets*, 110:3107–3214, 2009.

[CHO+11] M.B. Chadwick, M. Herman, P. Obložinský, M.E. Dunn, Y. Danon, A.C. Kahler, D.L. Smith, B. Pritychenko, G. Arbanas, R. Arcilla, R. Brewer, D.A. Brown, R. Capote, A.D. Carlson, Y.S. Cho, H. Derrien, K. Guber, G.M.

Hale, S. Hoblit, S. Holloway, T.D. Johnson, T. Kawano, B.C. Kiedrowski, H. Kim, S. Kunieda, N.M. Larson, L. Leal, J.P. Lestone, R.C. Little, E.A. McCutchan, R.E. MacFarlane, M. MacInnes, C.M. Mattoon, R.D. McKnight, S.F. Mughabghab, G.P.A. Nobre, G. Palmiotti, A. Palumbo, M.T. Pigni, V.G. Pronyaev, R.O. Sayer, A.A. Sonzogni, N.C. Summers, P. Talou, I.J. Thompson, A. Trkov, R.L. Vogt, S.C. van der Marck, A. Wallner, M.C. White, D. Wiarda, and P.G. Young. Endf/b-vii.1 nuclear data for science and technology: Cross sections, covariances, fission product yields and decay data. *Nuclear Data Sheets*, 112(12):2887–2996, 2011. Special Issue on ENDF/B-VII.1 Library.

[dK+20b] H. de Kerret et al. Double Chooz θ_{13} measurement via total neutron capture detection. *Nature Phys.*, 16(5):558–564, 2020.

[Fil17] Charles-Elie Fillon. Détermination de la puissance du réacteur de l'ILL pour la prédiction du flux de neutrinos. Internship report, CEA Paris Saclay, July 2017. Rapport de stage.

[HGH+14] N. Haag, A. Gütlein, M. Hofmann, L. Oberauer, W. Potzel, K. Schreckenbach, and F. M. Wagner. Experimental determination of the antineutrino spectrum of the fission products of ^{238}U. *Phys. Rev. Lett.*, 112:122501, Mar 2014.

[Hor74] D. L. Horrocks. *Applications of Liquid Scintillation Counting*. 1974.

[HSG+89] A.A. Hahn, K. Schreckenbach, W. Gelletly, F. von Feilitzsch, G. Colvin, and B. Krusche. Antineutrino spectra from 241pu and 239pu thermal neutron fission products. *Physics Letters B*, 218(3):365–368, 1989.

[Hub11] Patrick Huber. On the determination of anti-neutrino spectra from nuclear reactors. *Phys. Rev. C*, 84:024617, 2011. [Erratum: Phys.Rev.C 85, 029901 (2012)].

[JAC06] Bernard JACROT. *Neutrons for science*. ILL, 2006.

[JBB+12] M. Jandel, T. A. Bredeweg, E. M. Bond, M. B. Chadwick, A. Couture, J. M. O'Donnell, M. Fowler, R. C. Haight, T. Kawano, R. Reifarth, R. S. Rundberg, J. L. Ullmann, D. J. Vieira, J. M. Wouters, J. B. Wilhelmy, C. Y. Wu, and J. A. Becker. New precision measurements of the $^{235}U(n,\gamma)$ cross section. *Phys. Rev. Lett.*, 109:202506, Nov 2012.

[Kan17] Felix Kandzia. *Search for a sterile neutrino with the STEREO experiment : shielding optimisation and energy calibration*. PhD thesis, U. Grenoble Alpes, 2017.

[LAB21] L.-R. LABIT. The STEREO search for a sterile neutrino at the ILL reactor with full data sample. https://indico.ific.uv.es/event/6178/contributions/15595/, 2021. [Online; accessed 12-Feb-2022].

[LXC+11] Xiao-Bo Li, Hua-Lin Xiao, Jun Cao, Jin Li, Xi-Chao Ruan, and Yue-Kun Heng. Timing properties and pulse shape discrimination of LAB-based liquid scintillator. *Chinese Physics C*, 35(11):1026–1032, nov 2011.

[Man16] Luis Manzanillas. *Development of the source calibration system of the STEREO experiment and search for sterile neutrinos at the ILL*. PhD thesis, U. Grenoble Alpes, 8 2016.

[MBH+05] Dario Motta, Christian Buck, Francis Xavier Hartmann, Thierry Lasserre, Stefan Schonert, and Ute Schwan. Prototype scintillator cell for an in-based solar neutrino detector. *Nucl. Instrum. Meth. A*, 547:368–388, 2005.

[MCE+12] P. Mutti, F. Cecillon, A. Elaazzouzi, Y. Le Goc, J. Locatelli, H. Ortiz, and J. Ratel. Nomad - more than a simple sequencer. Contributions to the Proceedings of ICALEPCS 2011, page 1423, France, 2012. INSTRUMENTATION RELATED TO NUCLEAR SCIENCE AND TECHNOLOGY.

[MLF+11] Th. A. Mueller, D. Lhuillier, M. Fallot, A. Letourneau, S. Cormon, M. Fechner, L. Giot, T. Lasserre, J. Martino, G. Mention, A. Porta, and F. Yermia. Improved predictions of reactor antineutrino spectra. *Phys. Rev. C*, 83:054615, May 2011.

[P+16] C. Patrignani et al. Review of Particle Physics. *Chin. Phys. C*, 40(10):100001, 2016.

[Peq15] Maxime Pequignot. *Les expériences Nucifer et Stéréo : étude des antineutrinos de réacteurs à courte distance*. PhD thesis, Saclay, 2015.

[Pri] T. D. Pritychenko, B. Johnson. Thermal Neutron Capture γ's (CapGam). *www.nndc.bnl.gov/capgam/*.

[RAP17] Rapport de sureté. inb no 67, reacteur a haut flux. *ILL*, 2017.

[RLS15] David Regnier, Olivier Litaize, and Olivier Serot. An improved numerical method to compute neutron/gamma deexcitation cascades starting from a high spin state. *Computer Physics Communications*, 201, 12 2015.

[SCGV85] K. Schreckenbach, G. Colvin, W. Gelletly, and F. Von Feilitzsch. Determination of the antineutrino spectrum from 235u thermal neutron fission products up to 9.5 mev. *Physics Letters B*, 160(4):325–330, 1985.

[VB99] P. Vogel and J. F. Beacom. Angular distribution of neutron inverse beta decay, $\overline{\nu}_e + \vec{p}\ e^+ + n$. *Phys. Rev. D*, 60:053003, Jul 1999.

[vHS82] F. von Feilitzsch, A.A. Hahn, and K. Schreckenbach. Experimental beta-spectra from 239pu and 235u thermal neutron fission products and their correlated antineutrino spectra. *Physics Letters B*, 118(1):162–166, 1982.

[Zso16] Stephane Zsoldos. *Recherche d'un neutrino stérile avec l'expérience STEREO*. PhD thesis, LPSC, Grenoble, 2016.

CHAPTER 3

STEREO'S ENERGY NON-LINEARITY IN PHASE II

CONTENTS

3.1 Introduction

The non-linearity of the liquid scintillator is the main source of non-linearity in the energy reconstruction. Another source of non-linearity is the one associated with the PMTs signal and electronic readout system, however, the effect of the PMTs and electronics has been characterised with the LED calibration system and is contained in a ± 1 % band in the energy range of interest (see section 2.3.5 Electronic non-linearity).

Two main processes contribute to the liquid scintillator non-linearity: ionisation quenching and Cerenkov light emission.

3.2 Liquid scintillator non-linearities

Ionisation quenching

The ionisation quenching is the fact that particles with higher energy loss per unit length $\frac{dE}{dx}$ will produce less scintillation light for the same deposited energy than particles with lower energy loss.

A low $\frac{dE}{dx}$ implies that the excitation and ionisation of the molecules is spaced on several molecular distances apart along the particle track. In these conditions, the scintillation light output L_{scint} is proportional to the particle deposited energy dE, leading in the differential form to:

$$\frac{dL_{scint}}{dx} = S \cdot \frac{dE}{dx} \tag{3.1}$$

where S is the scintillation efficiency in photon·MeV^{-1}. The increase in $\frac{dE}{dx}$ results in a high density of ionised molecules, suppressing the excitation toward singlet states process (see section 2.3.2 Scintillation mechanism) and potentially saturating locally the liquid scintillator hence quenching the scintillation light output.

Birks developed a semi-empirical model to describe this behaviour, known as Birks' law [Bir64]. In these conditions, the effective scintillation efficiency is reduced below S and the light response L_{scint} is not proportional to the deposited energy dE:

$$\frac{dL_{scint}}{dx} = S \cdot \frac{\frac{dE}{dx}}{1 + K_B \times \frac{dE}{dx}} \tag{3.2}$$

Additionally, ionisation can lead to permanent molecular damage introducing quenching centres causing a gradual decrease of the scintillation efficiency.

Cerenkov effect

When a relativistic charged particle travels through a medium, it can transfer its energy to the molecules of the medium by electronically polarising these molecules. These molecules return to their normal state emitting a photon. This mechanism of light emission of light is called Cerenkov effect. For the Cerenkov effect to take place the particle's velocity must be higher than a threshold that depends on the speed of light in the medium:

$$v > \frac{c}{n} \tag{3.3}$$

where c is the speed of light in the vaccuum and n is the refractive index of the medium.

This velocity threshold leads to a threshold in the particle kinetic energy:

$$E_{th} = m_0 \left(\frac{1}{\sqrt{1 - \frac{1}{n^2}}} - 1 \right) \tag{3.4}$$

where m_0 is the rest mass of the particle. In the case of STEREO, the liquid scintillator has a refractive index n=1.5 which leads to a kinetic energy threshold for electrons of $E^e_{th} = 0.17$ MeV.

Cerenkov radiation is directional by nature, the half-angle of the emission cone ϕ is given by:

$$\cos\phi = \frac{c}{v \cdot n} \tag{3.5}$$

The number of Cerenkov photons per unit of track length and unit of Cerenkov photons energy for a particle with electric charge z is given by the Frank-Tamm formula [P+16]:

$$\frac{d^2N}{dEdx} = \frac{\alpha z^2}{\hbar c} \cdot \sin^2\phi \tag{3.6}$$

$$\approx 370 \cdot \sin^2\phi(E)\ [\mathrm{eV}^{-1} \cdot \mathrm{cm}^{-1}] \tag{3.7}$$

In the energy range of interest for STEREO (roughly from 1 to 8 MeV), electrons are relativistic with $\beta = \frac{v}{c}$ ranging from ∼0.941 to ∼0.998. Hence, the Cerenkov angle in the liquid scintillator of STEREO is comprised between 45° and 48°.

Detectable photons in STEREO have wavelengths between ∼ 200 and 600 nm or equivalently energy between 2.0 and 6.2 eV. Cerenkov photons are mostly in the UV range with wavelength between ∼200 and ∼400 nm. This leads to a number of detectable Cerenkov photons by unit of track length: $N_c = 860$ photons·cm^{-1}. Knowing that the track of an electron with energy of a few MeV is a few mm, this number has to be compared with the liquid scintillator light yield of ∼6500 photons·MeV^{-1} (see section 2.3.2 Liquid scintillator properties). Moreover, we did not consider here the efficiency of the wavelength shifter, it is likely that not all Cerenkov photons in the UV range are converted into visible light detectable by the PMTs.

To conclude, the contribution of the Cerenkov radiation to the overall light yield is of order of a few percent.

3.3 Phase I study of STEREO's energy non-linearity

STEREO's Geant4 simulation includes an implementation of Birks law in order to model the ionisation quenching effect as well as a Cerenkov light emission module. Instead of separately tuning these two contributions in MC, the approach of the STEREO collaboration is to use an effective value of the k_B parameter to model the Data-MC discrepancies in the non-linearity, regardless of their origin.

A first study of STEREO's non-linearity in the energy reconstruction was performed with Phase I data. It will be presented in this section, whereas my personal work, with Phase II data, will be described in the next section.

3.3.1 Tuning of the k_B parameter

Tuning procedure

The tuning of the k_B parameter was a collaborative effort, three different analyses were performed by three institutes with independent approaches.

- The LAPP analysis was based on the data-Monte Carlo comparison of the charge distribution collected in cell 5 for several radioactive sources deployed in cell 6 at mid-height (except for the AmBe point for which the source was deployed in cell 4 and the charge distribution was looked at in cell 5).
- The CEA analysis was based on the reconstructed energy distribution of sources deployed in cell 6.
- The MPIK analysis was based on the charge distribution in cell 6 from sources deployed in cell 6 as well (except for the AmBe whose charge distribution was studied in cell 5).

From these independent studies, a data-Monte Carlo ratio is obtained:

$$R(E, k_B, S) = \frac{\xi_{Data}(E)}{\xi_{MC}(E, k_B, S)} \tag{3.8}$$

where E is the energy of the radioactive source's gamma line, k_B the Birks constant, S the light yield of the liquid scintillator (see equation 3.2), ξ represent either the charge (MPIK, LAPP analyses) or the reconstructed energy (CEA analysis).

To be independent of the light yield, the deviation from the unity of the ratio to the anchor point energy of the data-to-MC ratio is computed:

$$r_N(E, k_B) = \frac{R(E, k_B, S)}{R(E^{\text{anchor}}, k_B, S)} - 1 \tag{3.9}$$

By definition, r_N is null for the anchor energy[1] and for the optimal Birks constant k_B^0:

$$r_N(E^{\text{anchor}}, k_B) = 0 \tag{3.10}$$
$$r_N(E, k_B^0) = 0 \tag{3.11}$$

Performing a Taylor expansion at the first order leads to:

$$r_N(E, k_B) = \underbrace{r_N(E, k_B^0)}_{=0} + \left.\frac{\partial r_N(E, k_B)}{\partial k_B}\right|_{k_B = k_B^0} \times (k_B - k_B^0) + \dots \tag{3.12}$$

$$r_N(E, k_B) = r'_N(E) \times (k_B - k_B^0) \tag{3.13}$$

The following model for $r'_N(E)$ has been chosen:

$$r'_N = \left(\frac{p_0 + p_1 \cdot E}{p_2 + p_3 \cdot E}\right) \tag{3.14}$$

Several functions for $r'_N(E)$ have been tested, all functions lead to compatible values for the optimal k_B^0.

Finally, a global free offset parameter p_4 is added to the model to account for the systematic uncertainty on the anchor point:

$$r_N(E, k_B) = \left(\frac{p_0 + p_1 \cdot E}{p_2 + p_3 \cdot E}\right) \times (k_B - k_B^0) + p_4 \tag{3.15}$$

[1] The anchor point is the nominal energy of the ^{54}Mn gamma line, 0.835 MeV

This model is fitted to several energy points and k_B values obtained by the three independent analyses presented in figures 3.1 (MPIK), 3.2 (LAPP), 3.3 (CEA).

The final k_B value is obtained by taking the mean of the optimal k_B^0 of the three analyses:

$$k_B = 9.63 \pm 0.69 \times 10^{-2}\ \text{mm} \cdot \text{MeV}^{-1}$$

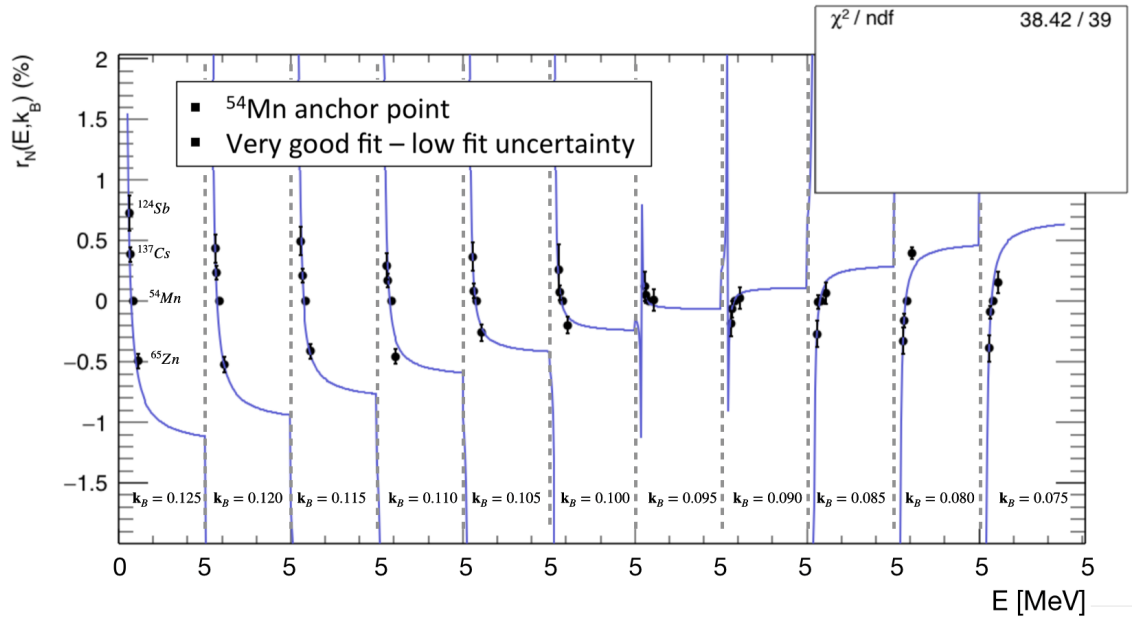

Figure 3.1: MPIK Phase I non-linearity study

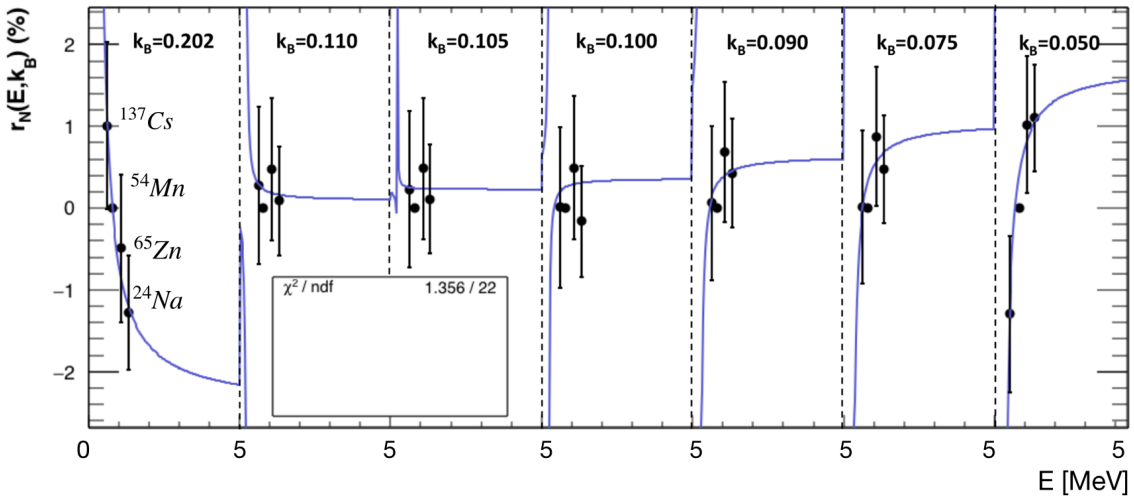

Figure 3.2: LAPP Phase I non-linearity study

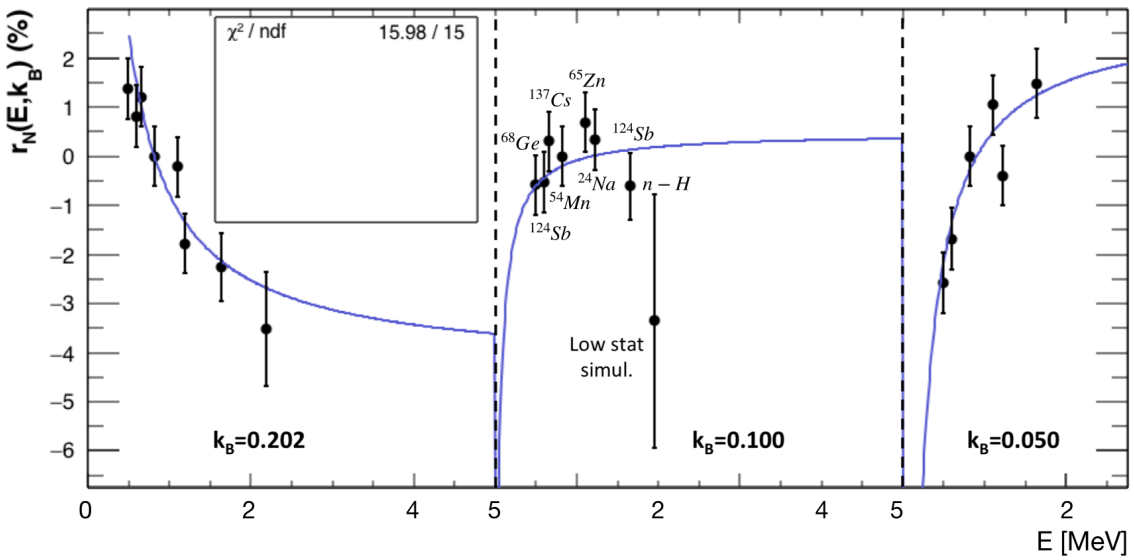

Figure 3.3: CEA Phase I non-linearity study

Result of the tuning procedure

The MPIK and LAPP analyses were combined to obtain the non-linearity curve and data-to-Monte Carlo ratio with the tuned k_B parameter (see Figure 3.4). The agreement between data and Monte Carlo is at the percent level.

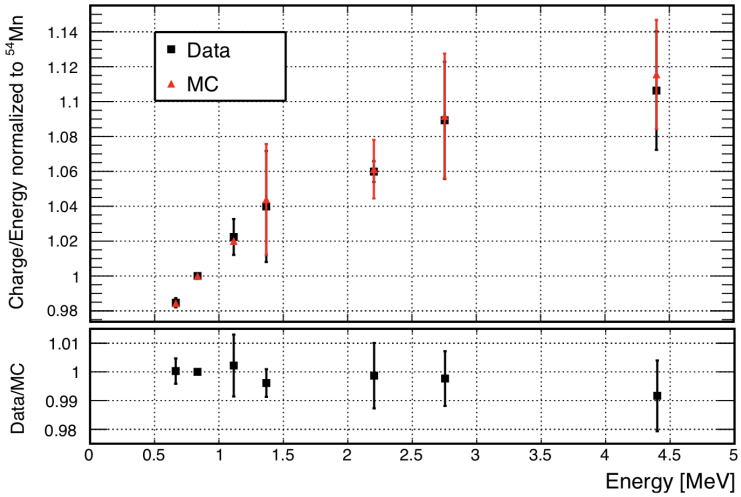

Figure 3.4: Non-linearity in the TG LS using different γ sources deployed at mid-height during Phase I. Data and MC points are normalized to the ^{54}Mn anchor point and k_B = 0.0963 mm·MeV^{-1} is used in the simulation.

The result presented in this section were obtained during Phase I of data taking.

My personal contribution to the study of the non-linearity was to refine the LAPP analysis in order to check whether the k_B value needed to be tuned again for Phase II data and to improve on the precision of Phase I's study if possible. This will be presented in the next sections.

3.4 LAPP's non-linearity study for Phase II

For this analysis radioactive sources were deployed inside the detector during three calibration campaigns (26th and 27th April 2018; 29th, 30th and 31st October 2018; 5th and 6th August 2019); the radioactive sources used in the analysis are listed in Table 3.1.

Source	^{137}Cs	^{54}Mn	^{65}Zn	^{42}K	^{24}Na	AmBe
γ energy [MeV]	0.662	0.835	1.11	1.52	1.37	4.43
	–	–	–	–	2.75	–

Table 3.1: List of γ energies used in the non-linearity study.

Limitations of the Phase I study

The raw charge distribution of the data taken for each source were compared to the MC simulations, after Full Energy Deposit cuts only. Although this method is appropriate for the γ sources, in the case of the AmBe source, the γ line peak is highly polluted by the n-Gd peak due to the neutron emitted simultaneously with the γ. The AmBe

4.44 MeV γ line being the only one at high energy it is of capital importance to get a clean measurement of this point.

The other goal was to reduce the systematic uncertainties affecting the pure γ lines measurements, that account for most of the errors of the points in Figure 3.4.

Approach

The procedure developed at LAPP consists in deploying a radioactive source at mid-height inside the calibration tube of a target cell and select events that deposit all their energy in a neighbouring cell. This specific selection has two goals: the first one is to better discriminate between the two γ lines of the ^{24}Na source. Indeed, it is less likely that two γ with different energy deposit their energy in the same neighbour cell than it is for the deployment cell (see Figure 3.5); the second goal is to mitigate proton recoils coming from the thermalisation of the neutron emitted by the AmBe source. Indeed, when the 4.44 MeV γ line is looked for in the cell where the source is located, there is a high chance for the fast neutron emitted in coincidence with the γ to have its first collision within the source cell. This first collision will result most often in the neutron transferring roughly half of its energy to a proton which in turn will depose it in the cell's liquid scintillator. Being in a high $\frac{dE}{dx}$ regime, the scintillation light from the proton recoil will likely be highly quenched. By how much, however, is not known for STEREO's liquid.

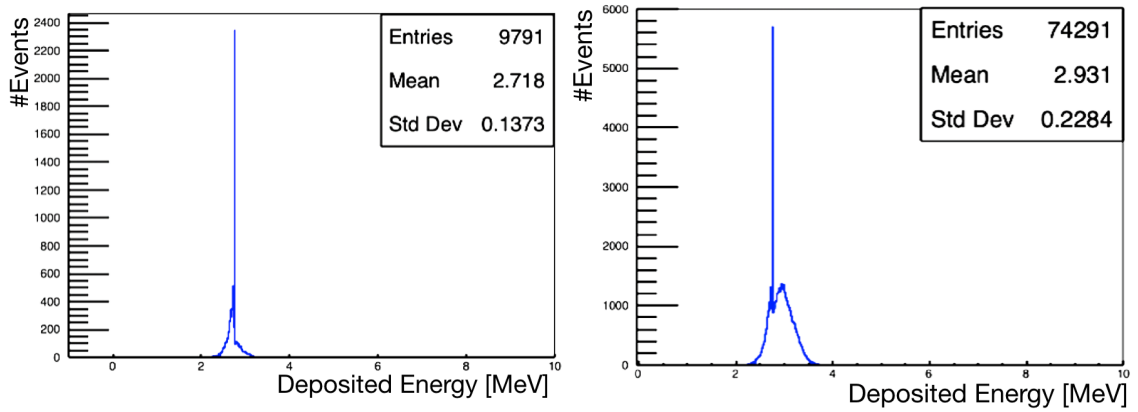

(a) (b)

Figure 3.5: Deposited energy (Monte Carlo) of full deposition events for the 2.75 MeV γ of the ^{24}Na source. Source deployed in cell 6, events selected in cell 5 3.5a and source deployed in cell 6, events selected in cell 6 3.5b. The energy mean is biased upward, and the standard deviation is about 2 times larger when the γ are selected in the deployment cell.

Event selection

A first set of selection cut composed of an isolation cut (anti-compton cut) and an anti-muon cut is applied.

The isolation cut is applied on both data and MC samples. For events to pass this cut, the ratio of charge in the first neighbour target cells (including the deployment cell) over the studied cell j must be lower than 20 %:

$$\frac{Q_{i\pm1}}{Q_j} < 0.2 \tag{3.16}$$

This cut ensures that most of the energy is deposited in the studied cell. The value of this cut has been tested for all cells in the range [0,0.5] as shown in Figure 3.6. The value that minimises the discrepancy between data and MC in a stable regime has been chosen, since the same cut value is applied for all sources in data and MC.

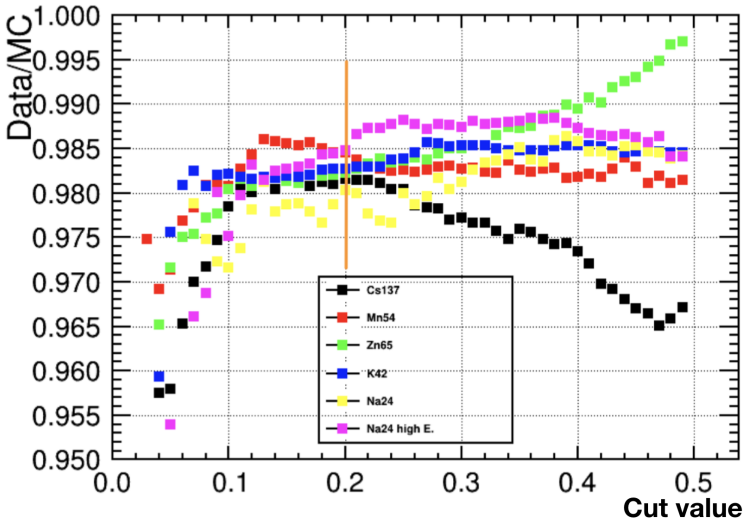

Figure 3.6: Data to MC charge ratio for different value of the anti-Compton cut. The anti-Compton cut is defined as the maximum ratio of the charge in the cells adjacent to the studied cell over the charge in the studied cell. All sources were deployed in cell 4 (z=45 cm) and cell 5 is the cell of study. The orange line represents the chosen value of the cut.

The anti-muon cut is applied solely in data samples: no muon must have been tagged in the last 100 μs. After the pre-selection cuts are applied an iterative fitting procedure is performed to obtain the mean of the charge distribution.

Iterative fitting procedure

To extract the mean of the charge distribution a series of fits is performed. First, the maximum of the charge distribution (most probable value) Q_{max} is measured. In the case of a gaussian distribution the maximum corresponds to the mean, however, because of the constrained volume of STEREO's cells and the presence of dead material around the cells (acrylic walls, buffer,...), part of the energy of an event does not lead to scintillation hence the charge distribution exhibit non-gaussian behaviour at low energy.

Then the iterative fitting procedure can start:

- A gaussian fit is performed in a limited range around Q_{max}: $[Q_{max} \pm 1.3\sqrt{Q_{max}}]$. The 1.3 value was chosen as large as possible for the fit to converge correctly but small enough to avoid a bias in the standard deviation of the fitted gaussian due to non-gaussian charge distribution.

- The mean Q_{mean}^{temp} and standard deviation σ^{temp} of the first fitted gaussian are given as initial parameters for a second gaussian fit performed on an asymmetrical range[2]: $[Q_{mean}^{temp} - 1\sigma^{temp}; Q_{mean}^{temp} + 3\sigma^{temp}]$

- The calibration coefficient (CC) is computed for each source, taking the mean of the second fit Q_{mean} and the average deposited energy evaluated in MC simulation:

$$CC = \frac{Q_{mean}}{< E_{dep} >} \tag{3.17}$$

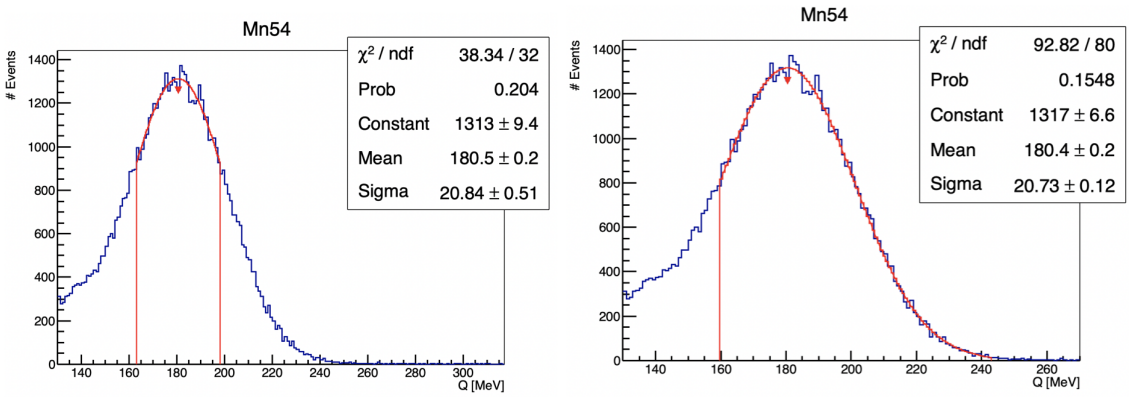

(a) (b)

Figure 3.7: First gaussian fit of the iterative fit procedure for the ^{54}Mn source, the fit is performed on a limited range (see text) 3.5a.
The Second gaussian fit of the iterative fit procedure for the fit is performed on an asymmetric range to avoid bias due to the non-gaussian low energy tail 3.5b.

Charge extraction bias due to non-gaussianity

The asymmetric range of the second fit has been chosen to reduce the uncertainty on Q_{mean}. It has been checked for all sources using toy MC that the extraction method did not induce a bias on Q_{mean}. To do so, the charge distribution is precisely modelled

[2] To avoid mixing up different gammas in the multi-gamma source, for the low energy gamma of the Na24 source the range is $[Q_{mean}^{temp} \pm 1.5\sigma]$ and for the high energy gamma the range is $[Q_{mean}^{temp} \pm 1.3\sigma]$

by a Crystal Ball function (see Figure 3.8; the Crystal Ball function is described in section 4.3 Analytical detector response model for Boron events), then 1000 pseudo-experiments are generated and fitted using the iterative fitting procedure described in the previous section. The pull [3] between the fitted mean and the generation mean is computed for the 1000 samples. The value of the bias for data and MC is reported in Table 3.2, no significant bias has been observed for mono-γ sources.

A small (but not compatible with 0) bias is observed for ^{24}Na and AmBe sources. For these sources, the bias is corrected and a systematic uncertainty corresponding to half the absolute value of the bias value is considered.

Sources	MC bias (%)	data bias (%)
^{137}Cs	0.008* ± 0.05	-0.002* ± 0.05
^{54}Mn	0.02* ± 0.13	-0.01* ± 0.13
^{65}Zn	0.008* ± 0.16	0.013* ± 0.16
^{24}Na	0.04±0.03	0.060.03
^{42}K	-0.008* ± 0.09	0.001* ±0.09
^{24}Na	-0.04±0.03	-0.06±0.03
AmBe	-0.11±0.05	-0.10±0.05

Table 3.2: Bias on Q_{mean} induced by the iterative fit procedure.
* the bias is compatible with 0 within errors for all sources except ^{24}Na and AmBe.

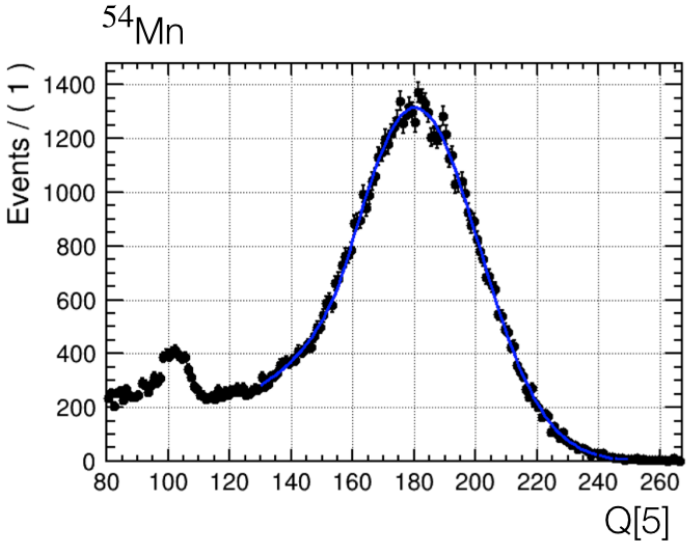

Figure 3.8: Charge distribution of the ^{54}Mn source and Crystal ball model (blue) used for the MC toy generation.

Additionally, a specific procedure to reduce the background in the AmBe source has been developed.

AmBe background reduction

The ^{241}Am-^{9}Be source is of high interest for the non-linearity study, since it provides the highest energy γ (4.44 MeV) available to calibrate the STEREO detector.

[3] fitted value minus generation value divided by error of the fit

Radioactive ^{241}Am decays via α emission, with a half-life of 432 years, to give ^{237}Np in an excited state. Np returns to its ground state via low-energy photon emission (36 % of the time a 0.06 MeV photon is emitted). The half-life of ^{237}Np in its ground state is over 2 million years. The α particle energy is about 5.5 MeV, it interacts with ^{9}Be which result in an excited ^{13}C. The excited ^{13}C decays to excited ^{12}C via the emission of a fast neutron. About 60 % of the times, ^{12}C returns to its ground state via the emission of a 4.44-MeV γ.

The AmBe source decay can be summarised in the following manner:

$$\begin{aligned} ^{241}Am &\rightarrow {}^{237}Np + \alpha \\ \alpha + {}^{9}Be &\rightarrow {}^{13}C^{*} \\ {}^{13}C^{*} &\rightarrow {}^{12}C^{**} + n[0-11\ MeV] \\ {}^{12}C^{**} &\rightarrow {}^{12}C + \gamma[4.438\ MeV] \end{aligned}$$

The kinetic energy of the neutron is different if the 4.44-MeV γ is emitted simultaneously or not. The energy spectrum of the neutron for a typical AmBe commercial source is given in Figure 3.9, the neutron energy ranges from 0 to 11 MeV.

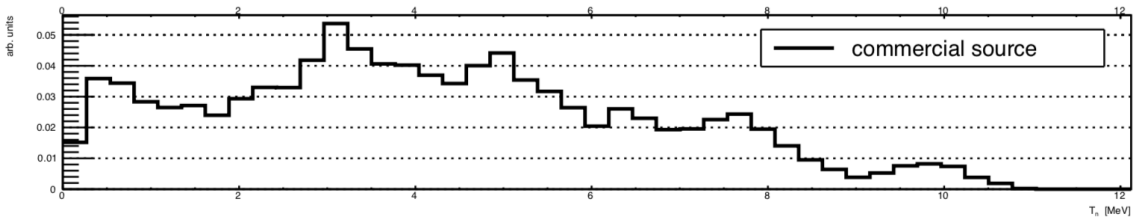

Figure 3.9: Kinetic energy spectrum of the neutron in a typical AmBe commercial source [MTB95]

The energy spectra of the neutron when a γ is emitted simultaneously is presented in Figure 3.10. The neutron has kinetic energy ranging between roughly 2 and 8 MeV.

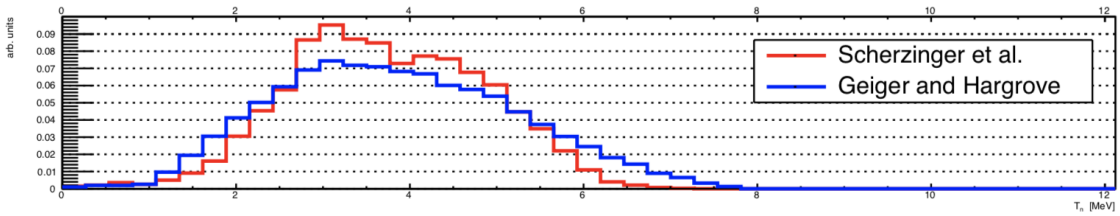

Figure 3.10: Kinetic energy spectrum of the neutron when a 4.44-MeV γ is emitted simultaneously with the neutron [S^{+}15, GH64]

The emitted neutron produces proton recoils before it is thermalised. Once thermalised, it can be captured on hydrogen resulting in a 2.22-MeV γ or on gadolinium producing a cascade of about 4 γ with a total energy of ~8 MeV. The γ cascade can be mistakenly identified as a 4.44-MeV γ. The simulated charge distribution of the AmBe source in the STEREO detector is presented in Figure 3.11.

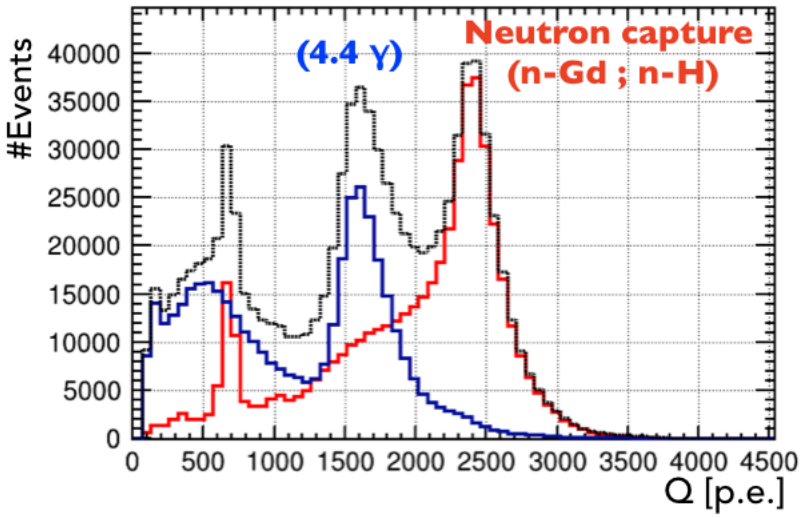

Figure 3.11: Simulated charge distribution of the AmBe source, all events (black), neutron capture on hydrogen or gadolinium (red), events, 4.44-MeV γ (blue).

Contamination of the 4.44-MeV γ energy peak by the Gd-cascade and proton recoils has been studied using MC samples. A simple charge selection around the 4.44-MeV peak gives a proportion of background of ∼50 % (see Figure 3.12).

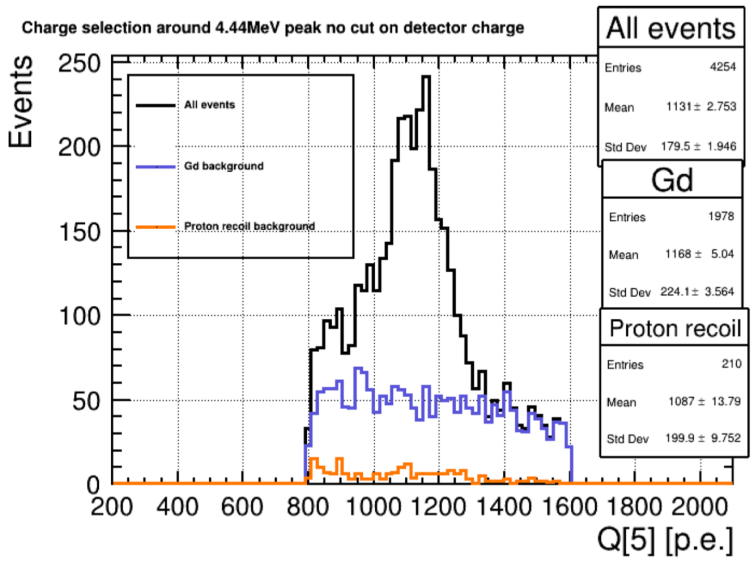

Figure 3.12: 4.44-MeV peak detected in cell 5 for the AmBe source deployed in cell 4 (black), events due to the neutron capture on Gd (blue) amount to 46 % of all events, events with proton recoils amount to 5 % of all events.

To try to reduce the Gd-cascade background, an additional cut on the charge in the whole detector has been set. This cut removes Gd-cascade events for which some of the γ escape the cell of interest but not the whole detector (see Figure 3.13). Even with this cut, the proportion of background stays high, with ∼41 % of all events being due to background.

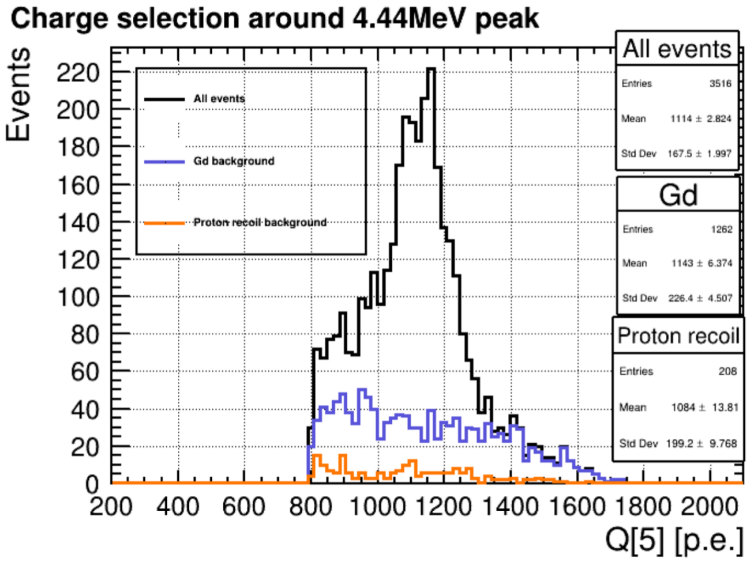

Figure 3.13: Charge selection around the 4.44-MeV peak with an additional cut on the whole detector charge Q_{Det}<2100 p.e.

To reduce further the amount of background, a novel strategy consisting of a time coincidence search between the 4.44-MeV γ and the neutron capture on Gd had been developed.

An event with the characteristics of a 4.44-MeV γ is taken as a prompt signal, then a neutron capture on Gd (delayed) is looked for in a 50 μs window in cells as far as possible from the studied cell: the deployment cell is cell 4, the studied cell is cell 5, the delayed signal is looked for in cells 1,2,3 front GC and long GC.

The idea behind this strategy is to bias the sample for events where proton recoils and Gd neutron capture happen further away from the study cell, hence reducing the background.

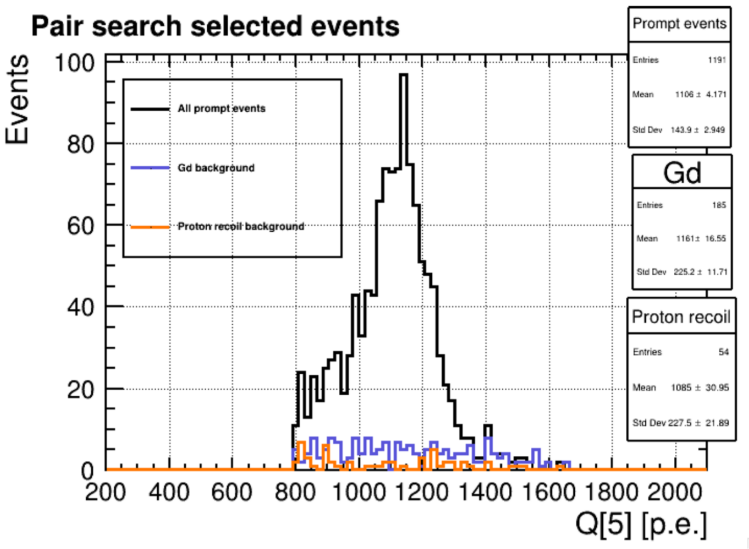

Figure 3.14: Prompt events from the time coincidence search. The amount of Gd-cascade (∼15 %) is reduced compared to a simple charge selection.

The proportion of background can be thus reduced from ∼50 % to ∼20 % with the coincidence search strategy, and the signal-to-background ratio goes from ∼1 to

∼4, (see Figure 3.14). The main drawback is a non-negligible loss of statistics (see Table 3.3). However, in data the loss of statistics is not an issue since the AmBe source has high activity.

Event selection	n-Gd	proton recoils	$\frac{S}{B}$	Stat. loss
Charge selection	46.5 %	5.0 %	0.94	0 %
Charge selection + full det. cut	36.0 %	6.0 %	1.39	-1 %
Coincidence selection +full det. cut	15.5 %	4.5 %	3.98	-54 %

Table 3.3: Selection strategy and associated background proportion, signal-to-background ratio and loss of statistics compared to the charge selection.

The bias induced by the remaining Gd background in the AmBe signal after coincidence search has also been evaluated. To do so, a model composed of Crystal ball function and a polynomial with 2 degrees of freedom is used (see Figure 3.15).

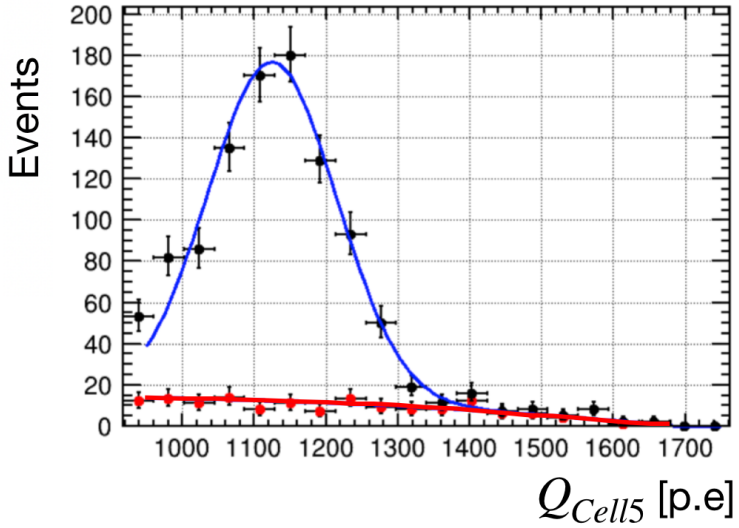

Figure 3.15: Crystal ball (blue) and polynomial (red) component of the model fitted on the AmBe MC sample after coincidence search. Background events are the red points.

To evaluate the Gd-background in data the polynomial shape was constrained to the shape of the background in simulation but the normalisation was let free. 1000 pseudo-experiments were generated for both simulation and data. Since the Gd background rates are not exactly equal in simulation and data, we treat both cases separately. Each pseudoexperiment is fitted according to the iterative fitting procedure with a slightly smaller range [μ-1σ;μ+1.5σ]. The relative bias between the fitted mean and the generation mean is computed.

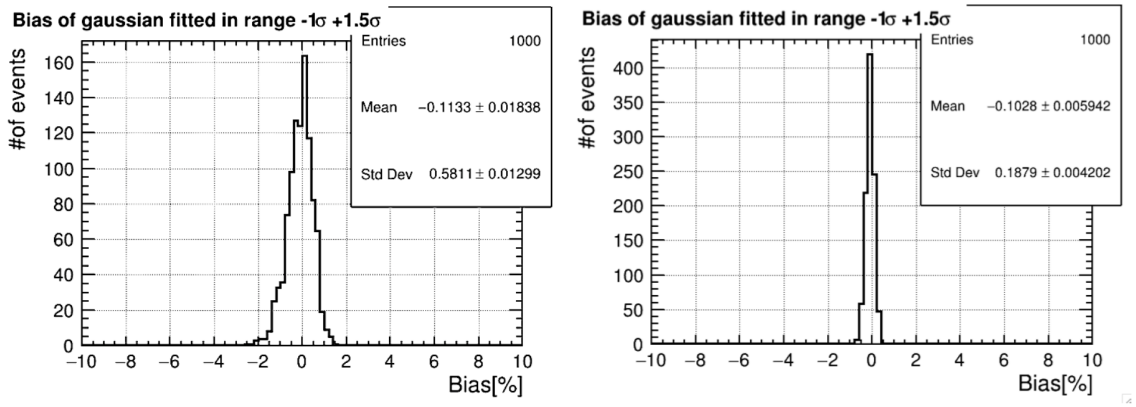

(a) (b)

Figure 3.16: Relative bias due to the remaining background in the AmBe source in MC 3.16a and in data 3.16b. In both cases, the mean relative bias is ∼0.1%.

Systematic uncertainties evaluation

The charge fit bias is compatible with 0 for all mono-γ sources. For the ^{24}Na and AmBe sources the bias is corrected and a systematic uncertainty corresponding to half the bias value is assigned. The bias is almost fully correlated between data and MC hence they cancel each other in the data to MC ratio.

In addition to the charge fit bias, two main sources of systematic uncertainty have been considered: the anti-compton cut and the choice of the fit range. To evaluate the systematic uncertainties on the anti-compton cut, a variation of ±5% of the cut value has been done and the standard deviation of the CC value over the variation is taken as the systematic uncertainty (see Table 3.4).

Sources		Cut=0.19	Cut=0.20	Cut=0.21	Std. dev.
^{137}Cs	data	226.346	226.059	226.031	0.14
	MC	230.718	230.314	230.303	0.19
^{54}Mn	data	231.586	231.351	231.291	0.13
	MC	235.209	234.982	235.102	0.09
^{65}Zn	data	236.15	236.22	236.069	0.06
	MC	240.469	240.476	240.23	0.11
^{42}K	data	241.644	241.528	241.528	0.05
	MC	245.904	245.789	245.371	0.07
^{24}Na(1.37 MeV)	data	246.516	246.913	247.015	0.21
	MC	251.884	251.867	252.064	0.08
^{24}Na(2.75 MeV)	data	252.402	252.356	252.521	0.07
	MC	256.407	256.244	255.934	0.20

Table 3.4: Variation of the calibration coefficient (in photoelectrons per deposited MeV) under a ± 5 % variation of the anti-compton cut value. The standard deviation of the calibration coefficient variation is taken as the associated systematic uncertainty.

To evaluate the systematic uncertainty due to the choice of the fit range, the standard deviation of the calibration coefficient over a variation of ±1 % of the centre of the fit range is computed (see Figure 3.17).

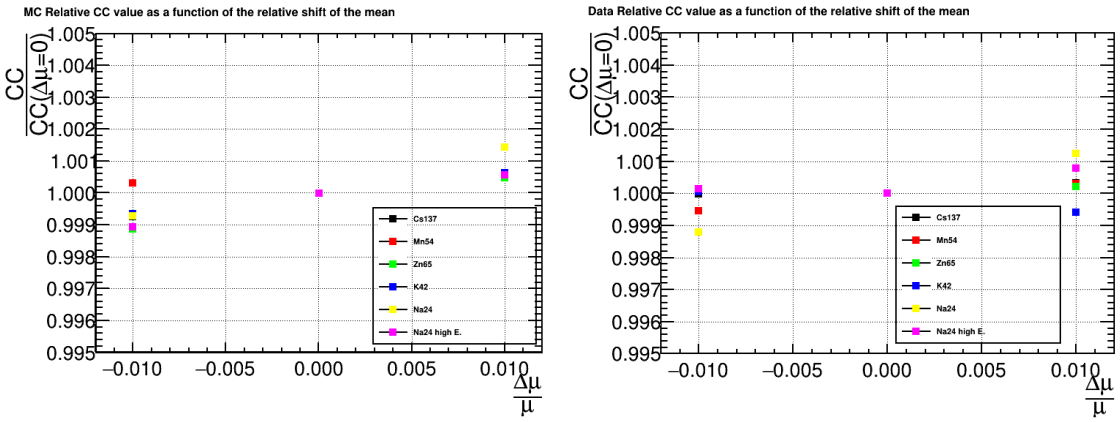

(a) (b)

Figure 3.17: Relative variation of the calibration coefficient over a variation of ± 1 % of the centre of the fit range in MC (3.17a) and in data (3.17b). The standard variation is taken as the associated systematic uncertainty.

The summary of all the systematic uncertainty is given in Table 3.5.

	MC			Data		
Sources	Range	Anti-compton	Bias syst.	Range	Anti-compton	Bias syst.
^{137}Cs	0.05 %	0.08 %	-	0.02 %	0.06 %	-
^{54}Mn	0.02 %	0.04 %	-	0.03 %	0.06 %	-
^{65}Zn	0.06 %	0.05 %	-	0.01 %	0.03 %	-
^{24}Na	0.09 %	0.03 %	0.02 %	0.03 %	0.03 %	0.03 %
^{45}K	0.05 %	0.03 %	-	0.03 %	0.02 %	-
^{24}Na	0.07 %	0.08 %	0.02 %	0.03 %	0.03 %	0.03 %
AmBe	0.10 %	0.33 %	0.05 %	0.07 %	0.37 %	0.05 %

Table 3.5: Systematic uncertainty associated with the fit range, the anti-compton cut and the extraction procedure bias for MC and data.

We acknowledge that the list of systematic uncertainties presented here is not exhaustive. In particular, another source of systematic uncertainty that has not been studied is the Geant4 description of the optical model.

Result of the non-linearity studies

Calibration coefficients are computed for all sources and normalised to the ^{54}Mn points. The data over MC ratio is then computed and we check that it is consistent with a constant.

The 1.3-MeV γ of the ^{24}Na source is systematically higher than the neighboring point in the plot: this is due to the presence of the 2.7-MeV γ emitted simultaneously by the source, that deposits energy in the detector. Some of the scintillation light coming from this energy deposition will reach the study cell due to the optical cross-talk between cells. However, the data-MC agreement for this point is satisfactory, showing that the optical cross-talk is well reproduced by the simulation.

For the data-to-MC ratio, the systematic uncertainty on the fit range is considered fully correlated between data and MC, hence it is the standard deviation of the ratio under a ± 1 % variation of the fit range that is taken as a systematic uncertainty.

The data-to-MC ratio is consistent with a constant for the 3 different calibration campaign of Phase II (see figures 3.18 3.19, 3.20), showing that the liquid non-linearity is well modelled by the simulation and that no new tuning of the k_B parameter is necessary. The data-to-MC ratio decreases with time: this is due to the loss of scintillation efficiency of the liquid scintillator over time (see Figure 3.21).

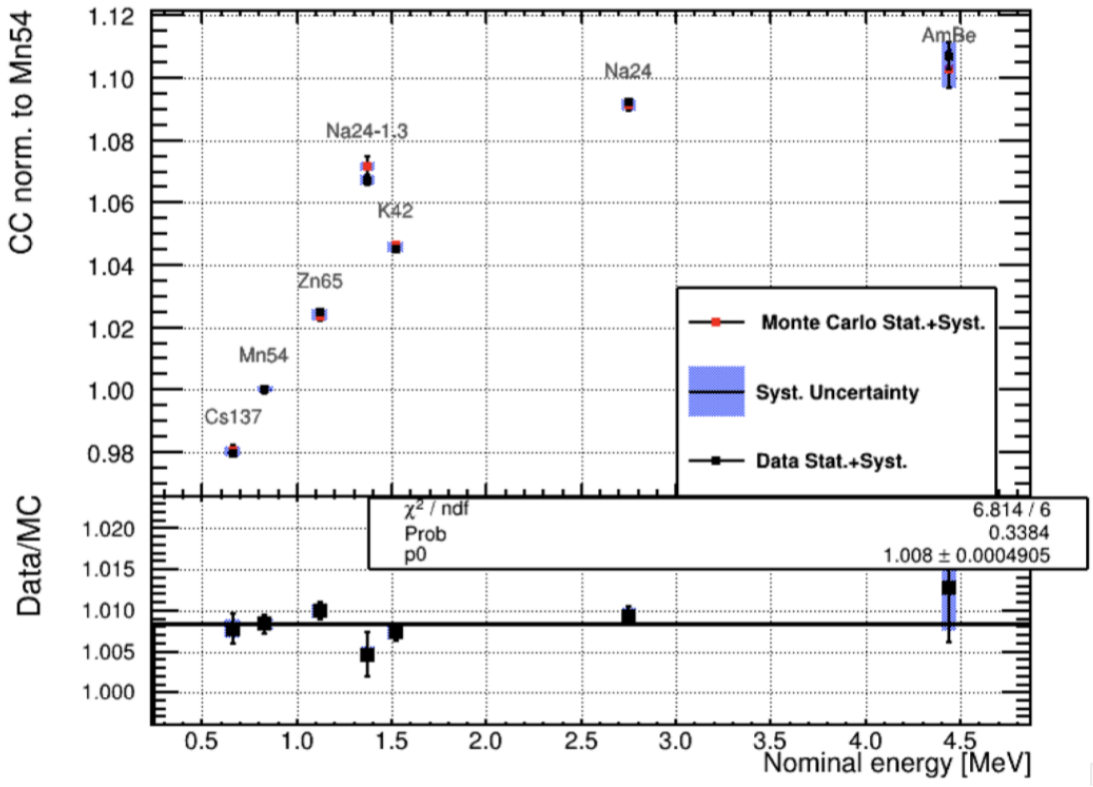

Figure 3.18: Non-linearity of the liquid scintillator response and data-to-MC ratio with calibration data of April 2018. The data-to-MC ratio is compatible with 1 meaning that the energy non-linearity is well reproduced by the MC simulation.

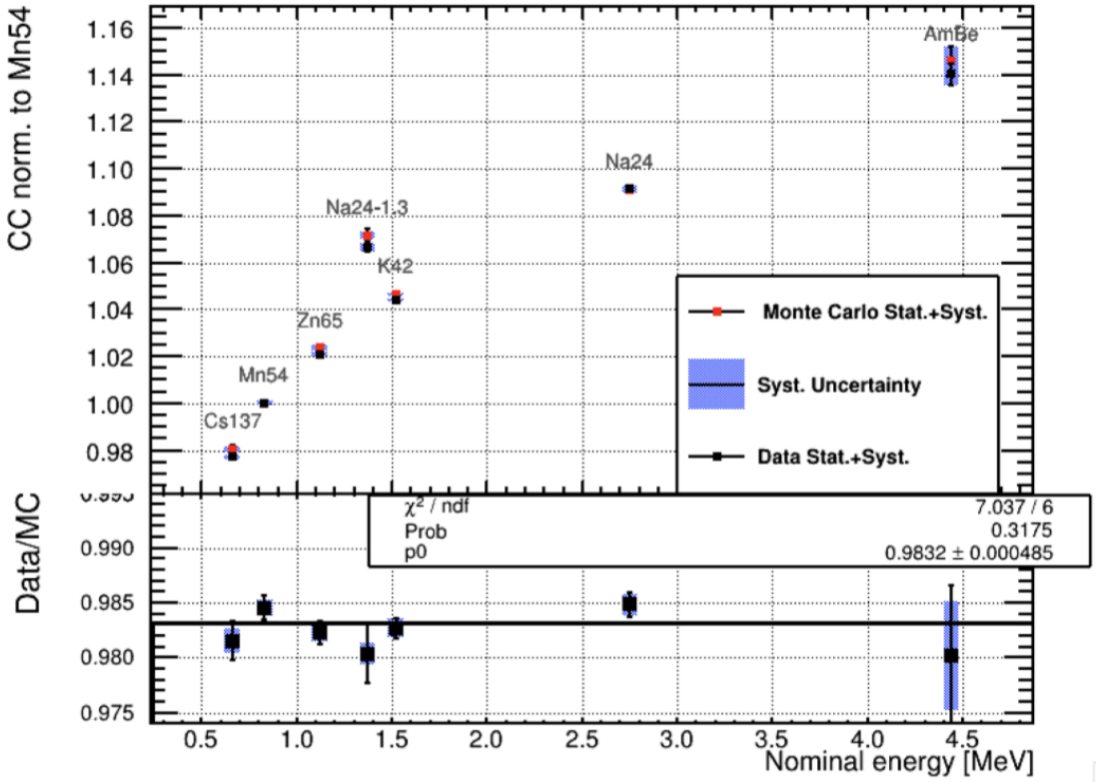

Figure 3.19: Calibration data of October 2018. The data-to-MC ratio is compatible with a constant, meaning that the non-linearity is still well reproduced. However, the constant is now smaller than 1; this is due to the decrease over time of the scintillator light yield.

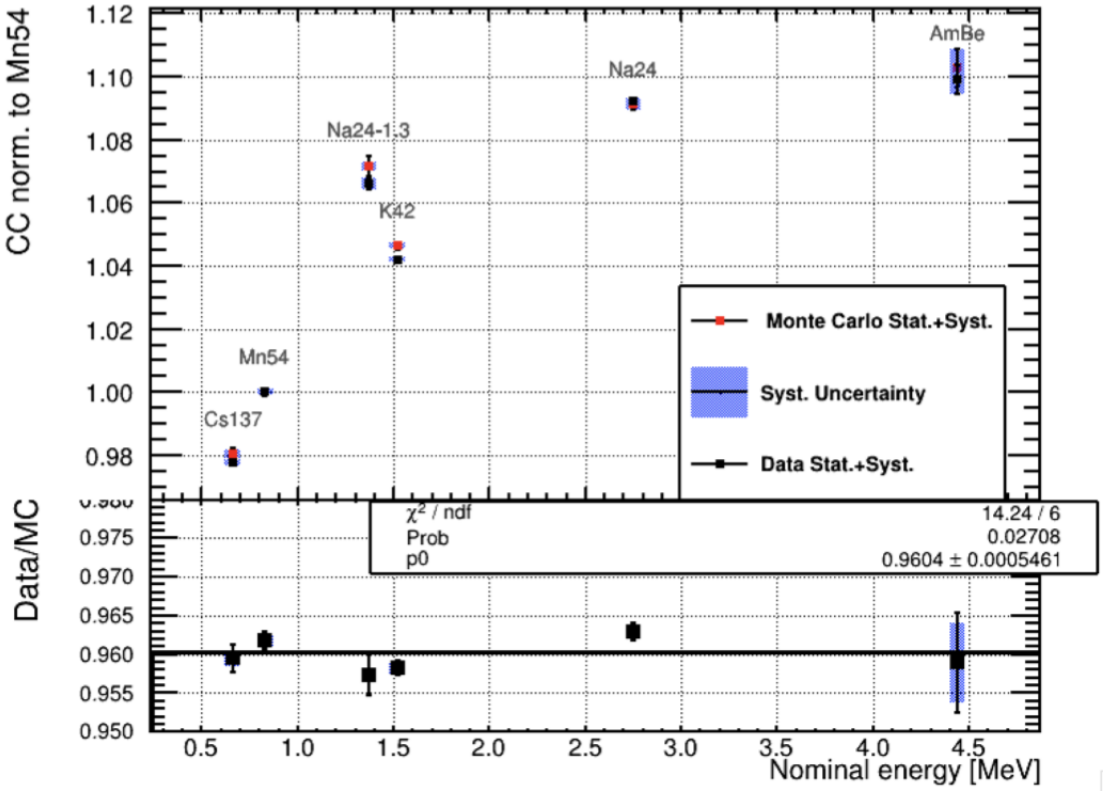

Figure 3.20: Calibration data of August 2019.

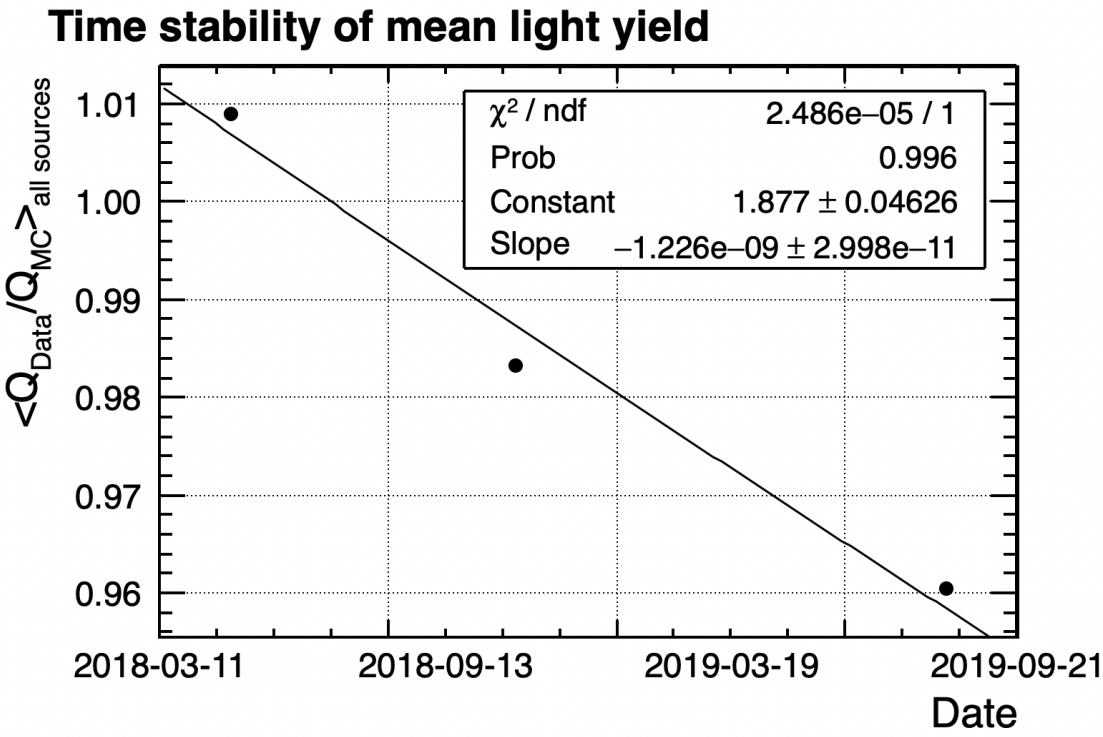

Figure 3.21: Mean value of the data-to-MC ratio for all sources as a function of the date. The values are fitted by an exponential function $f(t) = \exp\{Constant + Slope \times t\}$. $Slope = -1.226 \times 10^{-9}\text{s}^{-1} = -0.038\text{years}^{-1}$. The decrease indicates a loss of the scintillator efficiency over time.

3.5 Conclusions

In conclusion, the strategies presented in this chapter allowed to reduce the Phase II systematic uncertainties with respect to the analyses of Phase I presented in Figure 3.4, probing at the sub-percent level the energy non-linearity. We find that it is very well reproduced by the simulation. In particular, for the data-to-MC ratio of the Phase II calibration campaigns, a standard deviation of only $\sim$0.3 % is obtained.

Bibliography

[Bir64] John B. Birks. *The Theory and practice of scintillation counting*. 1964.

[GH64] K.W. Geiger and C.K. Hargrove. Neutron spectrum of an am241-be(, n) source. *Nuclear Physics*, 53:204–208, 1964.

[MTB95] J W* Marsh, D J Thomas, and M Burke. High resolution measurements of neutron energy spectra from ambe and amb neutron sources. *Nucl. Instrum. Methods Phys. Res.*, A366(2-3):340–348, 1995.

[P+16] C. Patrignani et al. Review of Particle Physics. *Chin. Phys. C*, 40(10):100001, 2016.

[S+15] J. Scherzinger et al. Tagging fast neutrons from an ^{241}Am/^{9}Be source. *Appl. Radiat. Isot.*, 98:74–79, 2015.

CHAPTER 4

ANALYTICAL MODELISATION OF THE DETECTOR ENERGY RESPONSE: THE CASE OF COSMOGENIC BORON EVENTS

CONTENTS

4.1 Introduction

In this chapter, we will present an analytical modelisation of the detector energy response that we have developed. The aim is to take into account all detector effects (energy scale, energy resolution, energy loss due to the finite volume of the detector,...) in the energy response of the detector.

An accurate modelisation of the detector response can be obtained through a precise description of the detector in the Geant4 framework (or other numerical MC simulation framework) and the confrontation of the MC samples thus obtained against calibration data. This has been the approach in STEREO. Although, the Geant4 framework is well established and robust, the tuning of the simulation and the generation of MC sample is time-consuming, a change in a single parameter of the Geant4 model requiring to redo completely computer-expensive simulations.

The framework we propose here aims at describing accurately the energy response in an analytical way with a limited number of parameters. This makes this framework much more flexible, allowing to fit directly on calibration data the relevant detector response parameters. Instead of tuning the Geant4 parameters describing the liquid scintillator light yield, Birks constant, the PMT quantum efficiency or the reflectivity of STEREO's surfaces... we could fit directly on calibration data the energy scale parameters such as the mean and the width of the energy response function, as well as other parameters describing the departure from gaussianity of the energy detector response. Moreover, the implementation of systematic uncertainties in this framework is natural as the response model parameters simply become nuisance parameters of the physics analysis. We will pursue this programme both in this Chapter and in the next one.

We present in this chapter a first implementation of this idea for events coming from the β decay of the cosmogenic Boron-12 isotope. We will demonstrate on a MC sample that we are able to fit part of the detector response parameters. Then, by comparing the analytical detector response model obtained for the measured Boron spectrum and for the Geant4 simulated spectrum, we will estimate systematic uncertainties on the model parameters that describe the energy scale. This systematic uncertainty is applied to the response model of the neutrino events described in the next chapter.

4.2 Cosmogenic Boron

Muon capture

A muon can be captured by an atom in matter when it stops. It can then cascade down to the 1s orbital, and be captured by the nucleus, in an analogue process to electron capture: a proton in the nucleus captures the muon to become a neutron [AS17]. A good description of the muon capture rate Λ_c is given by the Goulard-Primakoff formula [GP74]:

$$\Lambda_c(A,Z) = Z_{eff}^2 G_1 \left[1 + G_2\frac{A}{2Z} - G_3\frac{A-2Z}{2Z} - G_4\left(\frac{A-Z}{2A} + \frac{A-2Z}{8AZ}\right)\right] \tag{4.1}$$

with $Z_{eff} = Z\left[1+\left(\frac{Z}{37.2}\right)^{1.54}\right]^{-1/1.54}$

In STEREO, the main constituting element is Hydrogen, however since the capture rate is at first order proportional to the squared effective charge of the nuclei Z_{eff}^2, the

[1] $G_1 >> G_{2,3,4}$

muon capture mostly happens on the second most common element, ^{12}C. The muon capture on ^{12}C leads to the creation of ^{12}B as it has been observed by the Double Chooz experiment among others [A^{+}16a]. ^{12}B can also be produced by neutron spallation on ^{12}C.

^{12}B is a β^{-} emitter with a lifetime of 29.1 ms and an endpoint energy Q=13.4 MeV. The ^{12}B spectrum in STEREO is an interesting control sample, as the continuous β^{-} spectrum produced in the ^{12}B decay covers the whole energy range of interest for the neutrino events.

Boron events selection

A dedicated procedure has been developed by other STEREO collaborators to identify Boron events [Bon]. The procedure consists of a coincidence search with a stopping muon (but not decaying) as the prompt signal and the β^{-} as the delayed signal. The selection cuts are listed in Table 4.1:

Cut #1 selects low energy muons that are likely to stop in the detector and be captured on a nucleus.

Cut #2 selects ^{12}B candidate events between 2 and 20 MeV.

Cut #3 ensures that the prompt events take place in one of the target cells.

Cut #4 exploits the spatial correlation of the muon capture and the ^{12}B decay that must happen at the same location.

Cut #5 exploits the time correlation between the muon capture and the β decay, that has a lifetime of ∼29 ms.

Cut #6 ensures that the muon selected as the prompt signal is not a decaying muon[2]

Cut #7 ensures that the delayed signal is muon free.

Type	Cut	Condition
Energy	1	$60<E_{prompt}<120$ MeV
	2	$2<E_{delayed}<20$ MeV
Topology	3	$\text{Cell}_{prompt} \in$ Target
Coincidence	4	$\text{Cell}_{delayed}=\text{Cell}_{prompt}$
	5	2 ms$<\Delta t_{\text{prompt-delayed}}<$60 ms
Background rejection	6	0.25 μs$<\Delta t_{\text{before prompt}}<6$ μs and 0.25 μs$<\Delta t_{\text{after prompt}}<6$ μs for all events with $E^{detector} \in$ [5;70] MeV
	7	$\Delta t_{\text{before delayed}} > 200$ μs for muon events

Table 4.1: List of cuts for the selection of the Boron events

Accidental pairs are selected by the exact same selection with time-shifted windows and are statistically subtracted. The rate of Boron events has been measured to be R_{target}=793.2±3.5 day^{-1} (roughly twice the number of expected neutrinos in a reactor ON day). The measured energy spectrum of Boron events in the Target, as well as the accidental pairs, is given in Figure 4.1 and the Boron spectra cell-by-cell are given in Figure 4.2. The spectra are similar for all cells; this is expected as the events should be, a priori, evenly distributed across cells.

[2]The muon lifetime is 2.2μs.

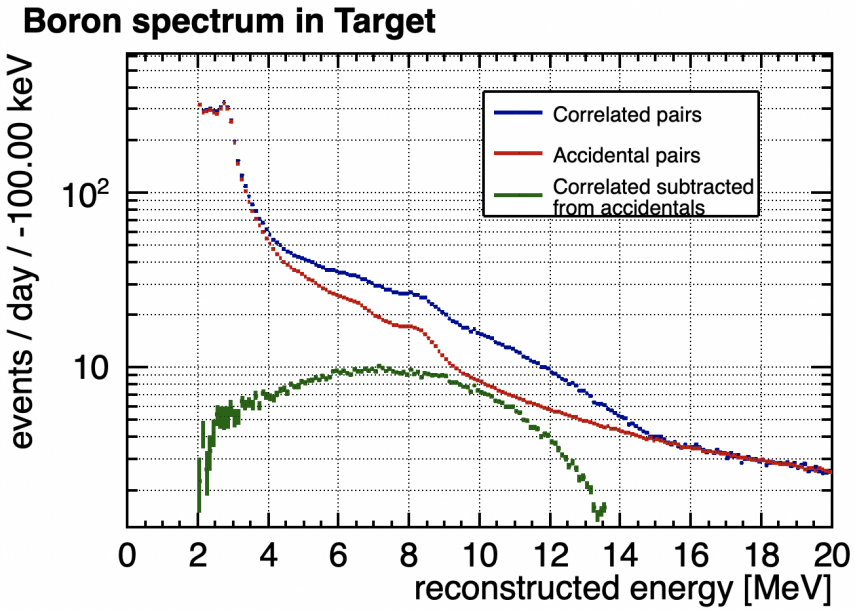

Figure 4.1: Measured Energy spectrum of boron events in Target. All correlated pairs are in blue, accidental pairs are in red, the difference in green is the spectrum of the boron events. Events below 2 MeV are cut because the signal-to-background ratio is too low below 2 MeV.

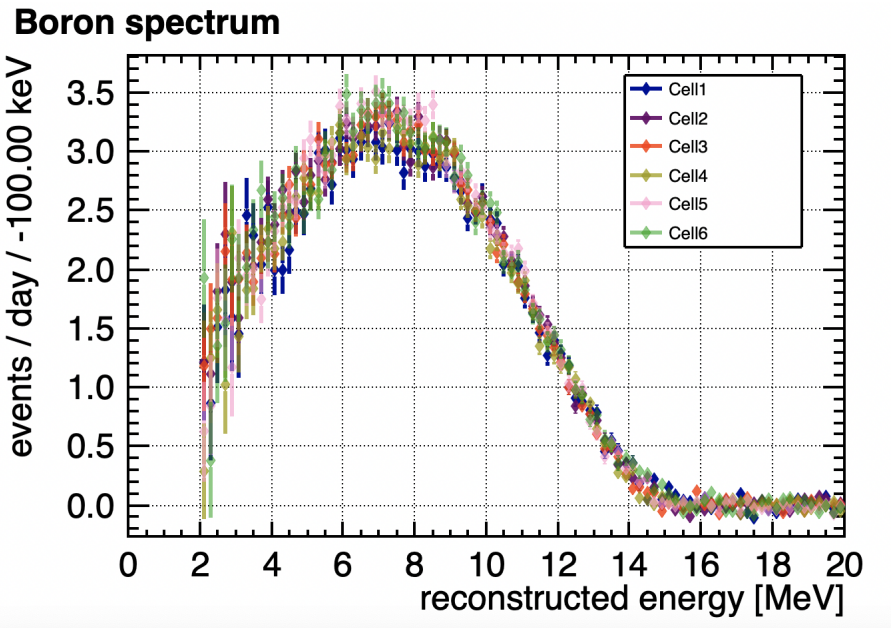

Figure 4.2: Measured Boron spectra by cells

Boron spectrum simulation

Geant4 simulations of Boron events have been set up by other STEREO collaborators [Rog]. To produce the Geant4 MC sample of Boron events, first, a MC sample of atmospheric muons is generated with the Cosmic-Ray shower library (CRY) [HLW07] at sea level[3]. The transport of the muon through the reactor building and the detector is simulated using the Geant4 framework. This step is necessary since the muons

[3]It has been checked that the muon spectrum exhibit no sizeable difference at the ILL's altitude (200 m) compared to sea level

are coming from cosmic rays they enter the detector from the top. The exact same selection as the data is performed to extract the stopping muon sample. It results in a non-uniform distribution of muon capture vertices along the z-axis, indeed most of the selected muons stop at the top of the detector as can be seen in Figure 4.3. The influence of the water level in the transfer channel over the detector has been checked, no effects on the vertices distribution has been observed [Rog].

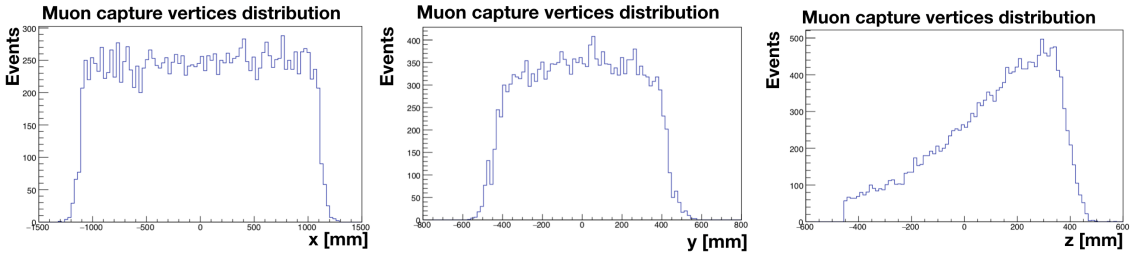

(a) (b) (c)

Figure 4.3: Spatial distribution of muon capture vertices along x-axis 4.3a, y-axis 4.3b, and z-axis 4.3c. The vertices are not uniformly distributed along the z-axis, more muons are stopping at the top of the detector than at the bottom.

The prediction of the energy spectrum of the β^- from the decay of the ^{12}B, represented in Figure 4.4, is obtained from the BESTIOLE (Beta Energy Spectrum Tool for an Improved Optimal List of Elements) code, developed and maintained by the CEA.

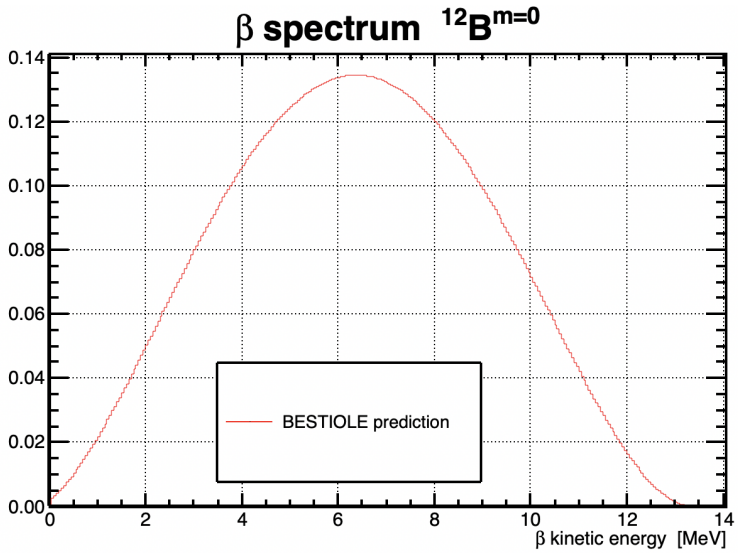

Figure 4.4: Energy spectrum prediction of the β coming from the decay of the ^{12}B as computed by the BESTIOLE code.

The β spectrum obtained from BESTIOLE and the vertices distribution of the muon capture are given as input to the Geant4 description of the detector and β particles are simulated in the detector to obtain the reconstructed energy spectrum in each cell (see Figure 4.5).

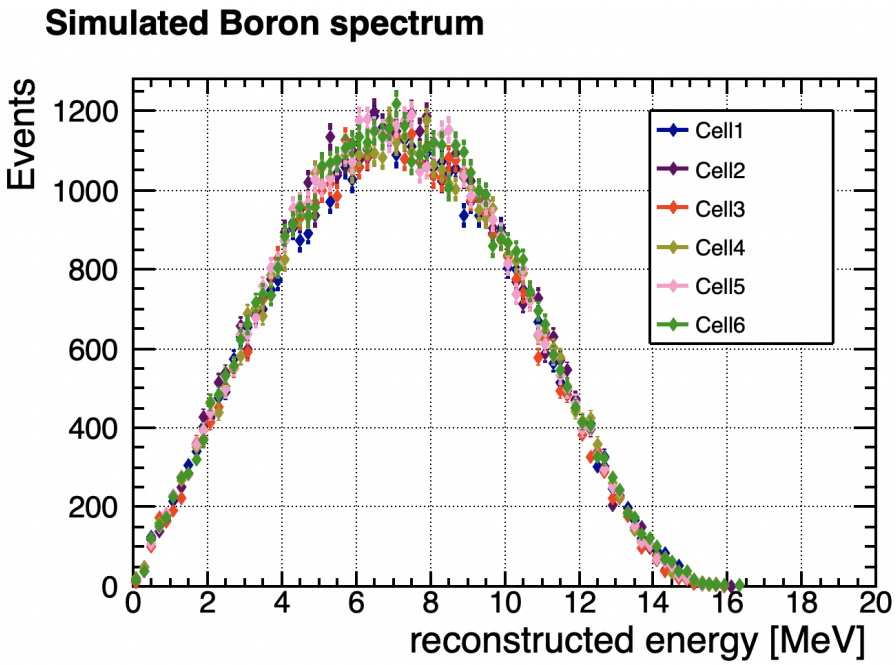

Figure 4.5: Simulated Boron spectra for all cells

4.3 Analytical detector response model for Boron events

In a good approximation, the prompt signal of an IBD formed by the positron ionisation and annihilation can be considered equivalent to that of a β^- particle to which two 511-keV γ are added, hence the detector response for Boron events will also describe the ionisation part of the detector response for the neutrino events.

The response model for the Boron events is described by a Crystal Ball distribution (CB). The Crystal Ball distribution, named after the Crystal Ball collaboration, consists of a main gaussian part and a power-law tail below a threshold:

$$CB(x,\mu,\sigma,\alpha,n) \propto \begin{cases} e^{-\frac{(x-\mu)^2}{2\sigma^2}} & \text{for} \frac{x-\mu}{\sigma} > -\alpha \\ A\cdot\left(B-\frac{x-\mu}{\sigma}\right)^{-n} & \text{for} \frac{x-\mu}{\sigma} \leq -\alpha \end{cases} \tag{4.2}$$

$$A = \left(\frac{n}{|\alpha|}\right)^n \cdot e^{-\frac{|\alpha|^2}{2}} \tag{4.3}$$

$$B = \frac{n}{|\alpha|} - |\alpha| \tag{4.4}$$

The gaussian part of the CB distribution describes full energy deposit events, whereas the low-energy tail describes events for which part of the energy escapes the detector. In our case the Crystal Ball reads:

$$CB(E_{rec}, \mu_{CB}(E_{true},\vec{\mu}), \sigma_{CB}(\mu_{CB},\vec{\sigma}), \alpha(\mu_{CB},\vec{\alpha}), n_0) \tag{4.5}$$

where E_{rec} is the energy reconstructed by the detector, E_{true} is the true deposited energy according to the MC simulation and the parameters μ_{CB}, σ_{CB}, α_{CB} and n describe the shape of the detector response. Since $\mu_{CB}(E_{true})$ links the most probable value of the reconstructed energy E_{rec} to the true deposited energy E_{true}, it actually encodes the energy scale. σ_{CB} describes the energy resolution and α and n, the departure from gaussianity.

Energy scale

Since Boron events are mostly high energy electrons and quenching happens at low energies, the relation between reconstructed energy and true energy is expected to be nearly linear. To allow for a slight non-linearity, the mean of the Crystal Ball μ_{CB} is described by a quadratic polynomial. We parametrise μ_{CB} as a function of $E'_{true} = E_{true}$-7.15 MeV:

$$\mu_{CB}(E'_{true}) = \mu_2 \times E'^2_{true} + \mu_1 \times E'_{true} + \mu_0 \tag{4.6}$$

The shift in E_{true} makes the fit more sensitive to the μ_0 parameter by translating the spectrum as to have the maximum of events for $E'_{true} = 0$. If no translation of the spectrum is made the value of μ_0 is determined in a region of the spectrum where no events are selected (below 2 MeV).

The linear coefficient μ_1 corresponds to the calibration coefficient, in the regime where the quadratic coefficient μ_2 can be neglected. A value of $\mu_1 \approx 1.15$ translates the fact that the energy scale is anchored at the relatively low energy point of the ^{54}Mn source (0.83 MeV), hence a ∼10 to 15% quenching is expected.

The quadratic coefficient μ_2 is added in the parametrisation of the energy scale to describe potential non-linearities.

Energy resolution

A general parametrisation of a realistic calorimeter [FG03] energy resolution is given by:

$$\frac{\sigma}{E} = \frac{\sigma_0}{\sqrt{E}} \oplus \frac{\sigma_1}{E} \oplus \sigma_2 \tag{4.7}$$

where $\oplus$ stands for a quadratic sum.

$\frac{\sigma_0}{\sqrt{E}}$ is called the stochastic term. This term is the consequence of fluctuations in the development of the particle shower induced by the interaction of a particle in a calorimeter, and in the number of photons arriving to the photosensor.

$\frac{\sigma_1}{E}$ term is called the noise term. This term comes from the electronic readout of the detector. The importance of this term depends on the detector technology and readout circuit. In general, scintillator based calorimeters have a small contribution from the noise term to the whole energy resolution because the first step of the electronic readout chain is a photomultiplier device, that provides an amplification of the original signal with almost no noise.

The last term σ_2 is the constant term, it includes contributions independent from the energy of the particle, such as instrumental effects (e.g. detector geometry,...) causing variations in the calorimeter response, smearing the measured energy.

Preliminary results showed that the noise term was constantly compatible with 0, hence it was removed from the parametrisation for the Boron events.

Since the dependence of σ_{CB} with the energy comes from the poissonian fluctuations of photons, and their number is proportional to E_{rec} but not necessarily to E_{true}, we choose to describe the dependence of σ_{CB} with the energy as a function of μ_{CB} instead of E_{true}, thus avoiding describing twice the same possible non-linearities. Hence,

$$\sigma_{CB}(\mu_{CB}) = \sqrt{\sigma_0^2 \times \mu_{CB} + \sigma_1^2 \times \mu_{CB}^2} \tag{4.8}$$

Energy escape

As stated above, the low-energy tail of the CB describes events for which energy escapes the detector. Boron events are well-contained events so the tail of the distribu-

tion for Boron events is small. The α parameter is parametrised by a linear polynomial.

$$\alpha(\mu_{CB}) = \alpha_1 \times \mu_{CB} + \alpha_0 \tag{4.9}$$

Finally, the power-law parameter was found to be compatible with a constant with the energy:

$$n(\mu_{CB}) = n_0 \tag{4.10}$$

Tuning procedure for the Boron model

The parameters $\vec{\mu}$, $\vec{\sigma}$, $\vec{\alpha}$, n_0 ($\vec{\mu} = (\mu_0, \mu_1, \mu_2)$, $\vec{\sigma} = (\sigma_0, \sigma_1)$, $\vec{\alpha} = (\alpha_0, \alpha_1)$ in blue in the formula below) completely define the detector response model.

To obtain the value of these parameters, a Geant4 MC sample of Boron events is separated into 106 E_{true} samples ranging from 1.6 to 12.2 MeV with a step of 0.1 MeV.

These 106 samples are fitted simultaneously with the analytical response model by minimising the following χ^2:

$$\chi^2 = \sum_t \sum_r \left(\frac{M_{t,r} - N_t \times CB(E_{rec}, \mu_{CB}(E_{true}, \vec{\mu}), \sigma_{CB}(\mu_{CB}, \vec{\sigma}), \alpha(\mu_{CB}, \vec{\alpha}), n_0)}{U_{t,r}} \right)^2 \tag{4.11}$$

where t is running over the E_{true} sample index and r over the E_{rec} bins, and N_t is the normalisation of the E_{true} sample, M are the MC sample and U the statistical uncertainty of the bin. The simultaneous fit is presented in Figure 4.6 for a selection of samples. Each E_{true} sample is fitted on a restricted range in E_{rec} to take in as thoroughly as possible the main peak and the non-gaussian low-energy tail but excluding threshold effects at very low reconstructed energy and empty bins at too high reconstructed energies.

In the simultaneous fit of the E_{true} samples, the normalisation of the model is independent from one sample to another; as we will see in the next section, this corresponds to a conditional PDF.

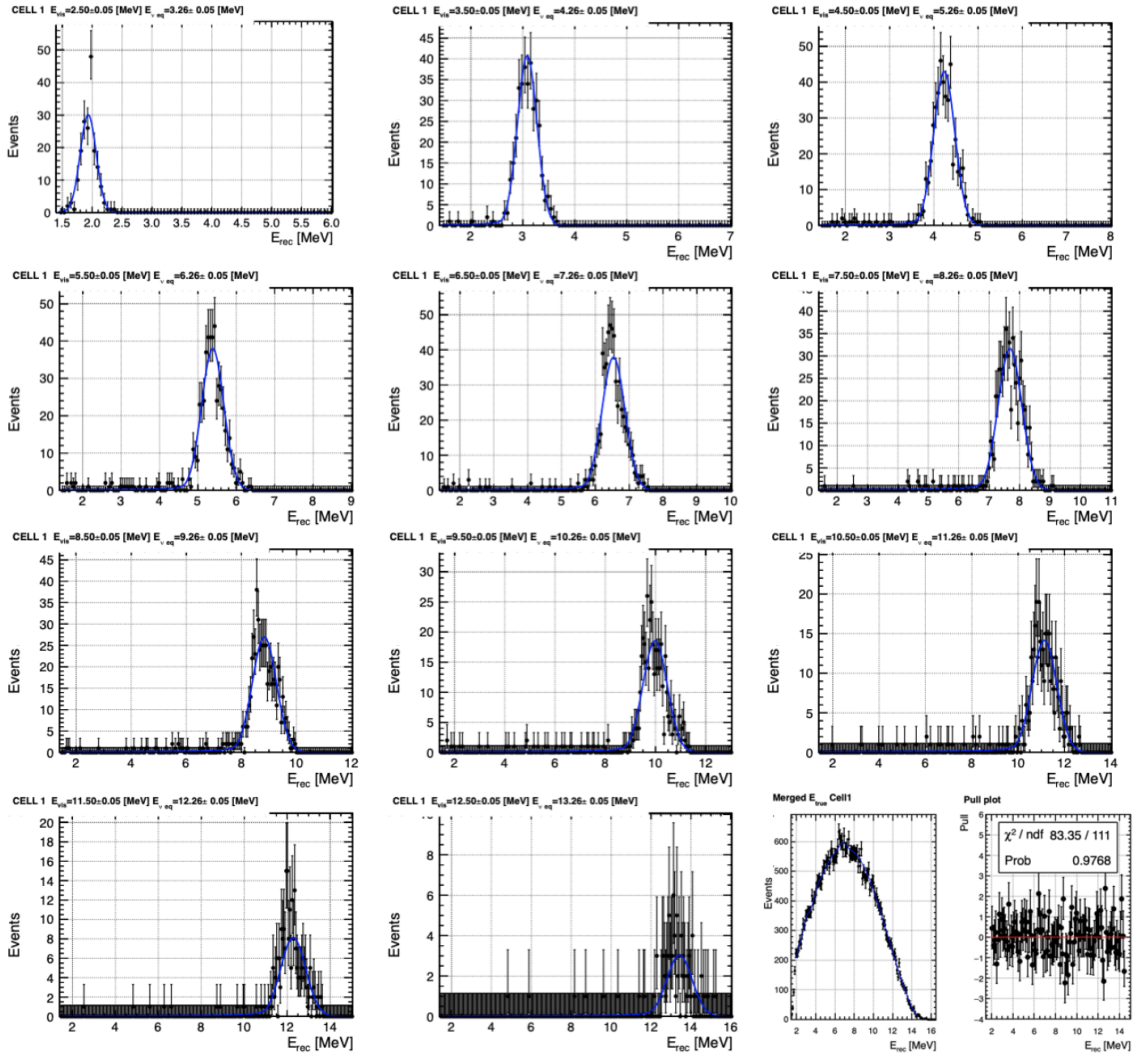

Figure 4.6: Selection of E_{true} samples from the simultaneous fit across all E_{true} samples to determine the parameters' value of the response model for the Boron events.

This procedure is repeated independently for the 6 cells, the result of the model tuning for each cell is presented in Figure 4.7.

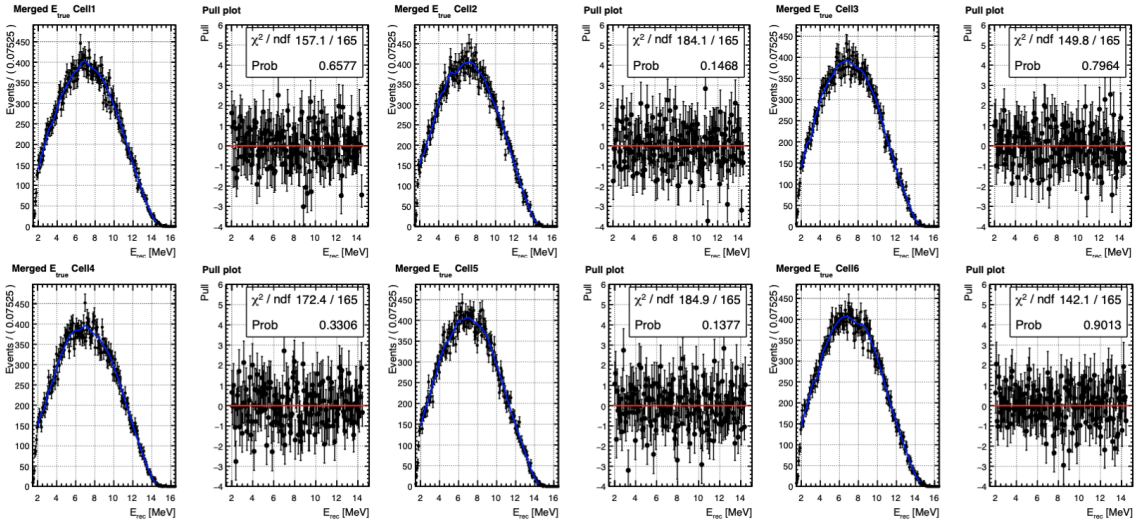

Figure 4.7: Merged MC E_{true} samples and analytical response model (blue line) for the Boron events in all cells. The agreement between the response model and MC is checked by computing the χ^2 between the pulls and a null constant (red line). The agreement is satisfactory for all cells. The 6 pairs of plots correspond to the 6 detector cells.

A very good agreement between the analytical response model and the MC sample is reached for all cells, thus proving the feasibility of an analytical description of the detector response.

4.4 Convolution of the input E_{true} spectrum and the response model

Conditional probability density function

A conditional probability density function (PDF) is a probability density function for a set of observables x giving the value of other observables y. It is denoted as $F(x|y)$ (read F of x knowing y). The mathematical difference between a multi-dimensional PDF and a conditional PDF lies in the normalisation. A multi-dimensional PDF is normalised to 1 across the x-y range:

$$\int\int F(x,y)dxdy = 1 \tag{4.12}$$

whereas a conditional PDF is normalised for each value of y:

$$\forall\ y, \int F(x,y)dx = 1 \tag{4.13}$$

A multi-dimensional PDF can be constructed from a conditional PDF by multiplying the conditional PDF by the PDF of the conditioning variable:

$$F(x,y) = f(y) \times F(x|y) \tag{4.14}$$

2-Dimensional model

The convolution of the E_{true} spectrum and the detector response model is done through the product of conditional PDF and conditioning PDF and marginalisation: to construct the whole 2-dimensional model $F_{celli}(E_{true}, E_{rec})$, the response model R_{celli} is used as a conditional PDF and it is multiplied by the E_{true} spectrum obtained from the BESTIOLE code, $S_{\text{pred}}(E_{true})$, and the acceptance of the cell, $\epsilon_{celli}(E_{true})$:

$$F_{celli}(E_{true}, E_{rec}) = S_{\text{pred}}(E_{true}) \times \epsilon_{celli}(E_{true}) \times R_{celli}(E_{rec}|E_{true}, \vec{p}) \tag{4.15}$$

with $\vec{p}$ the parameters of the response model.

The acceptance for each cell is obtained from the MC by comparing the number of events reconstructed in a given cell to the number of events truly generated in that cell. The acceptance is presented in Figure 4.8 for all cells.

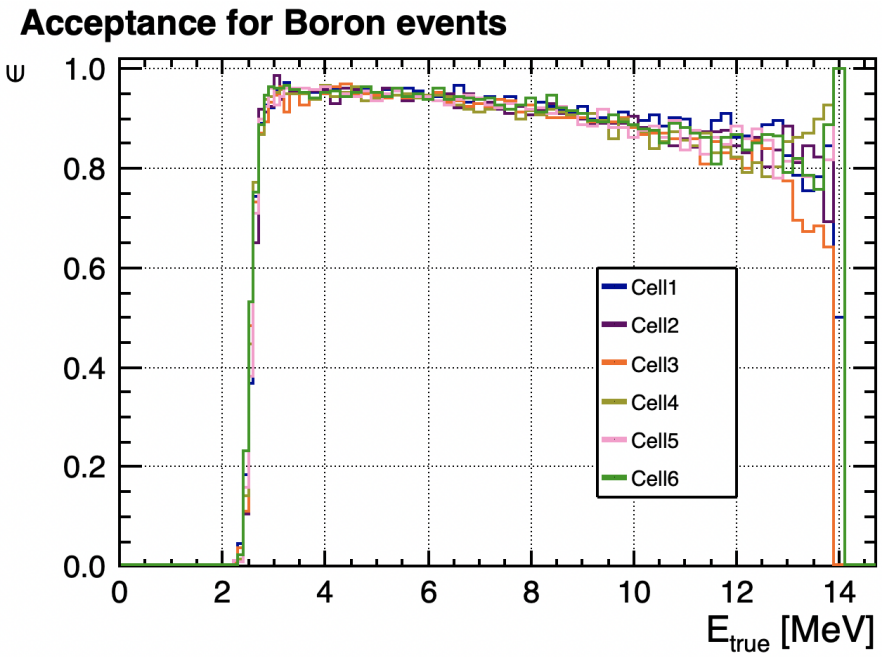

Figure 4.8: Acceptance of the boron events for each cell.

Marginalisation

In the data sample, we don't have access to the E_{true} information hence we can not use the 2-dimensional PDF directly. The 2-dimensional PDF must first be marginalised on E_{rec}:

$$F_{E_{rec}}(E_{rec}, \vec{p}) = \int S_{pred}(E_{true}) \times \epsilon(E_{true}) \times R_{celli}(E_{rec}|E_{true}, \vec{p}) dE_{true} \tag{4.16}$$

4.5 Validation of the extraction of the detector response parameters through a fit of the marginalised PDF

Test of the procedure

We first set to validate the marginalised fit by checking on a MC sample that the response model parameter values obtained from the marginalised fit (also referred to as

1D fit) match the values extracted from the simultaneous fits of MC samples binned in E_{true} (also referred to as 2D fit) The energy scale from the 1D fit and the 2D fit as well as their ratio is presented in Figure 4.9 for cell 3. The ratio of the energy scale function is in agreement at ± 1 %, very similar behaviour is observed for all cells.

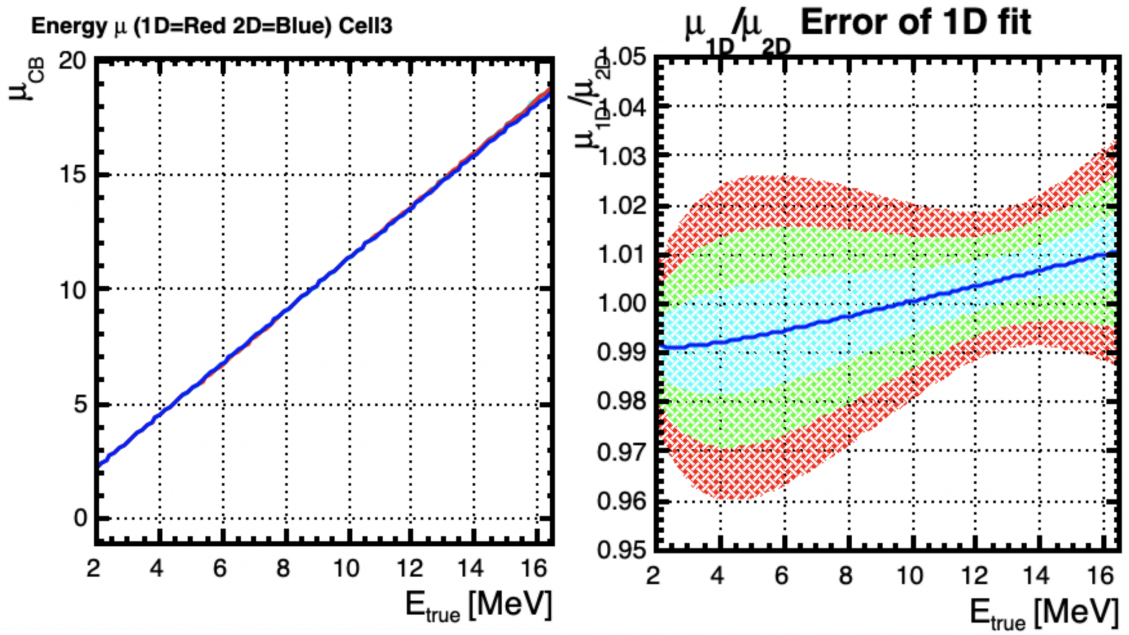

(a) (b)

Figure 4.9: Energy scale of the Boron events model when tuned with the marginalised fit (red) and the 2D tuning (blue) 4.9a. The ratio between the 1D and 2D tuned energy scale is in agreement at the ±1 % level, the colour bands correspond to 1 σ (cyan) 2 σ (green) and 3 σ (red) levels of statistical uncertainty 4.9b.

However, the energy resolution comparison presented in Figure 4.10 shows a disagreement between the 1D and 2D fit. After investigation, it appears that the 1D fit has very little sensitivity to the energy resolution. The parameters' value obtained by the 1D fit and their uncertainty is presented in Table 4.2 together with the parameters value obtained with the 2D fit and their uncertainty. The value of σ_0 is very low and the error is large, showing the lack of sensitivity of the 1D fit to this parameter. Additionally, parameters α_0, α_1 and n_0 show large correlations ($\geq$ 90 %) as shown in Table 4.3.

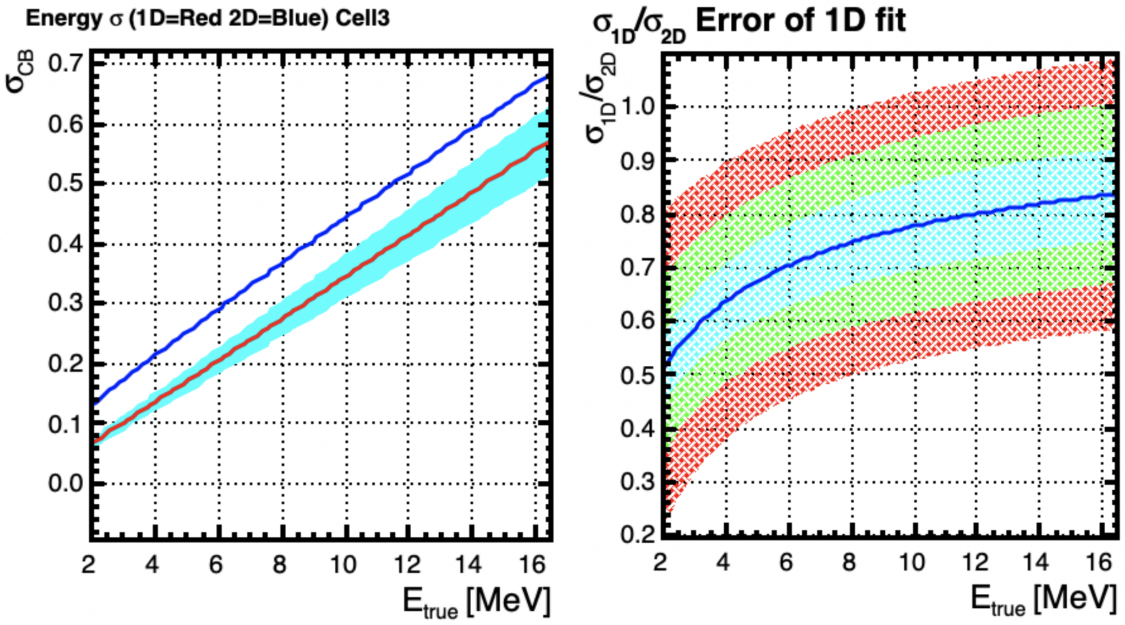

(a) (b)

Figure 4.10: Energy resolution of the Boron events model when tuned with the marginalised fit (red) and the 2D tuning (blue) 4.10a. The ratio between the 1D and 2D tuned energy resolution is not in agreement, the colour bands correspond to 1 σ (cyan) 2 σ (green) and 3 σ (red) levels of statistical uncertainty 4.10b.

	1D fit		2D fit	
Parameter	Fit value	Error	Fit value	Error
μ_0	7.21	0.07	7.240	0.002
μ_1	1.145	0.008	1.140	0.009
μ_2	0.001	0.002	-0.0006	0.0003
σ_0	0.0004	0.8	0.0728	0.002
σ_1	0.03	0.003	0.0325	0.0008
α_0	2.5	0.5	2.35	0.05
α_1	-0.08	0.04	-0.051	0.005
n_0	1.1	0.4	0.97	0.04

Table 4.2: Parameters' value resulting from the 1D fit of the Boron events for cell 3; similar results are observed for the other cells. The fit has very little sensitivity to the energy resolution and energy escape, as can be seen by the large error on the small value of σ_0

	μ_0	μ_1	μ_2	σ_0	σ_1	α_0	α_1	n_0
μ_0	1	0.80	-0.92	-0.09	0.19	0.65	-0.73	-0.70
μ_1		1	-0.55	-0.06	-0.15	0.72	-0.88	-0.60
μ_2			1	0.09	-0.34	-0.48	0.49	0.63
σ_0				1	-0.20	-0.002	0.02	-0.001
σ_1					1	-0.29	0.18	0.22
α_0						1	-0.90	-0.92
α_1							1	0.72
n_0								1

Table 4.3: Correlation matrix of the parameters for the response model of cell 3 from the 1D fit, α_0, α_1, n_0 show large correlation.

For these reasons, it has been decided to add pull terms on the parameters α_0, α_1, n_0, σ_0, σ_1.

Addition of pull terms on the energy resolution and energy escape parameters

Pull terms π were added on $\vec{\sigma}$, $\vec{\alpha}$ and n_0 parameters. The energy resolution parametrisation incremented by the pull terms is given by:

$$\sigma_{CB}(\mu_{CB}) = \sqrt{[\sigma_0(1+\pi_{\sigma_0})]^2 \times \mu_{CB} + [\sigma_1(1+\pi_{\sigma_1})]^2 \times \mu_{CB}^2} \tag{4.17}$$

The α and n parameters are now given by:

$$\alpha(\mu_{CB}) = \alpha_0(1+\pi_{\alpha_0}) + [\alpha_1(1+\pi_{\alpha_1})] \times \mu_{CB} \tag{4.18}$$

$$n = n_0(1+\pi_{n_0}) \tag{4.19}$$

The $\vec{\sigma}$, $\vec{\alpha}$ and n_0 parameters are now fixed to the value obtained in the 2D tunning of the detector response model, and the $\vec{\pi}$ parameters are allowed to vary. The fits presented in the next section are made by minimising the following χ^2:

$$\chi^2 = \sum_r \left(\frac{M_r - N \times F_{E_{rec}}(E_{rec}, \vec{\mu}, \vec{\pi})}{U_r} \right)^2 + \sum_i \left(\frac{\pi_i}{U_i} \right)^2 \tag{4.20}$$

The uncertainty of the pull term U_i for these parameters has been set to 10% in order to be conservative. With the implementation of pull terms, we can no longer use the cosmogenic ^{12}B control sample to determine systematic uncertainties on the energy resolution and energy escape parameters. The determination of the systematic uncertainties on the energy scale parameters is still valid, nonetheless.

The systematic uncertainty on the energy resolution and energy escape parameters could be extracted from the γ calibration sources. Unlike the Boron events, which have a continuous spectrum, calibration sources present mono-energetic γ lines. The marginalised fit should be more sensitive to the energy resolution in this case.

Validation of marginalised fit with pull terms

To validate the procedure, the marginalised fit is performed on MC and the resulting detector response model is compared to the detector response model obtained in the 2D fit. The results of both fits should be compatible.

The result of the fit of the marginalised PDF on the MC sample with the added pull terms on the energy resolution parameters $\vec{\sigma}$ and tail parameters $\vec{\alpha}$, n_0 is presented in Figure 4.11. The fitted model describes well the MC data.

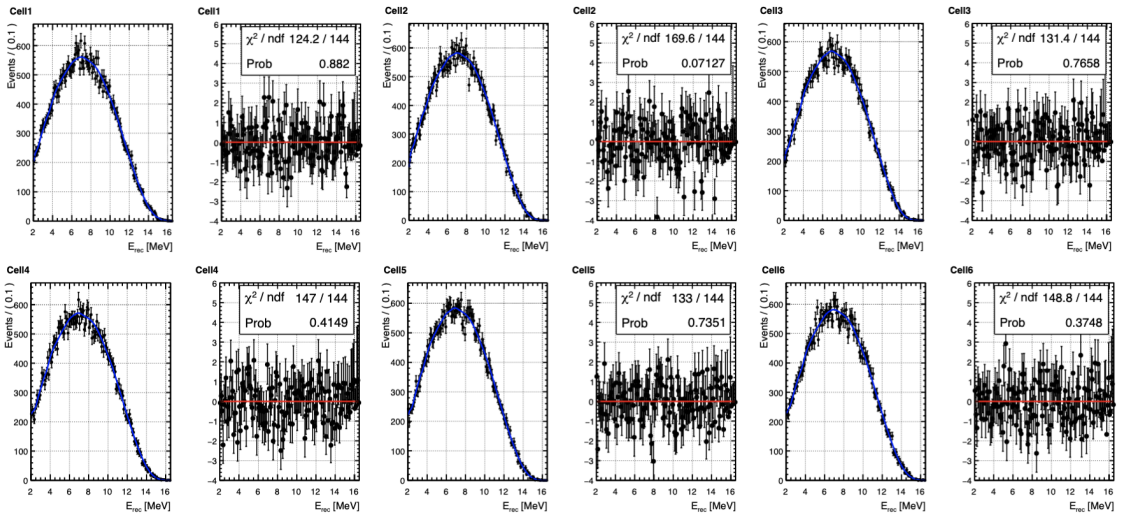

Figure 4.11: Fit of the marginalised PDF with added pull terms on $\vec{\sigma}$, $\vec{\alpha}$ and n_0 parameters. The pull plot is compatible with a null constant for all cells, showing the good agreement of the model with the MC sample. The 6 pairs of plots correspond to the 6 detector cells.

The energy scale of the 1D and 2D fits are presented in Figure 4.12.

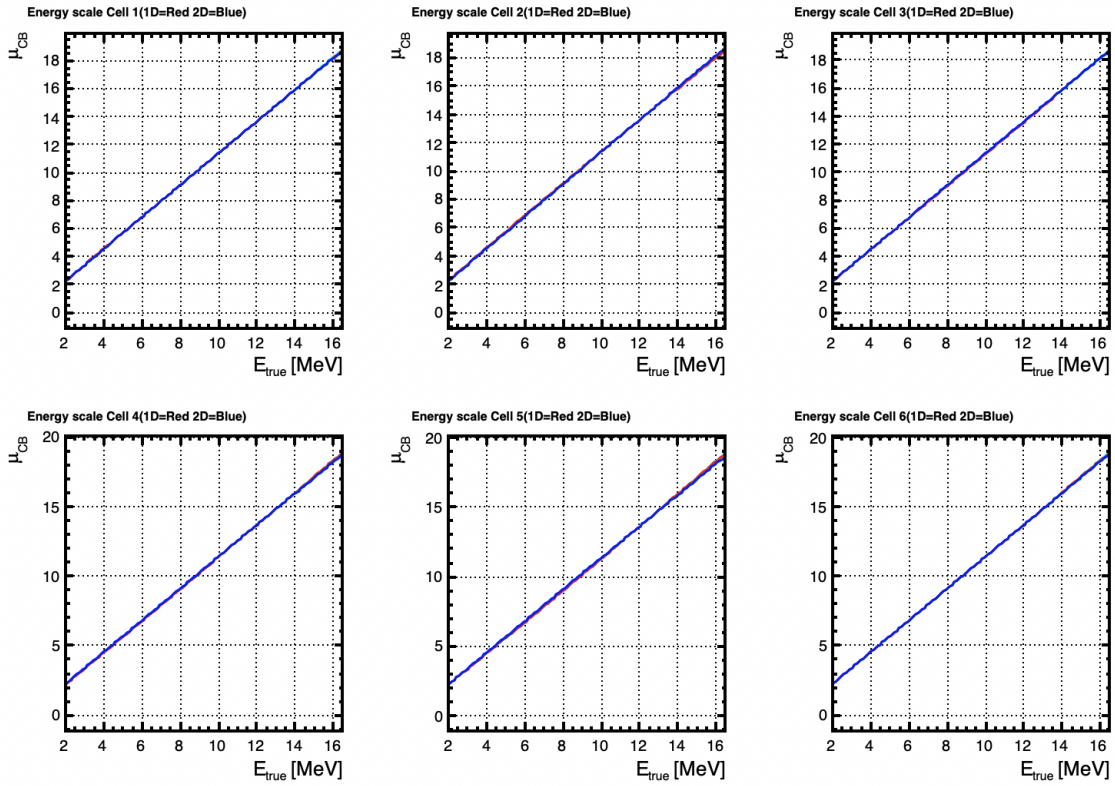

Figure 4.12: Energy scale given by the 1D fit (red) and 2D fit (blue)

The ratio between the 1D and 2D fit energy scale is presented in Figure 4.13. The ratio is statistically compatible with 1 for all cells, proving that the marginalised fit

gives consistent results with the 2D tuning of the response model.

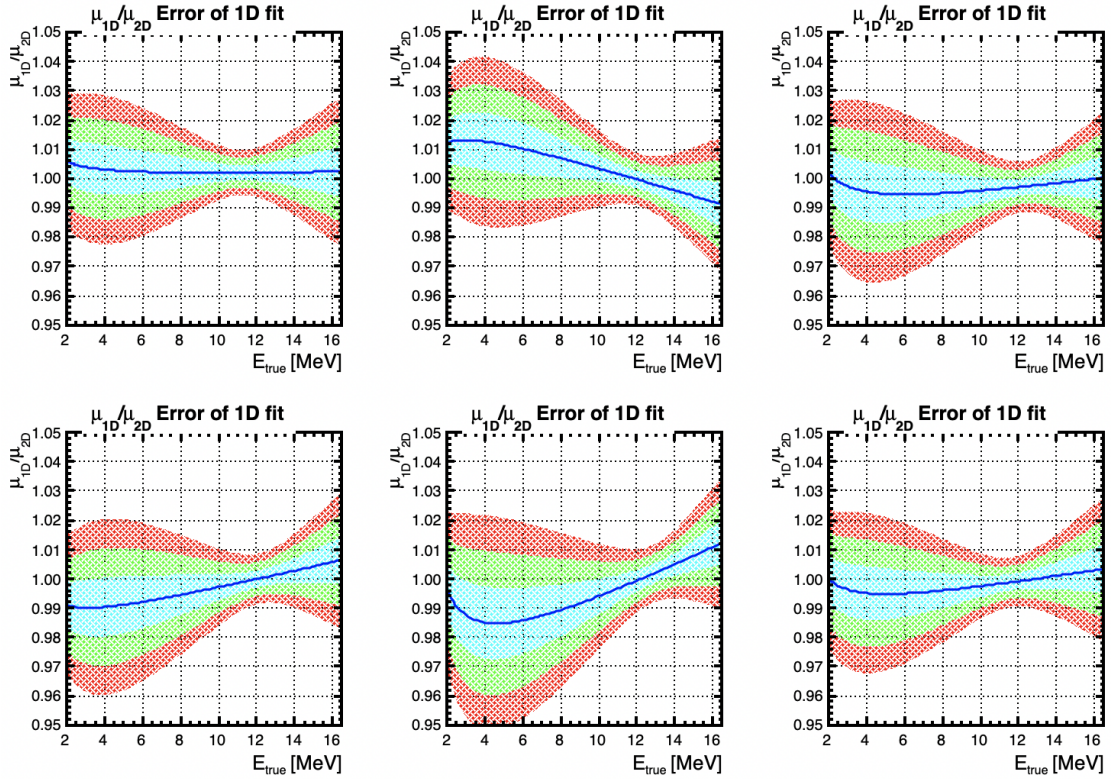

Figure 4.13: Ratio of the energy scale between the 1D and 2D fits. The ratio is compatible with 1 for all cells, the colour bands correspond to 1 σ (cyan) 2 σ (green) and 3 σ (red) levels of statistical uncertainty.

The energy resolution and its ratio between 1D and 2D fit are presented in figures 4.14 and 4.15 respectively, although the pull terms on these parameters limit the freedom of the 1D fit to deviate significantly from the 2D model. The large errors on the energy resolution given by the 1D fit show the low sensitivity of the marginalised fit to these parameters.

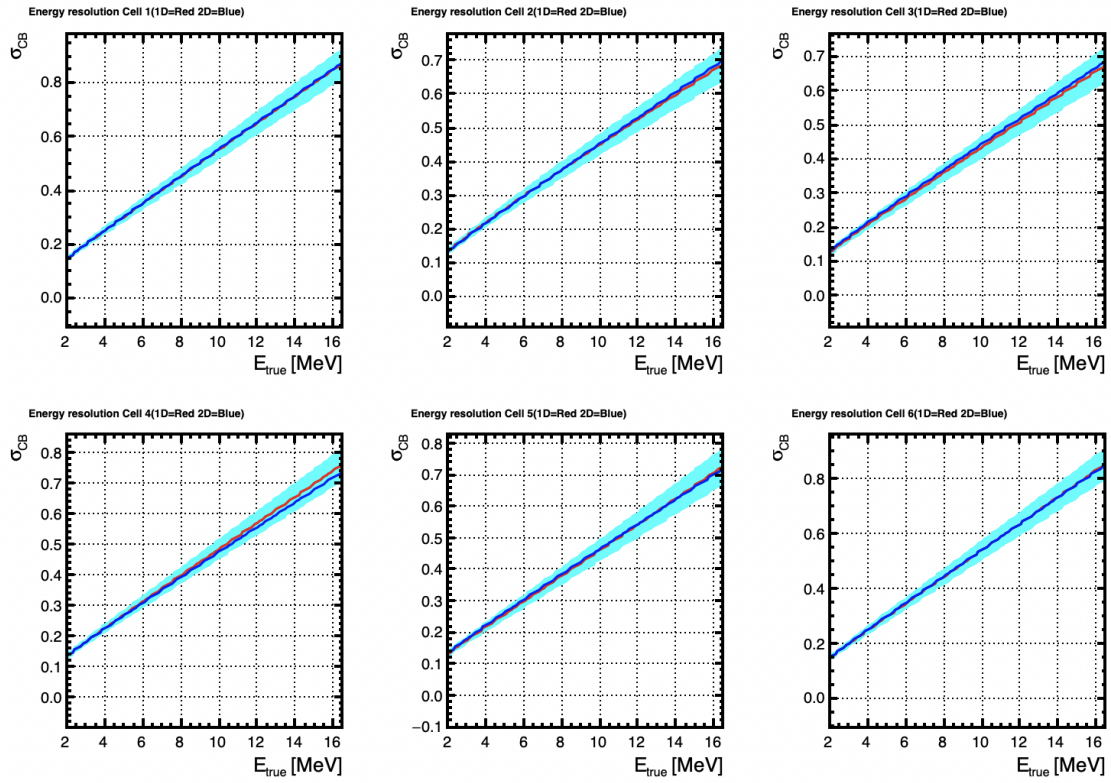

Figure 4.14: Energy resolution given by the 1D fit with pull terms (red) and 2D fit (blue).

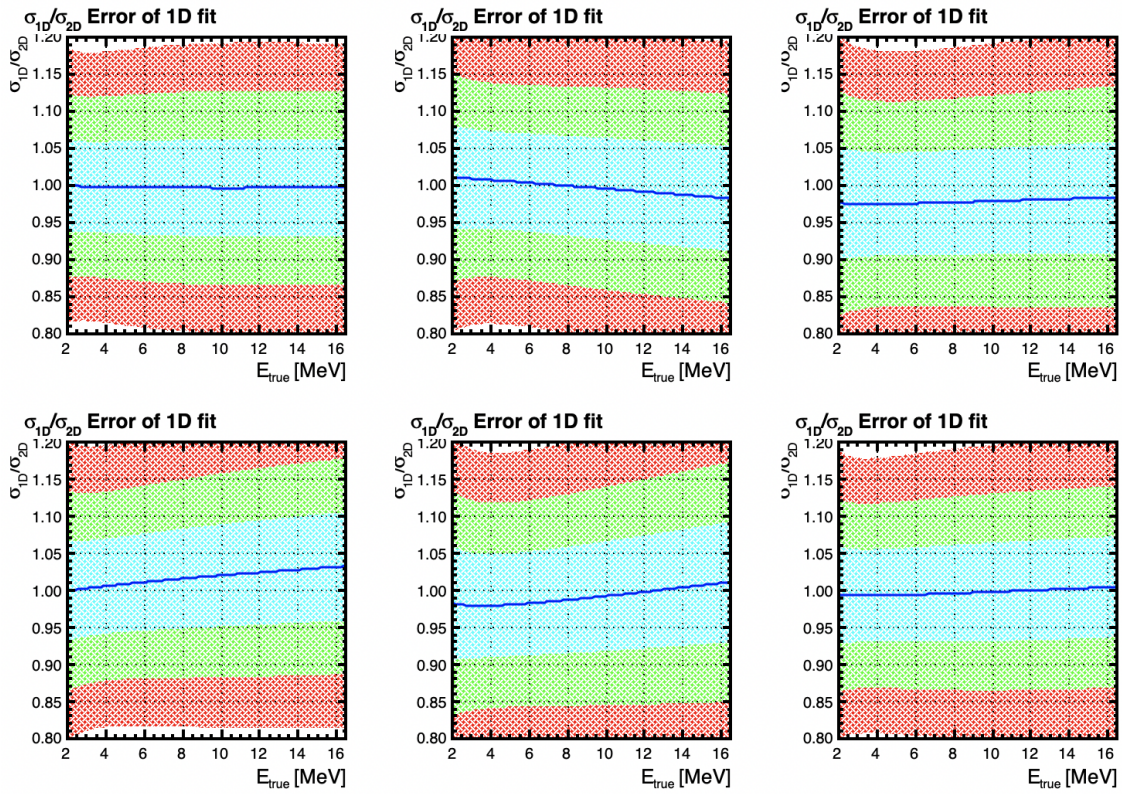

Figure 4.15: Ratio of the energy resolution between the 1D and 2D fits. The ratio is compatible with 1 for all cells, the colour bands correspond to 1 σ (cyan) 2 σ (green) and 3 σ (red) levels of statistical uncertainty. The pull terms on these parameters limit the freedom of the fit to deviate significantly. The large errors show the low sensitivity of the marginalised fit to the energy resolution parameters.

The good agreement of the detector response model obtained from the marginalised fit and the 2D tunning validates the procedure.

4.6 Marginalised fit comparison between Data and MC: extraction of systematics of the detector response model

The marginalised fit is performed on the measured data spectrum of Boron events, and it is compared to the marginalised fit on MC Boron events, in order to extract systematic uncertainties on the energy scale of the detector response model.

The result of the marginalised fit is presented in Figure 4.16. A good agreement between the fitted model and the measured data is reached for all cells.

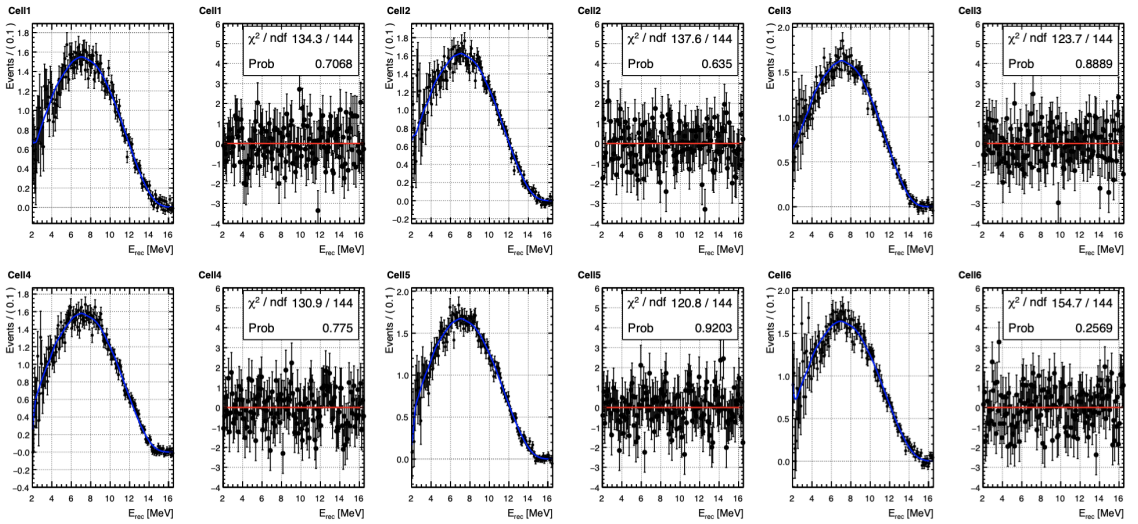

Figure 4.16: Marginalised fit on measured Boron spectrum for each cell. The fits show good agreement for all cells.

The energy scale obtained from the marginalised fit on measured data is compared to the one obtained from the marginalised fit on the MC sample (see Figure 4.17). The ratio of the energy scale is presented in Figure 4.18, the energy scales are globally in agreement, light tension with 2.5σ significance are visible at low energy for cells 4 and 5.

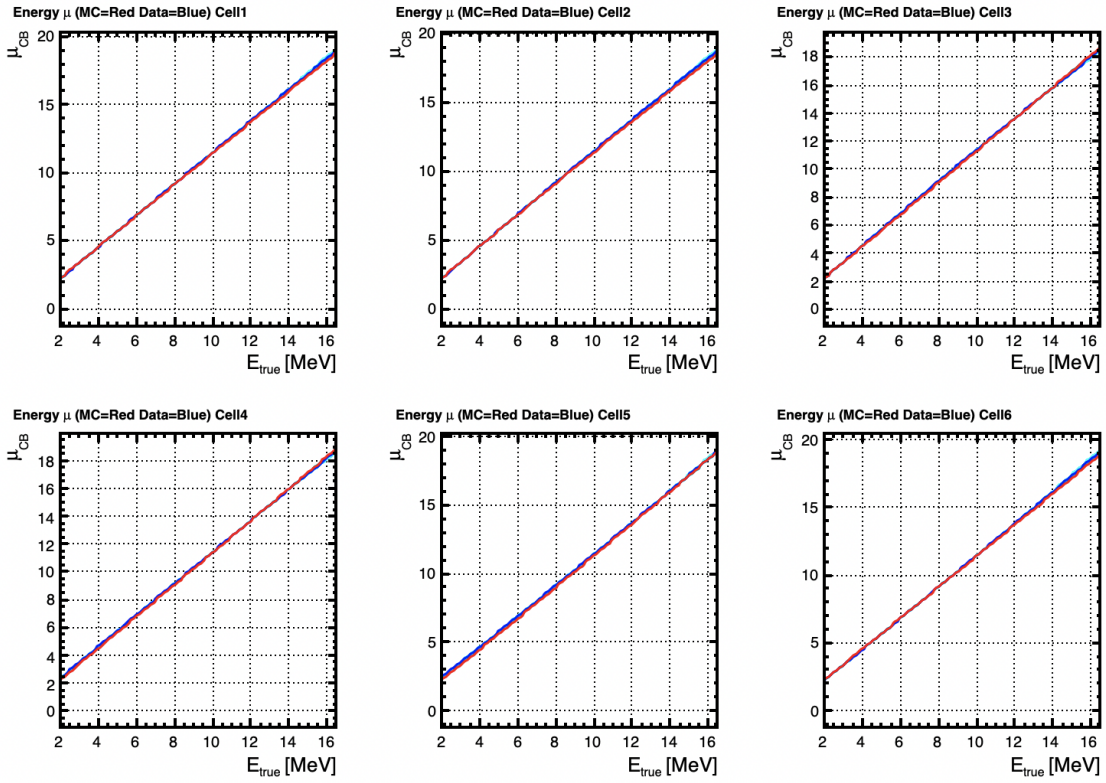

Figure 4.17: Energy scale from marginalised fit on Data and MC.

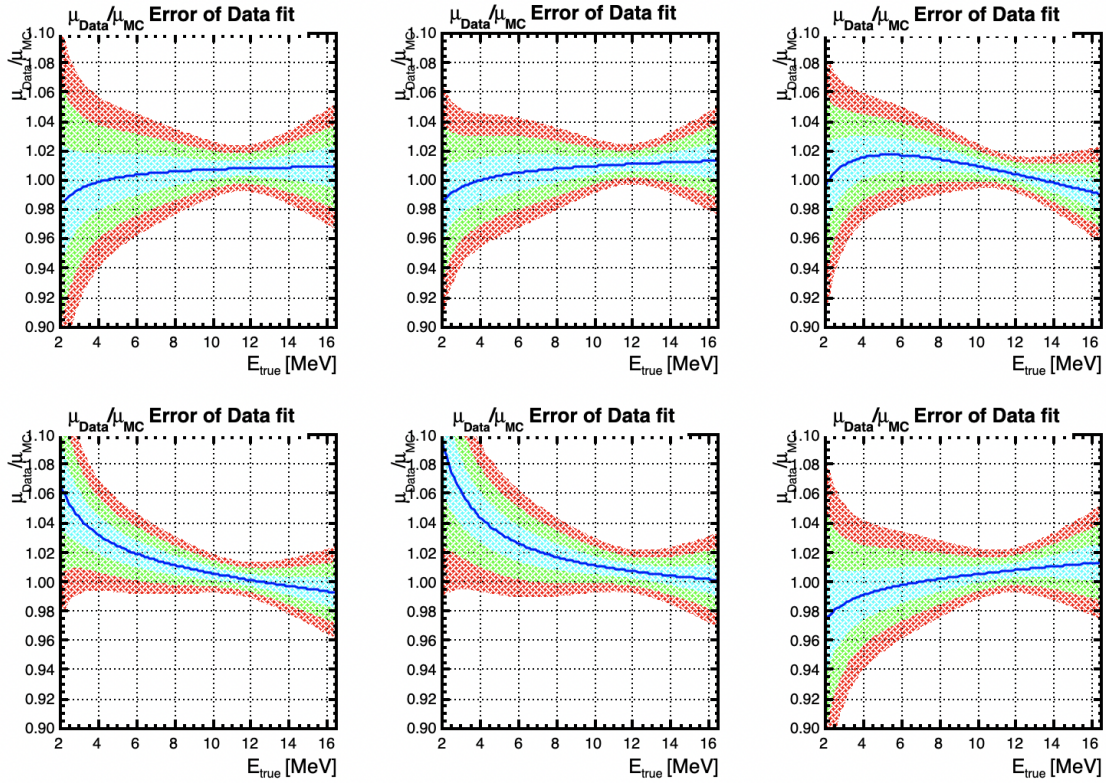

Figure 4.18: Ratio of the energy scale obtained from the marginalised fit on Data and MC. The energy scales are globally in agreement, light tensions of 2.5σ significance are visible for cells 4 and 5 at low energy.

The values of the energy scale parameters $\vec{\mu}$ obtained from the marginalised fit for

data and MC are presented in Table 4.4. The values from data and MC are statistically compatible. Therefore, the sytematic uncertainties of the response model come solely from the statistical uncertainties of its parameters. The μ_2 parameter, describing a possible non-linearity in the energy scale, is compatible with 0 in both MC and data for all cells, so no systematic uncertainty is determined on this parameter. Concerning the parameters μ_1 and μ_0, the statistical uncertainty of the parameters for data and MC is added in quadrature (see Table 4.5).

Cell	MC/Data	μ_0	μ_1	μ_2
1	MC	7.29±0.05	1.146±0.003	-0.0007±0.002
	Data	7.32±0.09	1.161±0.009	-0.0008±0.003
2	MC	7.31±0.06	1.142±0.004	-0.003±0.002
	Data	7.36±0.09	1.160±0.008	-0.002±0.003
3	MC	7.20±0.06	1.135±0.004	-0.0004±0.002
	Data	7.32±0.07	1.146±0.008	-0.004±0.003
4	MC	7.23±0.06	1.145±0.004	-0.0007±0.002
	Data	7.35±0.06	1.134±0.008	-0.0008±0.002
5	MC	7.15±0.08	1.137±0.005	-0.003±0.002
	Data	7.32±0.08	1.126±0.008	-0.002±0.003
6	MC	7.26±0.06	1.145±0.004	0.0007±0.002
	Data	7.25±0.009	1.160±0.009	0.002±0.003

Table 4.4: Energy scale parameters for data and MC obtained from the marginalised fit. The parameters are statistically in agreement.

Cell	Syst. uncertainty	
	μ_0	μ_1
1	1.4%	0.9%
2	1.5%	0.8%
3	1.2%	0.8%
4	1.0%	0.8%
5	1.5%	0.8%
6	1.4%	0.9%

Table 4.5: Systematic uncertainty on parameters μ_0 and μ_1 of the energy scale, the uncertainty is computed as the quadratic sum of the uncertainty of the marginalised fit on data and MC.

4.7 Conclusions

In this chapter we have proposed an analytical detector response model for cosmogenic ^{12}B events and we have shown that it is able to describe accurately MC as well as data. We have demonstrated that a fit of our model to data allows to retrieve the values of part of the detector response parameters. The remaining detector response parameters may likely be fitted from γ sources calibration data, but that work goes beyond the scope of this thesis. A comparison of the detector response parameters obtained from the fits to the data and MC samples yields very compatible models and

leads to the assignment of sub-percent systematic uncertainties on the linear coefficient μ_1.

Since we haven't been able to retrieve all the detector response parameters from the ^{12}B data, for the antineutrino sample we will fit the response model to the Geant4 MC simulation. Given the similarities of the ^{12}B and $\overline{\nu_e}$ signals in our detector, we extrapolate to the $\overline{\nu_e}$ sample our conclusions for ^{12}B events:
- the detector model obtained from MC describes very well the data,
- hence a systematic uncertainty on the detector response model parameters equal to their statistical uncertainty from the fit to MC will be assumed for the $\overline{\nu_e}$ detector response model. Only the μ_0 and μ_1 parameters, for which systematic differences are observed, get assigned additional systematic uncertainties, $\sim$1.4 and 0.9 %, respectively.

Bibliography

[A+16a] Y. Abe et al. Muon capture on light isotopes measured with the Double Chooz detector. *Phys. Rev. C*, 93(5):054608, 2016.

[AS17] Shinichiro Abe and Tatsuhiko Sato. Implementation of muon interaction models in phits. *Journal of Nuclear Science and Technology*, 54(1):101–110, 2017.

[Bon] A. Bonhomme. STEREO internal communication, DocDB-998.

[FG03] C. W. Fabjan and F. Gianotti. Calorimetry for particle physics. *Rev. Mod. Phys.*, 75:1243–1286, 2003.

[GP74] B. Goulard and H. Primakoff. Nuclear muon-capture sum rules and mean nuclear excitation energies. *Phys. Rev. C*, 10:2034–2044, Nov 1974.

[HLW07] Chris Hagmann, David Lange, and Douglas Wright. Cosmic-ray shower generator (cry) for monte carlo transport codes. In *2007 IEEE Nuclear Science Symposium Conference Record*, volume 2, pages 1143–1146, 2007.

[Rog] R. Rogly. STEREO internal communication, DocDB-959.

CHAPTER 5

ANALYTICAL DETECTOR ENERGY RESPONSE MODEL FOR NEUTRINO EVENTS. OSCILLATION SEARCH WITH PHASE II DATA

CONTENTS

5.1 Introduction

In this chapter, we will expand the framework described in the previous chapter to develop an analytical detector response model for the neutrino events. This modelisation will be used to search for an oscillation signal in STEREO's Phase II neutrino data by setting up an oscillation fit that uses the analytical detector response model. Finally, a statistical analysis of the oscillation signal will be performed to determine the accepted and excluded regions in the oscillation parameters space.

The analytical modelisation of the energy response of the detector aims at having a minimal Geant4 MC input. In principle, the relatively small number of parameters defining the model could be deduced from calibration data, in a data-driven approach. However, lacking time and having proved with ^{12}B events the very good agreement of STEREO's Geant4 simulation with data, the exercise is not done in this thesis, but remains open for later studies. The use of the analytical detector response model does bring an advantage: the implementation of systematic uncertainties on the model is straightforward as it simply translates to errors on the detector model parameters, which simply become nuisance parameters in the oscillation search fit.

5.2 Detector response effects for oscillation searches

5.2.1 Baseline resolution effects

A first study was performed to determine the effects of the baseline resolution of the detector on the measured oscillation pattern. In the STEREO experiment, there are two sources of uncertainty on the baseline of a detected neutrino: the volume of the reactor core and the volume of the detection cell. The effect of the baseline resolution is studied using a sample of ∼150 000 simulated neutrinos with the Geant4 framework. The Geant4 simulation of the detector includes the detailed geometric description and positions of the reactor core and the STEREO detector. The distribution of the true baseline for events reconstructed in the TG cells is shown in Figure 5.1. By solid angle considerations, the number of neutrino that could potentially interact in the detector is smaller for larger baselines, hence the decreasing shape of the baseline distribution in Figure 5.1.

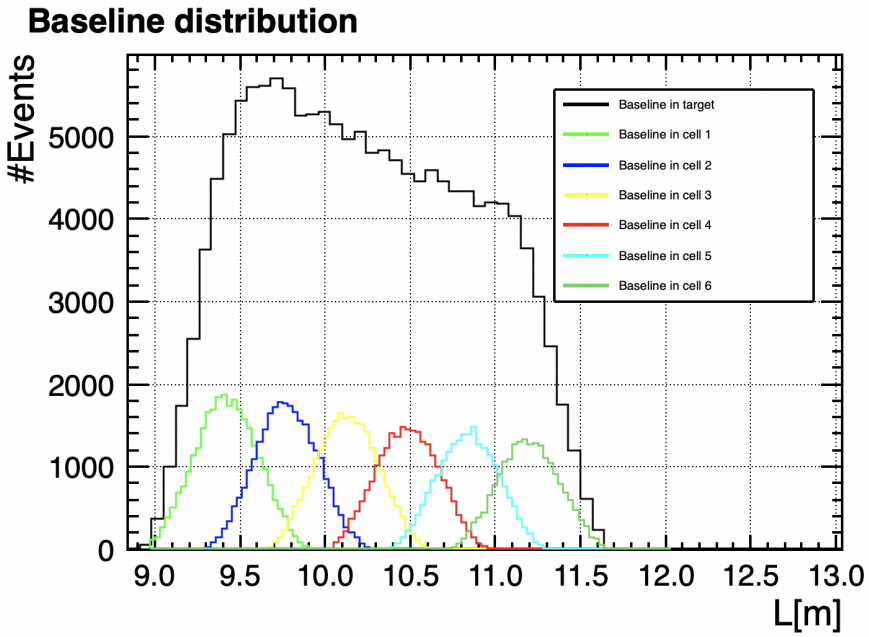

Figure 5.1: Baseline distribution for ∼150 000 simulated neutrino events for the TG cells and the whole Target (black). The decreasing shape of the distribution is due to a decreasing solid angle.

To evaluate the effect of the baseline resolution on the oscillation pattern, the true energy spectra of the simulated neutrino events is weighted by the survival probability for an oscillation with the RAA parameter values ($\sin^2(2\theta)$=0.17; Δm^2=2.3 eV^2). First, the true baseline of the event is taken to obtain the survival probability. Then the computation is done again using the mean baseline of the interaction cell instead. The oscillated spectrum with the true baseline is compared to the spectrum with the mean baseline in Figure 5.2.

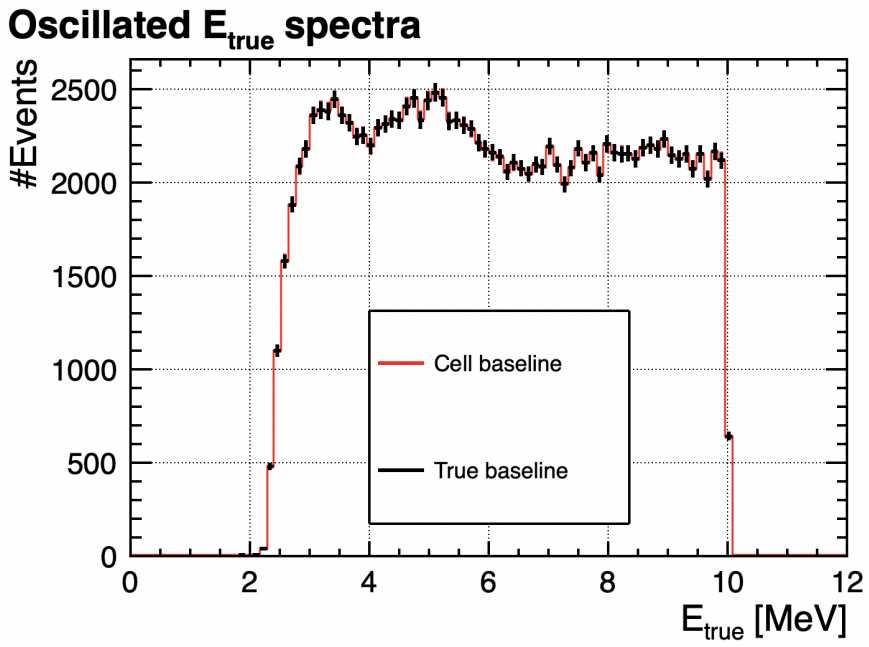

Figure 5.2: Comparison of true energy spectra of simulated neutrino events weighted by the survival probability of an oscillation with the RAA parameters with the true baseline of the event (black) and the mean baseline of the cell (red).

The residuals between the two spectra are presented in Figure 5.3. It follows the oscillation pattern of the RAA. However, the mean difference between both spectra is ∼0.3 % of the statistical uncertainty, computed here as the poissonian fluctuation of a sample of 150 000 events. The statistical fluctuations estimated this way are very conservative. Although, the 150 000 events is a realistic estimate of the number of neutrino detected during the lifetime of STEREO, a mean signal-to-background ratio of ∼1 must be considered, resulting in larger statistical uncertainties. To conclude, effects of the baseline resolution on the oscillation pattern can be considered negligible.

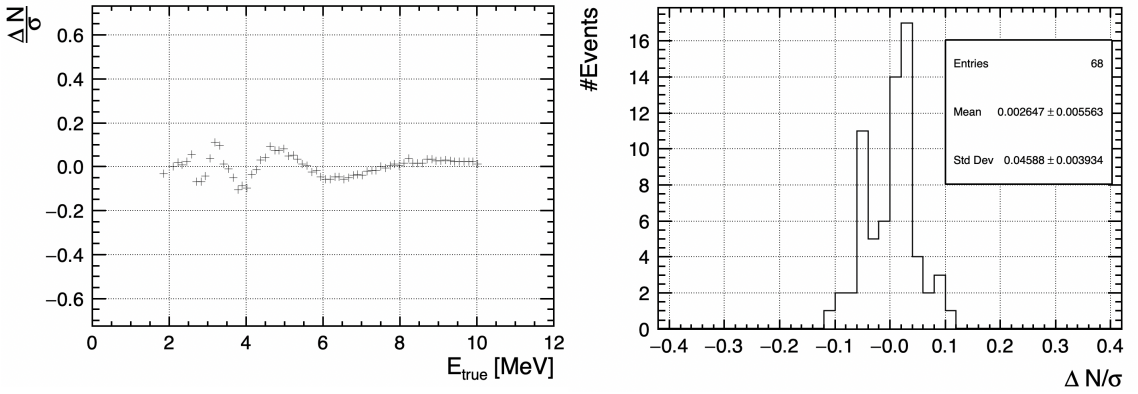

(a) (b)

Figure 5.3: Residuals between oscillated spectra with true baseline and mean baseline 5.3a, the residual shows an oscillation pattern. The mean value of the residual is ∼0.3 % of the statistical uncertainty 5.3b.

5.2.2 Energy resolution effects

The energy-related detector effects (energy scale, energy resolution, energy leaks...) on the oscillation pattern is highlighted by comparing true and reconstructed energy spectra weighted by the survival probability for an oscillation (see Figure 5.4).

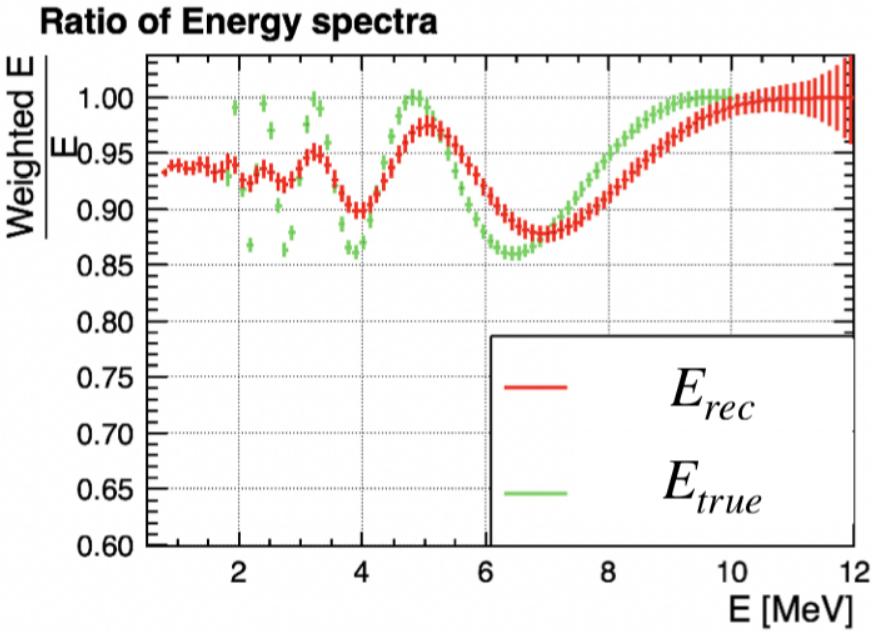

Figure 5.4: Ratio between oscillated and non-oscillated energy spectra for the reconstructed energy (red) and true energy (green) coming from the Geant4 MC simulation. The oscillation parameters have the values of the RAA best-fit.

In this case, both spectra come from the Geant4 MC simulation of the detector. As can be seen in Figure 5.4, for the reconstructed energy spectra, the effective amplitude and frequency of the oscillation are reduced. A good understanding of the detector effects is thus required to properly estimate the oscillation parameters.

5.2.3 Analytical model of the detector energy response for neutrino events

Parameterisation of the detector energy response model

The analytical model of the detector response for neutrino events, $R(E_{rec}, E_{true})$, is composed of a gaussian (G) and a Crystal Ball (CB) distribution. The gaussian part of the CB describes the main energy peak, constituted of events that deposit all their energy in the active volume of the detector; the non-gaussian tail of the Crystal Ball describes events for which a part of the energy escapes the detector. The gaussian distribution is necessary to describe a secondary component due to one of the two annihilation γ escaping the detector.

$$R(E_{rec}, E_{true}) = f_G \times G(E_{rec}, \mu_G, \sigma_G) + f_{CB} \times CB(E_{rec}, \mu_{CB}, \sigma_{CB}, \alpha, n) \tag{5.1}$$

where f_G and f_{CB} are relative normalisation parameters given by:

$$f_G = \frac{(1-f_0)}{\int G(E_{rec}, \mu_G, \sigma_G) dE_{rec}} \tag{5.2}$$

$$f_{CB} = \frac{f_0}{\int CB(E_{rec}, \mu_{CB}, \sigma_{CB}, \alpha, n) dE_{rec}} \tag{5.3}$$

The f_0 parameter describes the amplitude of the gaussian with respect to the amplitude of the Crystal Ball.

The relation between reconstructed energy and true energy is expected to be roughly linear, with non-linearities described by a quadratic term in the polynomial of E_{true} parametrising the mean of the CB:

$$\mu_{CB}(E_{true}) = \mu_2 \times E_{true}^2 + \mu_1 \times E_{true} + \mu_0 \tag{5.4}$$

The parameters $\vec{\mu}$ completely define the energy scale of the detector. The gaussian component that models events for which an annihilation γ escaped, should follow the same dependence on E_{true}, hence the mean of the gaussian shares these parameters with the Crystal Ball; only a shift in E_{true} due to the escape of energy is included:

$$\mu_G(\Delta) = \mu_2 \times \Delta^2 + \mu_1 \times \Delta + \mu_0 \tag{5.5}$$

where

$$\Delta = E_{true} - d \tag{5.6}$$

The amount of escaping energy is found to be independent of the event's energy therefore the parameter d does not depend on the energy.

The parametrisation of the energy resolution follows the same principles as the ones presented in the previous chapter for the Boron model, except that the noise term is not compatible with 0 for the neutrino model.

The parametrisation of the standard deviation of the Crystal Ball is given by:

$$\sigma_{CB}(\mu_{CB}) = \sqrt{\sigma_0^2 \times \mu_{CB} + \sigma_1^2 \times \mu_{CB}^2 + \sigma_2^2} \tag{5.7}$$

For the standard deviation of the gaussian component, we enforce the same dependence with the energy but we allow a difference for the parameter σ_2 that does not depend on the energy, hence the parametrisation of the standard deviation of the gaussian component is given by:

$$\sigma_G(\mu_G) = \sqrt{\sigma_0^2 \times \mu_G + \sigma_1^2 \times \mu_G^2 + \sigma_{2G}^2} \tag{5.8}$$

The α parameter of the CB that describes the threshold from which the gaussian gives way to the power law, is parameterised by a saturation function:

$$\alpha(\mu_{CB}) = (\alpha_0 + \alpha_1 \times \mu_{CB} + \alpha_2 \times \mu_{CB}^2) - \exp(-1 \times (\alpha_3 \times \mu_{CB} + \alpha_4 \times \mu_{CB}^2)) \tag{5.9}$$

Finally, the power-law parameter of the Crystal Ball has been found to be compatible with a constant independent of the energy:

$$n(\mu_{CB}) = n_0 \tag{5.10}$$

Tuning of the detector response model parameters

The parameters in blue completely define the detector response model. To determine the value of these parameters, a Geant4 MC sample of neutrino events with a flat E_{true} spectrum is separated (after selection cuts and pair search procedure) in 78 E_{true} samples ranging from 2.2 to 10 MeV with a step of 0.1 MeV. These 78 samples are fitted simultaneously with the analytical response model, the resulting fit is presented in Figure 5.5 for a selection of samples. As for the Boron model, the normalisations of the model for the E_{true} samples are independent from one another, as per the definition of a conditional PDF. Each E_{true} sample is fitted on a restricted range in E_{rec} to take in as thoroughly as possible the main peak and the non-gaussian low-energy tail, but

excluding threshold effects at very low reconstructed energy and empty bins at too high reconstructed energies.

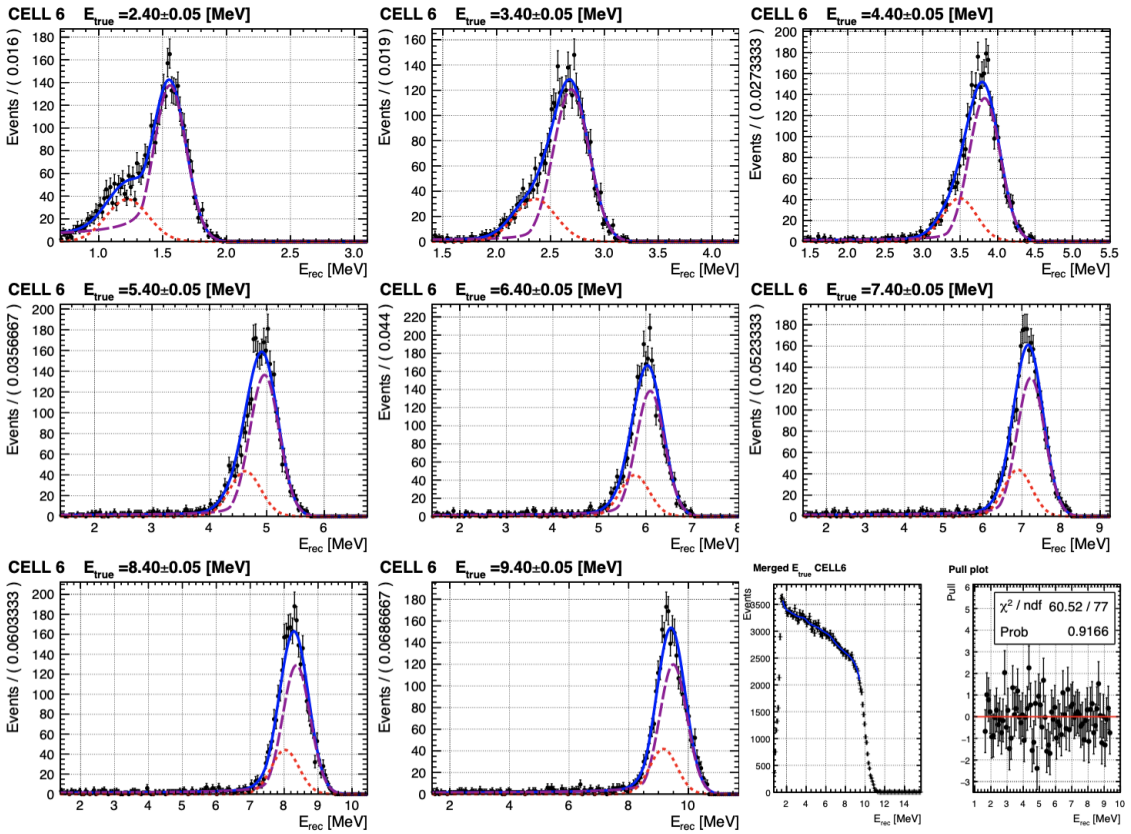

Figure 5.5: Some of the E_{true} samples used in the simultaneous fit of the analytical response model for cell 6. The complete model (blue) has a Crystal Ball component (violet) and a gaussian component (red). The data points come from a Geant4 MC neutrino sample after official selection cut and pair search procedure. The plot at the right bottom corner shows the model when all E_{true} samples are merged together and the pulls between the model and the data points, the pulls are fitted with a null constant the $\chi^2/\text{ndf} = 60.52/77$ reflecting the excellent agreement between the analytical response model and the Geant4 MC.

This procedure is iterated for each cell, the analytical response models of the cells being independent from one another. The agreement between the analytical response model and the Geant4 MC is checked by merging all E_{true} samples for a cell and computing the pulls between the model and the MC points. The χ^2 of the pulls and a null constant is computed for all cells. The agreement between the response model and the Geant4 MC is satisfactory for all cells (see Figure 5.6).

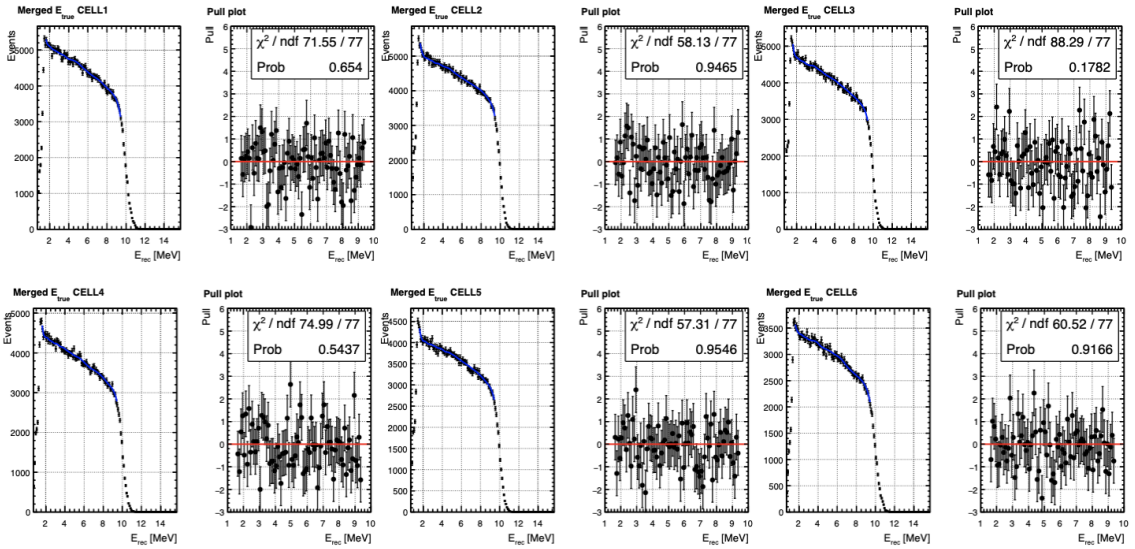

Figure 5.6: Merged MC E_{true} samples and analytical response model (blue line) for all cells, the agreement between the response model and MC is checked by computing the χ^2 between the pulls and a null constant (red line). The agreement is satisfactory for all cells. The χ^2 for cell 3 is slightly worse than for the other cells, but the value is driven by a limited number of points and stays compatible with statistical fluctuations.

5.3 Construction of the neutrino oscillation model

5.3.1 Convolution of the predicted E_{true} spectrum and the response model

Similarly to what has been done in the case of the Boron spectrum, a 2-dimensional PDF is created for each cell by multiplying the conditional PDF of the detector response R_{celli} (characterised by the parameters $\vec{p}$), the acceptance of the cell ϵ_{celli}, the predicted neutrino energy spectrum S_{pred} and the survival probability $\mathscr{P}_{\overline{\nu_e}\to\overline{\nu_e}}$ averaged over the E_{true} bin:

$$F_{celli}(E_{true}, E_{rec}, \vec{p}, \sin^2 2\theta_{new}, \Delta m^2_{4,1}) = S_{pred}(E_{true}) \times \epsilon_{celli}(E_{true}) \times \frac{1}{w_{E_{true}}} \int_{bin\ E_{true}} \mathscr{P}_{\overline{\nu_e}\to\overline{\nu_e}}(\sin^2 2\theta_{new}, \Delta m^2_{4,1}, E_{true}, L_{celli}) dE_{true} \times R_{celli}(E_{rec}|E_{true}, \vec{p}) \tag{5.11}$$

where $w_{E_{true}}$ is the width of the binning in E_{true}. Instead of the survival probability evaluated at the center of the bin, we use its average over the bin width, is order to avoid a bias in the oscillation parameter extraction.

Predicted spectrum $S(E_{true})$

The Huber prediction [Hub11] for pure ^{235}U to which is added a gaussian component with amplitude A_{bump}=12.1%, mean μ_{bump}=5.29 MeV and standard deviation σ_{bump}=0.55 MeV is taken as predicted E_{true} spectrum (see Figure 5.7). This is the excess observed by STEREO in the Phase II data [A$^+$21b]. A similar enhancement is observed by the PROSPECT, Daya-Bay and Double Chooz experiments [dK$^+$20c, A$^+$21c,

A+19b], This excess can not be explained by an oscillation, since the same enhancement is observed at various baselines. For the generation of pseudoexperiments, a fine binning of 50 keV is retaines for $S(E_{true})$.

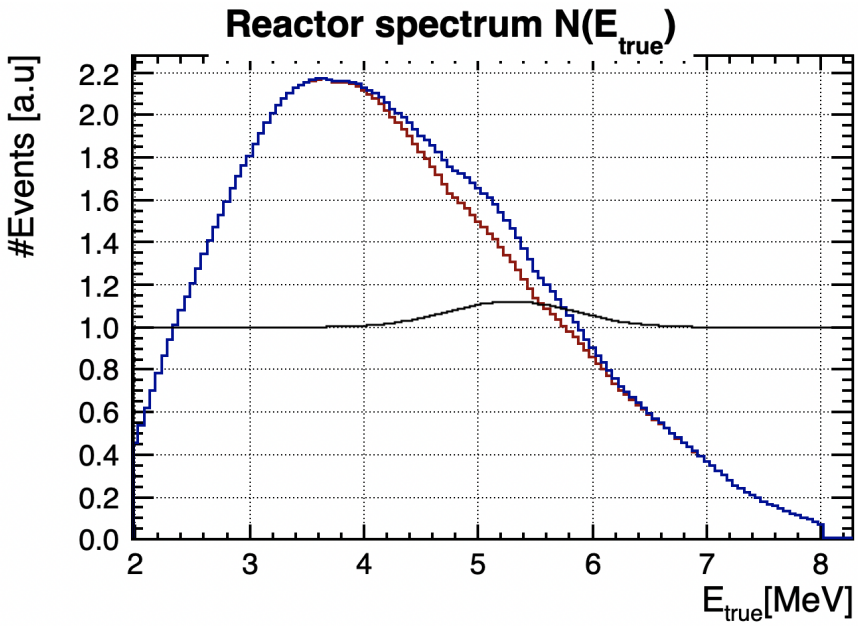

Figure 5.7: Huber predicted spectra (red), Huber predicted spectra with STEREO's excess added (blue) and ratio between the 2 spectra.

In the fit of the energy spectra, the shape of the predicted spectrum is free to vary. This is made possible by making each bin value of $S(E_{true})$ a free parameter. The bins of the measured data spectrum in E_{rec} are 250 keV wide. This binning is imposed by the PSD fit extraction of the neutrino rate described in section 2.4.4 Neutrino signal extraction. In the E_{true} space however, larger bins are seen to greatly facilitate the fit convergence. Indeed, tests showed very large anticorrelations (∼99%) between adjacent E_{true} bins when their width is set to 250 keV. Increasing the bin width in the E_{true} spectrum to 350 keV reduced the correlations to acceptable level (∼50 %) between bins and allowed the fit to converge in reasonable time lengths.

Acceptance ϵ_{celli}

The acceptance for each cell is computed using MC and comparing selected neutrino events (after selection cuts and pair search) in the cell to neutrino events truly generated in that cell. The acceptance for all cells is given in Figure 5.8. Unlike the predicted E_{true} spectrum, the acceptance is fixed in the fit, tests showed that a fine binning of the acceptance was required to avoid inducing a bias in the fitted oscillation parameters (mostly in the region where the acceptance is increasing or dropping very fast). A binning of 50 keV for the acceptance was therefore retained.

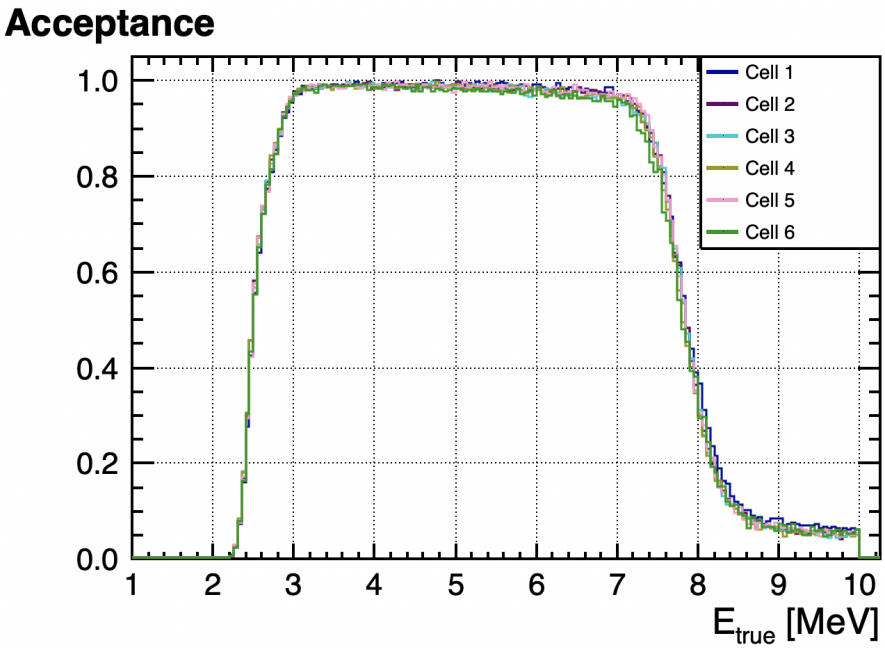

Figure 5.8: Acceptance of the neutrino events after pair search and selection cuts. The acceptance is computed as the ratio of the number of neutrino reconstructed in the cell of interest over the number of neutrino truly generated in that cell. The characteristic "step" shape of the acceptance distribution is due to the cuts at 1.625 MeV and 7.125 MeV on the reconstructed energy.

Marginalisation

The 2-dimensional PDF $F_{celli}(E_{true}, E_{rec}, \vec{p}, \sin^2 2\theta_{new}, \Delta m^2_{4,1})$ is marginalised on E_{rec} to obtain a PDF that does not depend on E_{true}:

$$F^{E_{rec}}_{celli}(E_{rec}, \vec{p}, \sin^2 2\theta_{new}, \Delta m^2_{4,1}) = \int F_{celli}(E_{rec}, E_{true}, \vec{p}, \sin^2 2\theta_{new}, \Delta m^2_{4,1}) dE_{true} \tag{5.12}$$

In practice, the fitting library RooFit is used in order to define the PDFs and perform all the integrations[1].

5.3.2 Test of the model

To check that the model does not induce a bias on the oscillation parameters when fitted to a data sample, the marginalised PDF was fitted to 10 Geant4 MC samples of 80 000 events in which an oscillation with the RAA parameters ($\sin^2 2\theta_{new}$=0.14, Δm^2_{41}=2.4 eV^2) was injected.

The number of samples was limited by the MC statistics, although 2.3×10^6 Geant4 MC events were generated, they were generated with a flat E_{true} spectrum in the range [1.8;10] MeV. The reshaping of the E_{true} spectrum to impose the Huber spectrum with an oscillation was done by an accept-reject procedure. In order to have statistically independent MC samples, an event can be used only once, hence we ended up with ~800 000 events.

A sample of 80 000 events has approximately the same statistical uncertainty has the nominal statistics of the full STEREO data collection which amounts to ~160 000 events with a mean signal-to-background ratio $\frac{S}{B} \approx 1$.

[1] Hence the name of our oscillation search fitting package: RooSTER

In the fit of the 10 MC samples, the oscillation parameters and the 250 keV-wide bins of the neutrino spectrum $S(E_{true})$ are left free.

The distribution of the bias on the oscillation amplitude and frequency retrieved by the fit are presented in Figure 5.9. No significant mean bias is observed for the amplitude nor the frequency parameters. The standard deviation is compatible with 1 for both the amplitude and the frequency, indicating that the errors of the fit are well estimated.

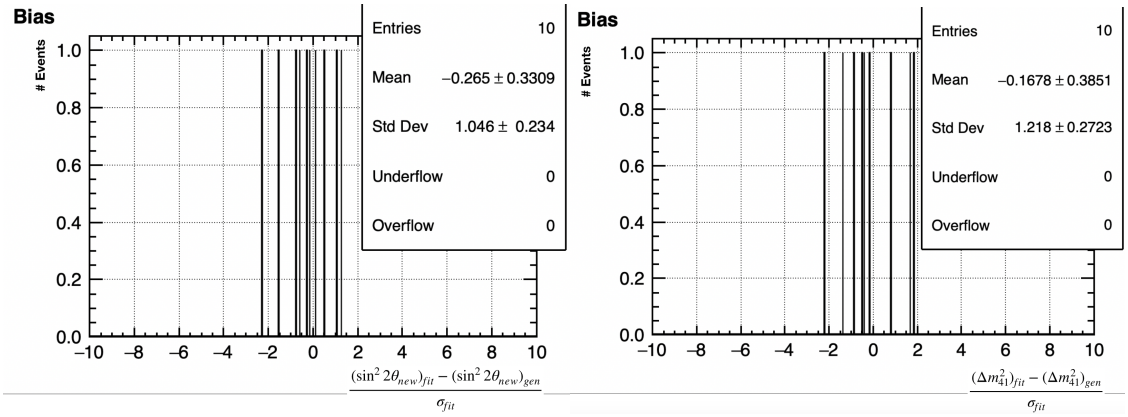

(a) (b)

Figure 5.9: Bias obtained on the oscillation amplitude 5.9a and frequency 5.9b from the fit of 10 MC samples of 80 000 events. The mean bias are both compatible with 0 (significance of 0.7σ for the amplitude and 0.4σ for the frequency). Besides, the standard deviation is compatible with 1, indicating that the errors of the fit are correctly estimated.

For illustrative purposes, a typical example of these fits is presented in Figure 5.10. The fitted value of the amplitude and frequency are very close to the injected value.

Somewhat strong fluctuations in the fitted values of the bins of the neutrino spectrum $S(E_{true})$, typical of unfolding problems can be observed. The anticorrelation of these fluctuations for neighbouring $S(E_{true})$ bins, is also to be noted.

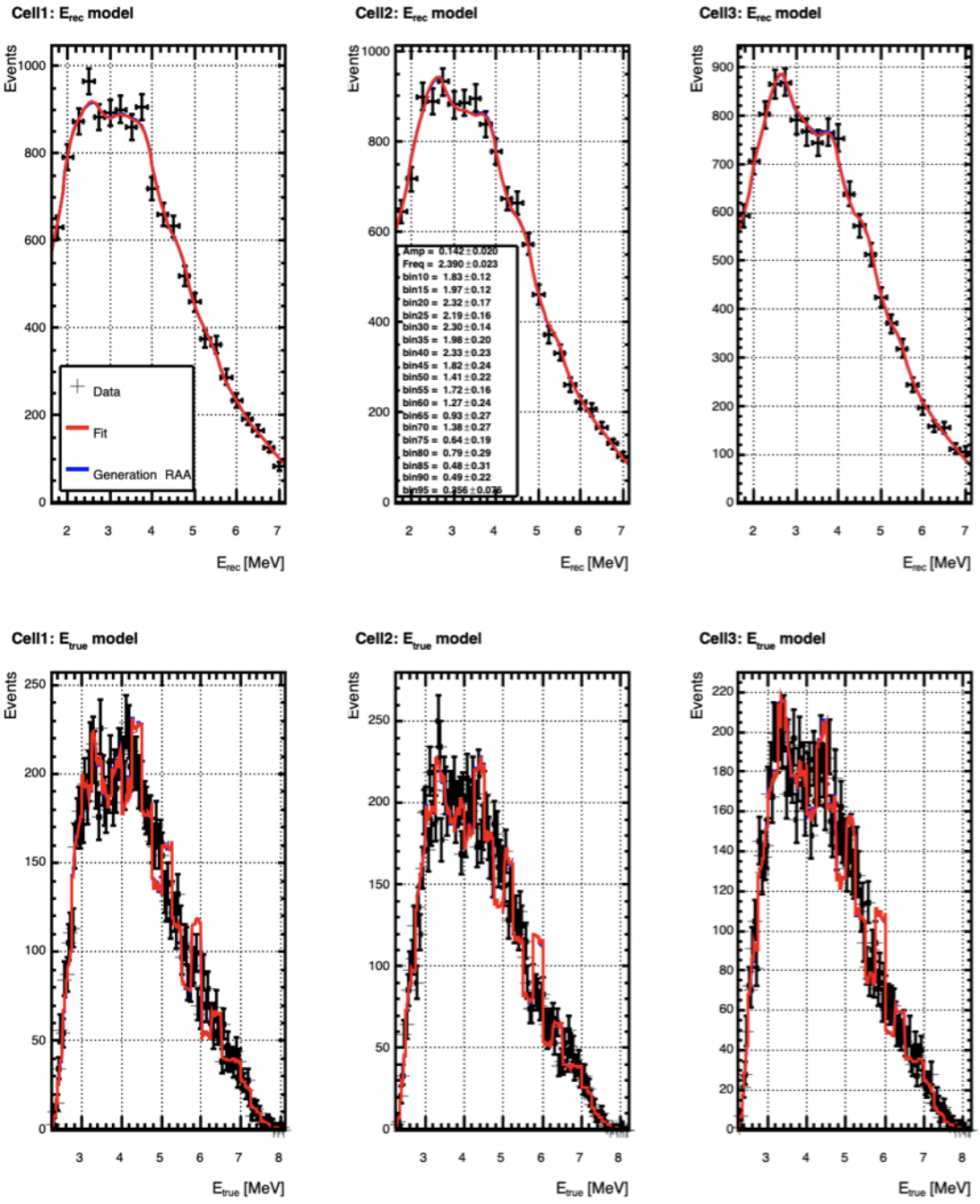
Cell1: E_rec model
Cell2: E_rec model
Cell3: E_rec model
Events
E_rec [MeV]
Data
Fit
Generation RAA
Amp = 0.142 ± 0.020
Freq = 2.390 ± 0.023
bin10 = 1.83 ± 0.12
bin15 = 1.97 ± 0.12
bin20 = 2.32 ± 0.17
bin25 = 2.19 ± 0.16
bin30 = 2.30 ± 0.14
bin35 = 1.98 ± 0.20
bin40 = 2.33 ± 0.23
bin45 = 1.82 ± 0.24
bin50 = 1.41 ± 0.22
bin55 = 1.72 ± 0.16
bin60 = 1.27 ± 0.24
bin65 = 0.93 ± 0.27
bin70 = 1.38 ± 0.27
bin75 = 0.64 ± 0.19
bin80 = 0.79 ± 0.29
bin85 = 0.48 ± 0.31
bin90 = 0.49 ± 0.22
bin95 = 0.256 ± 0.036
Cell1: E_true model
Cell2: E_true model
Cell3: E_true model
Events
E_true [MeV]

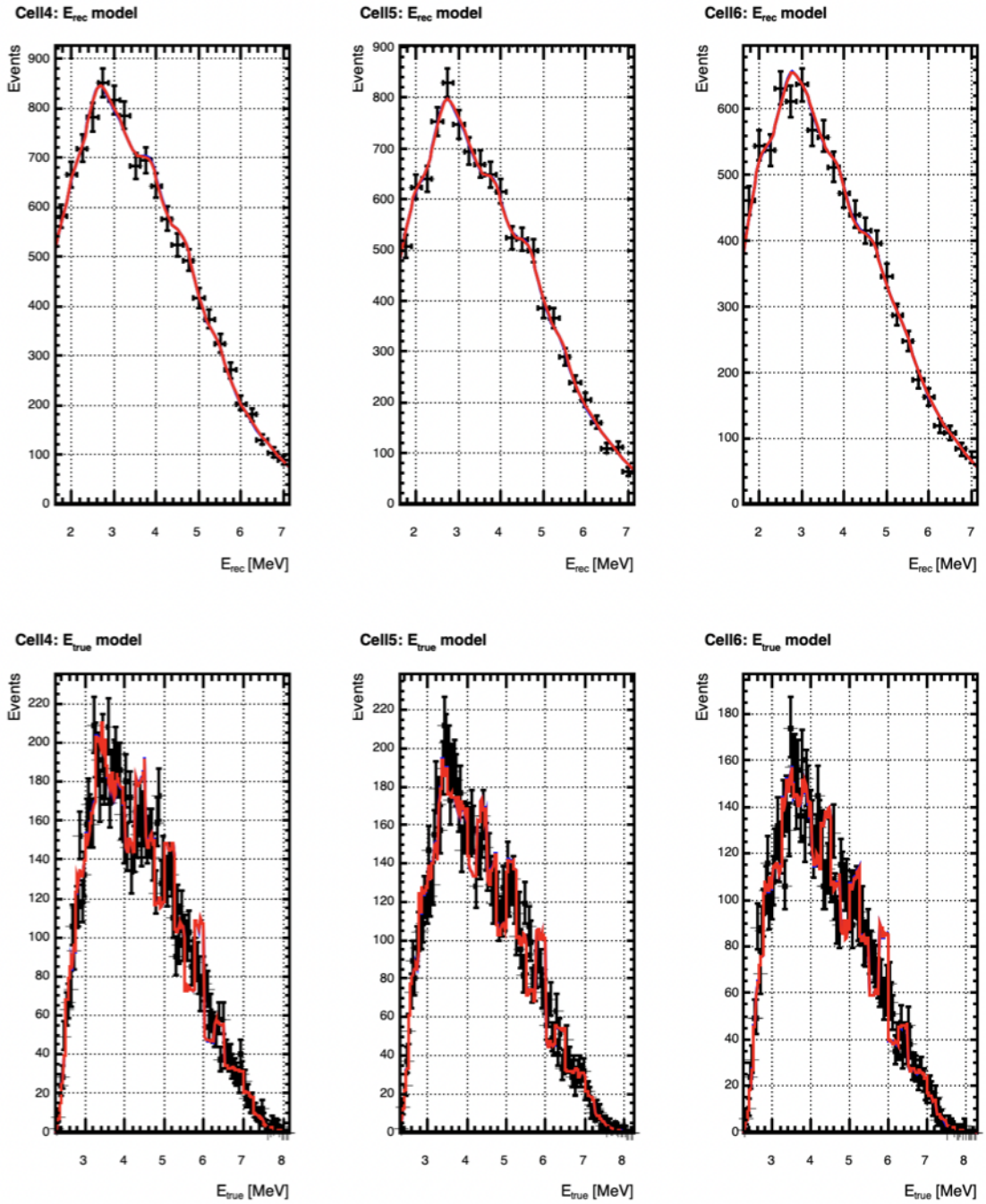

Figure 5.10: Example of the marginalised PDF fitted to a neutrino MC sample of 80 000 events in which an oscillation with the RAA parameters ($\sin^2 2\theta_{new}$=0.14, Δm^2_{41}=2.4 eV^2) was injected. The result of the fit is very close to the injected value of the parameter, as shown by the fact that the fitted PDF (red) is almost perfectly superimposed to the PDF with the injected parameter value in blue. The E_{true} spectrum resulting from the fit is visible in the bottom plots. Anticorrelation in the fluctuations of the fitted values of neighbouring $S(E_{true})$ bins is observed, as is often the case in unfolding problems.

5.3.3 Inclusion of the systematic uncertainties

Systematic uncertainties on the detector response model are taken into account by adding pull terms on the detector response parameters. In the PDF of the model, each

detector response parameter p is replaced by $p(1+\pi)$, with p now fixed in the fit and π allowed to vary. The following pull term is also added in the χ^2:

$$\left(\frac{\pi}{\sigma_\pi}\right)^2 \tag{5.13}$$

where σ_π is the relative uncertainty on the fit parameter.

For the energy scale parameters $\vec{\mu}$, σ_π is the quadratic sum of the fit error of the tuning of the detector response parameter and the systematic uncertainty extracted from the analysis of the ^{12}B as described in the previous chapter.

For the other detector response parameters, only the fit errors of the tuning of the detector response parameters is considered.

The pull terms are all independent from one another and from one cell to another. This equates to having only uncorrelated uncertainties and in that, it is a conservative approach.

5.4 Principles of the statistical analysis

The analysis presented here is a shape only analysis, in that only information from the spectrum shape in each cell is considered. The information on the absolute rate is not taken into account in order to be independent from the predicted absolute rate. The analysis is designed to be independent from the predicted spectrum shape, by letting free in the fit the values of the E_{true} spectrum bins

The goals of the statistical analysis of the neutrino data can be listed in four points:

- determining the most likely value for the parameters of interest $\sin^2\theta_{new}$ and Δm^2_{41};
- evaluating the goodness of fit, to estimate if the model can describe accurately the data;
- performing a discovery test: this comes down to trying to reject the no-oscillation hypothesis ($\sin^2\theta_{new}$=0; Δm^2_{41}=0) and any other interesting hypothesis such as the RAA hypothesis;
- constructing the confidence interval. The confidence interval includes the true parameters' value at a given confidence level. In the case of neutrino oscillation, it takes the form of a 2D exclusion/acceptance contour. In addition, the sensitivity confidence intervals can be constructed. This plot shows the area of the parameter phase space, for which, if an oscillation exists the experiment will be able to detect it at a given confidence level.

5.4.1 Determination of the most likely value of the oscillation parameters

χ^2 function

The determination of the most likely value of the oscillation parameters $\sin^2 2\theta_{new}$ and Δm^2_{41}, is made by minimising the following χ^2 function between the measured energy

spectrum $D_i(Erec)$ and the neutrino oscillation model:

$$\chi^2(sin^2 2\theta, \Delta m^2, \vec{\pi}) = \sum_{celli} \left(\frac{D_i(E_{rec}) - N_{celli} \times F_{celli}^{E_{rec}}(E_{rec}, sin^2 2\theta, \Delta m^2, \vec{\pi_{celli}})}{U_i} \right)^2 + \sum_{celli} \sum_{p} \left(\frac{\pi_{p,celli}}{\sigma_{p,celli}} \right)^2 \quad (5.14)$$

where $\vec{\pi}$ are pull terms, representing nuisance parameters on the detector response and N_{celli} is the number of observed events the Data spectrum of cell i.

The PDF of the model for each cell $F_{celli}^{E_{rec}}$ is by definition normalised to 1 and the normalisation N_{celli} is not a parameter of the fit but given by the data spectra. In other words, the information of the relative normalisation of the cells is not taken into account in the analysis presented here. Indeed, the effect of an oscillation at the RAA parameters value on the cells relative normalisation has been found to be negligible compared to the statistical uncertainty for a MC sample of 80 000 events, as shown in Figure 5.11. Furthermore, systematic uncertainties of order ∼1 % in the target volume of each cell [A$^+$20d] render the cell's normalisation even more insensitive to differences induced by oscillations.

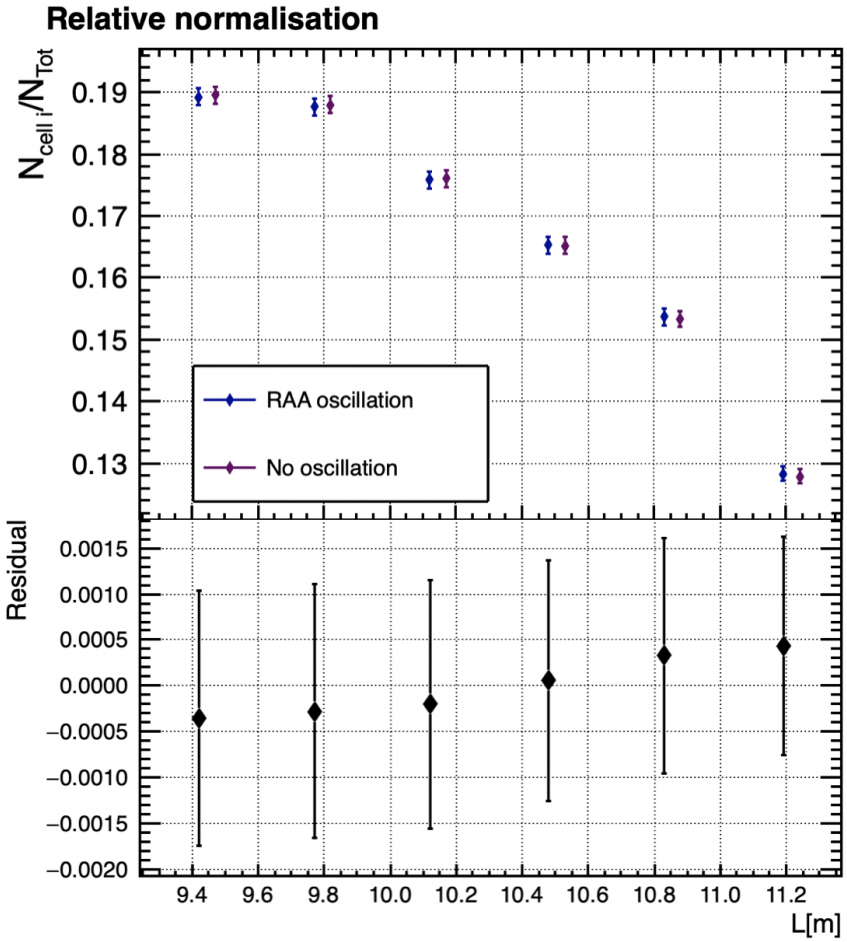

Figure 5.11: The top plot shows the effect of the RAA oscillation on the relative cell normalisation for a MC sample of ∼80 000 events. The relative normalisation of each cell for the RAA oscillation (blue) is compared to the no-oscillation (magenta). The no-oscillation points are slightly shifted to ease the comparison with the RAA points. The effect is small compared to the statistical uncertainty. The bottom plot shows the residuals between the RAA and the no-oscillation cases.

A specific procedure has been developed to minimise the χ^2 function.

χ^2 minimisation procedure

Because of the sinusoidal dependence on the Δm^2 parameter the χ^2 function is not globally parabolic but presents an alternation of local minima and maxima, as shown in Figure 5.12. Due to this shape for the χ^2 function, traditional gradient descent minimisation algorithms (such as MINUIT) get stuck in local minima. Although the χ^2 is not globally parabolic, it is locally parabolic, and once the right frequency is given as initial value of the fit, the gradient descent is able to find the true global minimum.

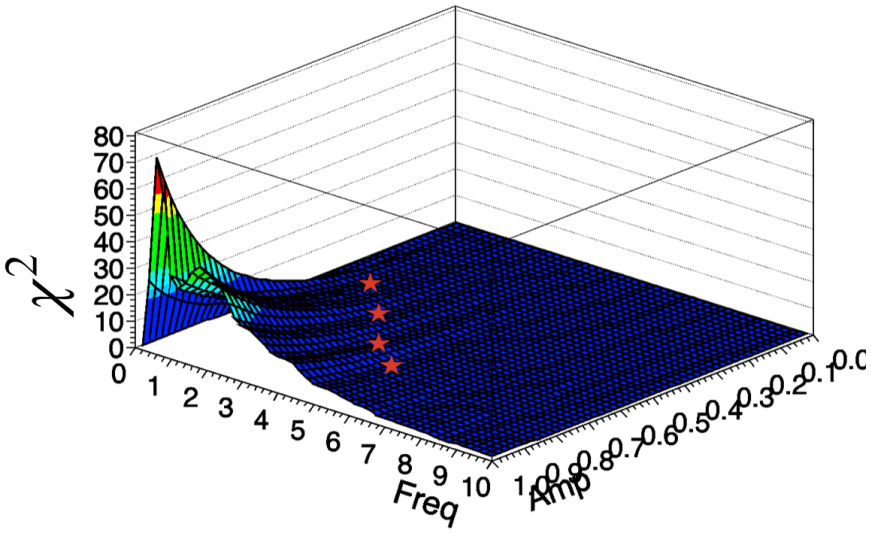

Figure 5.12: χ^2 as a function of the oscillation amplitude and frequency, the local minima are represented by the red stars.

The first step of our minimisation procedure is to scan the χ^2 value along the frequency axis at a fixed amplitude. We restrict the scan to the range [0,10] eV^2. The chosen amplitude is 0.5, but tests showed that the chosen amplitude value had little impact on the result. An example of such a scan is presented in Figure 5.13. Each frequency giving a local χ^2 minimum obtained from the scan is a candidate frequency. Each candidate frequency is tested: to do so we let the MINUIT algorithm perform a fast minimisation (MINUIT's `STRATEGY=0`) of the χ^2 starting from the frequency candidate given by the scan. For this preliminary minimisation the amplitude, the frequency and the $S(E_{true})$ bins are free parameters of the fit but the pull terms are fixed.

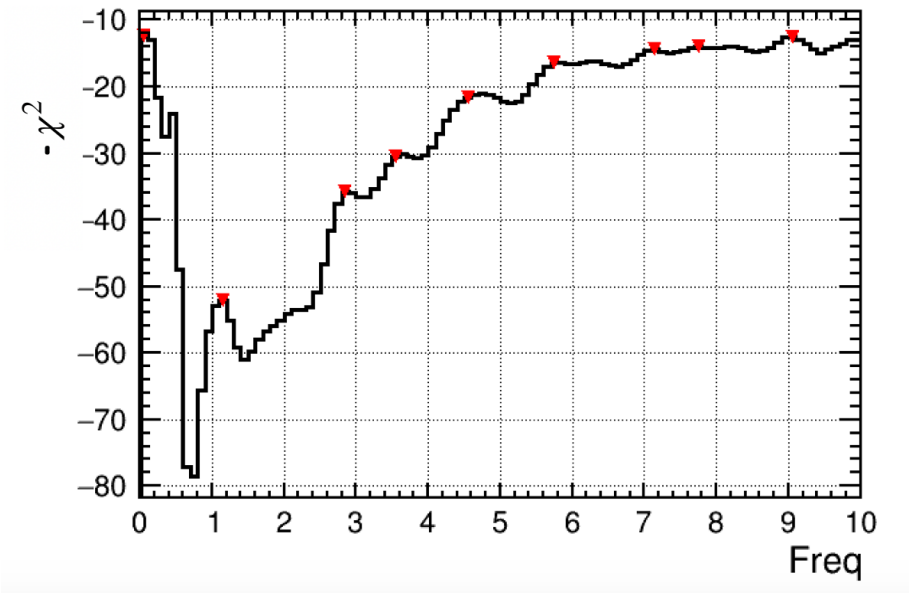

Figure 5.13: Negative χ^2 scan along the frequency for an amplitude fixed to 0.5, the local maxima are represented by the red triangle. The frequency associated to the local maxima are candidate frequencies to be tested (see text).

The candidate giving the best χ^2 minimum is taken to perform the final minimisa-

tion, where all parameters are left free in the fit.

This minimisation strategy was compared to systematically testing with MINUIT 20 evenly spaced frequency values in the allowed interval [0,10] eV^2 for a hundred toys. The two strategies yields similar results (see Figure 5.14), but the strategy of the 1D scan along the frequency is much faster.

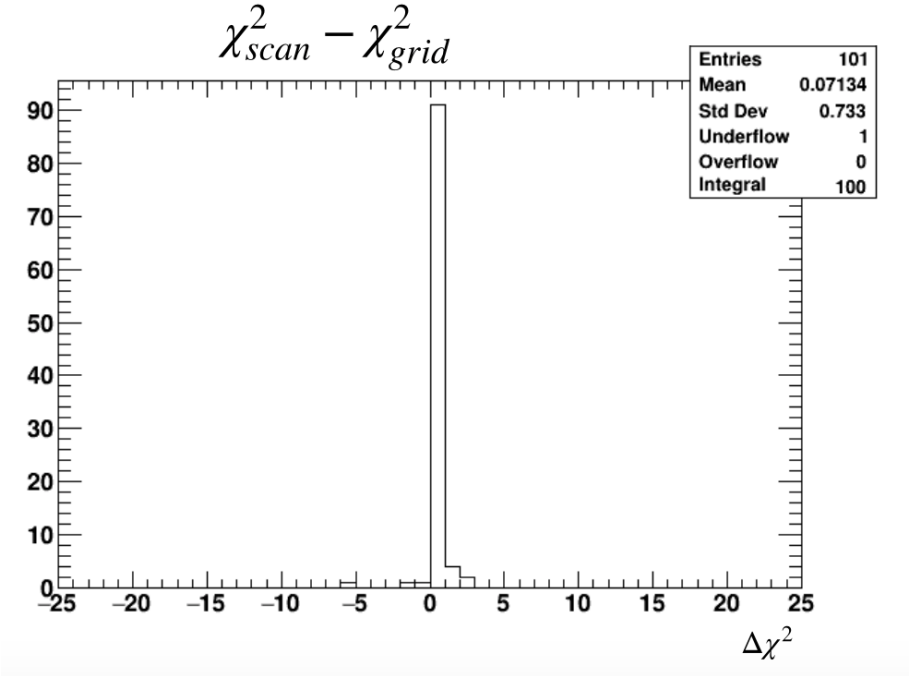

Figure 5.14: Difference between the χ^2 obtained by the frequency scan strategy and systematically probing a grid of frequency values. Both strategies yields very similar result. However, the frequency scan strategy is much faster.

Measured dataset

The analysis presented here is limited to the Phase II of data taking. We use reconstructed energy spectra with a binning of 250 keV. This binning is imposed by two effects: as stated above the binning in E_{true} must be slightly larger than the binning in E_{rec} for the fit to converge properly (otherwise very large anticorrelations between adjacent bins prevent the fit to converge), however an E_{true} binning too large induces a bias in the oscillation parameter fit.

The best compromise is a 250 keV binning, although some PSD neutrino extraction fits at high energy did not converge, resulting in empty bins in the spectra. The empty bins are in the spectra of cells 2, 5 and 6 as presented in Figure 5.15. In the fit, the empty bins are set to 0 and an uncertainty as large as the spectrum maximum is attributed. That amounts to say that we do not have any information about the value of these bins. STEREO's published oscillation analysis does not encounter this problem as they use a 500 keV binning in E_{rec}.

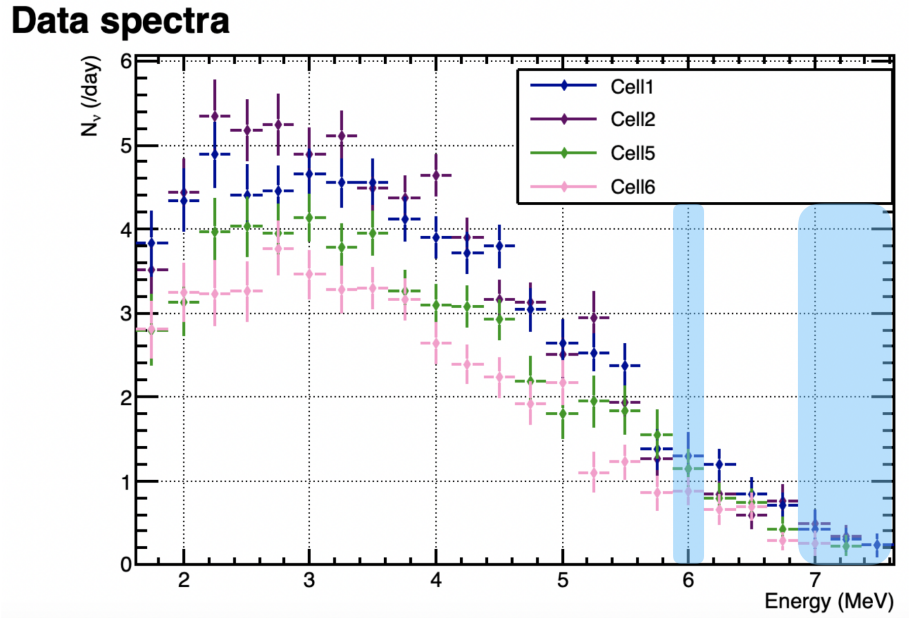

Figure 5.15: Energy spectra of the Phase II data for cell 1 (blue), cell 2 (magenta), cell 5 (green), cell 6 (pink). Cell 2, 5 and 6 have empty bins at high energy as indicated by the blue bands.

Fit of the data spectra

The fit of the data spectra is shown in Figure 5.16, the resulting values of the oscillation parameters are $\sin^2 2\theta$=0.35±0.12 and Δm^2=9.13±0.09 eV^2, and a χ^2=77.9. Fitted values of the pull terms are all well within the estimated values of their associated uncertainties, thus showing that the detector response model is well suited to data. The one exception are the μ_1 parameters: the fitted pull term value for the μ_1 parameter for cell 6 is 1.09 times the estimated uncertainty σ_{μ_1}, while for the other cells, the pull associated to μ_1 is varies by a significant fraction of σ_{μ_1} (see Table 5.1).

Cell	Param.	Pull [σ]	Cell	Param.	Pull [σ]	Cell	Param.	Pull [σ]
1	μ_0	0.12	2	μ_0	0.03	3	μ_0	0.18
	μ_1	0.62		μ_1	0.28		μ_1	0.03
	μ_2	0.09		μ_2	0.008		μ_2	0.03
	Δ	0.03		Δ	0.002		Δ	0.05
	σ_0	0.04		σ_0	0.008		σ_0	0.07
	σ_1	0.01		σ_1	0.006		σ_1	0.03
	σ_2	0.01		σ_2	0.004		σ_2	0.04
	σ_G	0.008		σ_G	0.0001		σ_0	0.007
	α_0	0.03		α_0	0.02		α_0	0.10
	α_0	0.15		α_0	0.11		α_0	0.07
	α_0	0.08		α_0	0.07		α_0	0.01
	α_0	0.02		α_0	0.04		α_0	0.01
	α_0	0.04		α_0	0.06		α_0	0.03
	n_0	0.02		n_0	0.01		n_0	0.03
	f_0	0.05		f_0	0.005		f_0	0.09

Cell	Param.	Pull [σ]	Cell	Param.	Pull [σ]	Cell	Param.	Pull [σ]
4	μ_0	0.04	5	μ_0	0.29	6	μ_0	0.36
	μ_1	0.14		μ_1	0.54		μ_1	1.09
	μ_2	0.02		μ_2	0.06		μ_2	0.12
	Δ	0.01		Δ	0.005		Δ	0.05
	σ_0	0.03		σ_0	0.01		σ_0	0.02
	σ_1	0.01		σ_1	0.004		σ_1	0.02
	σ_2	0.01		σ_2	0.01		σ_2	0.007
	σ_G	0.008		σ_G	0.009		σ_G	0.02
	α_0	0.01		α_0	0.003		α_0	0.16
	α_0	0.01		α_0	0.02		α_0	0.23
	α_0	0.005		α_0	0.009		α_0	0.09
	α_0	0.005		α_0	0.01		α_0	0.003
	α_0	0.001		α_0	0.02		α_0	0.002
	n_0	0.001		n_0	0.001		n_0	0.05
	f_0	0.01		f_0	0.004		f_0	0.11

Table 5.1: Value of the pull terms for the fit of the Phase II data

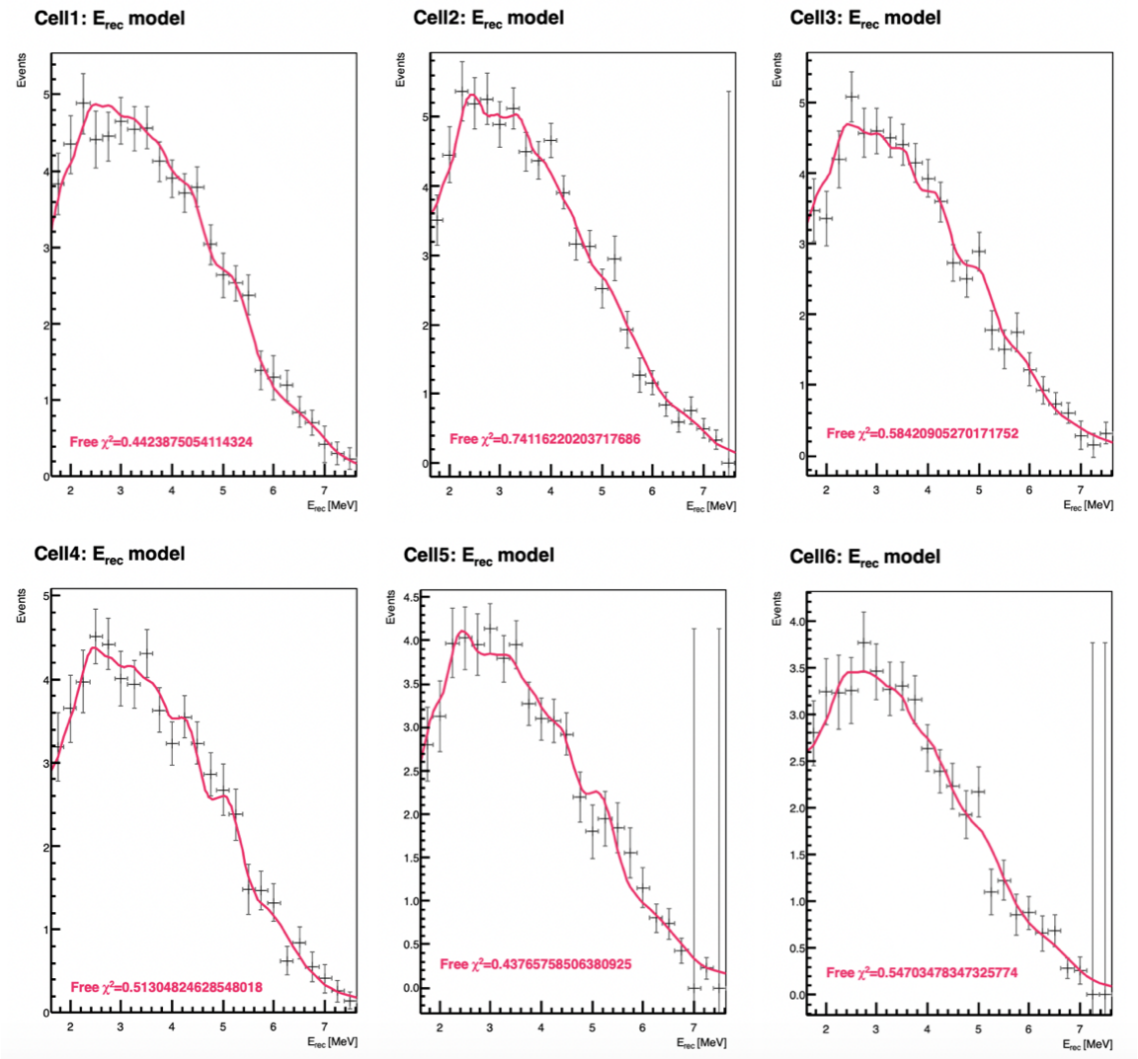

Figure 5.16: Result of the fit of the Phase II data E_{rec} spectra, the fitted oscillation parameters are $\sin^2 2\theta$=0.35±0.12 and Δm^2=9.13±0.09 eV^2. The fit gives a best χ^2=77.9

Although the fit converges to non-null values for the oscillation parameters, this can not be interpreted as an evidence of an oscillation. The reason is that statistical fluctuations across bins mimic an oscillation pattern and so the minimal χ^2 is always found far from the no-oscillation hypothesis. This can be seen in Figure 5.17, that shows the distribution of the fitted oscillation parameters obtained for non-oscillated toys.

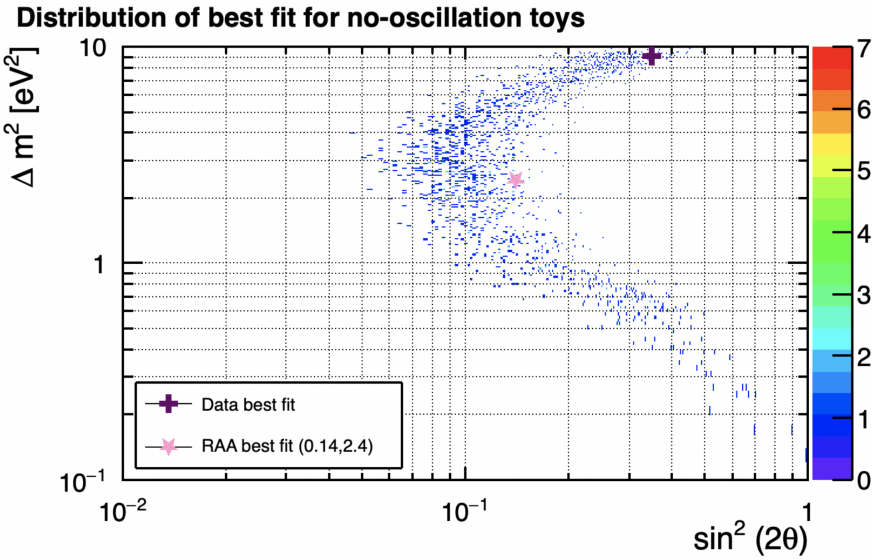

Figure 5.17: Distribution of the oscillation parameters given by the fit of non-oscillated toys. Although, the toys are generated with no oscillation, the oscillation parameters found by the fit are far from zero. This is explained by the fact that statistical fluctuations across bins mimic oscillations and so the best χ^2 is always found for non-zero oscillation parameters.

5.4.2 Goodness of fit evaluation

The goodness of fit allows to judge if the model is able to describe accurately the data or not.

χ^2 law

Traditionally, the χ^2 value obtained in the data is compared to the χ^2 distribution for the corresponding degrees of freedom. The χ^2 distribution for k degrees of freedom is given by:

$$f(x,k) = \frac{1}{2^{0.5k}\Gamma(\frac{k}{2})} \times x^{0.5k-1}e^{-\frac{x}{2}} \ \forall \ x \geq 0 \tag{5.15}$$

where Γ is the Euler Gamma function and x the χ^2 value.

The goodness of fit is then quantified by the p-value of the measured χ^2_{Data} with respect to the corresponding χ^2 distribution.

Withal, the χ^2 law applies only if a set of regularity conditions required by Wilk's theorem [Wil38] are verified, which is generally not the case in neutrino oscillation searches [AN20]. That is why in our case the expected χ^2 distribution must be computed from numerous pseudo-experiments.

The wrong way to generate pseudo-experiments

To generate pseudo-experiments (or toys), the E_{true} spectrum with STEREO's excess added is propagated through the detector response model to obtain an Asimov[2] E_{rec}

[2]The term "Asimov dataset" is used to define a dataset representative of the whole population (without fluctuations whatsoever). This term was coined by Cowan, Cranmer, Gross and Vitells [CCGV11]: it alludes to the novel "Franchise" by Isaac Asimov in which the single most representative individual is chosen in an election to replace the whole electorate.

spectrum (see Figure 5.18a). The same bins that are empty in the data spectra are set to 0 in the toys and their associated uncertainty is set to the spectrum maximum (as it is done for the data spectra). This ensures that both data spectra and toy spectra have the same number of degrees of freedom, otherwise the comparison is not possible. To make sure that the uncertainties on the detector response are taken into account in the evaluation of the goodness of fit, we vary within their uncertainties the response model parameters when we generate each toy experiment. Finally, each bin of the Asimov dataset is fluctuated independently from the others, the size of the fluctuation in each bin being given by the parametrisation of the PSD fit errors (more details on the determination of this parametrisation are presented in the thesis of L. Bernard [Ber19]).

The relative error on the neutrino rate in this parametrisation is given by the quadratic sum of the signal a and background b contributions in the E_{rec} space:

$$\frac{\Delta N^{\nu}_{l,i}}{N^{\nu}_{l,i}} = \sqrt{a^2_{l,i} \times \frac{1}{x_{l,i}} + b^2_{l,i} \times \frac{1}{x^2_{l,i}}} \tag{5.16}$$

where l denotes the cell and i the energy bin, and $x = \frac{N_\nu(\sin^2 2\theta, \Delta m^2)}{N_\nu(0,0)}$

Naturally, the size of the error in each bin depends on the oscillation hypothesis, and the cell, since the number of events is smaller in the cells further away from the nuclear reactor core.

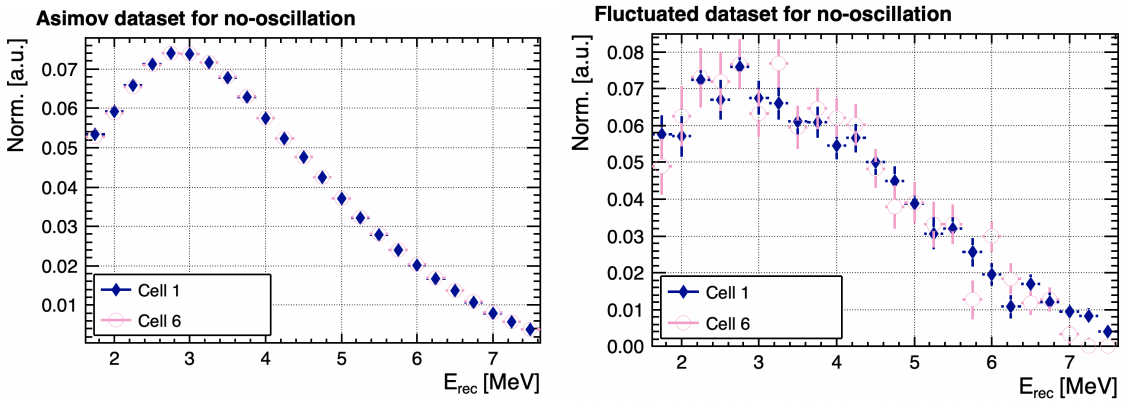

(a) (b)

Figure 5.18: Asimov E_{rec} spectra for cells 1 (blue) and 6 (pink). These spectra are obtained by propagating the E_{true} spectrum through the detector response (5.18a). The Asimov dataset is fluctuated bin-to-bin independently with gaussian standard deviations given by the PSD fit error parametrisation (5.18b).

500 non-oscillated toys were generated this way and fitted to compute the χ^2 distribution, as it can be seen in Figure 5.19. The χ^2_{Data} value in red is not typical of the obtained distribution, with a p-value $\gtrsim 98$ %. Although such a value is not completely impossible, it is quite unlikely and hints at a mismodelisation of some effect.

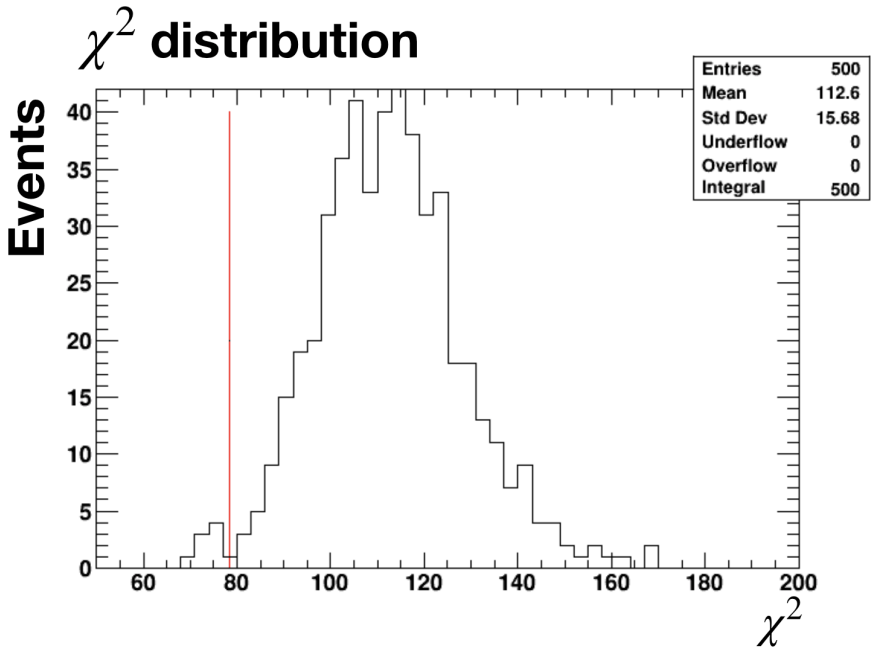

Figure 5.19: χ^2 distribution obtained for the toy generated according to the procedure given above (black), The χ^2_{Data} value is given by the red vertical line. We obtain a p-value of ∼98 %.

Toy generation: a better way

Many attempts were made at refining the model to have a χ^2_{Data} typical with respect to the χ^2 distribution of the toys.

Among other things, we checked that the minimisation strategy lead to the true χ^2 minimum: if for some reason the minimisation does not lead to the true minimum for the toys this could explain the discrepancy. We tried switching between the Huber spectrum with and without excess. We also investigated increasing the errors in the toys given by the PSD fit parametrisation. All of these trials led to no significant improvement.

We then decided to fix separate groups of parameters in the fit to see which group of parameters was making the difference between toy and data. The parameters belong in one of three groups: oscillation parameters, pull term parameters and E_{true} spectrum bins parameters. The following fits were made on a toy experiment chosen to be typical of the whole distribution and generated with the Huber plus excess prediction, and on the data:

- all parameters free: $\chi^2_{osc+spec+pulls}$
- fixing pull terms to 0, all others parameters free: $\chi^2_{osc+spec}$
- fixing all E_{true} spectrum bins, all other parameters free: $\chi^2_{osc+pulls}$
- only amplitude and frequency free, all other parameters fixed: χ^2_{osc}
- Amplitude and frequency fixed to 0, all other parameters free: $\chi^2_{spec+pulls}$

From these fits, we can deduce the gain in χ^2 brought by each parameter group. For the toy:

- $\Delta\chi^2_{pulls} = \chi^2_{osc} - \chi^2_{osc+pulls} \approx 3.5$
- $\Delta\chi^2_{spec} = \chi^2_{osc} - \chi^2_{osc+spec} \approx 13.5$
- $\Delta\chi^2_{osc} = \chi^2_{spec+pulls} - \chi^2_{osc+spec+pulls} \approx 2.4$

and for the data:

- $\Delta\chi^2_{pulls} \approx 4$
- $\Delta\chi^2_{spec} \approx 24$
- $\Delta\chi^2_{osc} \approx 5.5$

The values of $\Delta\chi^2_{pulls}$ are very similar for the data and the typical toy; the remaining difference (0.5 χ^2 unit) is very small, confirming that the response model describes accurately the data.

The difference between data and toy for the $\Delta\chi^2_{spec}$ is more puzzling because, the E_{true} spectrum used to generate the toy is as close as it can be to the E_{true} spectrum in the data: the excess added to Huber's spectrum is that one observed by STEREO in the Phase II data, precisely the dataset that is currently being analysed. Somehow the fit is able to accommodate the E_{rec} spectrum for data more than for the toys.

One hypothesis that has been overlooked in the toy generation is the bin-to-bin independent gaussian fluctuation of the bins. A more realistic approach is to include poissonian bin-to-bin independent fluctuations in the E_{true} spectrum and propagate this fluctuated E_{true} spectrum through the detector response to obtain a fluctuated E_{rec} spectrum, since the detector response and in particular the energy resolution of the detector will smear the fluctuations across several bins in E_{rec}. However, since we do not have the E_{true} predicted spectrum for the background events, the spectrum must be fluctuated in two steps: first, the signal spectrum $S(E_{true})$ is poisson fluctuated bin-to-bin independently, according to the nominal (Huber predicted) normalisation in each cell, and the E_{true} spectrum is propagated through the response model. The E_{rec} spectrum obtained this way has signal fluctuations that are correlated across bins. Second, the fluctuations due to the presence of background in the PSD fit are added to the E_{rec} spectrum, bin-to-bin independently, by taking the error given by the PSD fit error parametrisation for the background term only:

$$\frac{\Delta N^{\nu}_{l,i}}{N^{\nu}_{l,i}}\Big|_{B\ only} = \frac{b_{l,i}}{x_{l,i}} \tag{5.17}$$

We note the background part of the fluctuation is lacking bin-to-bin correlations.

About 1700 toys were generated with the new treatment of the fluctuations, the goodness of fit obtained for these toys is presented in Figure 5.20, we obtain a p-value of 54 %. The χ^2_{Data} is much more typical of the toy distribution obtained this way.

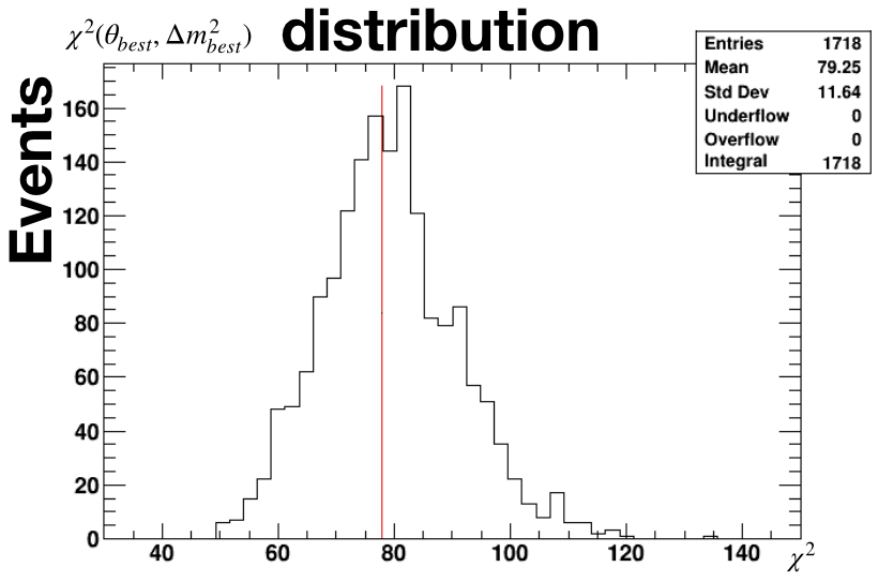

Figure 5.20: χ^2 distribution obtained for the toy generated with the correct treatment of the statistical fluctuations. The χ^2_{Data} value is given by the red vertical line, we compute a p-value of ∼54 %.

To conclude, since the χ^2 law is not valid in neutrino oscillation searches, the number of degrees of freedom can not directly be deduced from the number of free parameters, and the generation of toy MC is mandatory to obtain the χ^2 distribution. Nevertheless, the χ^2 distribution obtained from the toys depends on the treatment of the statistical fluctuations, an erroneous treatment of the fluctuations (lack of correlation for example) results in a miscomputation of the χ^2 distribution.

5.4.3 Discovery test

As stated above, a non-zero value of the oscillation parameters given by the fit is not an evidence of an oscillation, since the form of the oscillation probability can accommodate statistical fluctuations across bins, resulting in non-zero fitted oscillation parameters.

Test statistic

To claim or to refute the existence of a neutrino oscillation, the way to go is to perform a hypothesis test, considering as the null-hypothesis the no-oscillation hypothesis: H_0 : $\{\sin^2 2\theta = 0; \Delta m^2 = 0\}$ and as alternate hypothesis an unspecified oscillation: H_1 : $\{0 \leq \sin^2 2\theta \leq 1; 0 \leq \Delta m^2\}$.

From these two hypothesis, a test statistic is built on a dataset $\vec{D}$. In this analysis the test statistic used is a $\Delta\chi^2$ test, defined as:

$$\Delta\chi^2 = \min_{\vec{\pi}} \chi^2((\sin^2 2\theta = 0; \Delta m^2 = 0; \vec{\pi})|\vec{D}) - \min_{(\sin^2 2\theta; \Delta m^2; \vec{\pi})} \chi^2((\sin^2 2\theta; \Delta m^2; \vec{\pi})|\vec{D})) \quad (5.18)$$

The test statistic quantifies the agreement between the dataset and the H_0 hypothesis.

Although other test statistics exist, the choice of this specific test statistic is motivated by the fact that once inverted, it results in Feldman-Cousins confidence inter-

vals [FC98]. By construction Feldman-Cousins confidence intervals gives the proper coverage.

Test of the non-oscillation hypothesis

A discovery test comes down to testing the no-oscillation hypothesis, to do that, the test statistic constructed on the data: $\Delta\chi^2_{Data}$ is compared to the distribution of the test statistic constructed on non-oscillated toys:

$$\Delta\chi^2_{no-osc} = \min_{\vec{\pi}} \chi^2((\sin^2 2\theta = 0; \Delta m^2 = 0; \vec{\pi})|\vec{D}_{no-osc}) - \min_{(\sin^2 2\theta;\Delta m^2;\vec{\pi})} \chi^2((\sin^2 2\theta; \Delta m^2; \vec{\pi})|\vec{D}_{no-osc})) \quad (5.19)$$

The result we obtain for a distribution constructed on about 500 toys is presented in Figure 5.21. We obtain a p-value of 16.8 %, hence the no-oscillation hypothesis is **not** rejected.

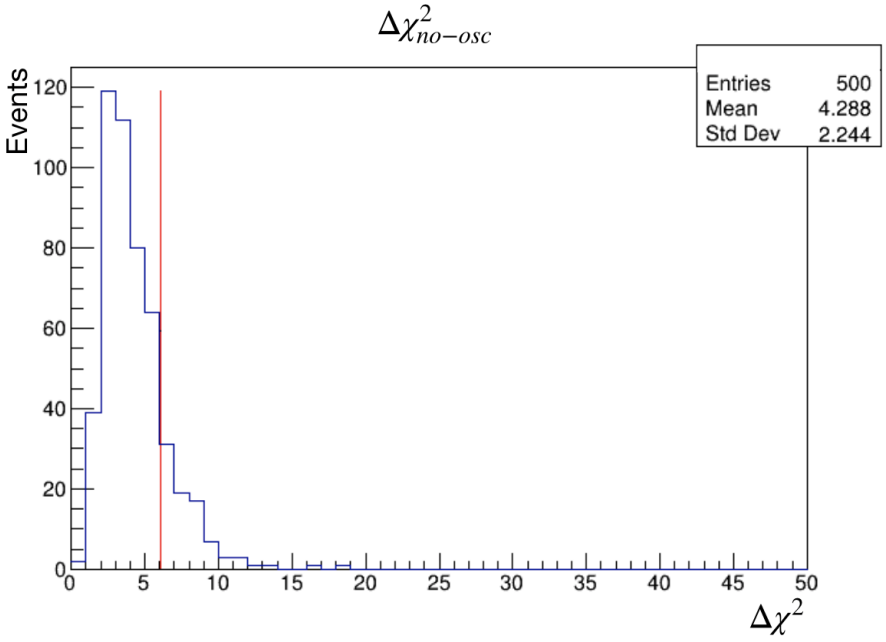

Figure 5.21: $\Delta\chi^2$ distribution for the non-oscillation hypothesis (blue) and $\Delta\chi^2_{Data}$ value (red). We report a p-value of 16.8 %. The no-oscillation hypothesis is not rejected.

Test of the RAA hypothesis

In addition to the non-oscillation hypothesis, it is interesting to see if the RAA oscillation can be rejected. The test statistic is then constructed on RAA-oscillation toys, the null hypothesis of the test H_0 is no longer the non-oscillation hypothesis but the RAA hypothesis:

$$\Delta\chi^2_{RAA} = \min_{\vec{\pi}} \chi^2((\sin^2 2\theta = 0.17; \Delta m^2 = 2.3; \vec{\pi})|\vec{D}_{RAA}) - \min_{(\sin^2 2\theta;\Delta m^2;\vec{\pi})} \chi^2((\sin^2 2\theta; \Delta m^2; \vec{\pi})|\vec{D}_{RAA})) \quad (5.20)$$

The results obtained with more than 1000 toys are presented in Figure 5.22. The computed p-value is 1.1 % hence the RAA hypothesis is rejected at the 98.9 % C.L.

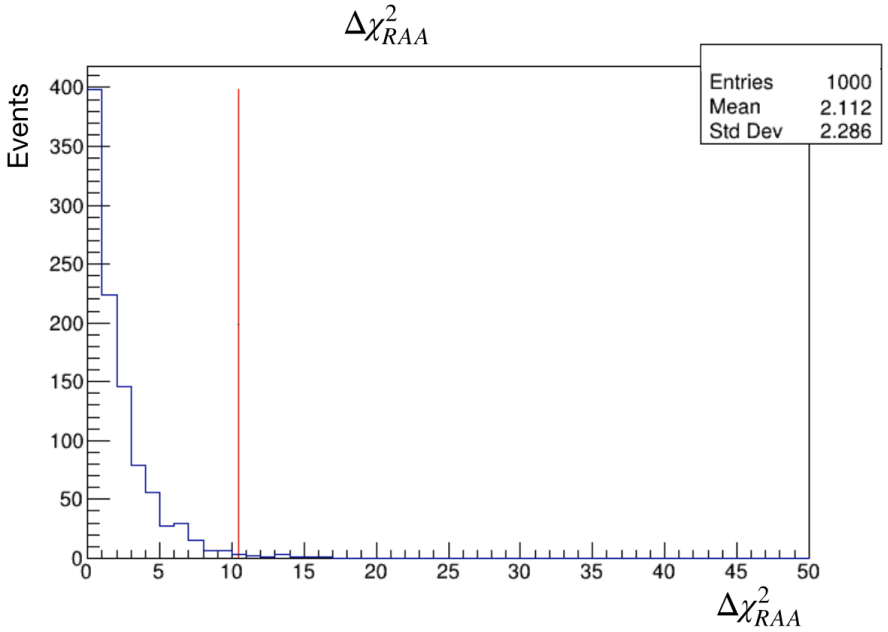

Figure 5.22: $\Delta\chi^2$ distribution for the RAA hypothesis $(\sin^2 2\theta, \Delta m^2) = (0.17, 2.3)$ from RAA-oscillated toys (blue). The $\Delta\chi^2_{Data}$ value is given by the red vertical line, we report a p-value of 1.1 %. The RAA hypothesis is rejected at the 98.9 % confidence level.

Comparison with the collaboration official framework

We compare our result with that obtained using the official framework of the collaboration described in [A+20d]. A preliminary re-analysis of the Phase II data with the official framework gives a p-value of ∼3 % for the test of the non-oscillation hypothesis and a p-value of ∼0.1 % for the test of the RAA hypothesis [Via21]. In comparison our framework, gives a p-value of ∼17 % and ∼1 % respectively.

5.4.4 Sensitivity confidence intervals

There are two ways to construct a sensitivity confidence interval: the exclusion sensitivity and the discovery sensitivity.

Discovery sensitivity confidence interval

The discovery sensitivity confidence interval is the set of hypothesis, that rejects the no-oscillation hypothesis 50 % of the time at the desired confidence level, if they are true.

To construct this sensitivity interval, the distribution of $\Delta\chi^2(\sin^2 2\theta = 0, \Delta m^2 = 0|\vec{D}_{no\ osc})$ is constructed where $\vec{D}_{no\ osc}$ denote non-oscillated toys. Then for each hypothesis $(\sin^2 2\theta = A, \Delta m^2 = F)$ of the parameter phase space the median of the distribution of $\Delta\chi^2(\sin^2 2\theta = 0, \Delta m^2 = 0|\vec{D}_{A,F})$ is computed, and if the p-value of the median with respect to the $\Delta\chi^2(\sin^2 2\theta = 0, \Delta m^2 = 0|\vec{D}_{no\ osc})$ distribution is smaller than 1-C.L. (with C.L. the desired confidence level) the (A, F) hypothesis is added to the confidence interval (because the no-oscillation hypothesis will be rejected 50 % of the times if this hypothesis is true).

Exclusion sensitivity confidence interval

Assuming there is no signal, the exclusion sensitivity confidence interval is the set of hypothesis that will be rejected 50 % of the time at the desired confidence level.

To construct this sensitivity interval, the distribution of $\Delta\chi^2(\sin^2 2\theta = A, \Delta m^2 = F|\vec{D}_{A,F})$ is constructed for each (A,F) oscillation hypothesis. Then the median of the distribution of $\Delta\chi^2(\sin^2 2\theta = A, \Delta m^2 = F|\vec{D}_{no-osc})$ is computed. If the p-value of the median with respect to $\Delta\chi^2(\sin^2 2\theta = A, \Delta m^2 = F|\vec{D}_{A,F})$ distribution is smaller than 1-C.L. the (A, F) hypothesis is added to the confidence interval.

Result

In principle, both computation should yield similar results although some differences are formulated in [AN20].

Our computation of the discovery sensitivity at 95% (90%) confidence level is presented in Figure 5.23 (Figure 5.24).

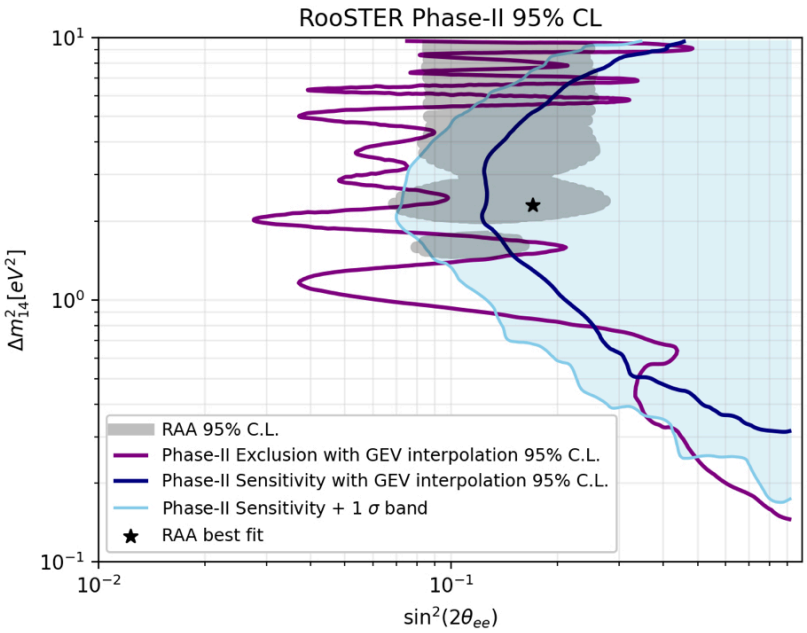

Figure 5.23: Exclusion contour of the oscillation parameter space (violet) and sensitivity contour with a statistic equivalent to the Phase II of the data sample (dark blue), the $+1\sigma$ of the sensitivity contour is also shown by the light blue line. These contours are computed at the 95% confidence level.

5.4.5 Confidence interval from observed data

The confidence interval at a given C.L. obtained from observed data is the region of the parameter space that would contain the true value of the parameters C.L. % of the time, if we were to redo the experiment many times.

To determine the confidence interval, for each oscillation (A, F) we compute the distribution of $\Delta\chi^2(\sin^2 2\theta = A, \Delta m^2 = F|\vec{D}_{A,F})$ and the value of $\Delta\chi^2(\sin^2 2\theta = A, \Delta m^2 = F|\vec{D}_{obs})$ on the measured data. If the p-value for the observed data is bigger than 1-C.L., then the (A, F) hypothesis is added to the "accepted" region

of the parameter space (equivalently, if the p-value is smaller than 1-C.L., the (A, F) hypothesis is added to the "excluded" region of the parameter space).

The confidence interval obtained for the Phase II data at 95% (90%) is presented in Figure 5.23 (Figure 5.24).

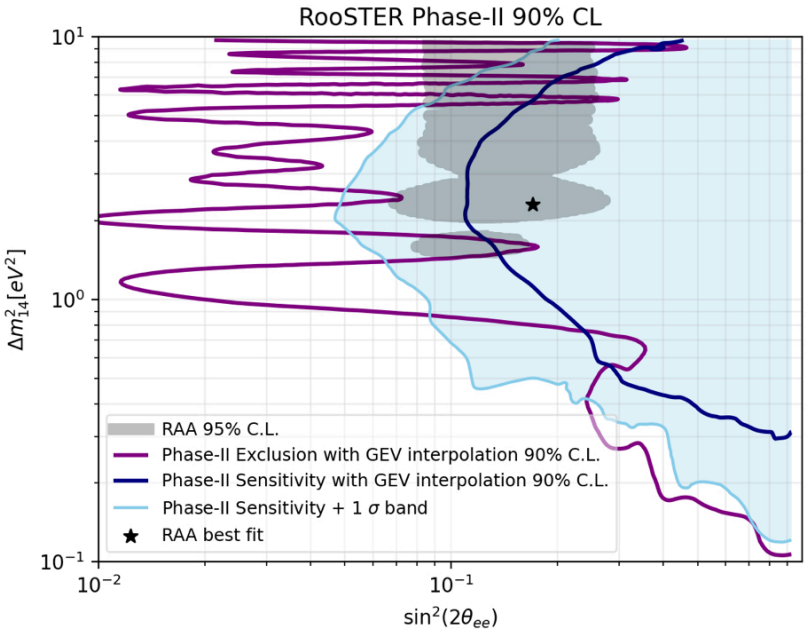

Figure 5.24: Exclusion contour of the oscillation parameter space (violet) and sensitivity contour with a statistic equivalent to the Phase II of the data sample (dark blue), the $+1\sigma$ of the sensitivity contour is also shown by the light blue line. These contours are computed at the 90% confidence level.

Comparison with the collaboration official framework

The results obtained with our framework are globally consistent with the published result [A$^+$20d]. We note that our framework performs better at high frequencies: this is likely due to the use of a finer binning that allows a better sensitivity at high frequency. On the other hand, our framework shows less sensitivity at low frequencies; this could be explained by the fact our analysis performs solely a comparison of the shape of the cells' spectra, whereas published results also make use of the relative normalisation between cells. We have shown that the sensitivity given by the relative norm between cells is negligible at the RAA best fit point, but it is not the case at low frequencies.

Contrary to the official framework, in our case, the p-value for the rejection of the no-oscillation hypothesis is greater than 10% which allows us to compute an exclusion contour at 90% confidence level (see Figure 5.24).

5.5 Conclusions

We have developed a new oscillation search framework that uses an analytical detector response model. In this approach, the detector response parameters can be fitted from calibration data or constrained directly by it.

When we apply our framework to STEREO's Phase II data, we obtain a p-value of 16.8 % for the no-oscillation hypothesis and a p-value of 1.1 % for the RAA hypothesis. Hence, we do **not** reject the no-oscillation hypothesis but we **do** reject the RAA best fit point at nearly 99 % C.L. Our 95% confidence level exclusion contour is consistent with STEREO 's published results; the small differences can be attributed to technical choices made in our framework (finer binning and no relative cells normalisation). Most of the RAA hypothesis allowed parameter space is rejected at the confidence levels considered.

Bibliography

[A+19b] J. Ashenfelter et al. Measurement of the Antineutrino Spectrum from ^{235}U Fission at HFIR with PROSPECT. *Phys. Rev. Lett.*, 122(25):251801, 2019.

[A+20d] H. Almazán et al. Improved sterile neutrino constraints from the STEREO experiment with 179 days of reactor-on data. *Phys. Rev. D*, 102(5):052002, 2020.

[A+21b] H. Almazán et al. First antineutrino energy spectrum from ^{235}U fissions with the STEREO detector at ILL. *J. Phys. G*, 48(7):075107, 2021.

[A+21c] F. P. An et al. Antineutrino energy spectrum unfolding based on the Daya Bay measurement and its applications. *Chin. Phys. C*, 45(7):073001, 2021.

[AN20] Matteo Agostini and Birgit Neumair. Statistical Methods Applied to the Search of Sterile Neutrinos. *Eur. Phys. J. C*, 80(8):750, 2020.

[Ber19] Laura Bernard. *Recherche d'un neutrino stérile avec l'expérience STEREO : détermination des spectres neutrinos et caractérisation du bruit de fond*. PhD thesis, LPSC, Grenoble, 2019.

[CCGV11] Glen Cowan, Kyle Cranmer, Eilam Gross, and Ofer Vitells. Asymptotic formulae for likelihood-based tests of new physics. *Eur. Phys. J. C*, 71:1554, 2011. [Erratum: Eur.Phys.J.C 73, 2501 (2013)].

[dK+20c] H. de Kerret et al. Double Chooz θ_{13} measurement via total neutron capture detection. *Nature Phys.*, 16(5):558–564, 2020.

[FC98] Gary J. Feldman and Robert D. Cousins. A Unified approach to the classical statistical analysis of small signals. *Phys. Rev. D*, 57:3873–3889, 1998.

[Hub11] Patrick Huber. On the determination of anti-neutrino spectra from nuclear reactors. *Phys. Rev. C*, 84:024617, 2011. [Erratum: Phys.Rev.C 85, 029901 (2012)].

[Via21] M. Vialat. Private communication. 2021.

[Wil38] S. S. Wilks. The Large-Sample Distribution of the Likelihood Ratio for Testing Composite Hypotheses. *Annals Math. Statist.*, 9(1):60–62, 1938.

APPENDIX A

THE MSW EFFECT

We can write the potential induced by the neutral and charged current in matter, acting on the various neutrino flavours as:

$$V_{\nu_\mu} = V_{\nu_\tau} = V^n_{NC} = -G_F N_n/\sqrt{2} \quad \text{(A.1)}$$

$$V_{\nu_e} = V^e_{CC} + V^n_{NC} = \sqrt{2} G_F (N_e - N_n/2) \quad \text{(A.2)}$$

These potentials must be added to the Hamiltonian that dictates the time evolution of the neutrino eigenstates. This results in an effective oscillation probability described by an effective mixing angle θ_{MSW} (here we restrict ourselves to the case of the 2 flavours neutrino oscillation for the electron neutrino) and mass splitting Δm^2_{MSW}:

$$\mathscr{P}^{MSW}_{\nu_e \to \nu_e}(L,E) = 1 - \sin^2 2\theta_{MSW} \sin^2\left(\frac{\Delta m^2_{MSW}}{4E}\right) \quad \text{(A.3)}$$

The effective oscillation parameters are given by:

$$\sin 2\theta_{MSW} = \frac{\sin 2\theta}{\sqrt{(A - \cos 2\theta) + sin^2 2\theta}} \quad \text{(A.4)}$$

$$\Delta m^2_{MSW} = \Delta m^2 \sqrt{(A - \cos 2\theta)^2 + \sin^2 2\theta} \quad \text{(A.5)}$$

with $A = 2\sqrt{2} G_F N_e E/\Delta m^2$. These equations quantify the modification to the oscillation probability due to the matter effect. In particular, the effective oscillation depends on the sign of the A term:

- if A and $\cos 2\theta$ have the same sign, the oscillation probability is enhanced, in particular if A=$\cos 2\theta$ the oscillation is maximally enhanced because $\sin 2\theta_{MSW} = 1$,
- if A and $\cos 2\theta$ have opposite signs, the oscillation probability is reduced.

Both cases are compared to the vacuum oscillation in Figure 1.8.